The Pennsylvania State University

The Graduate School

Department of Meteorology

MODELING THERMOSPHERIC NEUTRAL DENSITY

A Thesis in

Meteorology

by

Liying Qian

Submitted in Partial Fulfillment
of the Requirements
for the Degree of

Doctor of Philosophy

August 2007

The thesis of Liying Qian was reviewed and approved* by the following:

Timothy J. Kane
Professor of Electrical Engineering and Meteorology
Thesis Advisor
Chair of Committee

James F. Kasting
Professor of Geosciences

Sukyoung Lee
Professor of Meteorology

Victor Pasko
Associate Professor of Electrical Engineering

Stanley C. Solomon
Senior Scientist of the National Center for Atmospheric Research

David B. Spencer
Associate Professor of Aerospace Engineering

William H. Brune
Professor of Meteorology
Head of the Department of Meteorology

*Signatures are on file in the Graduate School

ABSTRACT

Satellite drag prediction requires determination of thermospheric neutral density. The NCAR Thermosphere-Ionosphere-Electrodynamics General Circulation Model (TIEGCM) and the global-mean Thermosphere-Ionosphere-Mesosphere-Electrodynamics General Circulation Model (TIMEGCM) were used to quantify thermospheric neutral density and its variations, focusing on annual/semiannual variation, the effect of using measured solar irradiance on model calculations of solar-cycle variation, and global change in the thermosphere. Satellite drag data and the MSIS00 empirical model were utilized to compare to the TIEGCM simulations.

The TIEGCM simulations indicated that eddy diffusion and its annual/semiannual variation is a mechanism for annual/semiannual density variation in the thermosphere. It was found that eddy diffusion near the turbopause can effectively influence thermospheric neutral density. Eddy diffusion, together with annual insolation variation and large-scale circulation, generated global annual/semiannual density variation observed by satellite drag.

Using measured solar irradiance as solar input for the TIEGCM improved the solar-cycle dependency of the density calculation shown in $F_{10.7}$-based thermospheric empirical models. It has been found that the empirical models overestimate density at low solar activity. The TIEGCM simulations did not show such solar-cycle dependency.

Using historic measurements of CO_2 and $F_{10.7}$, simulations of the global-mean TIMEGCM showed that thermospheric neutral density at 400 km had an average long-term decrease of 1.7% per decade from 1970 to 2000. A forecast of density decrease for solar cycle 24 suggested that thermospheric density will decrease at 400 km from present to the end of solar cycle 24 at a rate of 2.7% per decade. Reduction in thermospheric density causes less atmospheric drag on earth-orbiting space objects. The implication of this long-term decrease of thermospheric neutral density is that it will increase the lifetime of satellites, but also it will increase the amount of space junk.

TABLE OF CONTENTS

LIST OF FIGURES

LIST OF TABLES

ACKNOWLEDGEMENTS

I would like to thank my thesis advisor Professor Tim Kane. He has provided vital guidance through the course of my thesis study. His direction and trust have motivated me to improve my scientific skills.

Dr. Stanley Solomon, my supervisor, has mentored me with his knowledge in aeronomy and his gracious encouragement and support. Many discussions with Dr. Solomon have deepened my understanding and interest in upper atmospheric science.

I would like to express my appreciation to my other thesis committee members: Professor James Kasting, Professor Sukyoung Lee, Professor Victor Pasko, and Professor David Spencer, for helping me to develop this thesis.

Bruce Bowman of Air Force Space Command and Frank Marcos of Air Force Research Lab have provided me high quality satellite drag data. Dr. Ray Roble and Dr. Alan Burns, as well as other scientists at NCAR High Altitude Observatory (HAO): Dr. Art Richmond, Dr. Hanli Liu, Dr. Wenbing Wang, Dr. Gang Lu, Dr. Barbara Emery, Dr. Maura Hagan, Dr. Qian Wu, have helped me greatly in learning the upper atmosphere and the NCAR upper atmospheric models. Many thanks to HAO software engineer Ben Foster for his support with the NCAR models, and the HAO administration team, especially Louise Beierle, for administrative support.

I appreciate Ms. Patricia Weis-Taylor very much for her professional editing of my thesis and her kindness.

I am very grateful to my friends, especially Valerie Senger, John and Debbie Zisch, Yali and Roger Madison, for their support.

My parents, my older sister, and my younger sister are far away in China, yet their unconditional love always gives me strength.

My husband Kevin Connolly has encouraged and supported me to finish my PhD from the beginning to the end. My mother-in-law Vivian Durand has provided exceptional help with my children.

And my children Daniel, Vivian, Joseph, and Kristin, are my constant inspiration and motivation to be better, in my profession and beyond.

This research was supported by the NASA Living with a Star program, the NASA TIMED mission, and the National Center for Atmospheric Research, which is sponsored by the National Science Foundation.

Chapter 1

INTRODUCTION

1.1 Statement of Problem and Contributions to Knowledge

Satellites orbit in the Earth's upper atmosphere where the atmosphere is near vacuum. However, satellites encounter drag from this very thin atmosphere. The atmospheric parameter that determines satellite drag is atmospheric neutral density, the total mass density of the ambient atmosphere. Errors in estimating neutral density cause a difference between predicted satellite orbit and actual satellite orbit. These errors reduce the ability of satellite operations to maintain a catalog of all space objects; to provide collision avoidance warnings; to predict satellite positions; to predict satellite reentries; and to optimize satellite design in terms of lifetime, on-board fuel, and satellite attitude control.

Satellite drag calculation and prediction requires multi-faceted efforts which include understanding atmospheric neutral density and its variability. This thesis study quantifies atmospheric neutral density and its variations using a physical-based upper atmospheric general circulation model. This study made the following contributions to knowledge:

- Identified lower atmospheric contribution to the annual/semiannual variation in upper atmospheric neutral density; Identified eddy diffusion as the mechanism for the lower atmosphere to have this influence on the upper atmosphere.
- Demonstrated that the source of errors in the solar-cycle dependency of neutral density, calculated by the $F_{10.7}$-based empirical density models, is inadequate representation of solar variability at low solar activity.
- Obtained long-term trend of upper atmospheric neutral density driven by gradual increase of CO_2 concentration, using a physical-based upper atmospheric numerical model.

This work has been presented at several conferences including conferences hosted by the Committee on Space Research (COSPAR), the American Geophysical Union (AGU), and the Coupling, Energetics, and Dynamics of Atmospheric Regions (CEDAR) program. The thesis work on global change of the upper atmosphere was in 2006 Fall AGU press release. Publications so far related to this thesis study include Qian et al. [2006], Qian et al. [2007], and Solomon and Qian [2005].

1.2 An Overview of the Thermosphere/Ionosphere System

The region of the Earth's atmosphere where satellite drag estimations are important is between 200 km and 600 km. Below 200 km, satellite drag is too large for satellites to maintain orbits; while above 600 km, satellite drag is small and has less impact on satellite operations. This 200-km to 600-km region of the atmosphere is the overlapped thermosphere/ionosphere, the top region of the Earth's atmosphere. The Earth's atmosphere is divided into layers according to its vertical temperature structure. The lowest layer is the troposphere where temperature decreases with altitude since the Earth's surface absorbs most of the solar visible radiation. The troposphere is where daily weather occurs and extends from the Earth's surface to approximately 15 km. The layer above the troposphere is the stratosphere, ranging from the top of the troposphere to about 50 km, where temperature increases with altitude caused by absorption of solar irradiance by ozone. Above the stratosphere, temperature again declines with altitude due to infrared cooling by carbon dioxide. This region is identified as the mesosphere which covers the atmosphere approximately from 50 to 90 km, the mesopause. The thermosphere is the layer above the mesopause where temperature increases with altitude due to absorption of solar ultraviolet radiation by the atmospheric constituents. Absorption of solar ultraviolet radiation ionizes the thermospheric constituents and creates the ionosphere. The thermosphere and ionosphere overlap with each other. Figure 1.1 illustrates schematically the atmospheric vertical temperature structure and the associated layers.

The thermosphere is characterized by a rapid increase of temperature with altitude in the lower thermosphere, to an altitude around 300 km above which the atmosphere is nearly isothermal. The major constituents of the thermosphere are O, O_2, and N_2; and minor constituents include N, H, He, Ar, NO, and CO_2. Thermospheric constituents are gravitationally (diffusively) separated according to their molecular weights while the atmospheric constituents below are well mixed. The transition region between the mixed atmosphere and the diffusively separated atmosphere is identified as the turbopause, at an altitude around 105 km. The thermosphere is largely in diffusive equilibrium, with lighter species such as O, H, and He decreasing more slowly than heavier species such as N_2, O_2, and Ar due to smaller gravitational forces. However, thermospheric constituents are also subject to dynamic influence by wind, and to less degree, by chemical reactions, which drive the thermosphere away from diffusive equilibrium. The combined contributions from diffusion, wind, and chemical reactions determine the distribution of thermospheric constituents (composition). Figure 1.2 shows the distribution of the thermospheric constituents, of which the total mass density is referred to as the thermospheric neutral density. On the plot, "total" is total number density.

The ionosphere extends from about 80–1000 km. The major ions in the lower ionosphere are O_2^+ and NO^+. Above 200 km, O^+ becomes dominant, to an altitude about 1000 km, where H^+ becomes the dominant ion and the protonsphere begins (figure 1.3). The ionosphere includes three regions identified by inflection points of the electron density profile, which determine the reflection feature of radio waves by the ionosphere: the D-layer, the E-layer, and the F-layer. The F-layer is further divided into the F1-layer and the F2-layer (figure 1.1). Other than the D-layer, the ionosphere includes positively charged ions. The ionosphere has approximately no net charge which means that the electron density is equal to the total of positive ion densities. As a result, the ionosphere is usually described in terms of electron density. The ionosphere is weakly ionized, with electron density approximately 1000 times less than the thermospheric neutral concentration at the F2 peak (figure 1.3).

The primary energy input to the thermosphere/ionosphere system is solar irradiance. The thermosphere absorbs solar irradiance in XUV (the soft X-ray ultraviolet,

1– 30 nm), EUV (Extreme Ultra-Violet, 30–120 nm), and FUV (Far Ultra-Violet, 120–200 nm). Although some XUV and FUV can penetrate to the mesosphere; solar EUV is completely absorbed in the thermosphere. The solar EUV ionizes, dissociates, and excites the thermospheric constituents. Through these processes, it transfers its energy to the kinetic energy of electrons and ions and to the chemical potential energy of ions and neutrals. The neutral atmosphere is then heated through exothermic ion-neutral and neutral-neutral chemical reactions and through collisions of neutral constituents with electrons and ions. Figure 1.4 shows solar spectral irradiance from the XUV to the infrared. The solar XUV and EUV are the most variable part of the solar irradiance as the Sun's activity changes from low to high. Consequently, thermospheric temperature exhibits large solar-cycle variation, from about 700^{o} K at solar minimum to above 1500^{o} K at solar maximum.

The secondary energy input to the thermosphere/ionosphere system is from geomagnetic activity. Geomagnetic activities result from the interaction between the solar wind and the Earth's magnetic field. The solar wind is a highly supersonic plasma flow ejected from the Sun. When the solar wind encounters the Earth's magnetic field, it makes a sudden transition from supersonic to subsonic speed, compresses the Earth's magnetic field on the dayside, and drags the magnetic field into a comet-shaped tail on the night side and forms the Earth's magnetosphere. The magnetosphere consists of electric fields and currents (due to interaction between the solar wind and the Earth's magnetic field) and energetic charged particles derived from the solar wind. The magnetospheric currents flow into the ionosphere along the Earth's magnetic field lines and form a closed magnetosphere-ionosphere current system. The current system drives plasma (the ionospheric ions and electrons) convection in the ionosphere. The plasma convection heats the thermosphere through collisions between the plasma and the neutral atmosphere, a process called Joule heating. Energetic charged particles precipitate into the underlying thermosphere/ionosphere along the Earth's magnetic field lines into the auroral region, a region encircling the Earth's magnetic poles at high latitude, heating the thermosphere/ionosphere mainly through ionization of the thermospheric constituents. Figure 1.5 presents a schematic illustration of the magnetosphere-ionosphere current

system and an aurora image obtained by the Visible Imaging System instruments aboard the NASA POLAR spacecraft.

The thermosphere and ionosphere are closely coupled energetically, dynamically, and chemically. For example, the ionospheric plasma convection at high latitudes transfers energy and momentum through collisions between the plasma and the neutral species, heats the neutral atmosphere (Joule heating), and accelerates the neutral atmosphere (ion drag); the thermospheric neutral wind moves the electrically conducting plasma through the Earth's geomagnetic field and generates electric fields (dynamo). The dynamo electric field and current then affect both the neutral and plasma dynamics; and the daytime ionosphere E-layer and F-layer up to the F2 peak are in photochemical equilibrium between production of ions through ionization and loss of ions through ion-neutral and ion-electron chemical reactions.

1.3 Thermospheric Neutral Density and its Variations

Although the atmosphere is near vacuum in the thermosphere, it does not preclude drag and perturbations on satellites orbiting in the region. Thermospheric neutral density is the atmospheric parameter that determines the drag and perturbations exerted on satellites. Satellite drag prediction necessitated and initiated observational and empirical determination of thermospheric neutral density. With the maturing of upper atmospheric physics and upper atmospheric numerical modeling, it is both essential and possible to understand thermospheric neutral density from a numerical modeling perspective.

Thermospheric neutral density varies in time scales from hours to decades in response to solar irradiance, geomagnetic activity, lower atmospheric processes, and anthropogenic changes. EUV heating is the primary heating source in the thermosphere and thus governs the mean thermal and composition structure of the thermosphere. As a result, thermospheric neutral density is mainly modulated by changes of solar EUV heating resulting from solar flares, diurnal variation, solar 27-day rotational variation, and solar-cycle variation of around 11 years. Recent measurements by the STAR accelerometer aboard the Challenging Minisatellite Payload (CHAMP) satellite [Sutton,

et al., 2005] and results of a model study [Solomon et al., 2005] found that thermospheric neutral density can increase on the order of 20% in a few hours in response to a large solar flare event. Diurnal variation of density is around 100% (figure 4.3, Chapter 4). Solar-cycle modulation of density is much larger, about one order of magnitude [Fuller-Rowell, 1998]. Solar rotational modulation of thermospheric density varies with solar activity, from around 10% during low solar activity periods to almost as large as a solar-cycle variation under strong solar activity conditions [Fuller-Rowell, 1998; Lean, et al., 2006].

Thermospheric neutral density exhibits impulsive and intense variations due to geomagnetic activity, particularly at high latitudes. Satellite observations show that density responds to strong geomagnetic storms with an enhancement of several times at high latitudes, with little time delay. Subsequently, aurora particle heating and Joule heating, together with solar EUV heating, generate circulation and waves that propagate the density enhancement to lower latitudes, with the disturbance weakened and with a delay of several hours [Bruinsma et al., 2006; Forbes et al., 2005; Liu et al., 2005; Sutton et al., 2005].

A different type of variation is the annual density variation. Dynamics plays an important role in the annual variation. The annual variation has a latitude-dependent component and a latitude-independent component. The seasonal-latitudinal variation in solar heating drives an annual temperature variation with a summer pole to winter pole amplitude of about 27% (figure 4.4, Chapter 4; and Mayr and Volland, 1972). Then, the interhemispheric asymmetric heating invokes a summer to winter large-scale circulation. The large-scale circulation redistributes composition, with summer minimum and winter maximum for lighter species and the opposite for heavier species. This circulation, together with thermal expansion/contraction resulting from the annual variation in temperature, generates the latitude-dependent annual variation in density with maximum in the summer and minimum in the winter. The latitude-independent component has a global density minimum around July and a maximum around January. This is driven by the sun-earth distance change between the aphelion point, where the Earth is farthest from the Sun at the beginning of July, and the perihelion point, where the Earth is nearest

to the Sun at the beginning of January. The sun-earth distance change introduces an annual insolation difference of 7% which generates a global annual variation in temperature and density (see Chapter 4).

Closely related to annual variation is semiannual variation where dynamics also play an important role. Paetzold and Zschörner [1961] analyzed satellite drag data and found that thermospheric density maximizes in April and October, shortly after equinoxes, and minimizes around July with a secondary minimum around January. Harmonic analysis by Paetzold and Zschörner [1961] showed that the variation is a semiannual variation superimposed on an annual variation with similar amplitude. Subsequently, theoretical studies [e.g. Fuller-Rowell, 1998] and observations [e.g. Bowman, 2004a] clearly demonstrate the semiannual variation of thermospheric neutral density. Thermospheric neutral density is high after equinox and low after solstice, with a maximum generally in October and minimum in July. Both amplitude and phase vary from year to year, and the larger amplitude occurs in the solar maximum condition. The causes of the semiannual density variation are not well defined. Fuller-Rowell [1998] proposed that density scale height is larger during equinoxes than solstices due to weaker mixing resulting from weaker large-scale inter-hemisphere circulation at equinoxes, which causes semiannual variation in neutral density. The semiannual density variation has weak latitude dependency. The latitude-dependent component is also called seasonal-latitudinal variation of thermospheric neutral density [Jacchia 1971; Jacchia 1977; Mayr and Volland, 1972; Volland and Mayr, 1973]. The seasonal-latitudinal component is small compared to the global uniform component due to horizontal transport of energy and mass, even though the latitude dependency of composition and temperature can be significant.

In addition, thermospheric neutral density shows a long-term decreasing trend. The global change in the upper atmosphere was first investigated through model studies [Roble and Dickinson, 1989; Rishbeth and Roble, 1992; Akmaev and Fomichev, 1998, 2000]. It has become evident through recent analyses of satellite orbital decay data [Keating et al., 2000; Emmert et al., 2004a, b; Marcos et al., 2005; Lean et al., 2006]. The secular decreasing trend is in the order of a few percent per decade and is considered of

anthropogenic origin. The concentration of greenhouse gases, mainly CO_2, increases due to anthropogenic processes. It increases infrared cooing. As a result, there is a long-term cooling of the thermosphere, and thus a long-term decrease of thermospheric neutral density.

Geographically, thermospheric neutral density shows relatively small latitudinal variation compared to the large latitudinal variations in thermospheric temperature and composition. The latitudinal variation in solar irradiance heating causes an overall summer hemisphere to winter hemisphere temperature gradient. The latitude-dependent solar heating and geomagnetic heating at high latitudes induce large-scale circulation that depletes lighter species and enhances heavier species at the heating source and enhances the lighter species and depletes the heavier species in the area away from the heating source. The lighter species O becomes the dominant constituent at higher altitudes (figure 1.2). Near the heat source, temperature increases tend to increase thermospheric density through thermal expansion, while depletion of O by large-scale circulation decreases the density. Farther from the heat source, the O enhancement augments the smaller density increase due to the thermal expansion. Consequently, thermospheric neutral density is relatively latitude-uniform (figure 2.1 and figure 2.2).

1.4 Observational Study of Thermospheric Neutral Density

Thermospheric neutral density has been measured directly and indirectly. Neutral density has been derived from satellite drag data beginning in the 1960s. Neutral density derived from satellite drag usually gives neutral density at satellite perigee locations. Jacchia and Slowey [1963] derived neutral density at satellite perigees from satellite accelerations for eight satellites and confirmed semiannual variation of thermospheric density. Jacchia [1965] developed the first empirical static diffusion model of thermospheric density based on such a data set. Satellite drag data contributed to the detection and investigation of the annual/semiannual density variation more than four decades ago [Paetzold and Zschörner, 1961; Cook, 1966]. Satellite drag observations were also used to detect the large winter He bulge [Keating and Prior, 1968]. Recently,

accurate determination of neutral density from routinely compiled satellite orbital elements for the past over 40 years [Storz et al., 2002; Picone et al., 2005; Bowman, et al., 2004b] has facilitated investigation of density variations in various time scales, particularly the annual/semiannual variation and the secular variation. Bowman [2004a] found that there is clearly a semiannual density variation superimposed on an annual density variation, with equinox maximum and solstice minimum. Both the amplitude and phase of the annual/semiannual variation can change greatly from year to year. The amplitude also increases with height, with maximum amplitude around 600–700 km during solar minimum conditions and around 800–900 km during solar maxima. Climatologically, the analysis of density derived from satellite drag data suggests that thermospheric density has a mean long-term decrease of a few percent per decade for the past 40 years [Keating et al., 2000; Emmert et al., 2004a, b; Marcos et al., 2005; Lean et al., 2006], with a larger decrease during low solar activity than during high solar activity.

After the development of the Jacchia model, a parallel density measurement was conducted based on a combination of in-situ measurements of neutral composition by mass spectrometers aboard satellites and ground-based incoherent scatter radar measurements of thermospheric temperature [Carignan and Pinkus, 1968; Hedin et al., 1974]. Mass spectrometers aboard satellites were used to measure the density of minor and major species. Optical and radar backscatter data were also used to measure O and O_2 density [e.g. Norton and Roble, 1974; Strickland and Thomas, 1976; Hedin and Alcaydé, 1974]. The measurements revealed winter bulge of lighter species such as He, O, and N; and depletion of O and He at high latitudes during geomagnetic storms. Subsequently, the Mass Spectrometer and Incoherent Scatter (MSIS) empirical model has been developed and updated based on the composition and temperature data [Hedin et al., 1977a, 1977b; Hedin, 1983; Hedin, 1987; Hedin, 1991].

In-situ neutral density measurements have been conducted by satellite-borne accelerometers [Marcos, et al., 1977; Berger and Barlier, 1981; Forbes et al., 1996]. Unlike satellite drag derivation of neutral density that only measures density at perigee locations, the in-situ accelerometer measurements provide density along orbits and thus have better temporal and spatial resolution. Early accelerometer observations were

confined to lower altitude (<250 km) due to sensitivity limitation. Recent accelerometers aboard the CHAMP satellite [Reigber et al., 1996] and the Gravity Recovery and Climate Experiment (GRACE) satellite [Tapley et al., 2004] have sufficient sensitivity to make measurements up to 450 km and 550 km, respectively. The accelerometers on CHAMP and GRACE measure density nearly from pole to pole at four different local times and thus provide a global perspective of thermospheric variation due to solar and geomagnetic forcing. The data provided by the GRACE and the CHAMP satellites have advanced understanding of the effect of solar flare and geomagnetic activity on thermospheric neutral density and thermospheric waves induced by in-situ solar energy deposition and geomagnetic energy deposition. Liu et al. [2005] investigated global distribution of neutral density at 400 km using the CHAMP accelerometer measurements and found morphology of density enhancement at both sides of the equator consistent with the equatorial electron density anomaly. Using the CHAMP density data, Forbes et al. [2005] detected the equatorward propagation of large-scale traveling atmosphere disturbances (TADs) generated at both hemispheres at high latitude due to heating from the 15–24 April 2002 geomagnetic storms. Sutton et al. [2005] analyzed the CHAMP satellite data for the storm period of 29 October to 1 November 2003 and found that the maximum density enhancement during the storm period was 200% to 300% and nighttime density disturbance propagated more readily toward lower latitude compared to daytime. This is probably due to equatorward flow at both hemispheres at night but polarward flow during the day due to the diurnal tides driven by in-situ solar EUV heating. Bruinsma et al. [2006] found that the 20–21 November 2003 storm enhancement of thermospheric neutral density was from 300% to 800% globally with little time delay at high latitude. They found about a 4-hour delay at the equator and they observed gravity waves induced by geomagnetic heating at high latitude that propagated towards lower latitude.

1.5 Empirical Models of the Thermosphere

Thermosphere empirical models have been developed based on knowledge of the physics in the thermosphere and the large amount of data available for temperature, composition, and density. The empirical models give a statistical representation of the thermospheric neutral structure given solar condition, geomagnetic condition, temporal, and geographic parameters. Two widely utilized thermospheric empirical models are the Jacchia model and the MSIS model. The Jacchia model, based on satellite drag data, is used in operations related to satellite orbit tracking and prediction while the MSIS model, based on satellite mass spectrometer and ground-based incoherent scatter radar data, is a standard research tool in the research community. It provides thermospheric neutral structure for ionospheric, dynamic, and aeronomic calculations; validates theoretical models; and can be used to compare various data sets. The MSIS model is also used for the thermospheric (above 120 km) part of the COSPAR (Committee on Space Research) International Reference Atmosphere (CIRA).

The Jacchia model was originally developed in 1965 [Jacchia, 1965] using satellite drag data as a constraint for thermospheric temperature, composition, and density, and it has been revised as more drag data and other types of data such as mass spectrometer (e.g. on board the Ogo 6 satellite) and EUV-absorption data have become available [Jacchia, 1970, 1971, 1977]. It extends from 90 km to 2500 km. It consists of two parts: the static diffusion models and variations from the static components. In the static diffusion models, constant boundary conditions for temperature and total mass density are specified at 90 km, the homopause is considered at 105 km, and analytical temperature profiles are defined. The coefficients of the analytical temperature profiles are then calculated and constrained using satellite drag data. The diffusion equation of individual neutral constituent is integrated following the empirical temperature profiles to obtain number density of each species and total mass density. The thermospheric variations considered in the Jacchia model are: variation with solar cycle, variation with the daily change in activity on the visible disk of the Sun (solar rotational variation), diurnal variation, variation with geomagnetic activity, semiannual variation, seasonal-

latitudinal variation, and rapid density fluctuation connected with gravity waves. Again, the departures of temperature, composition, and density are specified in analytical forms, and coefficients are determined mostly using satellite drag data. The Jacchia model stresses agreement of total mass density with satellite drag-derived total mass density. Therefore, it is widely used in the operational community for satellite orbital determination. The limitation of the Jacchia model is its assumed constant boundary condition, which causes the results below 200 km to be less reliable.

The initial version of the MSIS-class model was developed in 1977 [Hedin et al., 1977a, 1977b] using N_2 neutral density data from mass spectrometers aboard five satellites and neutral temperature data inferred from incoherent scatter radar from four ground stations. It was been updated in 1983 [Hedin, 1983], 1987, [Hedin, 1987], and 1991 [Hedin, 1991] when more mass spectrometer data, incoherent scatter data, and O_2 density data derived from occultation of solar ultraviolet emissions became available. The 1991 version, the MSIS90, is built upon data from the period 1965–1983, and extends from ground to the exobase. The temperature formulation of the MSIS model is based on the Bates [1959] temperature profiles for the thermosphere, an inverse polynomial temperature profile for the lower thermosphere, related diffusive equilibrium density profiles above 105 km, and a mixing density profile below 105 km. The coefficients of the temperature, density, and composition are mainly determined using mass-spectrometer data and incoherent scatter temperature data. Thermospheric variations considered in the MSIS model are the variations of neutral density and temperature with altitude, latitude, longitude, local time, day of year, $F_{10.7}$, geomagnetic activities. Picone et al. [2002] updated the MSIS90 to NRLMSISE-2000 in which the underlying dataset are extended to include total mass density from satellite accelerometers and from orbital determination, new temperature data from incoherent scatter radar observations from 1981–1997, and O_2 number density data from solar UV occultation aboard the Solar Maximum Mission. Picone et al. [2002] also added a new component, “anomalous oxygen,” that considers O^+ and hot atomic oxygen contributions to the total mass density at high altitude, e.g., above 500 km. The MSIS-class model is less accurate where data is sparse, mainly below 200 km and above 600 km. In addition, at high latitude and during

high geomagnetic activities, available datasets are also sparse. As a result, the model gives statistical representation of storm effects and does not capture individual storms that usually have short time and limited spatial scales.

1.6 Numerical Models of the Thermosphere

Thermospheric empirical models give valuable statistical descriptions of the thermosphere. However, the thermosphere is closely coupled with the ionosphere, the magnetosphere, and the mesosphere energetically, dynamically, and chemically. The thermosphere and the ionosphere interact through ion-neutral elastic and inelastic collisions and electrodynamic phenomena such as the thermospheric wind dynamo in the ionosphere E region. The magnetosphere and the ionosphere are interconnected through electric fields, conductances, and electric currents at the Earth's high latitudes. At lower altitudes, the mesosphere and the thermosphere/ionosphere system are coupled through molecular diffusion and eddy diffusion, energy and momentum transfer through waves and tides, etc. As a result, three dimensional time-dependent numerical models of the upper atmosphere are needed in order to fully account for the complex evolution of the coupled system. Such numerical models are also referred as upper atmospheric general circulation models.

1.6.1 The Models

Upper atmospheric numerical models solve continuity, momentum, and energy equations of the upper atmosphere self-consistently. They take into consideration the couplings through specified boundary conditions, empirical models, or they extend the lower boundary to the stratosphere and the upper boundary to include the plasmasphere. There are two main groups of upper atmospheric numerical models: the Coupled Thermosphere and Ionosphere Model [CTIM, Fuller-Rowell and Rees, 1980, 1983; Rees and Fuller-Rowell, 1988, 1990; Fuller-Rowell et al., 1996] and its subsequent versions

and variants, the Coupled Thermosphere/Ionosphere Plasmasphere (CTIP) model [Millward et al., 1996], and the Coupled Middle Atmosphere and Thermosphere (CMAT) general circulation model [Harris et al., 2002]. The other group is the Thermosphere General Circulation Model [TGCM, Dickinson et al., 1981, 1984] and its updated versions, the Thermosphere Ionosphere General Circulation Model [TIGCM, Roble et al., 1988], the Thermosphere Ionosphere Electrodynamic General Circulation Model [TIEGCM, Richmond et al., 1992], the Thermosphere Ionosphere Mesosphere Electrodynamic General Circulation Model [TIMEGCM, Roble and Ridley, 1994], and the Thermosphere Ionosphere Nested Grid [TING, Wang et al., 1999] model.

The CTIM assumes hydrostatic equilibrium to use pressure coordinates and has a vertical resolution of one scale height. It extends from 80 km to around 500 km depending on solar activity. Its horizontal resolution is 2^o latitude by 18^o longitude. Its time step is 60 seconds. The CTIM includes O, O_2, N_2 as major neutral species and H^+ and O^+ as ions. It solves continuity, momentum, and energy equations for the neutrals and the ions. At high latitude, the CTIM uses empirical models of the convection pattern and energetic particle precipitation as its high latitude energy and momentum inputs. At low and mid latitudes, the CTIM considers electrodynamic coupling with a self-consistent dynamo calculation. At the lower boundary, the CTIM specifies oscillation of temperature, wind, and pressure from tidal and wave forcing. The CTIP varies from the CTIM by adding a low-latitude, self-consistent plasmasphere that extends to 10,000 km. The CMAT evolved from the CTIM by extending its lower boundary to around 30 km and some other updates: increasing vertical resolution to one-third scale height, replacing O with $O+O_3$, adding hybrid Matsuno-Lindzen gravity wave parameterization, and using the MSIS90 and the Global Scale Wave Model [GSWM, Hagan and Forbes, 2002, 2003] as its lower boundary condition.

The TGCM also assumes hydrostatic equilibrium in the thermosphere and uses pressure coordinates. It extends from around 97 km to around 600 km depending on solar activity and has 0.5 scale height resolution vertically. The horizontal resolution is 5^o latitude by 5^o longitude. The model time step is several minutes. It solves neutral wind, neutral temperature perturbation (perturbation from a global mean temperature obtained

from thermosphere empirical models such as the MSIS), and mass mixing ratio equations for major species (O, O_2, N_2) and minor species ($N(^2D)$, $N(^4S)$, NO). At the lower boundary, vertical propagating of semi-diurnal and diurnal tides from the mesosphere to the thermosphere is included as described by Fesen et al. [1986] and Forbes et al. [1993]. High latitude ion convection and auroral particle precipitation are parameterized using empirical models [Roble et al., 1982; Roble and Ridley, 1987].

Roble et al. [1988] incorporated a self-consistent aeronomic scheme [Roble et al., 1987] into the TGCM. The Eulerian ionosphere model is coupled with the thermosphere model of the TGCM and the new coupled thermosphere ionosphere model is called the TIGCM. The ionospheric model calculates global distributions of O^+, NO^+, O_2^+, N_2^+, N^+, electron density, and ion and electron temperature. Ion drift is obtained from the empirical model developed by Richmond et al. [1980] for the low and mid latitudes. At high latitude, the ionospheric convection pattern is specified using the empirical model developed by Heelis et al. [1982]. Auroral particle precipitation is parameterized by the auroral model developed by Roble and Ridley [1987].

Richmond et al. [1992] developed and implemented a scheme for electrodynamic coupling between the thermosphere and the ionosphere for the TIGCM and updated the TIGCM to the TIEGCM. The scheme calculates dynamo effects of the thermospheric neutral wind and the feedback of the dynamo electric fields and currents on the neutral and plasma dynamics. The effect of the lower atmosphere processes is either specified by climatological tidal data or the GSWM.

Roble [1995] developed a self-consistent aeronomic scheme for atmosphere from 30 km to 500 km. Roble and Ridley [1994] implemented the aeronomic scheme into the TIEGCM and extended the TIEGCM lower boundary to around 30 km (10 mb). This extended model is called the TIMEGCM. Compared to the TIEGCM, O is replaced by O_x = ($O+O_3$), NO is replaced by NO_x = ($NO+NO_2$), and many mesosphere species are added such as H_2O, H_2, CH_4, CO, CO_2. A gravity wave parameterization [Lindzen, 1981] is used to represent momentum deposition and turbulence due to gravity wave breaking. Tides are specified at the lower boundary the same way as that of the TIEGCM.

The TING model uses a nested grid of three-times higher resolution within the TIGCM model domain in a limited area, typically the northern hemisphere auroral region, to resolve geomagnetic activities that usually have smaller time and spatial scales. It has been developed for studies of geomagnetic activity at high latitude.

The TIEGCM, with its altitude coverage from 97 km to up to 600 km, is suitable and efficient for thermosphere/ionosphere studies and thus is selected to be the primary model for this thesis study. The global mean version of the TIMEGCM [Roble, 1995] will be used for investigation of global change in the thermosphere.

1.6.2 External Forcing for the Models

1.6.2.1 Solar Irradiance

The aeronomic calculations in numerical models require accurate specification of solar spectral irradiance to fully account for the influence of solar input on thermospheric chemistry, energetics, and dynamics. Solar spectral irradiance is defined as the integrated solar irradiance over the full solar disk for each wavelength measured at one astronomical unit (AU). One AU is the mean distance between the Earth and the Sun. Due to the limited amount of XUV and EUV measurements and due to low spectral and time resolution of most of the measurements, empirical solar irradiance models of XUV, EUV, and FUV (often called solar proxy models) have been used in numerical modeling. A solar proxy model is an empirical representation of solar irradiance and its variability. It usually includes two parts, a reference spectrum at solar minimum and a wavelength-dependent solar variability. The variability is usually parameterized by solar indices that are historically available. The most widely used solar index is $F_{10.7}$ index. The $F_{10.7}$ index is the radio flux from the Sun at a wavelength of 10.7 centimeter. It correlates well with the sunspot number and has been used as a proxy for solar irradiance in wavelengths that are of interest for thermospheric study, i.e., XUV, EUV, and FUV. Recently, more solar indices, such as Mg II core-to-wing index (Mg II C/W) and S_{10}, are used to parameterize

solar spectral irradiance more accurately considering their different origin from the solar atmosphere, i.e., the chromosphere, the transition layer, and the corona [Bowman, et al., 2006; Tobiska, et al., 2006; Bowman and Tobiska, 2006]. Examples of such proxy models are the Hinteregger model [Hinteregger, et al., 1981a, 1981b], the SERF2 model [Tobiska and Barth, 1990], the EUV91 [Tobiska, 1991], the EUVAC [Richards et al., 1994], the EUV 97 [Tobiska and Eparvier, 1998], the SOLAR2000 [Tobiska et al., 2000], and the Woods and Rottman model [Woods and Rottman, 2002].

The EUVAC model is the default solar EUV input for the TIEGCM model. EUVAC is based on the F74113 reference spectrum and the solar-cycle variation of the flux measured by the Atmosphere Explorer E (AE-E) satellite. The F74113 spectrum was measured on April 23, 1974 by a rocket flight [Heroux and Higgins, 1977; Heroux and Hinteregger, 1978] at low solar activity. The EUVAC covers the solar spectral range from 5 nm to 105 nm. The FUV for the TIEGCM covers the wavelength range from 105 nm to 175 nm. It is based on the Woods and Rottman model [Woods and Rottman, 2002]. Both the EUVAC and the Woods and Rottman model use the $F_{10.7}$ index to represent solar variability.

On the solar irradiance measurement side, most early measurements of solar XUV and EUV have been inadequate in temporal and spectral resolution, as well as temporal and spectral coverage. Measurements of solar XUV and EUV began in 1960s. The SOLRAD-1-11 measured irradiance from 1–10 nm from 1960–1976; the OSO-3-6 for 2–40 nm and 27–131 nm from 1967–1970; the AEROS-A-B for 20–104 nm from 1973–1975. These measurements lead to the AE-C-E satellite measurements for wavelengths 14–185 nm and 27–122 nm from 1974–1981, which were the most comprehensive measurements in terms of spectral and temporal coverage, as well as spectral resolution. AE measurements, together with several sounding rocket measurements, became the basis for the widely used early reference spectra and solar proxy models [e.g. Hinteregger, et. al., 1981a, 1981b; Richards et al., 1994]. The GOES satellites have provide X-ray (0.05–0.4 nm and 0.1–0.8 nm) measurements since 1974. Some other measurements include the Yohkoh/SXT for 0.2–3 nm from 1992–2002; the SOHO/SEM for 26–34 nm from 1996 to present; the SNOE/SXP for 0.2–20 nm from 1998–2003.

Most of the measurements are broadband and there is a gap in EUV measurements since the comprehensive AE measurements.

The recent thermosphere-Ionosphere-Mesosphere Energetics and Dynamics (TIMED) Solar EUV Experiment (SEE) provides the opportunity to use solar spectral measurements in the upper atmospheric general circulation model. The TIMED/SEE has measured solar spectral irradiance from 0.1–195 nm from 2002 to present. It uses two types of instruments: the XUV Photometer System (XPS) and the EUV Grating Spectrograph (EGS). The XPS measures solar irradiance from 0.1–34 nm with a resolution of 5–10 nm. The EGS measures irradiance from 27–195 nm with 0.4 nm spectral resolution. The TIMED satellite was launched on 7 December 2001. It has a circular orbit of 625 km altitude with a 74.1^{o} inclination. Its period is about 90 minutes per orbit. The TIMED/SEE data products have been available since 8 February 2002. The data products are: 1) daily-averaged solar spectral irradiance from 0–195 nm with 1 nm resolution and center on 0.5 nm and 2) orbital solar spectral irradiance in the same format as the daily averaged spectra. An interface has been developed to process the TIMED/SEE solar spectral irradiance for use in the TIEGCM (see Chapter 2). The TIMED/SEE measurements from near solar maximum to solar minimum of the solar cycle 23 were used as solar input to calculate thermospheric neutral density in Chapter 4.

Other new solar spectral irradiance measurements will provide additional data for the upper atmospheric general circulation models. The Solar Radiation and Climate Experiment (SORCE) measures X-Ray, ultraviolet, visible, near infrared, and total solar radiation. The Spectral Irradiance Monitor (SIM) aboard the SORCE satellite measure spectral irradiance from 0.1–2400 nm but excludes EUV from 34–115 nm. It was launched on January 25, 2003. The soft X-ray measurements (0.1–34 nm) of the SORCE have been integrated into the TIMED/SEE data products for the soft X-ray wavelengths due to the TIMED/SEE XPS instrument failure.

The Solar Dynamic Observation (SDO) mission is planned to launch in August 2008. The SDO EUV Variability Experiment (EVE) will measure solar EUV irradiance from 1–1216 Angstrom at high temporal cadence. The SDO mission phase is planned to be five years, half of the next solar cycle, with a possibility of a five-year extension. The

SDO/EVE will provide EUV measurements as a relay to the TIMED/SEE measurements. The TIMED/SEE and the SDO/EVE will compile the most comprehensive EUV data set for model studies, and facilitate the development and improvement of empirical and physical solar irradiance models.

1.6.2.2 Geomagnetic Activity

The second energy source and forcing for the upper atmosphere is geomagnetic activity. Geomagnetic activity results from the interaction between the solar wind and the Earth's magnetic field. During the encounter of solar wind with the Earth's magnetic field, magnetic field lines embedded in the solar wind connect with Earth's magnetic field lines at the magnetopause on the dayside. The two newly formed open field lines are carried over the Earth's poles and reconnected at the tail to become the Earth's new magnetic lines. These new magnetic lines then move around the Earth towards the dayside and repeat the same process. The motion of the open field lines that were carried over poles and the new closed magnetic fields line that were moved back to the dayside drive ionospheric plasma into convection around the polar caps. The ionospheric plasma flow then drives the neutral atmosphere into similar convection patterns through friction. The neutral winds in turn generate new electric fields and currents through the dynamo with the Earth's magnetic field. The ionospheric current system then connects with the current systems at the magnetopause along the magnetic field aligned currents and forms a closed magnetosphere-ionosphere current system. In the mean time, as the new closed magnetic field lines move from the tail towards the dayside, magnetospheric charged particles, mainly electrons with energy between 1–100 kev, precipitate into the Earth's upper atmosphere where they collide with neutral species in the thermosphere and generate the aurora.

The ionosphere and the magnetosphere are coupled through the magnetosphere-ionosphere current system and through magnetospheric charged particle precipitation in the auroral region. The ionospheric currents heat the neutral atmosphere through ion-neutral collisions, a process called Joule heating. The auroral energetic particles heat the

neutral atmosphere through ionization, dissociation, and excitation of the neutral species. In the process, energy is transferred from the magnetosphere to the thermosphere. Although the Sun's electromagnetic radiation carries a million times more energy away from the Sun than the solar wind, the solar wind governs the magnetosphere, which in turn governs the high-latitude region of the Earth. During the Sun's Coronal Mass Ejections (CME), the high latitude upper atmosphere experiences geomagnetic storms with intensified magnetosphere-ionosphere current systems and auroral particle precipitation. The effect can reach the lower latitude upper atmosphere. In addition, variation of geomagnetic activities is generally more dynamic and impulsive than solar irradiance variation.

The geomagnetic energy for upper atmospheric general circulation models is usually parameterized by empirical models. Examples of empirical models are Heelis model [Heelis et al., 1982], Weimer model [Weimer, 2001], and the Assimilative Mapping of Ionospheric Electrodynamics [AMIE, Richmond, 1992]. Energy from particle precipitation in the auroral oval is usually parameterized by geomagnetic indices, solar wind parameters such as solar wind velocity, and interplanetary magnetic fields [Reiff and Luhman, 1986; Foster, et al., 1986].

The Coupled Magnetosphere-Ionosphere-Thermosphere model (CMIT), which is being developed as part of the Center for Integrated Space Weather Modeling (CISM) program, couples the Lyon-Fedder-Mobarry (LFM) global magnetosphere-ionosphere simulation model [Lyon, Fedder, and Mobarry, 2004] to the thermosphere/ionosphere model the TING or the TIEGCM. The geomagnetic energy input for the TING/TIEGCM is calculated by LFM in this integrated model.

1.6.2.3 Waves

The thermosphere/ionosphere is also coupled to the mesosphere energetically, dynamically, and chemically, particularly with momentum and energy forcing from various waves in the mesosphere and lower thermosphere (MLT) region. There are many wave activities in the MLT where either the lower boundary or the lower domain of an

upper atmospheric general circulation model resides. The important waves for the MLT region are gravity waves, tides, and planetary waves. Numerous observations by ground-based instruments, rockets, and satellites along with theoretical studies show that waves play an important role in MLT dynamics and the effects manifest themselves in wind, temperature, composition, air glows, and electrodynamics, etc. These waves are mostly generated in the lower atmosphere and propagate upward to the MLT region. As the waves propagate upward, the wave amplitudes become larger and larger since the atmosphere becomes less and less dense. The waves with large amplitudes become unstable. The gravity waves break in the mesosphere while tides dissipate in the MLT region due to eddy diffusion, molecular diffusion, gravity wave drag, and ion drag. Tides and gravity waves can also be generated in-situ in the thermosphere due to solar heating and geomagnetic heating at high latitude. The wave breaking and dissipation deposit energy and momentum, produce turbulence and mixing, influence the mean circulation, and affect the thermal structure and composition in the MLT region. The waves generated in the lower atmosphere are external forcing for the upper atmospheric general circulation models.

Gravity waves are the dominant momentum forcing in the upper mesosphere. The middle atmosphere gravity waves were first investigated by Hines [1960], and were followed by theoretical, numerical, and observational studies [e.g. Fritts, 1984; Fritts and Alexander, 2003]. Gravity waves are mainly generated in the lower atmosphere, especially in the troposphere. The main trigger mechanisms of the gravity waves are topography, convection, and frontal systems. Other sources of the gravity waves are jet streams and wave-wave interaction. Such gravity waves propagate upward into the MLT region where they eventually break due to wave instability. The breaking of gravity waves deposits momentum, causes zonal mean flow to reverse, and drives a summer-to-winter meridional circulation due to the Coriolis force. The induced meridional circulation leads to adiabatic warming at winter mesopause and adiabatic cooling at summer mesopause, and thus a warm winter mesopause and a cold summer mesopause. The gravity wave breaking also produces turbulence. Both observations [Kirchhoff and Clemesha, 1983; Fukao, et al., 1994; Lübken, 1997; Khattatov, et al., 1997; Rao, et al.,

2001; Sasi and Vijayan, 2001] and model studies [Blum and Schuchardt, 1978; Garcia and Solomon, 1985; Akmaev, 2001b] have indicated that eddy diffusion in the MLT region exhibits an annual/semiannual variation with minimum during equinoxes, maximum during summer, and secondary maximum during winter. The amplitude between minimum and maximum can reach one order of magnitude.

Tides are mainly excited by absorption of solar irradiance by H_2O in the troposphere and by O_3 in the stratosphere and lower mesosphere. The tides then propagate vertically into the upper mesosphere and lower thermosphere where the tides dissipate due to gravity wave drag, eddy diffusion, molecular diffusion, and ion drag. Tides are global-scale harmonic oscillations that can be seen as a special class of gravity waves that have unique characteristics of periods and horizontal wavelength. Due to periodic solar heating, tides have periods of a day or a fraction of a day. Diurnal and semidiurnal tides are the most common and important tides to the MLT region. Tides also have horizontal wavelength of a fraction of a latitude circle of the Earth; several such tides would fit around the latitude circle. Therefore, compared to gravity waves, tides have larger time and spatial scales. As a result, the curvature of the Earth and the Coriolis force need to be taken into account in describing tides. The dissipation of upward propagating tides results in net acceleration and heating in the MLT region, with propagating diurnal tides being the primary contributor. The effect is largely confined at latitudes within 30^o on both sides of the equator. Miyahara and Wu [1989] investigated the effect of momentum deposition of solar tides in the MLT region with a zonal mean dynamic model. They found that tides have significant impact on the mean zonal wind in the MLT region, with significant influence by upward-propagating diurnal tides below 120 km. Above 120 km, the effect of semidiurnal tides becomes more important, with contributions from both upward-propagating semidiurnal tides and from in-situ semidiurnal tides. By imposing diurnal and semidiurnal tides at the lower boundary of the TIGCM, Forbes et al. [1993] found that tidal dissipation from upward propagating diurnal and semidiurnal tides would cause a westward jet in the order of 10–30 ms^{-1} in the equatorial lower thermosphere. In the vicinity of 110 km, the zonal mean N_2 and O_2 number densities increase 10–30% due to enhanced upward transport from heat deposited

by tidal dissipation while atomic oxygen depletes 30–50% due to enhanced recombination from enhanced O_2 and N_2. In addition, tides influence the ionosphere through neutral wind dynamo in the E region at low latitudes, and the influence can be mapped to the F region through geomagnetic field.

Planetary waves can be forced by topographical features at the Earth's surface and by meteorological patterns. They propagate upward into the higher atmosphere where they dissipate, deposit momentum, accelerate the mean flow, and cause signature of long-period oscillations in the neutral wind. Although planetary waves with periods of 2, 5, 10, and 16 days have been observed in the MLT region, most planetary waves dissipate at altitudes lower than the lower boundary of the TIEGCM.

The TIMEGCM includes a gravity wave parameterization scheme [Lindzen, 1981]. The TIEGCM uses a constant eddy diffusion to implicitly include the effect of turbulent mixing caused by gravity wave breaking. However, since the eddy diffusion is a constant, the effect of annual/semiannual variation of gravity wave breaking is not represented in the model. In Chapter 4, an annual/semiannual variation of eddy diffusion at the lower boundary is parameterized to include the effect of annual/semiannual variation of gravity wave breaking. In addition, the TIEGCM uses the GSWM to provide tidal forcing at the lower boundary. The planetary wave influence is not considered at the lower boundary of the TIEGCM.

1.7 Thesis Objectives and Approaches

Thermospheric neutral density is an important parameter for both the research community and the satellite operation community. Recent in-situ satellite measurements of thermospheric neutral density have detected impulsive and short-term density variation in response to solar flares and geomagnetic storms; while satellite-drag derived density dataset provide long-term data to investigate longer term variation of thermospheric neutral density. The purpose of this thesis is to facilitate the study of thermospheric neutral density in both the research and the operational communities by quantifying thermospheric neutral density and its variations using the TIEGCM and the global mean

version of the TIMEGCM. The focus will be on annual/semiannual variation, solar-cycle variation, and long-term trend of thermospheric neutral density. The MSIS model and satellite-drag derived density will be used to validate and compare with the TIEGCM simulations.

The annual/semiannual variation was discovered by Paetzold and Zschörner [1961] through satellite drag data analysis. Recent satellite drag data analysis [Bowman, 2004a] advanced the understanding of the characteristics of the annual/semiannual variation. The annual/semiannual variation has been represented in empirical models (the Jacchia model and the MSIS model) but the mechanisms are not well defined. Paetzold and Zschörner [1961] suggested that the annual/semiannual variation is caused by the interaction between the terrestrial upper atmosphere and interplanetary matter. Geomagnetic activity has been suggested to be the cause of the semiannual variation [Mayr and Volland, 1971; Walterscheid, 1982] due to the semiannual variation in geomagnetic activities that peaks at equinoxes [Russell and McPherron, 1973]. However, the semiannual variation in geomagnetic activities is too weak to cause the observed amplitude of the semiannual variation in thermospheric neutral density. Fuller-Rowell [1998] proposed mixing by the large-scale circulation as a mechanism for the semiannual density variation. The TIEGCM model confirmed large-scale circulation as a mechanism for the semiannual density variation. However, it also shows the amplitude resulting from large-scale circulation can not fully account for the observed amplitude of the semiannual variation. The TIEGCM model will be used in this thesis study to find mechanisms for the annual/semiannual density variation.

It has been found that thermospheric density calculated by $F_{10.7}$-index based thermospheric empirical models shows a solar-cycle dependency [Marcos, et al., 2005]. At low solar activity, neutral density calculated by the empirical models is systematically larger than satellite drag derived neutral density. The TIMED/SEE has made solar spectral irradiance measurements from near solar maximum to solar minimum. The TIEGCM will be used in this thesis to understand the nature of the solar-cycle dependency by investigating whether numerical-model simulation using measured solar irradiance has the solar-cycle dependency.

The long-term climatological influence of greenhouse gases to the upper atmosphere was first suggested by Roble and Dickinson [1989] using model sensitivity study. Subsequently, the long-term change in the thermosphere has been investigated using satellite drag measurements [Keating et al., 2000; Emmert et al., 2004a, b; Marcos et al., 2005; Lean et al., 2006] and through sensitivity studies using upper atmospheric general circulation models [e.g. Rishbeth and Roble, 1992; Akmaev and Fomichev, 1998, 2000]. Both approaches have confirmed a long-term cooling of the thermosphere, primarily due to increase of greenhouse gases. However, the magnitude of the long-term decrease in thermospheric neutral density differs. The global mean version of the TIMEGCM model will be used in this thesis, with historic CO_2 measurements and solar variability based on $F_{10.7}$ index, to quantify the long-term trend of thermospheric neutral density.

Chapter 2 describes the TIEGCM and the TIMEGCM; a new solar energy deposition scheme that was developed and implemented in the TIEGCM and TIMEGCM for the thesis study; important TIEGCM/TIMEGCM model parameters; and the MSIS empirical model. Chapter 3 introduces the satellite-drag derived density dataset that was provided by Bruce Bowman of Air Force Space Command; and the TIMED/SEE version 8 level 3 solar spectral irradiance dataset provided by Laboratory for Atmospheric and Space Physics of the University of Colorado. Chapter 4 gives an inclusive general description of thermospheric density variations using the TIEGCM simulations, followed by detailed analysis of the TIEGCM simulations on annual/semiannual density variation, solar-cycle dependency of density calculation seen in empirical models, and long-term trend of thermospheric neutral density. Chapter 5 concludes the thesis study and discusses further work.

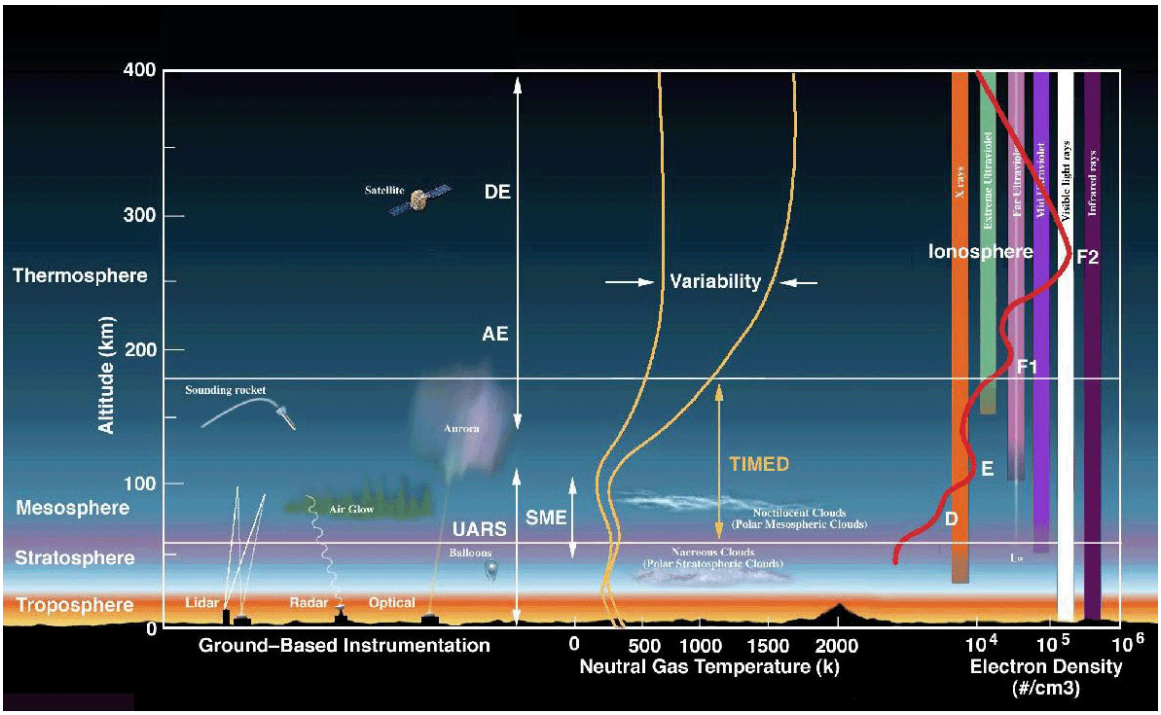

Figure 1.1: Vertical temperature structure of the atmosphere and the associated layers; the electron density profile of the ionosphere and its D, E, F1, and F2 layers; deposit altitudes of the solar spectral irradiance; altitude coverage of ground-based and satellite/rocket measurements of the upper atmosphere; and some upper atmospheric phenomena (courtesy of Dr. J.-H. Yee, Johns Hopkins University Applied Physics Laboratory).

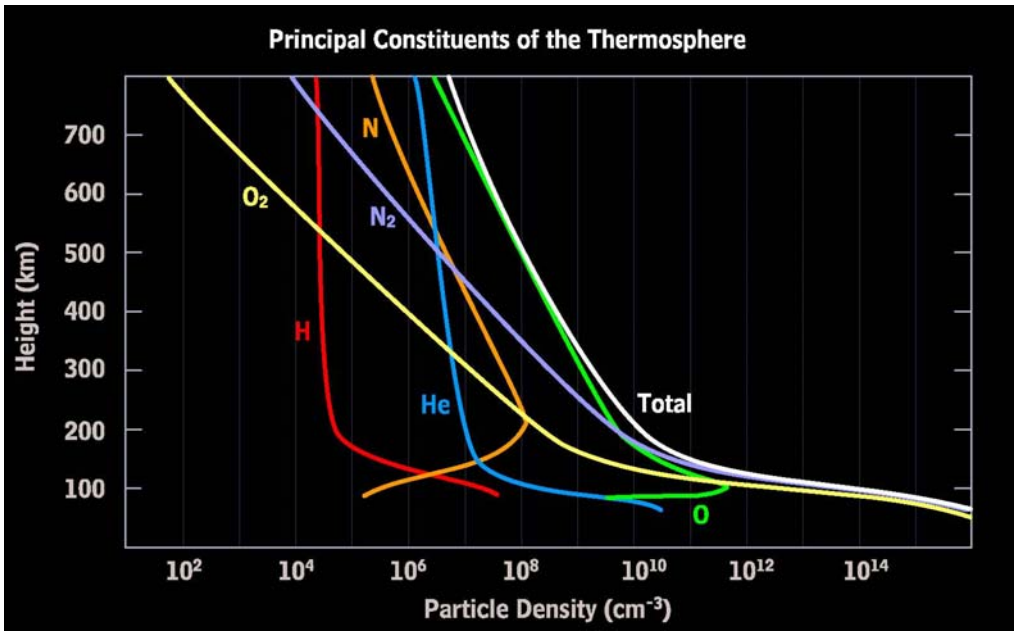

Figure 1.2: Distribution of the thermospheric constituents (courtesy of the NCAR High Altitude Observatory and the Cooperative Program for Operational Meteorology Education and Training, http://www.meted.ucar.edu/hao/aurora).

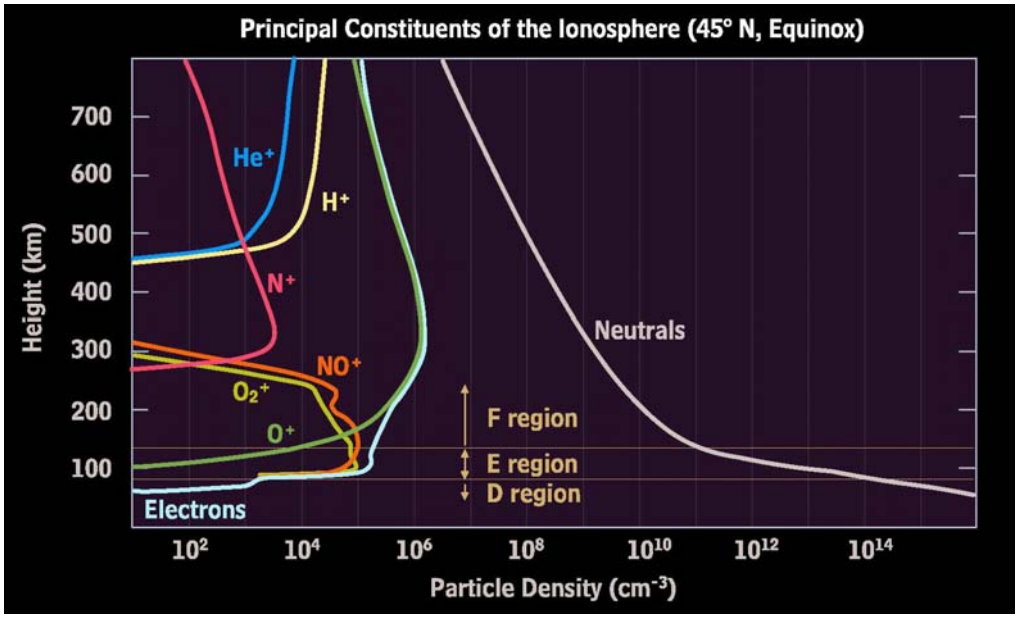

Figure 1.3: Distribution of the ionospheric constituents (courtesy of the NCAR High Altitude Observatory and the Cooperative Program for Operational Meteorology Education and Training, http://www.meted.ucar.edu/hao/aurora).

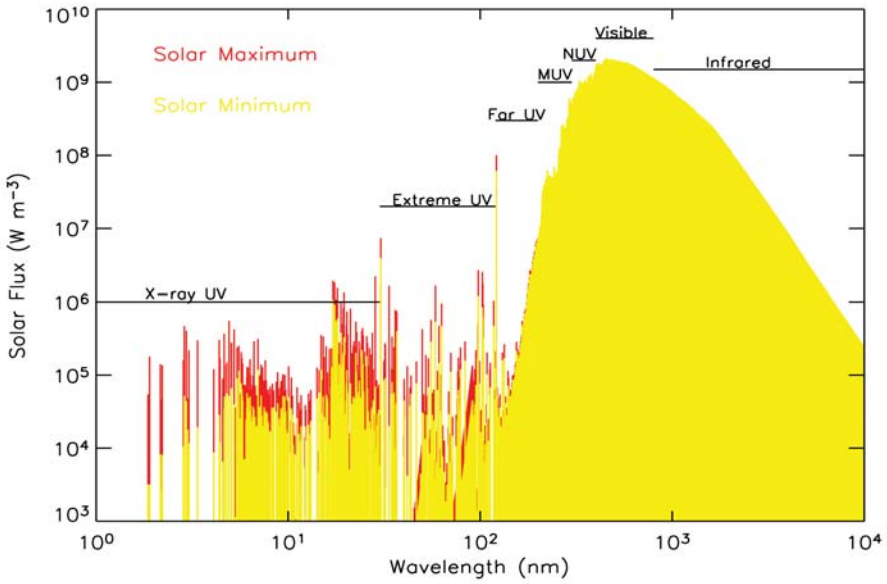

Figure 1.4: Solar spectral irradiance from the soft X-ray ultra-violet to the infrared at solar minimum (yellow) and solar maximum (red). 1–120 nm: the SC21REFW and the F79050 reference spectra by Hinteregger et al. [1981b]; 120–200 nm: the Wood and Rottman solar proxy model [Woods and Rottman, 2002]; 200–10^4 nm: ASTM (American Society for Testing and Materials) standard solar spectral irradiance (courtesy of Dr. S. C. Solomon, the NCAR High Altitude Observatory)

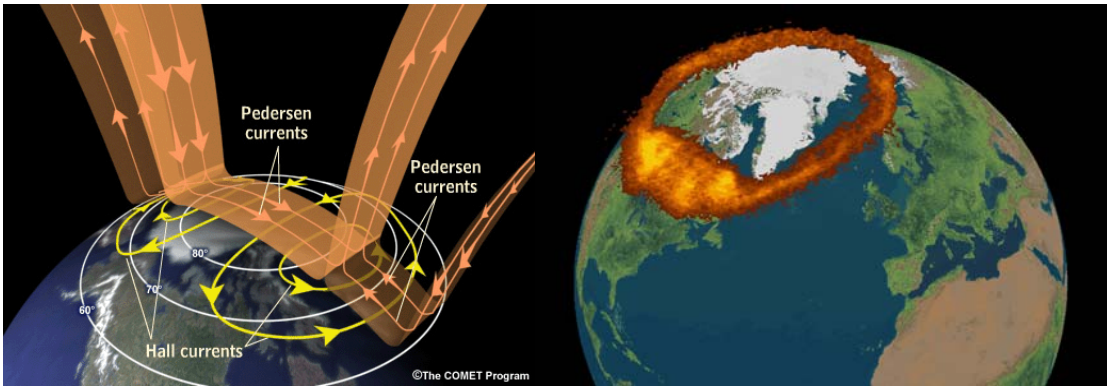

Figure 1.5: On the left: the magnetosphere-ionosphere current system (courtesy of the NCAR High Altitude Observatory and the Cooperative Program for Operational Meteorology Education and Training, http://www.meted.ucar.edu/hao/aurora); on the right: image of aurora taken by the Visible Imaging System (VIS) instrument on the NASA POLAR spacecraft (courtesy of Dr. L. Frank, Department of Physics and Astronomy, the University of Iowa).

Chapter 2

MODEL DESCRIPTIONS

Several upper atmospheric models are used in this study to understand and investigate thermospheric neutral density, its variations, and forcing: the Thermosphere-Ionosphere-Electrodynamics General Circulation Model (TIEGCM), the global mean Thermosphere-Ionosphere-Mesosphere-Electrodynamics General Circulation Model (TIMEGCM), and the MSIS00 empirical model. The TIEGCM is the primary model. Section 2.1 gives an overall description of the TIEGCM and its successors, the TIMEGCM; Section 2.2 focuses on solar input for the TIEGCM/TIMEGCM and introduces a new solar energy deposition scheme recently implemented in the TIEGCM/TIMEGCM; Section 2.3 addresses parameters related to physical and chemical processes in the coupled thermosphere/ionosphere system that are important in model tuning and validation; and Section 2.4 briefly describes the MSIS empirical model.

2.1 The TIEGCM

The TIEGCM is a first-principle numerical model that solves the Eulerian continuity, momentum, and energy equations for the coupled thermosphere/ionosphere system. It utilizes a spherical coordinate system fixed with respect to the rotating Earth, with latitude and longitude as the horizontal coordinates and pressure surfaces as the vertical coordinate. The pressure interfaces are defined as z=ln(P_0/P), with P_0 being a reference pressure of $5\times10^{-4}\ \mu b$. The vertical range of the pressure interfaces is from -7 to 7, and thus covers altitude range about 97–600 km depending on solar activity. The vertical resolution is 2 model grids per pressure scale height; the horizontal resolution is 5^o latitude by 5^o longitude, and the model time step is generally 3 minutes. The external

forcing of the system are solar irradiance, geomagnetic energy in the form of auroral particle precipitation and ionospheric electrical potential, and perturbation by waves at the lower boundary. The outputs of the model are neutral, electron, and ion temperature; winds; concentrations of major species O, O_2, and N_2; concentrations of minor species $N(^4S)$, $N(^2D)$, NO; concentrations of ions O^+,O_2^+, N_2^+, N^+, NO^+; electron density; and geopotential heights of pressure interfaces. The NCAR upper atmospheric general circulation model has undergone more than two decades of major development since its first version by Dickinson, et al. [1981]. The model has been continually improved over the time. Currently, there are three commonly used versions of the model: the TIEGCM model extends from approximately 97–600 km suitable for the thermosphere/ionosphere study; the TIMEGCM model covers upper stratosphere, mesosphere, and the coupled thermosphere/ionosphere extending from about 30–500 km for mesosphere, thermosphere and ionosphere study; and a global mean single-column version of the TIMEGCM. Important references include: Dickinson et al. [1981], Dickinson et al. [1984], Roble et al. [1982], Roble and Ridley [1987], Roble et al. [1987], Roble et al. [1988], Richmond and Roble [1987], Richmond et al. [1992], Roble and Ridley [1994], Roble [1995], Richmond [1995], and Solomon and Qian [2005].

The following sections briefly describe the important aspects of the TIEGCM. The equations are given without detailed description for some of the parameters used in the equations to facilitate understanding of the physical, chemical, and electrodynamic processes governing the thermosphere and the ionosphere.

2.1.1 Thermospheric Modeling

The independent variables of the thermosphere equation system are:

t: time; ϕ: latitude; λ: longitude; $z=\ln(P_0/P)$

The dependent variables are:

T: neutral temperature; u: eastward wind velocity;

v: northward wind velocity; w: vertical velocity (dz/dt);

$\Psi(\Psi_O, \Psi_{O_2})$: major species mass mixing ratio;

ψ : minor species mass mixing ratio;

Other model parameters used in the equations are:

C_p: specific heat per unit mass; P_0: reference pressure ($5\times10^{-4}\,\mu b$);

τ : diffusion time scale ($1.86\times10^{3}\,s$);

H: pressure scale height; K_T: molecular thermal conductivity coefficient;

K_E: eddy diffusion coefficient; ρ: mass density; g: gravity acceleration;

$\vec{V}$: horizontal wind vector; R: universal gas constant;

$\overline{m}$: mean molecular mass; m_{N_2} : N_2 molecular mass; f: Coriolis parameter;

μ: viscosity coefficient (sum of molecular and eddy);

Q: external heating (solar and geomagnetic); C: infrared cooling;

S: chemical production of a gas; L: chemical loss of a gas;

Φ : geopotential;

$(\lambda_{xx}, \lambda_{xy}, \lambda_{yx}, \lambda_{yy})$: ion drag tensor;

u_i: zonal ion drift velocity;

v_i: meridional ion drift velocity

The thermospheric energy equation describes time derivative of neutral temperature at a fixed point under dynamical, physical, and chemical influences:

$$\frac{\partial T}{\partial t} = \frac{g e^{z}}{P_0 C_p}\frac{\partial}{\partial z}\left\{\frac{K_T}{H}\frac{\partial T}{\partial z} + K_E H^2 C_P \rho\left(\frac{g}{C_p} + \frac{1}{H}\frac{\partial T}{\partial z}\right)\right\} - \vec{V}\bullet\nabla T$$

$$- w\left(\frac{\partial T}{\partial z} + \frac{RT}{C_P\overline{m}}\right) + \frac{(Q-C)}{C_P} \qquad \text{(Eq. 2.1)}$$

The terms on the right hand side of the equation are: downward molecular heat conduction; downward eddy heat conduction; horizontal heat advection; vertical advection and adiabatic heating or cooling by vertical wind; heating by solar irradiance and by geomagnetic activity; and infrared cooling. The solar irradiance heating is

initiated by photoionization, photodissociation, and photoexcitation of neutral constituents and then various subsequent processes including exothermic ion-neutral chemical reactions, exothermic neutral-neutral chemical reactions, dissociative recombination of molecular ions with electrons, collisions between neutral and electrons, and collisions between neutral and ions. The total infrared cooling breaks down to CO_2 infrared cooling at 15 μm, NO infrared cooling at 5.3 μm, and O(^{3}P) fine structure cooling at 63 μm. The temperature at the lower boundary is a background temperature of 181 K perturbed by diurnal and semi-diurnal tides calculated by the GSWM model [Hagan and Forbes, 2002, 2003] and climatological annual tides [Fleming et al., 1990]. Thermal diffusive equilibrium is assumed for the upper boundary.

The zonal momentum equation is:

$$\frac{\partial u}{\partial t} = \frac{ge^z}{P_0}\frac{\partial}{\partial z}\left(\frac{\mu}{H}\frac{\partial u}{\partial z}\right) + (f + \frac{u}{r}\tan\phi)v + \lambda_{xx}(u_i - u) + \lambda_{xy}(v_i - v) - \vec{V} \bullet \nabla u - w\frac{\partial u}{\partial z} - \frac{1}{r\cos\phi}\frac{\partial \Phi}{\partial \lambda} \quad \text{(Eq. 2.2)}$$

The meridional momentum equation is:

$$\frac{\partial v}{\partial t} = \frac{ge^z}{P_0}\frac{\partial}{\partial z}\left(\frac{\mu}{H}\frac{\partial v}{\partial z}\right) + (f + \frac{u}{r}\tan\phi)u + \lambda_{yy}(v_i - v) + \lambda_{yx}(u_i - u) - \vec{V} \bullet \nabla v - w\frac{\partial v}{\partial z} - \frac{1}{r}\frac{\partial \Phi}{\partial \phi} \quad \text{(Eq. 2.3)}$$

The terms on the right hand side of the momentum equations are: force by molecular and eddy viscosity; Coriolis force; ion drag; horizontal momentum advection; vertical momentum advection; pressure gradient force.

The vertical wind is solved using the continuity equation as follows:

$$\frac{1}{r\cos\phi}\frac{\partial}{\partial \phi}(v\cos\phi) + \frac{1}{r\cos\phi}\frac{\partial u}{\partial \lambda} + e^z\frac{\partial}{\partial z}(e^{-z}w) = 0 \quad \text{(Eq. 2.4)}$$

The upper boundary condition for the momentum and continuity equations is $\frac{\partial u}{\partial z} = \frac{\partial v}{\partial z} = \frac{\partial w}{\partial z} = 0$, and the lower boundary is the specified diurnal and semi-diurnal

tides calculated by the GSWM model [Hagan and Forbes, 2002, 2003] and climatological annual tides [Fleming et al., 1990].

The mass mixing ratio of O and O_2 are solved using major species' continuity equation as follows:

$$\frac{\partial \Psi}{\partial t} = -\frac{e^z}{\tau}\frac{\partial}{\partial z}\left[\frac{\overline{m}}{m_{n_2}}\left(\frac{T_0}{T_n}\right)^{0.25} F\left(\frac{\partial}{\partial z} - \left(1 - \frac{m}{\overline{m}} - \frac{1}{\overline{m}}\frac{\partial \overline{m}}{\partial z}\right)\right)\Psi\right] + S - L$$
$$+ e^z \frac{\partial}{\partial z}\left[K(z)e^{-z}\frac{\partial}{\partial z}\left(1 + \frac{1}{\overline{m}}\frac{\partial m}{\partial z}\right)\Psi\right] - \left(\vec{V} \bullet \nabla\Psi\right) - w\frac{\partial \Psi}{\partial z} \qquad \text{(Eq. 2.5)}$$

where F is a matrix operator representing mutual diffusion between the major gases. The terms on the right hand side are: molecular diffusion; chemical production; chemical loss; eddy diffusion; horizontal advection; and vertical advection. The mass mixing ratio of N_2 is then obtained by: $\Psi_{N_2} = 1 - \Psi_O - \Psi_{O_2}$. Diffusive equilibrium is assumed at the upper boundary. Constant mass mixing ratio 0.22 and 0.78 are specified for O_2 and N_2, respectively, and atomic oxygen density is calculated by assuming that the atomic oxygen peaks at the model lower boundary.

The minor species considered in the TIEGCM model are N(^{4}S), N(^{2}D), and NO due to their contribution to neutral gas heating through exothermic neutral-neutral chemical reactions [Roble et al., 1988] and NO infrared cooling at 5.3 μm. N(^{4}S) and NO are long-lived enough to consider transport effects. The mass mixing ratio of N(^{4}S) and NO is solved using the minor gas continuity equation as follows:

$$\frac{\partial \psi}{\partial t} = -e^{-z}\frac{\partial}{\partial z}A\left[\frac{\partial}{\partial z} - E\right]\psi + e^z \frac{\partial}{\partial z}e^{-z}K_E\left[\frac{\partial}{\partial z} + \frac{1}{\overline{m}}\frac{\partial \overline{m}}{\partial z}\right]\psi$$
$$- \vec{V} \bullet \nabla\psi - w\frac{\partial \psi}{\partial z} + S - L \qquad \text{(Eq. 2.6)}$$

where $E = \left[1 - \frac{m}{\overline{m}} - \frac{1}{\overline{m}}\frac{\partial \overline{m}}{\partial z}\right] - \alpha\frac{1}{T}\frac{\partial T}{\partial z} + F\psi$

where A is the vertical molecular diffusion coefficient and α is the thermal diffusion coefficient. The three terms of E represent gravitation effects, thermal diffusion effects, and frictional interactions with major species. F is a matrix operator representing frictional interaction between the minor species and major species. The terms on the right hand side are: vertical molecular diffusion; vertical eddy diffusion; horizontal advection; vertical advection; chemical production; and chemical loss. Photochemical equilibrium is assumed for both the upper and lower boundary conditions for N(^{4}S). The lower boundary condition for NO is a constant NO number density of $4\times10^6\,cm^{-3}$ while the upper boundary condition for NO is photochemical equilibrium. N(^{2}D) is short-lived and thus photochemical equilibrium is assumed to obtain its number density.

2.1.2 Ionospheric Modeling

The independent variables of the ionosphere equation system are:

t: time; ϕ: latitude; λ: longitude; z=ln(P_0/P)

The dependent variables are:

T_e: electron temperature;

T_i: ion temperature;

n_i: ion density;

n_e: electron density

Other model parameters used in the equations are:

k: Bolzman constant;

u_e: electron bulk velocity;

Q_e: total electron heating;

L_e: total electron cooling;

Q: chemical production of ions;

L: chemical loss of ions;

β_e: thermoelectric transport coefficient;

$\vec{E}$: electric field;

$\vec{B}$: magnetic field;

K: electron thermal conductivity

All major ionospheric ions except O^+ are in photochemical equilibrium in the ionosphere below 1000 km. The transport of O^+ by electric field and the Earth's magnetic field is important for O^+ concentration. The O^+ continuity equation is:

$$\frac{\partial n_i}{\partial t} = -\nabla \bullet (n_i \vec{V}) + Q - L n_i \qquad \text{(Eq. 2.7)}$$

where $\vec{V}$ is the ion velocity as follows:

$$\begin{gathered} \vec{V} = \vec{V}_{\parallel} + \vec{V}_{\perp} \\ \vec{V}_{\parallel} = \left\{ \vec{b} \bullet \frac{1}{\nu} \left[\vec{g} - \frac{1}{\rho_i} \nabla (P_i + P_e) \right] + \vec{b} \bullet \vec{U} \right\} \vec{b} \\ \vec{V}_{\perp} = \frac{\vec{E} \times \vec{B}}{|B|} \end{gathered} \qquad \text{(Eq. 2.8)}$$

and where $\vec{V}_{\parallel}$ is the ion velocity parallel to the Earth's magnetic field caused by the ambipolar diffusion, and $\vec{V}_{\perp}$ is the ion velocity perpendicular to the magnetic field caused by $\vec{E} \times \vec{B}$ electrodynamic force ($\vec{E} \times \vec{B}$ drift). $\vec{b}$ is a unit vector along the magnetic field; ν is ion-neutral collision frequency; ρ_i is ion mass density; $\vec{g}$ is gravity acceleration; P_i and P_e are the ion and electron pressure, respectively; $\vec{U}$ is the neutral wind; $\vec{E}$ is the electric field which is mainly magnetospheric-origin at high latitudes and neutral wind dynamo generated at low latitudes; $\vec{B}$ is the Earth's magnetic field. The first term of the right hand side of Eq. 2.7 represents transport of O^+ due to $\vec{E} \times \vec{B}$ drift and ambipolar diffusion along the magnetic field. The second term Q is total production of O^+ through ionization by photon and photoelectron, dissociative ionization by photon and photoelectron, and chemical reactions. The last term L is the total loss of O^+ through charge exchange and chemical reactions of O^+ with neutrals. Photochemical equilibrium is assumed at the lower boundary and an upward or downward O^+ flux is specified at the upper boundary to represent O^+ transport from and to the plasmasphere.

The density of other ions, i.e., O_2^+, NO^+, N^+, and N_2^+, is calculated assuming photochemical equilibrium once O^+ is determined. And the electron number density is the sum of number density of all ions based on charge neutrality in the ionosphere.

The electron temperature equation is:

$$\frac{3}{2}n_e k\frac{\partial T_e}{\partial t} = -n_e kT_e \nabla \bullet \vec{u}_e - \frac{3}{2}n_e k\vec{u}_e \bullet \nabla T_e - \nabla \bullet \vec{q}_e + Q_e - L_e \qquad \text{(Eq. 2.9)}$$

The terms on the right hand side are: effect of adiabatic expansion; heat advection; divergence of heat; total electron heating through ionization by photon and auroral particle precipitation; and total cooling by collisions with ions and neutrals. It is assumed that electron temperature is equal to the neutral temperature at the lower boundary. The upper boundary condition is specified as $K\frac{\partial T_e}{H\partial z} = F$, where F is a specified heat flux from the plasmasphere.

The ion temperature is calculated by assuming quasi-steady state of energy transfer among electrons, ions, and neutrals. Ion heating by ion-electron collisions and Joule heating is balanced by cooling through ion-neutral collisions as follows:

$$A(T_e - T_i) + \rho Q_J = B(T_i - T\ ) \qquad \text{(Eq. 2.10)}$$

where A and B are energy transfer coefficients between ions and electrons, and between ions and neutrals, respectively. Q_J is Joule heating, and T is neutral temperature.

2.1.3 Thermosphere and Ionosphere Coupling

The Eulerian thermosphere model and the ionosphere model are solved on the same spherical coordinates with same time step, but the electrodynamics of neutral wind dynamo of the ionosphere is calculated using magnetic apex coordinates [Richmond, 1995]. The apex coordinate system is based on the International Geomagnetic Reference Field (IGRF). The mutual coupling of the thermosphere and the ionosphere occurs at each model time step and at each point of the model grid. The coupled model calculates, in the following order, the electron and ion density, the electron and ion temperature,

concentration of minor neutral constituents, neutral temperature, and concentration of major neutral constituents. The ionospheric calculation needs information on concentrations of neutral constituents, neutral temperature, the electric field generated by the neutral wind dynamo, and ion-neutral and electron-neutral elastic and inelastic collisions (Eq. 2.7–2.10). Likewise, the thermospheric calculation depends on heating through ion-neutral and electron-neutral elastic and inelastic collisions, momentum source/sink caused by ion-drag through ion-neutral collisions, and chemical production and loss of neutral constituents by ions (Eq. 2.1–2.6). The electrodynamic interaction between the thermosphere and the ionosphere through the neutral wind dynamo process is calculated self-consistently using magnetic apex coordinates [Richmond et al., 1992]. The coupled model uses electron density and neutral wind to calculate the electric field and current resulting from wind moving the electrically conducting fluid through the Earth's geomagnetic field. Then it uses the electric field and current to calculate the dynamo feedback on the neutral and plasma dynamics.

2.1.4 Specification and Parameterization of External Forcing

The sources of external forcing of the coupled thermosphere/ionosphere are solar irradiance mainly in the Extreme Ultra-Violet (EUV) and Ultra-Violet (UV) region; geomagnetic energy input in the form of auroral energetic particle precipitation and ionospheric convection driven by the magnetosphere-ionosphere current system; perturbation at the lower boundary of the model by waves representing the interaction between the thermosphere/ionosphere system and the lower atmosphere processes; and a specified upward or downward plasma flux at the upper boundary representing the interaction of the system with the plasmasphere.

The time-varying solar irradiance can be specified either by a solar irradiance proxy model or measurements. The solar irradiance input and the photoionization and photodissociation calculation will be addressed in detail in Section 2.2.

The ionospheric convection driven by the magnetosphere-ionosphere current system is specified by the empirical model of Heelis et al. [1982]. The auroral particle

precipitation and its ionization and dissociation are calculated by an analytical auroral model described by Roble and Ridley [1987].

The effect of semi-diurnal and diurnal tides is specified at the lower boundary using the GSWM calculation [Hagan and Forbes, 2002, 2003]. In addition, a climatological annual tidal perturbation is specified at the lower boundary [Fleming et al., 1990]. Turbulent mixing caused by gravity wave breaking is specified using a constant eddy diffusion coefficient.

Figure 2.1 and figure 2.2 give sample output of some thermospheric and ionospheric variables simulated by the TIEGCM. Latitudinal and solar local time distributions of neutral temperature, neutral density, and horizontal winds at 300 km for 21 June 2004 are shown in figure 2.1 while the corresponding number densities of thermospheric major species O and N_2 and ionospheric species electron and O^+ are shown in figure 2.2.

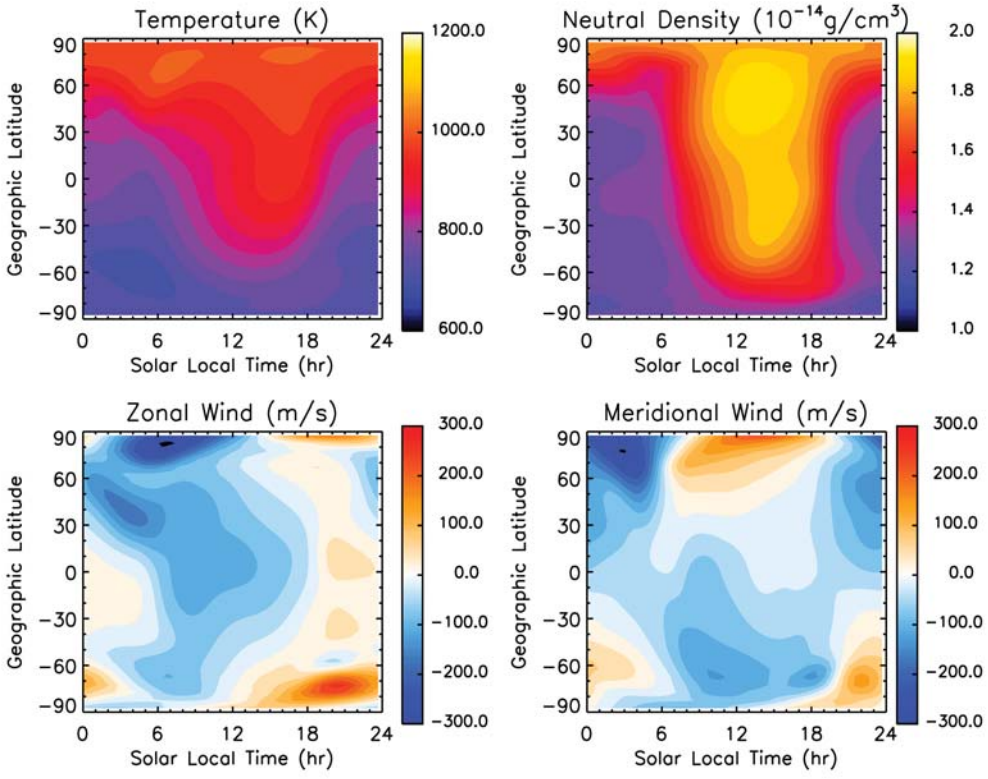

Figure 2.1: TIEGCM simulated neutral temperature, neutral density, zonal wind, and meridional wind at 300 km, for 21 June 2004.

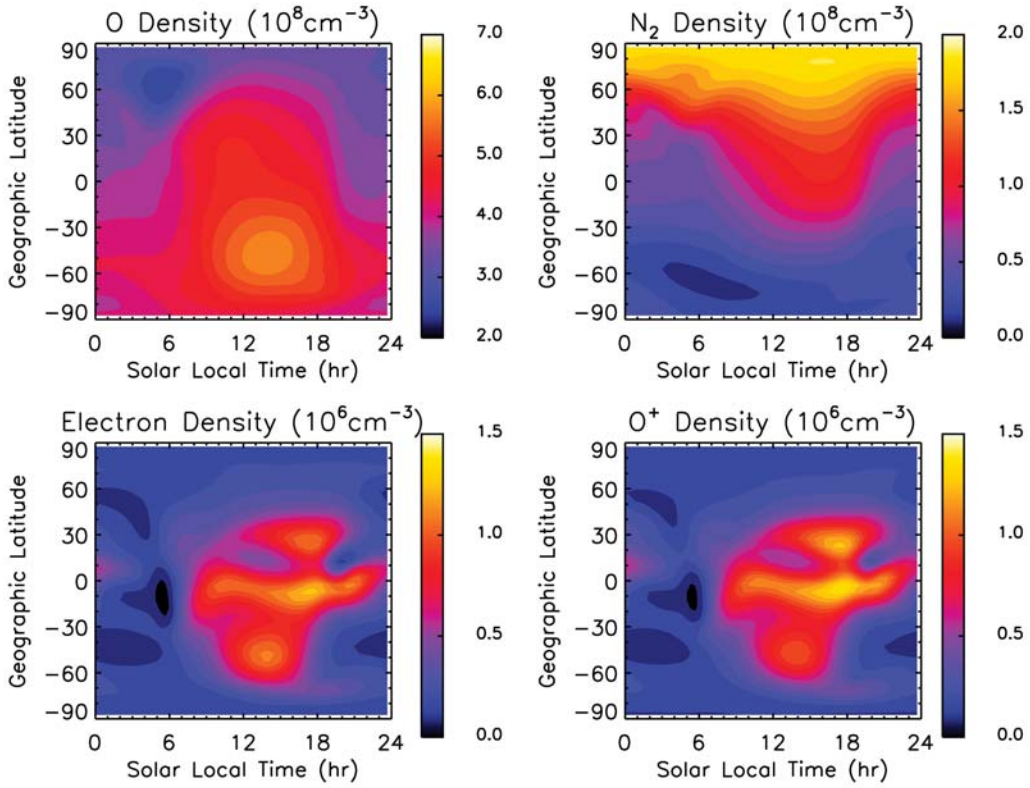

Figure 2.2: TIEGCM simulated O number density, N_2 number density, electron density, and O^+ number density at 300 km, for 21 June 2004.

2.1.5 The TIMEGCM

The TIEGCM is extended downward to the upper stratosphere [Roble and Ridley, 1994; Roble, 1995]. The aeronomic scheme of the TIEGCM is extended to include species important to the mesosphere and the upper stratosphere. The major species O is changed to $O_x = O + O_3$. The minor species transport equation is solved not only for N(^{4}S) and NO, but also for other long-live species: H_2O, H_2, CH_4, CO, CO_2, $HO_x = H + HO_2 + OH$, and $NO_x = NO + NO_2$. In addition, the gravity wave effect is

included using the gravity wave parameterization scheme of Lindzen [1981]. The global mean single column version of the TIMEGCM is described by Roble [1995]. The global mean model will be used in this thesis to investigate the climate change in the thermosphere caused by greenhouse gases, mainly CO_2.

2.2 Solar Energy Deposition

The Sun emits spectral electromagnetic radiation from its atmosphere at an equivalent black body temperature around 6000 K with most of its energy at visible wavelengths. The total solar irradiance is 1366 W/m^2 and the solar-cycle variation of the total solar irradiance is less than 0.1%. The solar atmosphere is divided into the photosphere, the chromosphere, the transition region, and the corona. As the solar atmosphere extends from the photosphere to the corona, it becomes hotter, less dense, and emits irradiance at shorter wavelength with increasingly large variability. Table 2.1 gives the acronyms used to indicate different regions of the solar spectrum from the X-ray to the infrared radiation, the wavelength range, the solar-cycle variability, the source of the irradiance, and the deposit area in the earth system.

The solar irradiance varies at time scales from minutes to years. The most import variations are the rapid variation with solar flares, the 27-day solar-rotational variation, and the 11-year solar-cycle variation. A solar flare is an explosion near sunspots at the Sun's surface that is characterized by its brightness in the X-rays. A solar flare produces a burst of solar radiation across its spectrum but especially in the shortest wavelengths. Solar flares are classified by the X-ray brightness in the wavelength range from 0.1–0.8 nm. A solar flare can increase X-ray irradiance more than 2 orders of magnitude in minutes, and it increases the XUV irradiance several times in minutes. The XUV deposits its energy between 100 and 200 km. Since photoelectrons generated by the XUV photoionization have enough energy to further ionize, dissociate, and excite neutral species, the XUV is very important to the E-region ionization, odd nitrogen and nitric oxide balance, and daytime airglow. The 27-day solar-rotational variation is associated with the appearance and disappearance of active regions on the solar disk as the Sun

rotates in its average 27-day period. The 27-day solar-rotational variation is typically one-third of the solar-cycle variation. The 11-year solar-cycle variation is caused by the 22-year solar magnetic field cycle driven by the internal solar dynamo process.

Table 2.1: Different regions of the solar spectrum and some general properties.

Acronym	λ(nm)	Solar Cycle Variability (Max/Min)	Source	Terrestrial Deposit
X-ray	0.01–1	~100	corona	thermosphere mesosphere
XUV (soft X-ray ultraviolet)	1–30	~10	corona	thermosphere mesosphere
EUV (extreme ultraviolet)	30–120	~0.2– 2	chromosphere	thermosphere
FUV (far ultraviolet)	120–200	~1.15	chromosphere photosphere	thermosphere mesosphere
MUV (middle ultraviolet)	200–300	~1.01	chromosphere photosphere	mesosphere stratosphere troposphere
NUV (near ultraviolet)	300–400	~1.001	chromosphere photosphere	stratosphere troposphere
VIS (visible)	400–700	<1.001	photosphere	troposphere Earth's surface
IR (infrared)	700–1,000,000	<1.001	photosphere	troposphere Earth's surface

The solar irradiance shortward of 175 nm is the most variable part of the solar spectrum, and its energy is mostly deposited in the thermosphere. The total irradiance of this wavelength range is less than 0.1 W/m^2 but its solar-cycle variability is around 20%. As a result, the thermosphere and the ionosphere are strongly influenced by solar activity.

The solar flare signatures can be clearly seen in the thermosphere/ionosphere system and the solar-rotational and solar-cycle variations are dominant variations in the thermosphere and ionosphere properties.

In addition, the variation in the sun-earth distance also causes variation of solar irradiance received by the Earth at 1 AU. The Earth's orbit has eccentricity of 0.017. The Earth is closest to the Sun at the beginning of January and farthest to the Sun at the beginning of July. It causes around 7% insolation variation at the top of the atmosphere from maximum in January to minimum in July. This variation contributes to an annual component of the thermosphere and ionosphere variation.

2.2.1 A Solar Irradiance Interface for the TIEGCM

The solar irradiance that is important to the thermosphere is the XUV, the EUV, and the Schumann-Runge continuum from 132–175 nm. The sources of solar input for an upper atmospheric general circulation model can be divided into three categories: solar irradiance models, high-resolution measurements, and low-resolution measurements.

Solar irradiance in the X-ray and the XUV regions are often measured at broadband with low resolutions, and the EUV and the FUV are measured at higher resolution of 1 nm or less (table 2.2). Some important solar irradiance measurements in this wavelength range are listed in table 2.2. In addition to satellite measurements, rocket measurements are usually made to calibrate instruments carried aboard satellites. A mission is usually designed to measure a particular range of solar irradiance. For example, the GOES satellites measure the X-ray region at two channels of 0.05–0.4 nm and 0.1–0.8 nm, the TIMED/SEE measures from the X-ray to the FUV, while the SORCE/SIM measures the solar spectrum from 0.1–2400 nm but excludes EUV from 34–115 nm. A mission usually lasts for several years and continuous measurements are usually not available. For example, there is a period from the AE/E mission to the TIMED/SEE mission (1981–2002) when there are no EUV measurements, and this period is called the "EUV hole."

Table 2.2: Important measurements and commonly used solar proxies for X-ray, XUV, EUV, and FUV.

Spectral Range	Measurements	λ (nm)	Δλ (nm)	Time Period	Proxies
X-ray (0.05–1 nm)	GOES*	0.05–0.4 0.1–0.8	entire channel	1974–present	
XUV (1–30 nm)	SOLRAD* OSO/SES* AE-E/EUVS* Yohkoh/SXT* SOHO/SEM* SNOE/SXP* TIMED/SEE* SORCE/XPS*	1–10 2–40 14–185 0.2–3 26–34 0.2–20 0.1–34 0.1–34	1 0.1 0.2–1 3 8 4–7 5–10 5–10	1960–1976 1967–1970 1974–1981 1992–2002 1996–present 1998–2003 2002–present 2003–present	$F_{10.7}$
EUV (30–120 nm)	OSO/EUVS* AEROS* AE-E/EUVS* TIMED/SEE*	27–131 20–104 14–185 27–195	0.2 1 0.2–1 0.4	1967–1970 1973–1975 1974–1981 2002–present	Coronal: $F_{10.7}$ Chromospheric: Lyman-α Mg II c/w
FUV (120–200 nm)	SME* UARS* TIMED/SEE* SORCE/SIM*	 119–420 27–195 115–310	 1 0.4 1	1982–1986 1991–2005 2002–present 2003–present	Chromospheric: Lyman-α Mg II c/w Phtospheric: PSI

* The following website provides detailed information about each experiment and its data set: http://nssdc.gsfc.nasa.gov/nmc/sc-query.html

Due to the difficulty in measuring solar irradiance in both temporal and spectral coverage, solar irradiance models have been developed based on observations. Solar irradiance models are often referred to as solar proxy models because variations of usually well-measured solar indices are used to represent variability of solar irradiance in a particular wavelength range. Some commonly used solar proxies are listed in table 2.2 for each wavelength range.

A solar proxy model needs to consider both the absolute solar irradiance and the solar activity variability. Both the solar irradiance and its variability strongly depend on wavelength. A solar proxy model constructs a reference spectrum, usually obtained by rocket or satellite measurements at low solar activity, and uses solar indices to model solar variability. Several widely-used reference spectra that are used in this study are F74113, SC21REFW, and F79050. The F74113 reference spectrum was constructed based on a rocket flight measurement on 23 April 1974 [Heroux and Higgins, 1977; Heroux and Hinteregger, 1978] to represent solar irradiance at low solar activity. The SC21REFW and the F79050 reference spectra are based on the AE-E EUV measurements and were constructed by Hinteregger et al. [1981b] as solar reference spectra for solar minimum condition and solar maximum condition, respectively. The solar fluxes shortward of 30 nm of the F74113 is a factor of 2 larger than those of the SC21REFW.

Several solar proxy models have been developed. The Hinteregger model [also referred to as the SERF 1 model, Hinteregger et al., 1981] and the EUVAC [Richards, et al., 1994] are based on AE-E measurements and several sounding rocket measurements during the same period. The Woods and Rottman model [Woods and Rottman, 2002] is based on UARS (Upper Atmosphere Research Satellite) SOLSTICE (SOLar STellar Irradiance Comparison Experiment) measurements from 119–200 nm, a 1994 rocket measurement, and AE-E relative variability from 0–119 nm. The Hinteregger model covers irradiance from 1.8–200 nm with overall 0.1-nm resolution and includes emission lines in the XUV, the EUV, and the FUV. The Hinteregger model uses the SC21REFW as its reference spectrum. It originally used the chromospheric emission H I Lyman-β (102.6 nm) as the proxy for chromospheric emissions and Fe XVI (33.5 nm) as the proxy

for coronal emissions. The solar variability was later changed to be represented by $F_{10.7}$ and the 81-day average $F_{10.7}$ due to the unavailability of H I Lyman-β and Fe XVI measurements. The Hinteregger model is considered an acceptable standard from ~30–103 nm but its irradiance short-ward 30 nm might be underestimated by as much as a factor of 4 [Richards and Torr, 1984; Solomon, 1991; Solomon, et al., 2001]. The EUVAC includes irradiance from 5–105 nm and uses a binning scheme proposed by Torr et al. [1979]. The scheme divides the wavelength range into 37 bins that have 5-nm resolution for continuum and individual bins for bright emission lines. The reference spectrum for the EUVAC is based on the F74113 with the EUV fluxes between 15 nm and 25 nm doubled and the EUV flux below 15 nm increased by a factor of 3. The solar variability scale factors are based on the AE-E and calibration rocket measurements. The solar proxies are $F_{10.7}$ and the 81-day averaged $F_{10.7}$. The Woods and Rottman model provides solar irradiance form 0–200 nm with 1-nm resolution centered on 0.5 nm. The reference spectrum is constructed from different sources: the SOLAR2000 [Tobiska et al., 2000] for the XUV, a sounding rocket measurement of 1994 [Woods et al., 1998] for the EUV, and UARS measurements for the FUV. The solar variability measured by the AE-E [Hinteregger et al., 1981b] is used to scale solar irradiance variation with solar activity. $F_{10.7}$ is used as the solar proxy. All these proxy models are $F_{10.7}$ based solar proxy models. Recently, it has been found that using different indices to represent solar irradiance originating from different layers of the solar atmosphere can improve empirical representation of the solar irradiance variation [Bowman, et al., 2006; Tobiska, et al., 2006; Bowman and Tobiska, 2006].

In order to bin solar spectral irradiance from various sources with different resolutions and different spectral coverage to the resolutions and spectral coverage required by models in a consistent and systematic way, a general solar irradiance interface was developed to bin solar spectra from various sources into desired binning schemes (figure 2.3). The commonly used binning schemes are 1-nm resolution scheme and the Torr et al. [1979] scheme (5 nm and lines). A low-resolution binning scheme has been developed and will be used in this study [Solomon and Qian, 2005]. It has approximately half of the number of bins of the Torr et al. [1979] binning scheme. It will

be introduced in Section 2.2.3. The solar irradiance interface processes solar spectral irradiances from difference sources that have different spectral resolutions and different spectral coverage into solar spectra with desired resolution and desired spectral coverage for aeronomy calculations, in an energy conserving way.

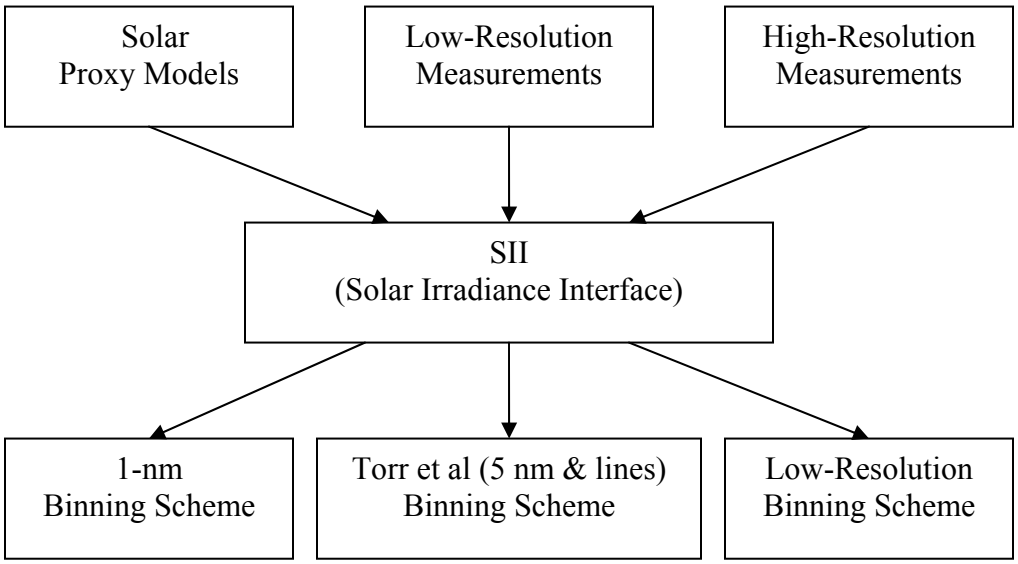

Figure 2.3: A solar irradiance interface that processes solar spectra from various sources with different resolutions into solar spectra on desired binning scheme.

2.2.2 Solar Spectrum Specification for the TIEGCM

The TIEGCM uses a solar proxy model as the default solar input. The spectral range required by the TIEGCM is 0.05–175 nm. The original TIEGCM used the Torr et al. binning scheme. In this study, the low-resolution binning scheme (Section 2.2.3) will be used instead. The reference spectrum and the solar variability factor are obtained from different sources for different wavelength ranges. The solar variability factor has the same meaning as the solar activity scaling factor for the EUVAC model. They are given in table 2.3.

Table 2.3: The reference spectrum and solar variability factor for the solar proxy model used in the TIEGCM.

λ_{min} (nm)	λ_{max} (nm)	Reference Spectrum(f_{ref}) (Photon/cm^2/s)	Variability Factor(A)
0.05	0.40	5.010e+01	6.240e-01
0.40	0.80	1.000e+04	3.710e-01
0.80	1.80	2.000e+06	2.000e-01
1.80	3.20	2.850e+07	6.247e-02
3.20	7.00	5.326e+08	1.343e-02
7.00	15.50	1.270e+09	9.182e-03
15.50	22.40	5.612e+09	1.433e-02
22.40	29.00	4.342e+09	2.575e-02
29.00	32.00	8.380e+09	7.059e-03
32.00	54.00	2.861e+09	1.458e-02
54.00	65.00	4.830e+09	5.857e-03
65.00	79.80	1.459e+09	5.719e-03
65.00	79.80	1.142e+09	3.680e-03
79.80	91.30	2.364e+09	5.310e-03
79.80	91.30	3.655e+09	5.261e-03
79.80	91.30	8.448e+08	5.437e-03
91.30	97.50	3.818e+08	4.915e-03
91.30	97.50	1.028e+09	4.955e-03
91.30	97.50	7.156e+08	4.422e-03
97.50	98.70	4.482e+09	3.950e-03
98.70	102.70	4.419e+09	5.021e-03
102.70	105.00	4.235e+09	4.825e-03
105.00	110.00	3.298e+09	3.007e-03
110.00	115.00	3.200e+09	2.099e-03
115.00	120.00	8.399e+09	2.541e-03
121.57	121.57	3.940e+11	4.230e-03
120.00	125.00	1.509e+10	3.739e-03
125.00	130.00	7.790e+09	2.610e-03
130.00	135.00	2.659e+10	2.877e-03
135.00	140.00	1.387e+10	2.632e-03
140.00	145.00	1.824e+10	1.873e-03
145.00	150.00	2.802e+10	1.202e-03
150.00	155.00	5.080e+10	1.531e-03
155.00	160.00	7.260e+10	1.125e-03
160.00	165.00	1.055e+11	1.043e-03
165.00	170.00	1.998e+11	6.089e-04
170.00	175.00	3.397e+11	5.937e-04

The GOES X-ray measurements at the two channels, 0.05–0.4 nm and 0.1–0.8 nm, are used to establish the reference irradiance and the solar variability factor for the first two bins. The third bin, i.e., from 0.8–1.8 nm, is based on some early X-ray/XUV measurements [DeJager, 1964; Smith and Gottlieb, 1974, Manson, 1977; Kreplin et al.,

1977; Horan and Kreplin, 1981]. The Hinteregger model is used for the wavelength range from 1.8–5 nm except that the SC21REFW and the F79050 solar fluxes are increased by a factor of 3. The EUVAC model is used between 5 nm and 105 nm, and the Woods and Rottman model from 105 nm to 175 nm. Once the low solar activity reference spectrum and the variability factor are defined (table 2.3), solar flux at a given solar activity is then obtained through $F_{10.7}$ and $\overline{F}_{10.7}$ as done by the EUVAC as follows:

$$f(\lambda) = f_{ref}(\lambda)[1 + A(\lambda)(P - 80)] \qquad \text{(Eq. 2.11)}$$

where f_{ref} and A are the reference spectrum and solar variability factor given in table 2.3, and $P = 0.5 * (F_{10.7} + \overline{F}_{10.7})$. It is apparent that the solar spectrum is equivalent to the solar minimum reference spectrum when P is 80. For solar minimum condition when P is less than 80, the proxy model assumes that solar irradiance is no less than 80% of the solar minimum reference spectrum.

Solar proxy models have been widely used in aeronomy studies. The proxy models discussed so far are all $F_{10.7}$ based solar proxy models. Recently, it has been found that using different indices to represent solar irradiance originating from different layers of the solar atmosphere, i.e., the chromosphere, the transition layer, and the corona, can improve the empirical representation of the solar irradiance variation. Nevertheless, solar irradiance can change significantly arising from solar flares, the solar 27-day rotation, and the 11-year solar cycle. Solar proxy models cannot simulate these variations precisely. Therefore, it is crucial to have the option to use daily solar measurements directly in a GCM. The TIMED/SEE has measured solar EUV since 8 February 2002. It covers nearly from the solar maximum to the solar minimum of solar cycle 23. As mentioned earlier, the TIMED/SEE data products include solar fluxes shortward of 200 nm at 1-nm resolution. The upper panel of figure 2.4 shows the TIMED/SEE solar irradiance for 8 February 2002 and 21 December 2006. Both $F_{10.7}$ and the 81-day average $F_{10.7}$ for 8 February 2002 are 192. For 21 December 2006, $F_{10.7}$ and the 81-day average $F_{10.7}$ are 72. Therefore, the two dates represent strong solar activity and solar minimum condition, respectively. The two spectra are processed by the solar irradiance interface

and binned into the low-resolution binning scheme. The solar fluxes on the low-resolution binning scheme are given in the lower panel of figure 2.4.

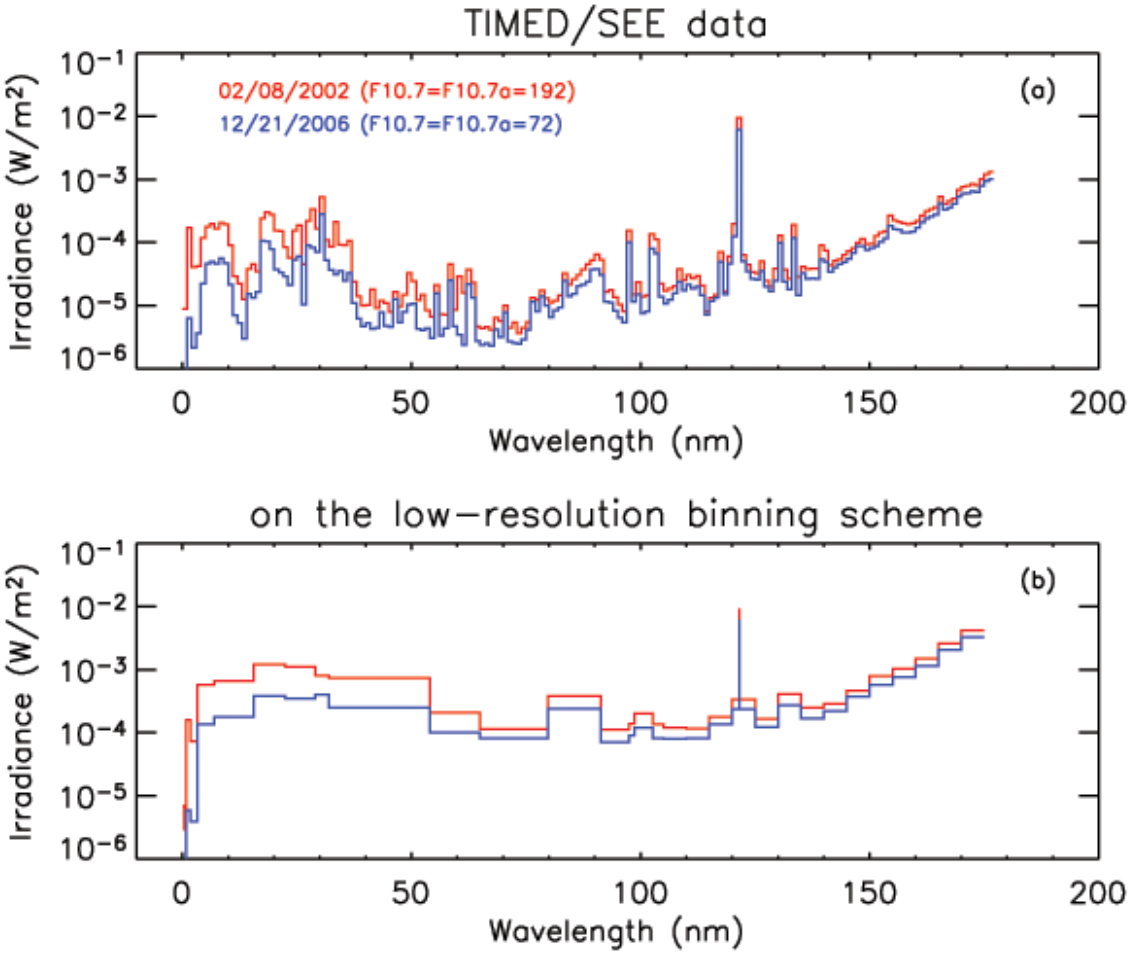

Figure 2.4: Daily-average solar irradiance shortward of 175 nm measured by the TIMED/SEE. Panel (a): daily-average solar irradiance in the TIMED/SEE data format, i.e., on the 1-nm binning scheme; Panel (b): daily-average solar irradiance binned into the low-resolution binning scheme using the solar irradiance interface [Solomon and Qian, 2005]. Red: 8 February 2002, $F_{10.7} = \overline{F}_{10.7} = 192$; Blue: 21 December 2006, $F_{10.7} = \overline{F}_{10.7} = 72$.

2.2.3 A new Solar Energy Deposition Scheme

Solar XUV and EUV are almost completely absorbed in the thermosphere, primarily by O, O_2, and N_2 through photon ionization and dissociation. The ionization threshold of O, O_2, and N_2 are 91.3 nm, 102.6 nm, and 79.8 nm, respectively. The dissociation threshold of N_2 is 98.6 nm. The spectrum longward of 102.6 nm is mainly absorbed by O_2 dissociation, especially at the Schumann-Runge continuum from 132–175 nm. Photoelectrons generated in the photon ionization process are energetic electrons that can further ionize, dissociate, and excite neutral constituents. Photon ionization and photoelectron ionization create the ionosphere. The products of ionization, dissociation, and excitation initiate a sequence of elastic and inelastic collisions that transfer initial photon and electron energy into kinetic energy of the electrons, ions, and neutral gases and thus heat the thermosphere and the ionosphere. Excited species cool the upper atmosphere through air glow and infrared radiation, and the thermosphere heat budget is balanced by downward molecular and eddy heat conduction and by geomagnetic heating at high latitudes.

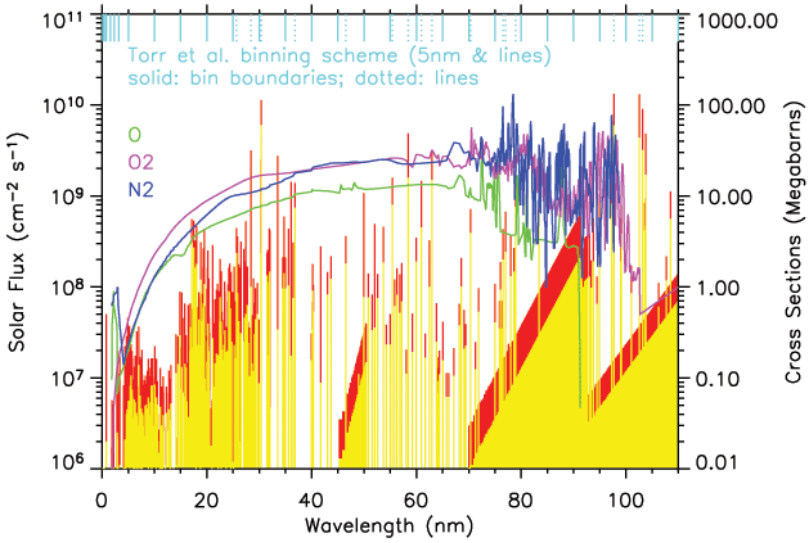

Figure 2.5: Solar EUV spectra for low solar activity (SC21REFW, yellow) and high solar activity (F79050, red), the major species absorption cross sections, and the Torr et al. binning scheme (5 nm and lines).

Improvement of the calculation of thermospheric solar energy deposition for a GCM is twofold: 1) a low-resolution binning scheme for calculation of photon ionization (photoionization) and photon dissociation (photodissociation) and 2) an adequate parameterization of ionization and dissociation by photoelectrons. The spectral range discussed here for the new solar energy deposition scheme is from 0.05–105 nm. The spectrum longward of 105 nm is binned into 5-nm bins evenly with an exception. A bin is made for Lyman-α to account for a window with low O_2 dissociation cross section at Lyman-α; Lyman-α is absorbed by NO ionization. The solar spectrum from 0.05–105 nm is highly structured and the major constituents' absorption cross sections are also highly structured in some of the wavelength range (figure 2.5). Therefore, precise calculations of ionization, dissociation, and excitation by photons need to be made using high spectral resolutions. But resource intensive global models, such as the TIEGCM and the TIMEGCM, must be made computationally efficient. In addition, the photon ionization process generates energetic electrons called photoelectrons or secondary electrons. Photoelectrons generated by shorter EUV wavelengths usually have sufficient energy to ionize, dissociate, and excite neutral species. The photoelectron flux and its impact on ionization, dissociation, and excitation can be calculated using models that are based on radiative transfer methods [e.g. Nagy and Banks, 1970; Solomon et al., 1988; Solomon and Abreu, 1989; Bailey et al., 2002]. However, such detailed calculations are not practical for a global circulation model. The photoelectron impact needs to be parameterized in a global circulation model.

A Low-Resolution Binning Scheme

The binning scheme utilized in past versions of the TIEGCM for the wavelength range from 5–105 nm is the Torr et al. [1979] binning scheme that uses 5-nm resolution plus selected strong EUV lines, which yields 37 bins and lines in this range (figure 2.5). It extends wavelength shortward to 0.05 nm and the wavelength from 0.05–5 nm is divided into 7 bins. Therefore, the total number of bins from 0.05–105 nm is 44 bins. For

simplicity, this binning scheme will be referred as Torr et al. binning scheme. The solid lines along the top of the x-axis in figure 2.5 are bin boundaries and the dotted lines are the selected EUV lines. Another commonly used binning scheme has 1-nm resolution that is used in the Woods and Rottman model [Woods and Rottman, 2002] and the TIMED/SEE data products. It has 105 bins from 0.05–105 nm. Our goal is to reduce the number of bins so that the EUV energy deposition calculation can be computationally effective. Reducing the number of bins will have significant impact on the speed of the solar EUV energy deposition calculation since the EUV calculation is within time, height, latitude, and longitude loops in a GCM. A low-resolution binning scheme has been developed that reduces the number of bins in the wavelength range of 0.05–105 nm from 44 bins to 22 bins [Solomon and Qian, 2005].

The goal of developing a binning scheme for the thermospheric solar energy deposition calculation in a GCM is to be low-resolution for computational efficiency and have sufficient accuracy compared to high resolution calculations. The absorption of solar irradiance at a particular location depends on the attenuated solar irradiance, the absorption species' number density, and the absorption cross sections. Both the solar irradiance and the major species' absorption cross sections strongly depend on wavelength (figure 2.5). In order to use low-resolution to achieve adequate accuracy, the size and bin boundaries for each bin need to be carefully selected by observing the solar irradiance spectrum and the absorption cross section for each species. Even though both solar irradiance and absorption cross sections can be highly variable with wavelength, in most of the wavelengths only one of the two is highly variable at a time. The highly variable regions of solar irradiance dominated by coronal and chromosphere lines between 30 nm and 70 nm correspond to slow variation of ionization continua for O, O_2, and N_2. And the H Lyman continuum from 70–91 nm and C I continuum from 91–105 nm corresponds to highly structured ionization and dissociation bands. The regions where both irradiance and cross sections are highly variable are relatively small. The highly variable X-ray and the hard EUV from 0.05–30 nm overlap the highly variable k-shell ionization cross sections of O, O_2, and N_2. The chromosphere lines in the region between

65 nm and 105 nm, especially the C III line at 97.7 nm, overlap the ionization and dissociation bands and ionization and dissociation thresholds of O, O_2, and N_2.

The low-resolution binning scheme divides the wavelength from 0.05–105 nm into 22 non-uniform bins based on the criteria of small change in cross sections within a bin and change in photon energy less than a factor of two. Some special considerations for strong lines were made along with adjustments by comparing to high resolution calculations. The low-resolution bins are shown in figure 2.6 together with absorption cross sections of major species and reference spectra for low and high solar activities. The first two bins correspond to the GOES satellites' two channels: 0.05–0.4 nm and 0.4–0.8 nm. The next bin boundary is 1.8 nm that corresponds to the low bound of the SC21REFW and the F79050 reference spectra. The k-shell ionization threshold of N_2 gives the next bin boundary. From 3.2–65 nm, coarse bins are used because of the small variation of ionization cross sections of major species, and a small bin is used that includes the bright He II line at 30.4 nm. The wavelengths from 65–97.5 nm are divided into three coarse bins due to the H Lyman continuum and C I continuum, but each bin uses virtual bins to account for the highly structured ionization and dissociation cross sections. Solar fluxes for each bin are sorted into different groups based on the N_2 absorption cross section of small (<4.0e-18 cm^2), medium (between 4.0e-18 cm^2 and 3.1e-17 cm^2) and large (>3.1e-17 cm^2). The three bins are 65–79.8 nm, 79.8–91.3 nm, and 91.3–97.5 nm. The number of virtual bins for each of them is 2, 3, and 3, respectively. The next bin is a high-resolution bin (97.5–98.7 nm) to account for the strong C III line. The next bin boundary corresponds to O_2 ionization threshold of 102.7 nm. The next bin ends at 105 nm, the end of EUV spectral range, by convention. The solid lines along the top x-axis are bin boundaries for the low-resolution binning scheme. It has 22 bins from 0.05–105 nm, including virtual bins.

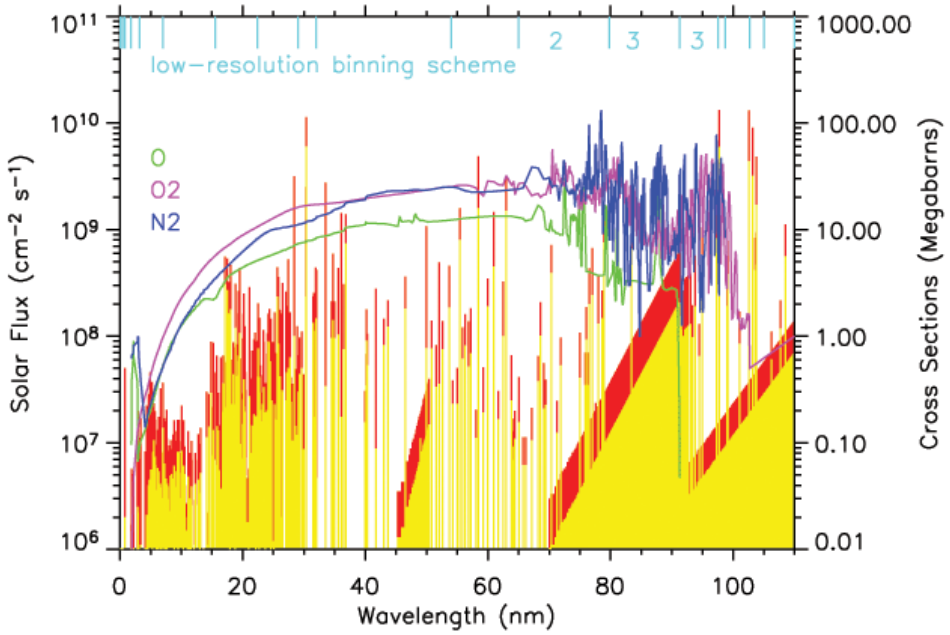

Figure 2.6: Solar EUV spectra for low solar activity (SC21REFW, yellow) and high solar activity (F79050, red), the major species absorption cross sections, and the low-resolution bins.

Photoionization and photodissociation by solar irradiance from 0.05–105 nm are calculated using the low-resolution binning scheme (22 bins), the Torr et al. scheme (44 bins), the 1-nm binning scheme (105 bins), and the high-resolution (813 bins) of Hinteregger et al. [1981] that overall has 0.1 nm resolution. The SC21REFW and the F79050 are used as solar input for low solar activity and high solar activity, respectively. The SC21REFW and the F79050 are binned into the low-resolution binning scheme, the Torr et al. scheme, and the 1-nm scheme using the solar irradiance interface described in Section 2.2.1. The solar irradiance shortward of the lower bound of the SC21REFW and the F79050 (1.8 nm) is based on some early X-ray/XUV measurements [DeJager, 1964; Smith and Gottlieb, 1974, Manson, 1977; Kreplin et al., 1977; Horan and Kreplin, 1981; Wagner, 1988]. The absorption and ionization cross sections for the major species from 5–105 nm are from Fennelly and Torr [1992] compilation and shortward of 5 nm is from Henke et al., [1993]. The cross sections are solar-flux weighted and binned into different binning schemes using the solar irradiance interface of Section 2.2.1. The MSIS00

atmosphere consistent with the low solar activity level of the SC21REFW reference spectrum or the high solar activity level of the F79050 is used to do the calculation of photoionization and photodissociation.

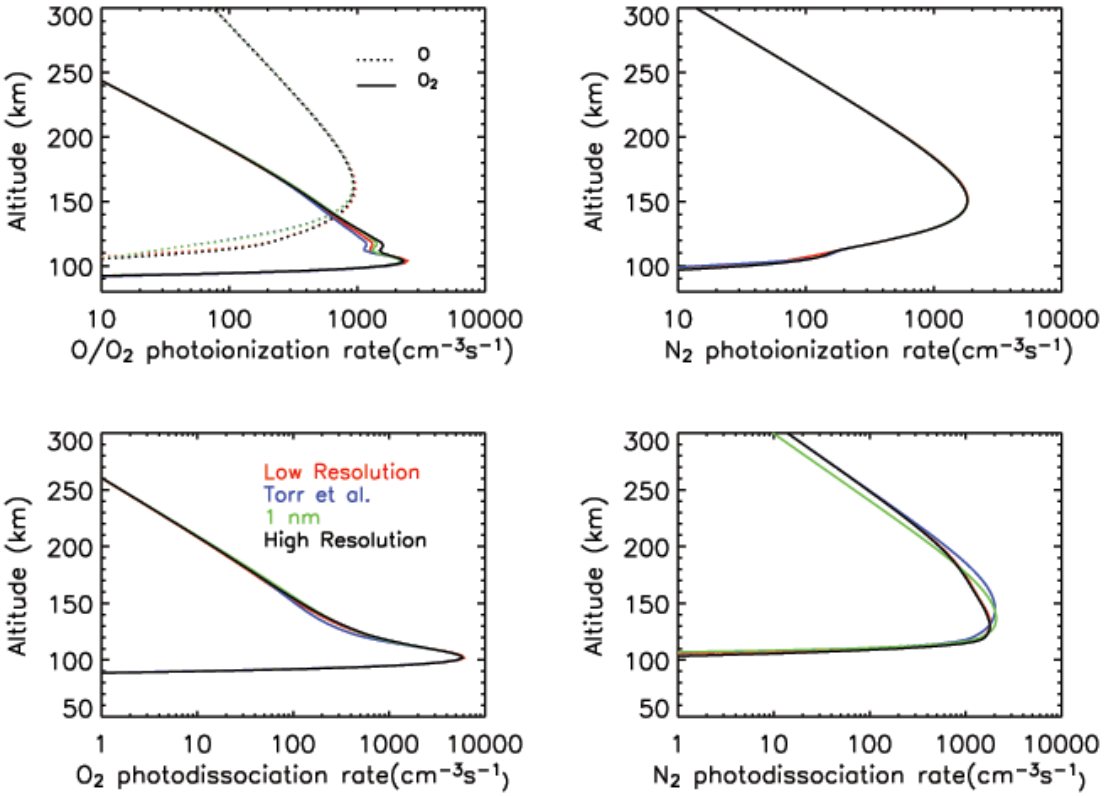

Figure 2.7: Photoionization and photodissociation rates calculated by different binning schemes at low solar activity (SC21REFW reference spectrum) with a solar zenith angle of 0^{o}.

Figure 2.7 shows the photoionization rates for O, O_2, and N_2, and photodissociation rates for O_2 and N_2 under low solar activity and with an overhead sun. The low-resolution binning, with only 22 bins, produces photoionization and photodissociation with good fidelity compared to the high-resolution calculation that has 813 bins. There is some disagreement in part of E region, where the low-resolution generates less photoionization and photodissociation, especially in O_2 and N_2 photoionization. Solar irradiance in short EUV wavelength between 1 nm to 20 nm is important in this region. Using more bins in this wavelength range can improve the

calculation if needed. Overall, the low-resolution binning improves photoionization and photodissociation calculation over the Torr et al. binning and the 1-nm binning, especially in the cases of O photoionization and N_2 photodissociation when the low-resolution binning is superior to both the Torr et al. binning and the 1-nm binning.

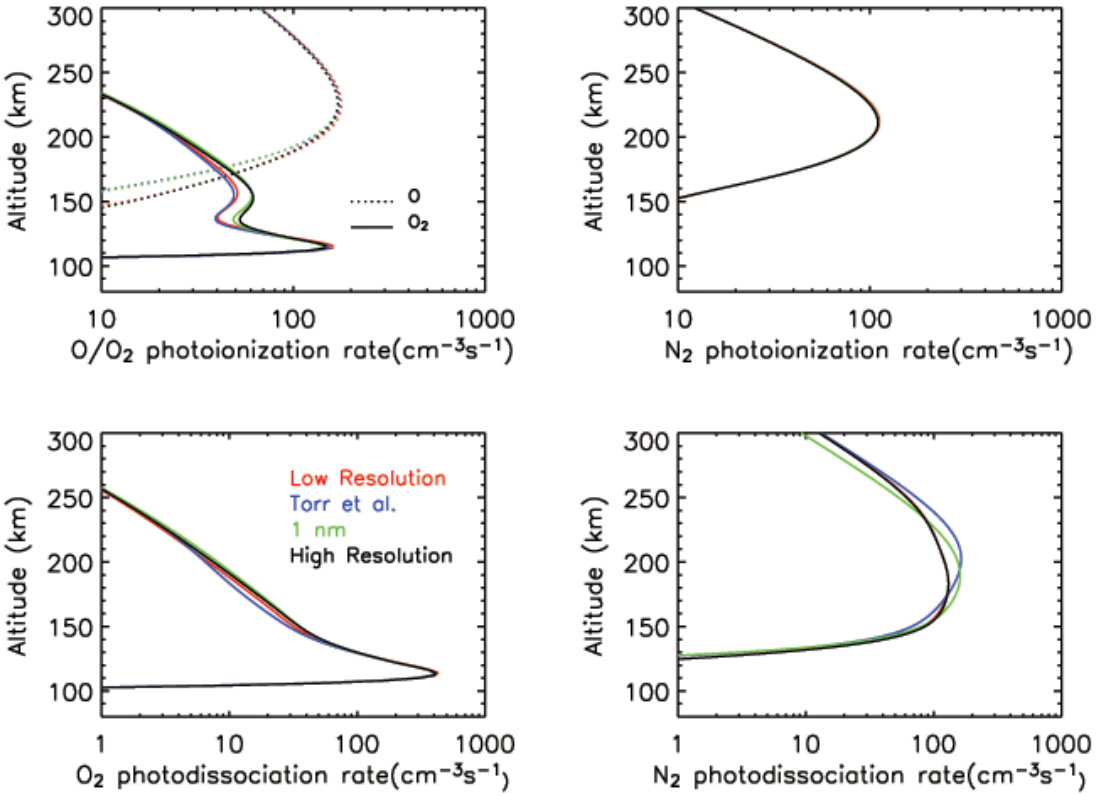

Figure 2.8: Photoionization and photodissociation rates calculated by different binning schemes at low solar activity (SC21REFW reference spectrum) with a solar zenith angle of 85°.

Figure 2.8 gives the results obtained with the same atmosphere and solar input as those of figure 2.7 except that it used a large solar zenith angle of 85°. The low-resolution binning is in good agreement with the high-resolution calculation except that the O_2 photoionization obtained by the low-resolution binning is around 20% less than that of the high-resolution calculation. However, the effect of this discrepancy is less significant due to the low photoionization rate under the large solar zenith angle condition. Again, the low-resolution binning improves upon the Torr et al. binning and 1-nm binning in O

photoionization and N_2 photodissociation calculations. Figure 2.9 shows the comparison of different binning schemes for high solar activity and with 0^o solar zenith angle. The conclusions are consistent with the case of figure 2.7. The comparison for the case of high solar activity and a large solar zenith angle is also conducted and gives consistent results as for the low solar activity and large solar zenith angle conditions. A figure is not shown to avoid repetition. The low-resolution binning scheme is adopted as the binning scheme for the new solar energy deposition scheme for the TIEGCM based on the comparisons.

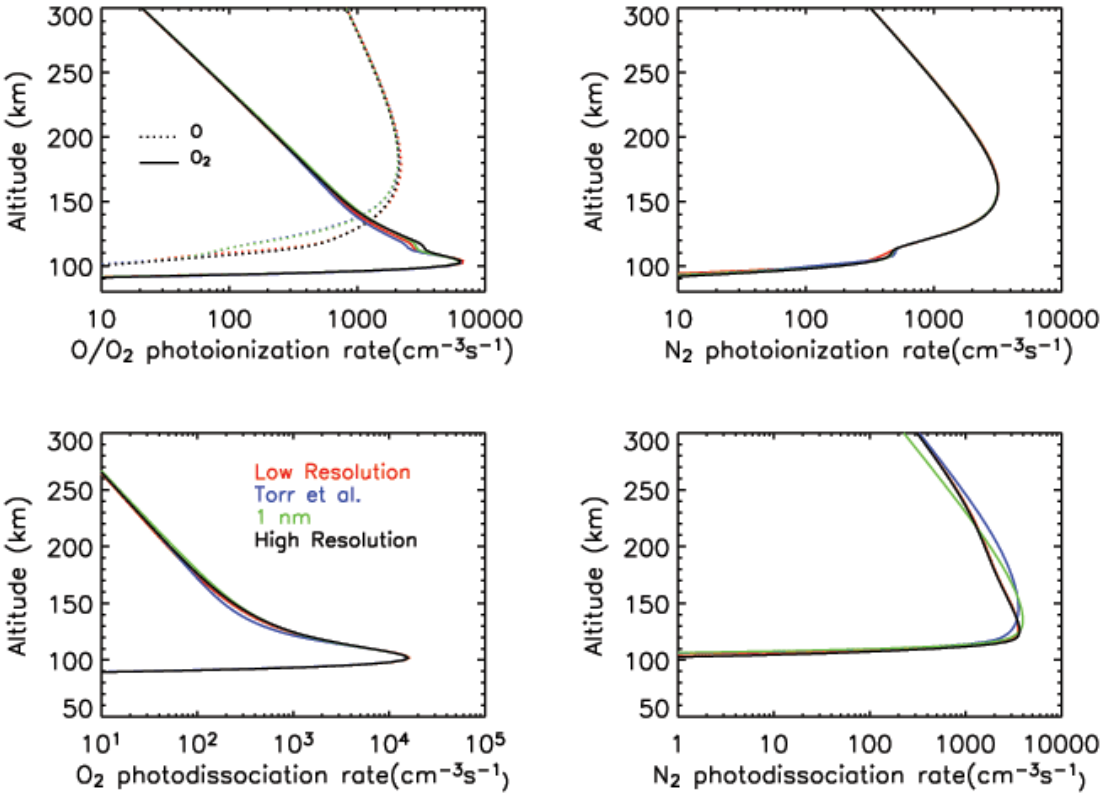

Figure 2.9: Photoionization and photodissociation rates calculated by different binning schemes at high solar activity (F79050 reference spectrum) with a solar zenith angle of 0^o.

Parameterization of Photoelectron Impact

Photoelectrons generated during photoionization can have enough energy to further ionize, dissociate, and excite the neutral atmosphere. Usually, solar EUV at shorter wavelengths has higher energy to generate such energetic photoelectrons. Since shorter EUV reaches the lower thermosphere, photoelectron impact becomes increasingly important with decreasing altitude, and is at least as important as photoionization for O and N_2 in the E region (figure 2.10). Some strong EUV lines at longer wavelengths ionize O_2 but are only lightly absorbed by O and N_2. These generated photoelectrons lack enough energy to further ionize O_2. As a result, the photoelectron impact for O_2 is relatively small compared to those for O and N_2 in the lower thermosphere region. Photoelectron ionization generates more energetic electrons, and these energetic electrons can further ionize, dissociate, and excite the neutral atmosphere. Therefore, there is a spectrum of energetic electrons involved in the photoelectron impact on the thermosphere. The energetic electron flux and the impact on the thermosphere can be calculated by models. For example, the GLOW model [Solomon et al., 1988; Solomon and Abreu, 1989] performs detailed calculations of energetic electron flux and its ionization, dissociation, excitation rates using the two-stream method of Nagy and Banks [1970]. However, detailed calculation of photoelectron impact is not practical in a general circulation model. Instead, photoelectron impact needs to be parameterized. Since the amount of photoelectrons is directly linked to the photoionization rate, it is straightforward to parameterize photoelectron impact based on the photoionization rate. The ratio of the photoelectron ionization rate to the photoionization rate is often referred to as the photoelectron enhancement factor. Nevertheless, representation of photoelectron impact is a particular problem for global models, since the photoelectron enhancement factor is highly variable with altitude (figure 2.10). It also varies with solar activity, geomagnetic activity, and composition.

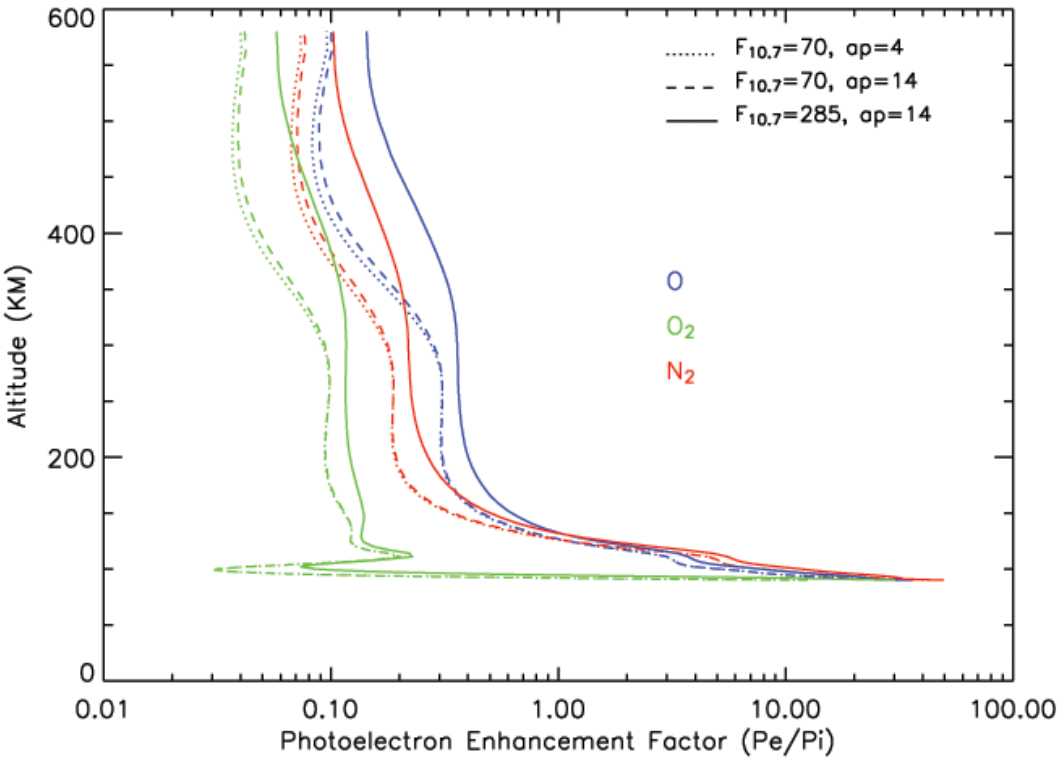

Figure 2.10: The ratio of the photoelectron ionization rate to the photonionization rate, i.e., photoelectron enhancement factor, as a function of altitude.

The current parameterization scheme for the photoelectron enhancement factor implemented in the TIEGCM is based on a parameterization scheme developed by Richards and Torr [1988]. For O^+ and N_2^+, it selects 225 Å to represent the solar EUV attenuation effect on the enhancement factor. For O_2^+, the parameterization adds the C III line (977.02 Å) to represent additional O_2 photon ionization at the longer wavelength where there are some very intense EUV fluxes and little absorption from O and N_2. It estimates the photoelectron ionization rate with little calculation. However, the parameterization is unreliable when optical depth for the selected wavelength exceeds 9 [Richards and Torr, 1988]. This limitation imposes a significant problem: the altitude when the optical depth of 225 Å reaches 9 is approximately 110 km for an overhead sun and around 140 km for a large solar zenith angle. However, photoelectron impact is important in E region where photoionization is mainly caused by shorter EUV irradiance.

And this is the region where the Richards and Torr [1988] parameterization is no longer reliable, especially at large solar zenith angles.

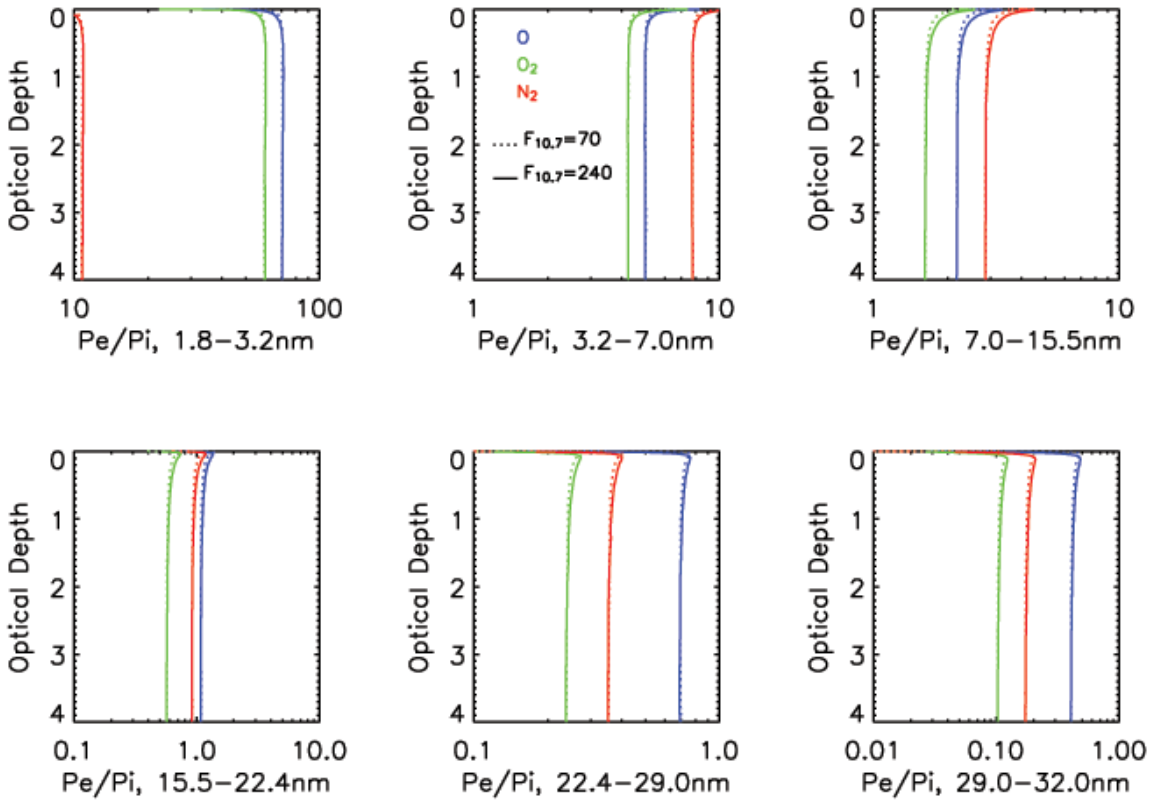

Figure 2.11: The ratio of photoelectron ionization rate to photoionization rate as a function of optical depth for 6 bins in the wavelength range where photoelectron ionization occurs. SZA= 2°. Solid: $F_{10.7} = \overline{F}_{10.7} = 240$; Dotted: $F_{10.7} = \overline{F}_{10.7} = 70$.

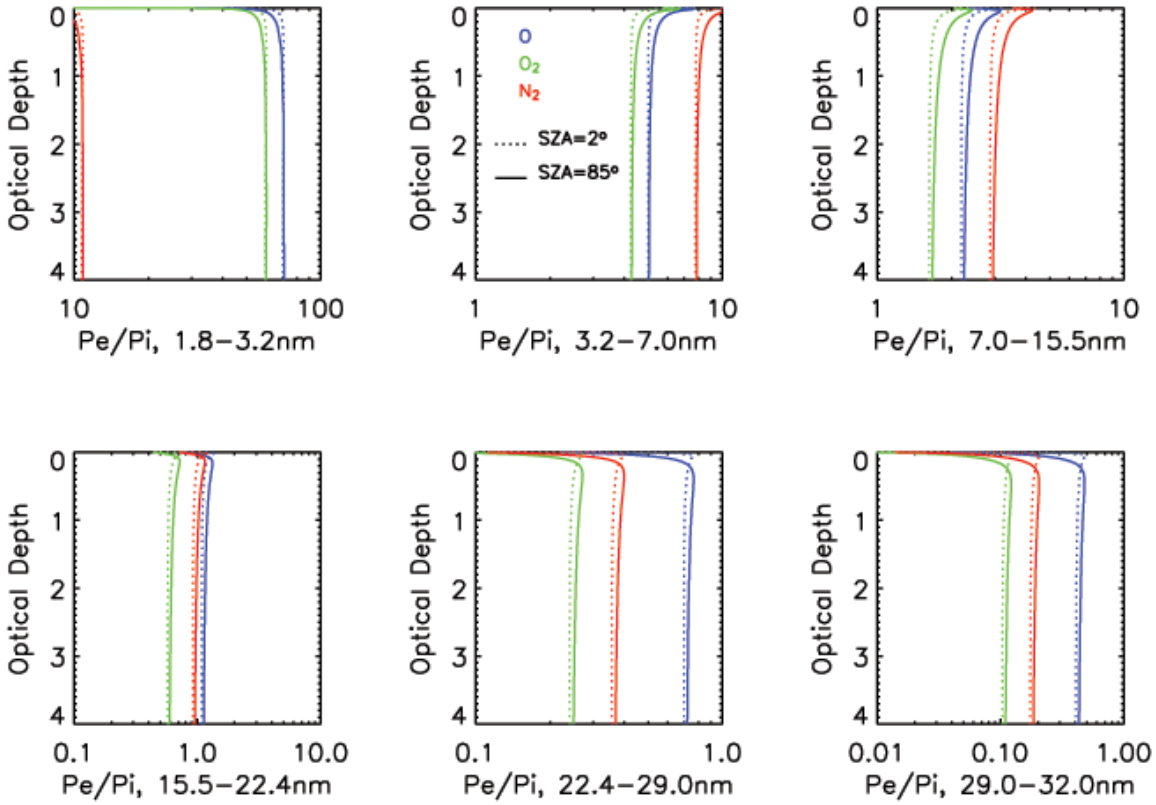

Figure 2.12: The ratio of photoelectron ionization rate to photoionization rate as a function of optical depth for 6 bins in the wavelength range where photoelectron ionization occurs. $F_{10.7} = \overline{F}_{10.7} = 70$. Solid: SZA=85°; Dotted: SZA=2°.

Photoelectron impact is determined by photoelectron flux, its energy, and photoelectron impact cross sections, all of which depend on wavelength. The photoelectron impact parameterization scheme described here parameterizes photoelectron impact for each wavelength bin and then integrates over all bins to obtain total photoelectron impact for each altitude; this is done for each species. To obtain the ratio of photoelectron impact to photoionization for each wavelength bin the GLOW model is run for each bin with solar flux included only for that particular bin and zero solar flux for the rest of bins. The GLOW calculates ionization, dissociation, and excitation by photons and ionization, dissociation, and excitation by photoelectrons for that particular bin. The GLOW model is run for extreme solar activity levels and extreme solar zenith angles. The wavelength range that has photoelectron impact is from 1–55 nm. Figure 2.11 shows photoelectron enhancement factors for the 3 major species as a

function of optical depth for six of the bins in this wavelength range on the low-resolution binning scheme, under solar minimum, and under solar maximum conditions. It indicates that photoelectron enhancement factors are nearly constant for each bin for each species around the unit optical depth where the peak photoionization rate occurs. They remain nearly constants as optical depths increase. It also shows that there is little variation of the enhancement factors with solar activity. At small optical depth, the enhancement factor varies with optical depth because photoelectron transport becomes important in the upper thermosphere above 250 km. Fortunately, at these altitudes, photoelectron impact is generally insignificant compared to photoionization, and the photoionization rate itself is also small compared to the peak photoionization rate at unit optical depth. Figure 2.12 compares the enhancement factors at extreme solar zenith angles at solar minimum conditions. The photoelectron enhancement factors show more variation with change of solar zenith angles than with variation with solar activity levels. However, the variation with solar zenith angles is small and acceptable considering the trade-off of the simplicity of parameterization. Based on the results of figure 2.11 and figure 2.12, a constant enhancement factor obtained at unit optical depth was selected for each species at each bin and forms a tabulated photoelectron enhancement factor for each species for a particular binning scheme. Photoelectron ionization rate can then be obtained by multiplying the tabulated enhancement factor and model calculated photoionization rate.

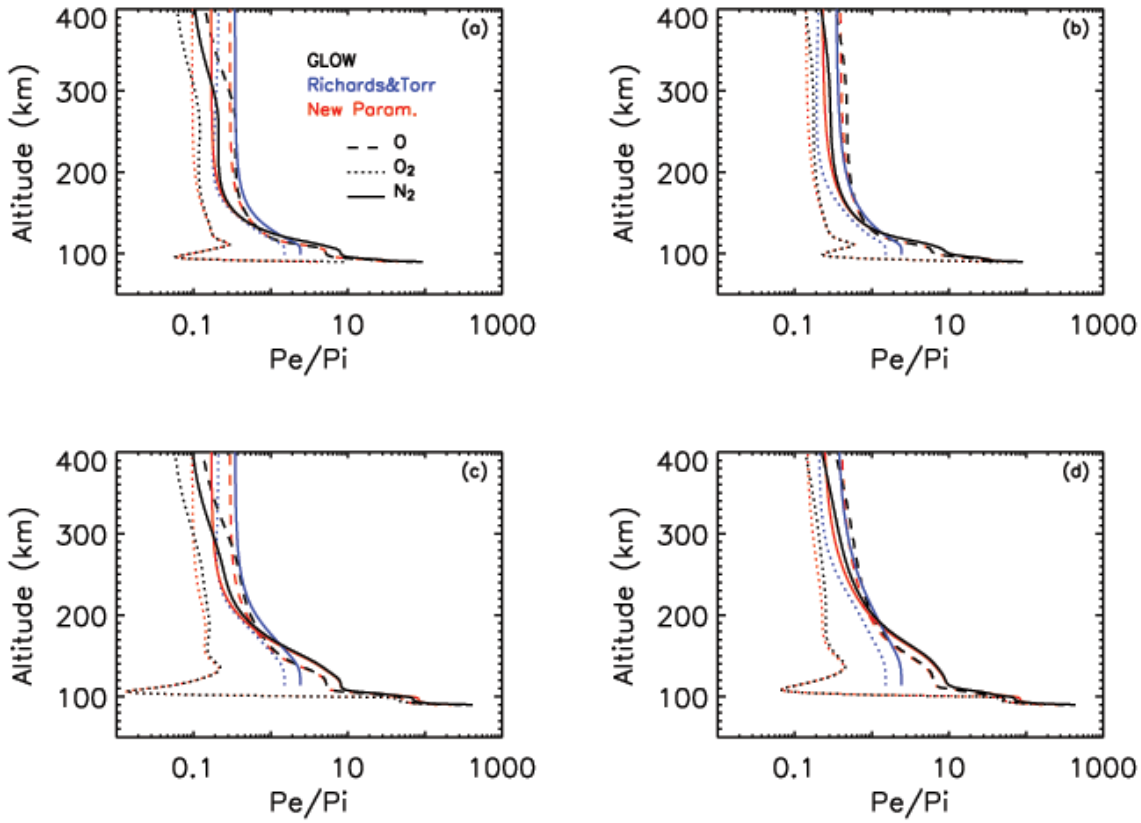

Figure 2.13: Photoelectron enhancement factor as a function of altitude for the three major species using different methods. Black: the GLOW model calculation; Blue: the Richards and Torr parameterization; Red: the new photoelectron impact parameterization. Panel (a): $F_{10.7} = \overline{F}_{10.7} = 70$, SZA=2°; Panel (b): $F_{10.7} = \overline{F}_{10.7} = 220$, SZA=2°; Panel(c): $F_{10.7} = \overline{F}_{10.7} = 70$, SZA=85°; Panel(d): $F_{10.7} = \overline{F}_{10.7} = 220$, SZA=85°.

In order to validate how well the tabulated enhancement factors can represent photoelectron ionization rates, comparisons were conducted for enhancement factors by the new method, the Richards and Torr [1988] method, and the detailed calculations by the GLOW model. Figure 2.13 shows the photoelectron enhancement factors as a function of altitude obtained by the different methods for each species, under combination of extreme solar activity and extreme solar zenith angle. Panel (a) is for $F_{10.7}$ = 70 and SZA = 2°; Panel (b) for $F_{10.7}$ = 220 and SZA = 2°; Panel (c) for $F_{10.7}$ = 70 and SZA = 85°; and Panel (d) for $F_{10.7}$ = 220 and SZA = 85°. The new parameterization method gives excellent agreement with the GLOW calculation under 150 km where the photoelectron ionization is as important as photoionization or even the dominant source

of ionization, for all the four combinations of solar activity and solar zenith angle. The new method starts to deviate from the GLOW calculation above 150 km, but the photoelectron ionization contribution is small and the photoionization itself becomes smaller as the altitude increases. The Richards and Torr [1988] method slightly overestimates photoelectron enhancement factors above 120 km, but it significantly underestimates the photoelectron impact below 120 km.

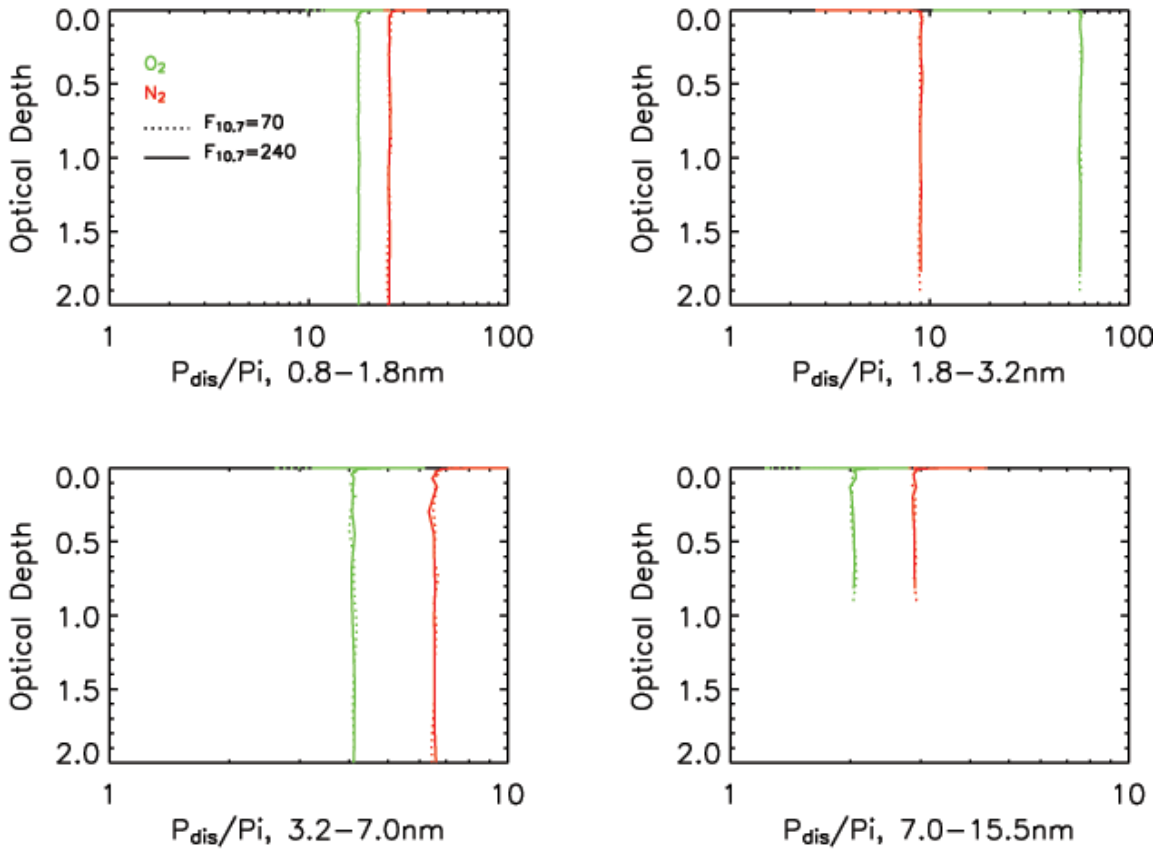

Figure 2.14: The ratio of photoelectron dissociation rate to photoionization rate as a function of optical depth for 4 bins in the wavelength range where photoelectron dissociation occurs. SZA= 2°. Solid: $F_{10.7} = \overline{F}_{10.7} = 240$; Dotted: $F_{10.7} = \overline{F}_{10.7} = 70$.

The photoelectron impact dissociation, dissociative ionization, and excitation can also be parameterized the same way as for photoelectron ionization. The GLOW model is run for each bin to obtain photoionization rate, photoelectron dissociation, dissociative ionization, and excitation for the particular bin. The ratios of photoelectron dissociation,

dissociative ionization, and excitation to photoionization rate are then calculated and tabulated for each bin and each species. Once the photoionization rate is calculated by a model, the photoelectron dissociation, dissociative ionization, and excitation rates can then be obtained by multiplying the tabulated ratios with the photoionization rate. Figure 2.14 shows the ratios of photoelectron dissociation rate to photoionization rate as a function of optical depth for O_2 and N_2 under solar minimum and solar maximum conditions with solar zenith angle of 20^o. Similar to the ratio of photoelectron ionization to photoionization, i.e., the photoelectron enhancement factor, the ratios of photoelectron dissociation to photoionization rate are also nearly constant within each bin except at very small optical depths. And the ratios vary little with solar activity. The ratios at unit optical depth are selected to be the ratio for each bin and each species the same way as the ratios for photoelectron ionization. A complete list of the tabulated ratios for photoelectron ionization including state-specific ionization, dissociation, dissociative ionization, and excitation, together with absorption cross sections, are given in table 2.4 to table 2.6 for the three major species.

Table 2.4: Cross Sections and Branching Ratios for O.

λ_{min}, nm	λ_{max}, nm	σ_{abs}, $10^{-18}cm^2$	$\beta\ ^4S$	$\beta\ ^2D$	$\beta\ ^2P$	p_e/p_i total	p_e/p_i ^4S	p_e/p_i ^2D	p_e/p_i ^2P
0.05	0.4	0.0023	0.390	0.378	0.224	217.12	81.240	88.526	47.358
0.4	0.8	0.0170	0.390	0.378	0.224	50.593	18.896	20.691	11.007
0.8	1.8	0.1125	0.390	0.378	0.224	23.562	9.425	9.365	4.772
1.8	3.2	0.1050	0.390	0.378	0.224	71.378	28.622	28.199	14.556
3.2	7.0	0.3247	0.393	0.374	0.226	4.995	2.019	1.962	1.014
7.0	15.5	1.3190	0.389	0.377	0.227	2.192	0.902	0.853	0.436
15.5	22.4	3.7832	0.367	0.392	0.233	1.092	0.470	0.418	0.203
22.4	29.0	6.0239	0.350	0.402	0.241	0.694	0.325	0.253	0.116
29.0	32.0	7.7205	0.346	0.403	0.246	0.418	0.209	0.148	0.061
32.0	54.0	10.7175	0.317	0.424	0.260	0.127	0.084	0.034	0.009
54.0	65.0	13.1253	0.298	0.451	0.252	0.000	0.000	0.000	0.000
65.0	79.8	8.5159	0.655	0.337	0.009	0.000	0.000	0.000	0.000
65.0	79.8	4.7889	0.930	0.070	0.000	0.000	0.000	0.000	0.000
79.8	91.3	3.0031	1.000	0.000	0.000	0.000	0.000	0.000	0.000
79.8	91.3	4.1048	1.000	0.000	0.000	0.000	0.000	0.000	0.000
79.8	91.3	3.7947	1.000	0.000	0.000	0.000	0.000	0.000	0.000
91.3	97.5	0.0000	0.000	0.000	0.000	0.000	0.000	0.000	0.000
91.3	97.5	0.0000	0.000	0.000	0.000	0.000	0.000	0.000	0.000
91.3	97.5	0.0000	0.000	0.000	0.000	0.000	0.000	0.000	0.000
97.5	98.7	0.0000	0.000	0.000	0.000	0.000	0.000	0.000	0.000
98.7	102.7	0.0000	0.000	0.000	0.000	0.000	0.000	0.000	0.000
102.7	105.0	0.0000	0.000	0.000	0.000	0.000	0.000	0.000	0.000

Table 2.5: Cross Sections and Branching Ratios for O_2.

λ_{min}, nm	λ_{max}, nm	σ_{abs}, $10^{-18}cm^2$	β O_2^+	β D. I.	β Dissoc.	p_e/p_i total	p_e/p_i O_2^+	p_e/p_i D. I.	p_e/p_i Dissoc.
0.05	0.4	0.0045	0.000	1.000	0.000	210.83	134.69	76.136	87.864
0.4	0.8	0.0340	0.000	1.000	0.000	50.156	32.212	17.944	20.318
0.8	1.8	0.2251	0.000	1.000	0.000	20.290	13.309	6.981	17.821
1.8	3.2	0.2101	0.000	1.000	0.000	59.953	39.615	20.338	56.969
3.2	7.0	0.6460	0.108	0.892	0.000	4.271	2.834	1.437	4.113
7.0	15.5	2.6319	0.347	0.653	0.000	1.613	1.092	0.521	2.041
15.5	22.4	7.6283	0.553	0.447	0.000	0.579	0.416	0.163	1.271
22.4	29.0	13.2125	0.624	0.376	0.000	0.242	0.189	0.052	0.996
29.0	32.0	16.8233	0.649	0.351	0.000	0.105	0.090	0.014	0.762
32.0	54.0	20.3066	0.759	0.240	0.000	0.024	0.023	0.001	0.653
54.0	65.0	27.0314	0.874	0.108	0.017	0.000	0.000	0.000	0.011
65.0	79.8	23.5669	0.672	0.001	0.327	0.000	0.000	0.000	0.000
65.0	79.8	24.9102	0.477	0.000	0.524	0.000	0.000	0.000	0.000
79.8	91.3	10.4980	0.549	0.000	0.451	0.000	0.000	0.000	0.000
79.8	91.3	10.9075	0.574	0.000	0.426	0.000	0.000	0.000	0.000
79.8	91.3	13.3122	0.534	0.000	0.466	0.000	0.000	0.000	0.000
91.3	97.5	13.3950	0.756	0.000	0.244	0.000	0.000	0.000	0.000
91.3	97.5	14.4042	0.786	0.000	0.214	0.000	0.000	0.000	0.000
91.3	97.5	32.5038	0.620	0.000	0.380	0.000	0.000	0.000	0.000
97.5	98.7	18.7145	0.830	0.000	0.170	0.000	0.000	0.000	0.000
98.7	102.7	1.6320	0.613	0.000	0.387	0.000	0.000	0.000	0.000
102.7	105.0	1.1500	0.000	0.000	1.000	0.000	0.000	0.000	0.000

Table 2.6: Cross Sections and Branching Ratios for N_2.

λ_{min}, nm	λ_{max}, nm	σ_{abs}, $10^{-18}cm^2$	β N_2^+	β D. I.	β Dissoc.	p_e/p_i total	p_e/p_i N_2^+	p_e/p_i D. I.	p_e/p_i Dissoc.
0.05	0.4	0.0025	0.040	0.960	0.000	342.66	263.99	78.674	245.00
0.4	0.8	0.0201	0.040	0.960	0.000	80.880	62.570	18.310	52.052
0.8	1.8	0.1409	0.040	0.960	0.000	32.162	25.213	6.948	25.255
1.8	3.2	1.1370	0.040	0.960	0.000	10.834	8.540	2.295	9.049
3.2	7.0	0.3459	0.717	0.282	0.000	7.789	6.142	1.647	6.532
7.0	15.5	1.5273	0.751	0.249	0.000	2.859	2.288	0.571	2.909
15.5	22.4	5.0859	0.747	0.253	0.000	0.933	0.786	0.146	1.371
22.4	29.0	9.9375	0.754	0.246	0.000	0.361	0.324	0.037	0.764
29.0	32.0	11.7383	0.908	0.093	0.000	0.178	0.169	0.008	0.515
32.0	54.0	19.6514	0.996	0.005	0.000	0.031	0.031	0.000	0.157
54.0	65.0	23.0931	1.000	0.000	0.000	0.000	0.000	0.000	0.000
65.0	79.8	23.0346	0.679	0.000	0.320	0.000	0.000	0.000	0.000
65.0	79.8	54.5252	0.429	0.000	0.571	0.000	0.000	0.000	0.000
79.8	91.3	2.1434	0.000	0.000	1.000	0.000	0.000	0.000	0.000
79.8	91.3	13.1062	0.000	0.000	1.000	0.000	0.000	0.000	0.000
79.8	91.3	71.6931	0.000	0.000	1.000	0.000	0.000	0.000	0.000
91.3	97.5	2.1775	0.000	0.000	1.000	0.000	0.000	0.000	0.000
91.3	97.5	14.4390	0.000	0.000	1.000	0.000	0.000	0.000	0.000
91.3	97.5	115.257	0.000	0.000	1.000	0.000	0.000	0.000	0.000
97.5	98.7	2.5465	0.000	0.000	1.000	0.000	0.000	0.000	0.000
98.7	102.7	0.0000	0.000	0.000	0.000	0.000	0.000	0.000	0.000
102.7	105.0	0.0000	0.000	0.000	0.000	0.000	0.000	0.000	0.000

Validation of the Photoelectron Impact Parameterization

The photoelectron impact parameterization presented in table 2.4 to table 2.6 was compared with the GLOW model calculation. As mentioned earlier, the GLOW model provides detailed calculations of ionization, dissociation, dissociative ionization, and excitation by both photons and photoelectrons. In the case of the parameterization run, the photoionization and photodissociation rates are calculated with the same solar irradiance, the solar zenith angle, and the same MSIS00 atmosphere as those for the GLOW model. The photoelectron impact rates are then calculated by multiplying the ratios in table 2.4 to table 2.6 with the calculated photoionization rates. Figure 2.15 compares the rates obtained by the two approaches for solar minimum and solar maximum conditions with an overhead sun. Panels (a) and (b) give the comparisons for the total ionization and dissociation rates, i.e., ionization and dissociation by both photons and photoelectrons, under solar minimum condition; Panel (c) and panel (d) show the total ionization rates and dissociation rates under solar maximum conditions. The photoelectron impact parameterization is in excellent agreement with the GLOW model calculation through most of the altitudes. Some disagreements occur at higher altitudes due to the photoelectron transport effect. Since ionization rates and dissociation rates become increasingly small as altitude increases, the disagreement at high altitude is insignificant. Figure 2.16 shows the solar zenith angle effect on the comparison under solar minimum conditions. Panel (a) and Panel (b) give total ionization rates and total dissociation rates with a solar zenith angle of 2^{o}; and panel (c) and panel (d) show the equivalents with a solar zenith angle of 85^{o}. These results indicate that the photoelectron impact parameterization provides good agreement with the GLOW model calculation under different solar zenith angles with some disagreement at high altitude where the disagreement is insignificant due to small ionization and dissociation rates. The results in figure 2.15 and 2.16 suggest that the photoelectron impact parameterization represent the photoelectron impact well under different solar activity and solar zenith angle conditions.

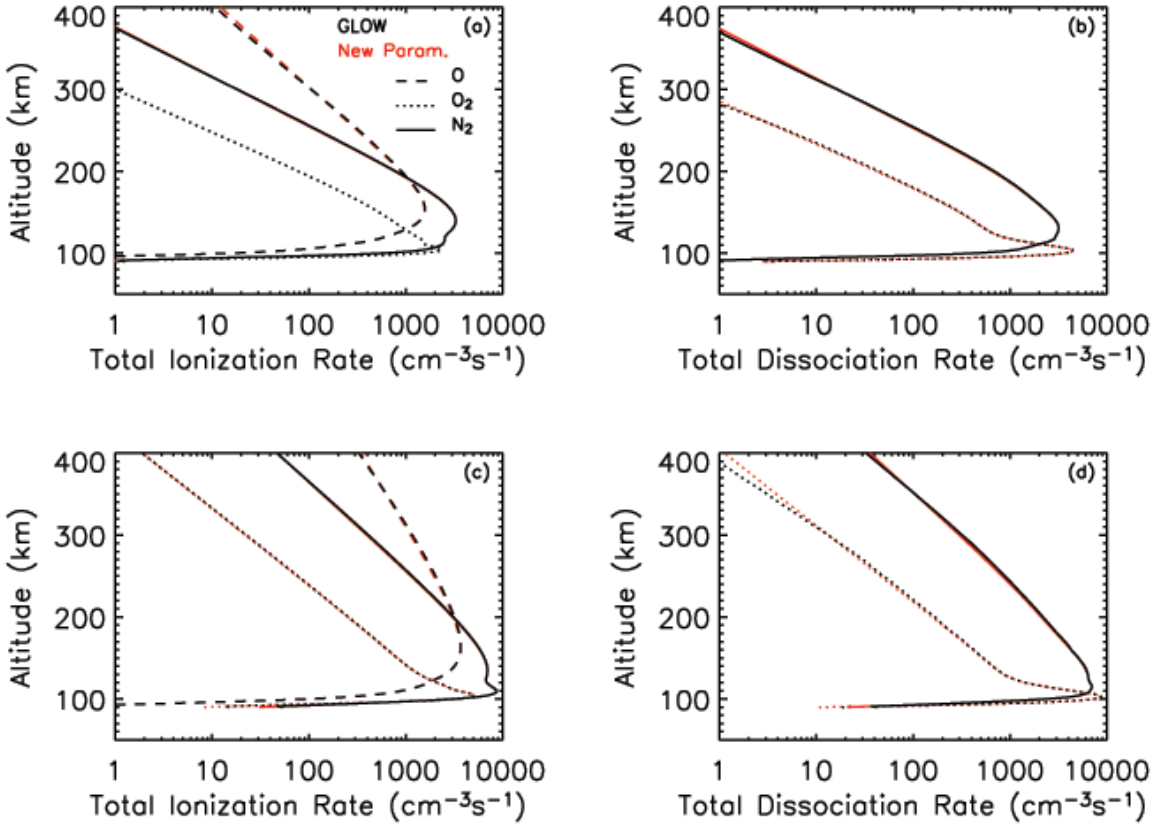

Figure 2.15: Total ionization rate and total dissociation rate (by both photos and photoelectrons) calculated by the GLOW model and using the new photoelectron impact parameterization on the low-resolution binning scheme. Black: The GLOW model calculation; Red: the new photoelectron impact parameterization. SZA=2°. Panel (a) and (b): $F_{10.7} = \overline{F}_{10.7} = 70$; Panel (c) and (d): $F_{10.7} = \overline{F}_{10.7} = 220$.

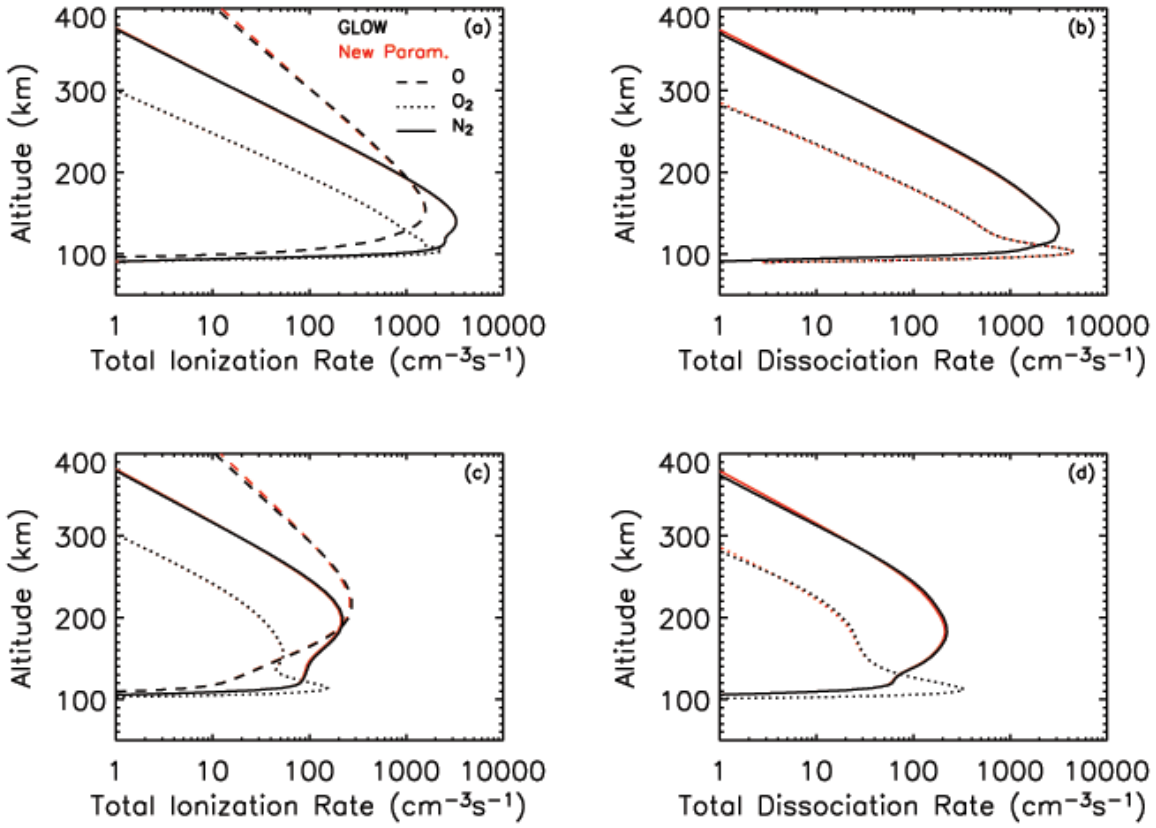

Figure 2.16: Total ionization rate and total dissociation rate (by both photos and photoelectrons) calculated by the GLOW model and using the new photoelectron impact parameterization on the low-resolution binning scheme. Black: The GLOW model calculation; Red: the new photoelectron impact parameterization. $F_{10.7} = \overline{F}_{10.7} = 70$. Panel (a) and (b): SZA=2^o; Panel (c) and (d): SZA=85^o.

Implementation of the New Solar EUV Energy Deposition Scheme

In previous sections, the low-resolution binning scheme was compared to the Torr et al. [1979] 5-nm and lines binning scheme, the 1-nm binning scheme, and the high resolution binning scheme in photoionization and photodissociation rate calculations, and the photoelectron impact parameterization was verified with the GLOW model calculation. In this section, both the low-resolution binning scheme and the photoelectron impact parameterization will be implemented in the TIEGCM, and the EUV energy deposition will be compared to the combination of the Torr et al. [1979] binning scheme

and the Richards and Torr [1988] photoelectron impact parameterization that has been utilized in the TIEGCM. Some important thermosphere and ionosphere parameters will be examined in the comparison.

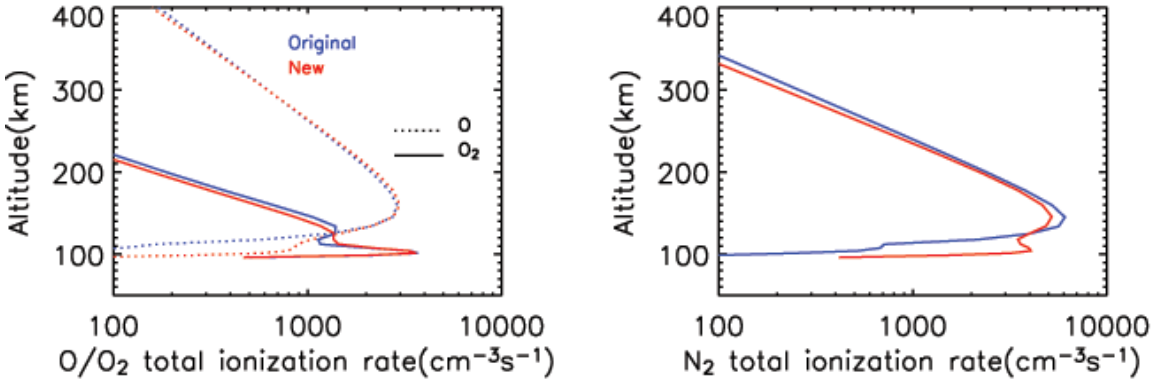

Figure 2.17: Total ionization rates from the TIEGCM using different solar EUV energy deposition schemes. Blue: the original scheme with Torr et al. (5 nm and lines) binning scheme and Richards and Torr photoelectron impact parameterization; Red: the new scheme with the low-resolution binning scheme and the new photoelectron impact parameterization. The date is March 30th, 2002, UT=0, latitude=27.5^{o}N, longitude=165^{o}E, SZA=28^{o}.

The solar input is the proxy model presented in Section 2.2.2. The TIEGCM was run with the new solar EUV energy deposition scheme and the original scheme for March 2002. Note that the TIEGCM adds ad-hoc X-ray ionization when the original EUV package is used, to improve the agreement of modeled E-region electron density with observations. The extra ad-hoc X-ray ionization was removed when the new EUV package was used because the new EUV package is expected to improve E-region ionization due to improved photoelectron ionization. Figure 2.17 shows the total ionization rate and dissociation for each major species. As shown in figure 2.13, the Richards and Torr scheme significantly underestimates the major species' photoelectron ionization in the E region and overestimates it above the E region. Both the atomic oxygen ionization rate in panel (a) and the molecular nitrogen ionization rate in panel (c) significantly increase when the new scheme is used. This indicates that photoelectron ionization dominates E-region ionization for atomic oxygen and molecular nitrogen. Molecular oxygen ionization in panel (b) does not have a significant increase except in a

narrow range of altitude. The total ionization rates calculated using the new method are much larger in the E region, especially for O^+ and N_2^+. This is an improvement in the E region for the TIEGCM because it has been recognized that E-region electron density from the TIEGCM is lower than observations.

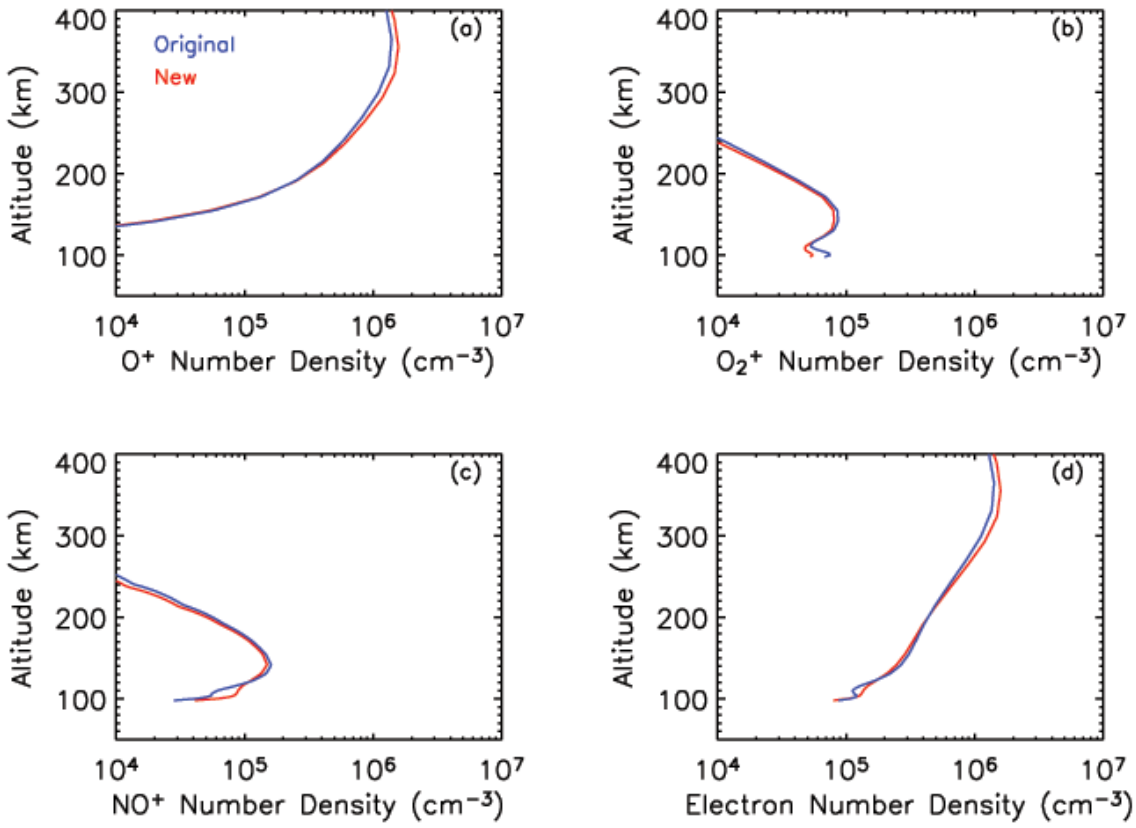

Figure 2.18: Ion and electron number densities from the TIEGCM using different solar EUV energy deposition schemes. Blue: the original scheme with Torr et al. (5 nm and lines) binning scheme and Richards and Torr photoelectron impact parameterization; Red: the new scheme with the low-resolution binning scheme and the new photoelectron impact parameterization. The date is 30 March 2002, UT=0, latitude=27.5^{o}N, longitude=165^{o}E, SZA=28^o.

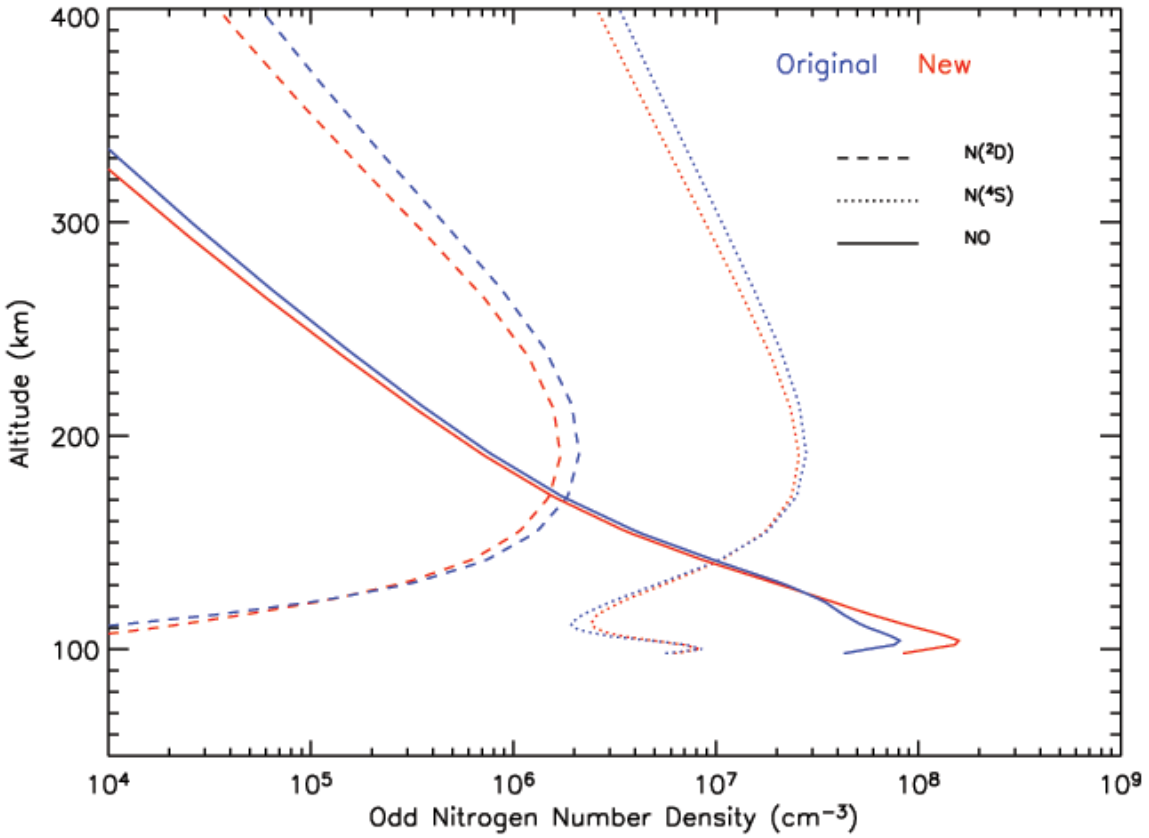

Figure 2.19: Odd nitrogen and nitric oxide number densities from the TIEGCM using different solar EUV energy deposition schemes. Blue: the original scheme with Torr et al. (5 nm and lines) binning scheme and Richards and Torr photoelectron impact parameterization; Red: the new scheme with the low-resolution binning scheme and the new photoelectron impact parameterization. The date is March 30th, 2002, UT=0, latitude=27.5°N, longitude=165°E, SZA=28°.

The important ions in the E region are O_2^+ and NO^+ due to converting of N_2^+ to O_2^+ and NO^+ through atom-ion interchange of N_2^+ with molecular and atomic oxygen, and O^+ becomes the dominant ion in the F-layer, especially the F2-layer. The ion number density and electron number density are given in figure 2.18. Panel (a) shows that there is more O^+ in the upper thermosphere where O^+ dominates when the new EUV package is used. There is less O_2^+ and more NO^+ in the lower thermosphere with the new package, probably due to the abundance of $N(^4S)$ and NO (figure 2.19). $N(^4S)$ and NO react with O_2^+ and transfer O_2^+ to NO^+. According to charge neutrality in the E-layer and F-layer,

electron number density is approximately the sum of NO^+ and O_2^+ number density in the E-layer and equals the O^+ number density in the F-layer. Panel (d) compares electron number density. The new EUV package produces more electrons in the E region than the original EUV package even without the extra ad-hoc X-ray ionization. The electron number density is also higher in the F2-layer with the new EUV package except for the F1-layer where the electron number density is slightly lower with the new EUV package compared to the original package.

Odd nitrogen is very important in thermospheric and ionospheric energetics due to NO infrared cooling at 5.3 μm. NO is mainly produced by reactions of $N(^4S)$ and $N(^2D)$ with O_2. The reaction of $N(^4S)$ and O_2 is temperature-dependent with larger reaction rates at higher temperature, and thus NO is more abundant in solar maximum years. The NO number density at solar maximum is around three times that at solar minimum. NO cooling varies significantly with solar activity level. NO cooling is much stronger under solar maximum conditions than under solar minimum conditions due to much higher NO concentration during solar maximum years. NO production and loss and NO cooling will be addressed in detail in Section 2.3.2 and Section 2.3.3. Figure 2.19 compares odd nitrogen number density and nitric oxide number density with the new EUV package and the original EUV package. The result is for 30 March 2002 at UT 0 at latitude 27.5°N and longitude of 165°E with a solar zenith angle of 28°. The $F_{10.7}$ and 81-day average $F_{10.7}$ are 188 and 186, respectively. The NO number density maximizes around 110 km and NO cooling dominates cooling in the lower thermosphere below around 150 km. $N(^4S)$ and $N(^2D)$ are sources of NO, and $N(^4S)$ and $N(^2D)$ are mainly generated in N_2 dissociation by photons and photoelectrons. Since the new photoelectron impact parameterization represents photoelectron dissociation of N_2 more accurately (figure 2.15 and figure 2.16) and produces more N_2 dissociation, the new scheme generates more $N(^4S)$ and $N(^2D)$, and thus more NO in the lower thermosphere. The increased NO number density improves the agreement between the model and recent observations [Solomon et al., 1999; Barth et al., 2003; Marsh et al., 2004].

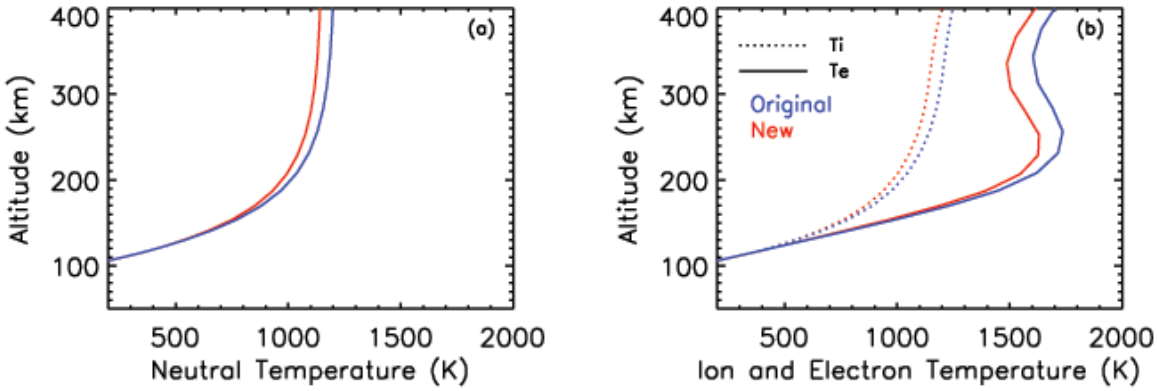

Figure 2.20: Global mean neutral, ion, and electron temperature from the TIEGCM using different solar EUV energy deposition schemes. Blue: the original scheme with Torr et al. (5 nm and lines) binning scheme and Richards and Torr photoelectron impact parameterization; Red: the new scheme with the low-resolution binning scheme and the new photoelectron impact parameterization. The date is 30 March 2002, UT=0.

Change of thermosphere energy balance is investigated by comparing the global mean neutral temperature, ion temperature, and electron temperature calculated using the two solar EUV energy deposition schemes. Thermospheric neutral temperature is determined by absorption of solar irradiance, energy input from geomagnetic activity, collisions with ions and ambient electrons, molecular and eddy heat conduction, and infrared cooling by O, NO, and CO_2. The neutral temperature obtained with the new EUV scheme is lower than that with the original EUV scheme (figure 2.20). Since the new EUV package generates more NO and thus increases NO cooling, the model has lower global mean neutral temperature. The lower neutral temperature with the new scheme propagates the effect to ion temperature and electron temperature through collisions of ions with neutral and collisions of electrons with neutral (figure 2.20).

Regarding efficiency, the original solar energy deposition calculation consumes 11% of the CPU time used by the TIEGCM model on a four-processor, Linux computer while the new low-resolution calculation reduces it to 5%.

2.3 Important Parameters in Model Tuning

Simulation of the aeronomic processes involves using such parameters as chemical reaction rates, collision rates, diffusion coefficients, among others. Many of these parameters are subject to some degree of uncertainty. It is important to identify the sensitivities of the model to these parameters, update the parameters with the best current knowledge, and take into consideration the sensitivities in evaluating model runs and in model tuning.

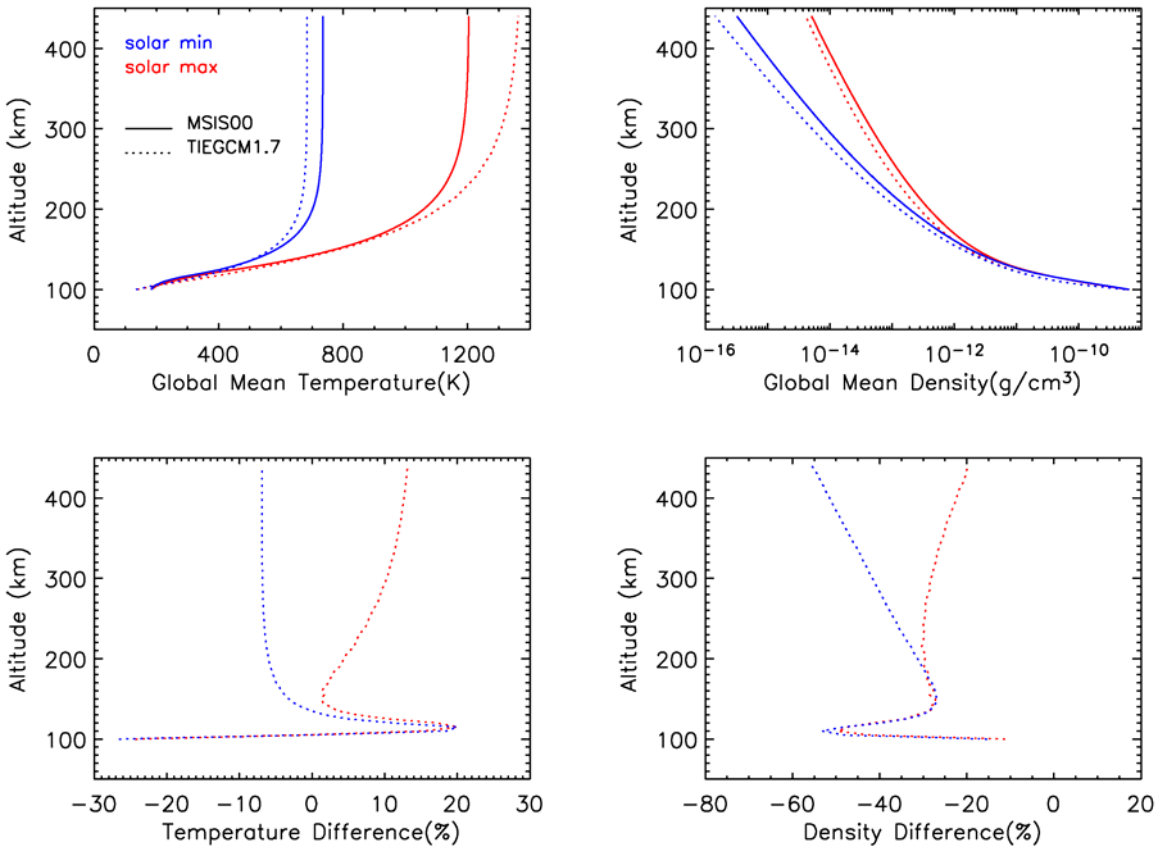

Figure 2.21: A comparison of the global mean temperature and density between the MSIS00 and the TIEGCM version 1.7 under solar minimum and solar maximum conditions. Upper panel: the global mean temperature and density profiles; Lower panel: the percentage difference.

Figure 2.21 compares the global mean temperature and density simulated by the TIEGCM version 1.7 (TIEGCM1.7, the version before this thesis work was started) and

the MSIS00. The TIEGCM1.7 simulated temperature has more solar-cycle variability: the TIEGCM1.7 temperature is lower than that of the MSIS00 (7%) under solar minimum conditions but higher than the MSIS00 temperature (13%) under solar maximum conditions. The TIEGCM1.7 density is lower than the MSIS00 density under both solar minimum and solar maximum conditions, with greater difference under solar minimum condition (55%) than under solar maximum conditions (20%). This section will address sensitivity tests of the TIEGCM to the following three types of parameters: eddy diffusion, infrared cooling rates, and chemical reaction rates. It will also address the TIEGCM tuning process as part of the thesis work so that the TIEGCM obtains better agreement with the MSIS00.

2.3.1 Eddy Diffusion

Eddy diffusion influences the thermosphere/ionosphere system through turbulent mixing of the composition and turbulent transport of energy. Changing composition subsequently alters absorption of solar heating. The eddy diffusion coefficient is specified as a constant at the lower boundary of the TIEGCM1.7 and then it decreases exponentially as the model pressure surfaces go upward. The eddy diffusivity specified at the lower boundary of the TIEGCM1.7 is $K_E = 5 \times 10^{-6} s^{-1}$. Assuming a scale height of about 5.5 km at 97 km, the eddy diffusion coefficient is 150 m^2/s.

In the global mean thermosphere, the thermospheric composition is largely affected by the eddy diffusion at the turbopause since composition changes by large-scale circulation are not significant in the global mean sense. Figure 2.22 shows variation in the global mean temperature and neutral density when the eddy diffusion coefficient is reduced from $K_E = 5 \times 10^{-6} s^{-1}$ to $K_E = 2.5 \times 10^{-6} s^{-1}$. Reduction in eddy diffusivity causes an increase in both temperature and neutral density. Reduced eddy diffusion causes increased atomic oxygen above the turbopause, thus increasing solar heating and temperature, then thermally increasing both atomic oxygen and molecular nitrogen. This mechanism will be discussed in detail in Chapter 4. The effect depends slightly on solar

activity. In the upper thermosphere, it introduces around a 1% increase in temperature and a 15% increase in density.

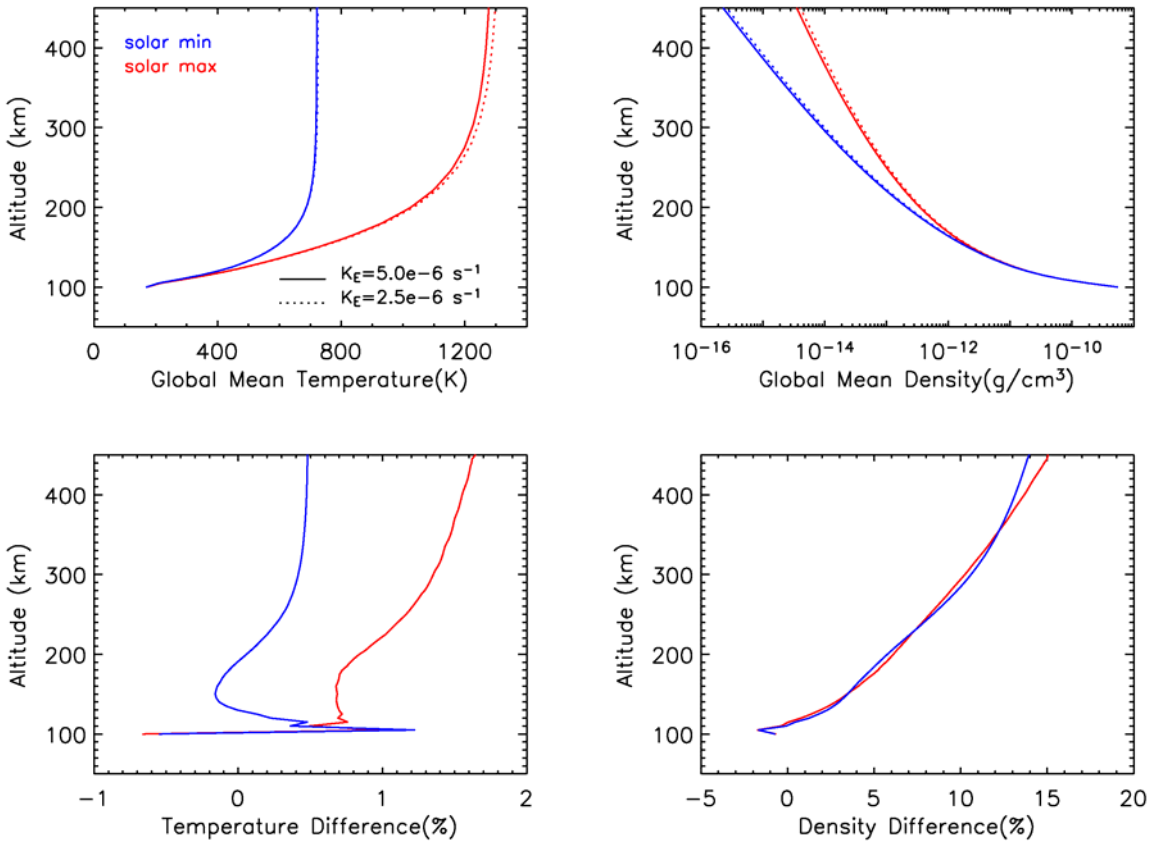

Figure 2.22: Variation in global mean temperature and density caused by decreasing the eddy diffusion coefficient under solar minimum and solar maximum conditions. Upper panels: variation in temperature and density profile; Lower panels: the percentage difference.

Thermospheric neutral density responds almost linearly to further variation in eddy diffusivity. Figure 2.23 shows model sensitivity to continuous increases in eddy diffusivity under moderate solar activity. K_E is increased from $5\times10^{-6}s^{-1}$ to $7.5\times10^{-6}s^{-1}$, then further to $1\times10^{-5}s^{-1}$. Increases in eddy diffusivity decrease temperature and density in the thermosphere; it causes around a 1% decrease in temperature and a 10% decrease in density in the upper thermosphere when K_E is

increased from $5\times10^{-6}s^{-1}$ to $7.5\times10^{-6}s^{-1}$. The effect causes a 2% decrease in temperature and a 20% decrease in density, when K_E is further increased to $1\times10^{-5}s^{-1}$.

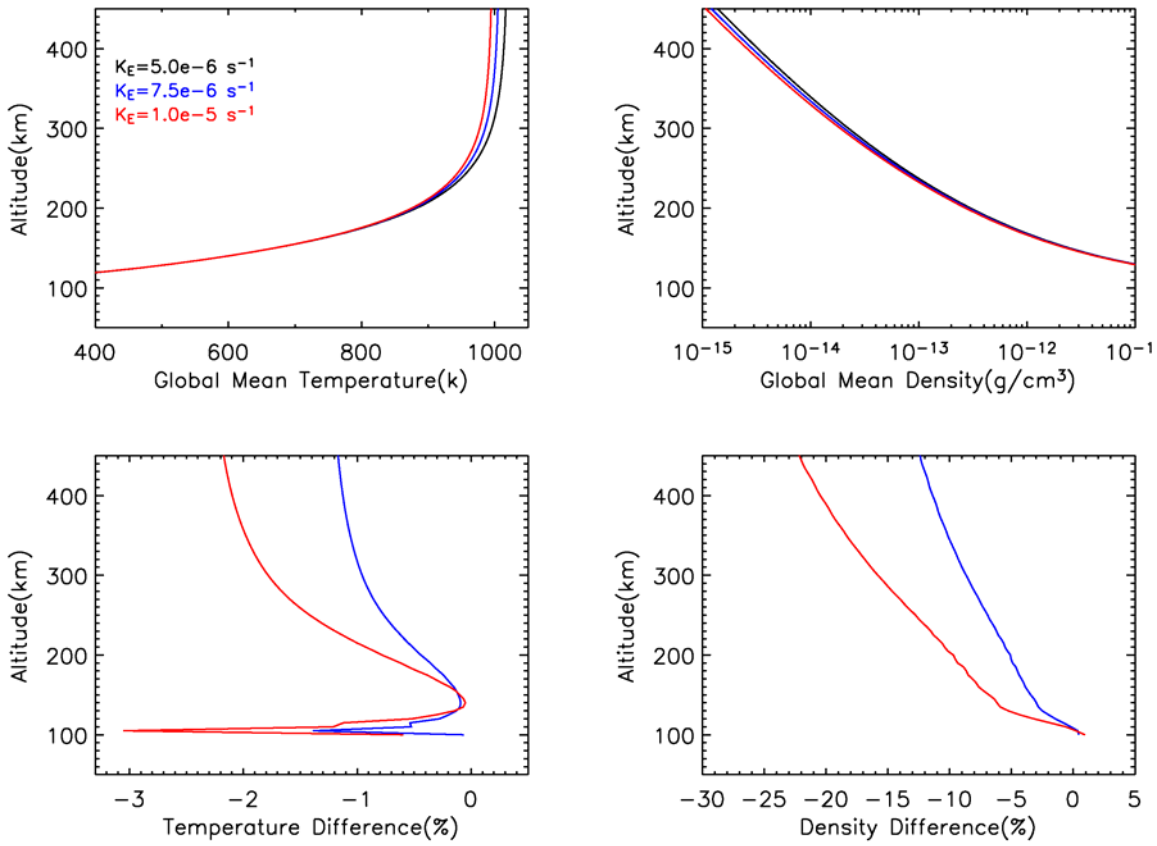

Figure 2.23: Variation in global mean temperature and density caused by continuous increase in eddy diffusion. Upper panels: variation in temperature and density profile; Lower panels: the percentage difference.

2.3.2 Infrared Cooling Rates

The cooling processes in the thermosphere are downward molecular thermal conduction, infrared radiative cooling, and downward eddy thermal conduction. The downward molecular thermal conduction dominates cooling above 150 km while infrared cooling dominates the lower thermosphere. Infrared cooling includes CO_2 radiative

cooling at 15 μm which peeks around 120 km, NO radiative cooling at 5.3 μm which peaks around 150 km, and O(^{3}P) fine structure cooling at 63 μm which maximizes above 200 km [Roble, 1995]. In the mesosphere and lower thermosphere region, NO and CO_2 are excited through collisions with neutral constituents (mainly atomic oxygen) and subsequently collisionally and radiatively quenched. The radiative quenching process becomes dominant as the atmosphere becomes thinner with increasing altitude. NO and CO_2 radiate kinetic energy in the infrared and cool the atmosphere in the process of radiative quenching. O(^{3}P) cools the atmosphere when it transits from a higher energy state to a lower energy state and radiates. There are uncertainties in the collisional excitation rates between NO and O, and CO_2 and O, and the model is sensitive to the specified collision rates.

The NO and O collision rate used in the TIEGCM1.7 is $6.5\times10^{-11} cm/s^2$. Hwang et al. [2003] measured the vibrational relaxation of NO (v=1) by O between 295 K and 825 K and the temperature dependency of the rate in the 300 K-1000 K region. They derived the vibrational excitation rate of NO by O to be $(4.2\pm0.7)\times10^{-11} cm^2 s^{-1}$, based on detailed balance, and assuming it exhibits little or no temperature dependency. The TIEGCM was run with the two different rates and figure 2.24 compares the global mean temperature and density difference. The smaller collision rate causes increase in temperature and density under both solar minimum and solar maximum conditions. The effect is stronger under solar maximum conditions, especially in temperature. The percentage increase in temperature is doubled under solar maximum conditions compared to the solar minimum conditions. The reason is that NO is more abundant under solar maximum conditions; stronger solar XUV/EUV and higher temperature due to strong solar activity favor the production of NO.

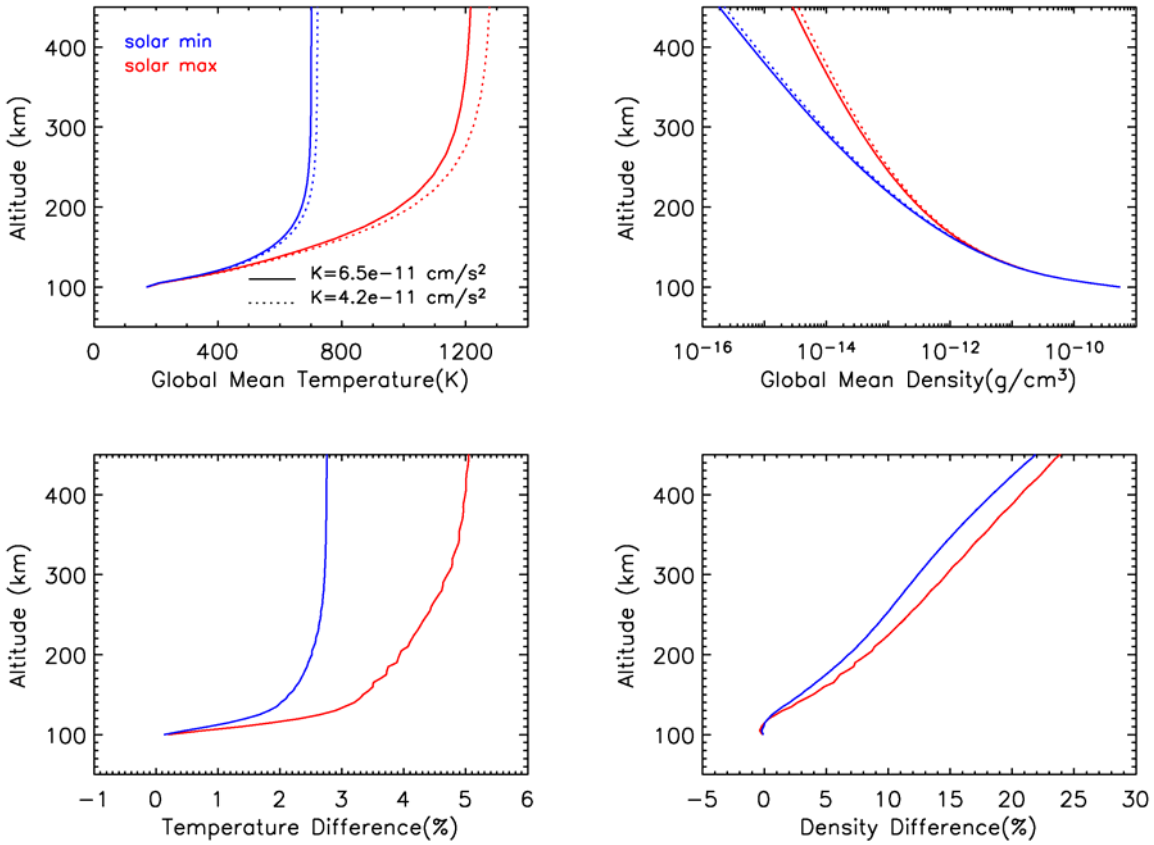

Figure 2.24: Difference in global mean temperature and density when the TIEGCM uses two different collision rates for NO and O collision, under solar minimum and solar maximum conditions. Upper panels: variation in temperature and density profile; Lower panels: the percentage difference.

The TIEGCM1.7 uses the following formula for the collision rate between CO_2 and O [Roble, 1995]:

$$T < 300K, k = 4.0 \times 10^{-12} cm^2 s^{-1}$$
$$T \geq 300K, k = 4.0 \times 10^{-12} \left(\frac{T}{300} \right) cm^2 s^{-1} \qquad \text{(Eq. 2.12)}$$

Khvorostovskaya et al. [2002] found, through the first laboratory measurement, that the collision rate of CO_2 and O is significantly smaller than those commonly used in solving the non local thermodynamic equilibrium CO_2 problem in the atmosphere of the Earth, Venus, and Mars. They suggested that the rate constant for quenching of the CO_2 (0110)

state during collisions of CO_2 molecules with O at temperatures realized near the Earth's mesopause should be as follows:

$$\begin{aligned} &T < 260K, k = 1.56\times10^{-12}\, cm^2 s^{-1} \\ &260K \le T \le 300K, k = (2.6 - 0.004T)\times10^{-12}\, cm^2 s^{-1} \\ &T > 300K, k = 1.4\times10^{-12}\, cm^2 s^{-1} \end{aligned} \qquad \text{(Eq. 2.13)}$$

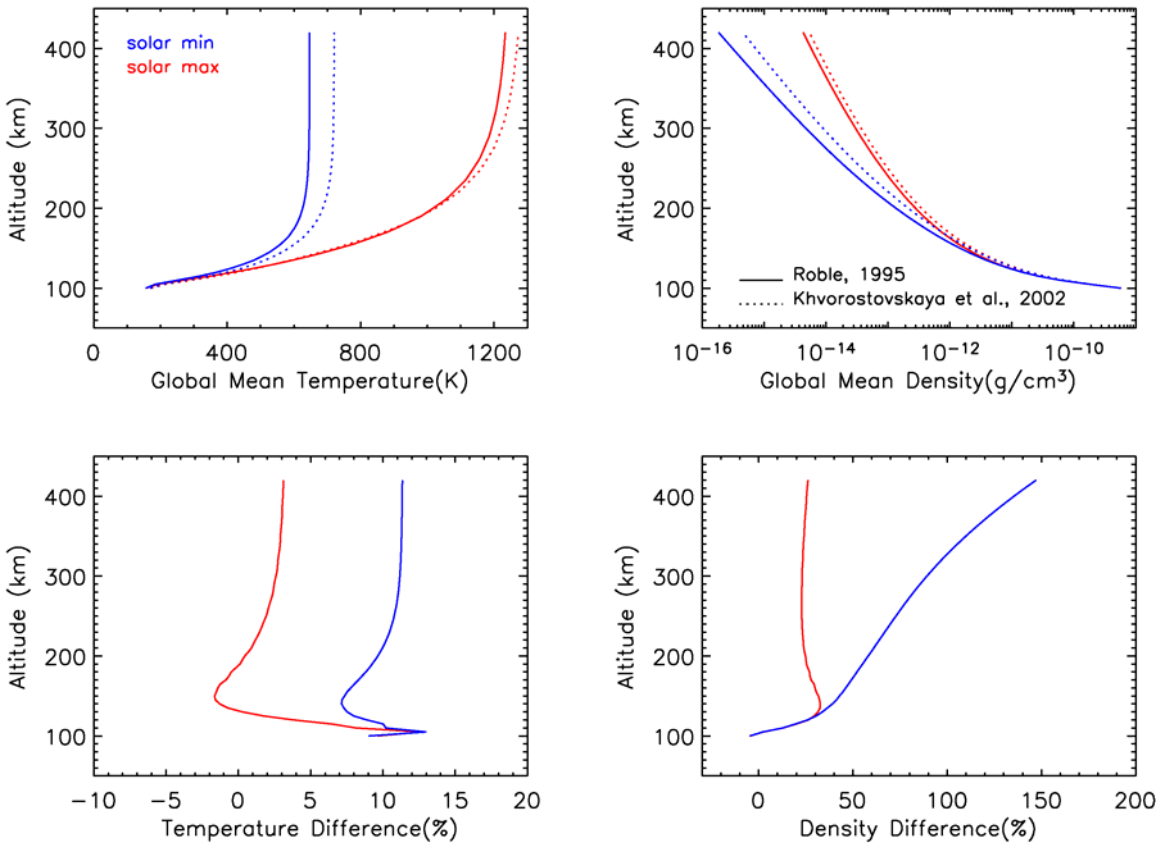

Figure 2.25: Difference in global mean temperature and density when the TIEGCM uses two different collision rates for CO_2 and O collision, under solar minimum and solar maximum conditions. Upper panels: variation in temperature and density profile; Lower panels: the percentage difference.

The TIEGCM simulated global mean temperature and density increases greatly when the model uses the rate by Khvorostovskaya et al. [2002] (figure 2.25), especially under solar minimum conditions. NO dominates the infrared cooling under solar maximum condition

due to its increased abundance under strong solar activity; CO_2 dominates the infrared cooling under solar minimum conditions. The latter smaller rate produces a temperature increase of 11% and a density increase of 150% under solar minimum conditions. Under solar maximum conditions, the temperature and density increases are 3% and 25%, respectively.

2.3.3 Chemical Reaction Rates

Important chemical reactions and their rates used in the TIEGCM1.7 aeronomic scheme were examined and it was found that the rate for the main loss of NO is not accurate at high temperatures.

$$N(^4S) + NO \rightarrow N_2 \qquad \text{(Eq. 2.14)}$$

Figure 2.26 shows some rates suggested for this reaction. The TIEGCM1.7 uses the rate recommended by Fox [1994]. It is a rate obtained for lower temperature:

$$k = 2.5\times10^{-10}\sqrt{\frac{T}{300}}e^{-\frac{600}{T}}\ cm^3s^{-1} \qquad \text{(Eq. 2.15)}$$

As the temperature increases, the formula of Fox [1994] gives a rate much higher than other recommended rates. The Jet Propulsion Laboratory (JPL) published the rate as a temperature independent value of $k = 3.4\times10^{-11}cm^{-3}s^{-1}$ [Demore et al., 1992]. The JPL rate was modified in this thesis study to add some temperature dependence:

$$k = 3.4\times10^{-11}\sqrt{\frac{T}{300}}cm^3s^{-1}.$$

This temperature dependence is based on the assumption that the JPL rate should be approximately correct at 300 K but may have positive temperature dependence at least as great as the increase in collision rate $\left(\sqrt{\frac{T}{300}}\right)_z$ due to temperature change.

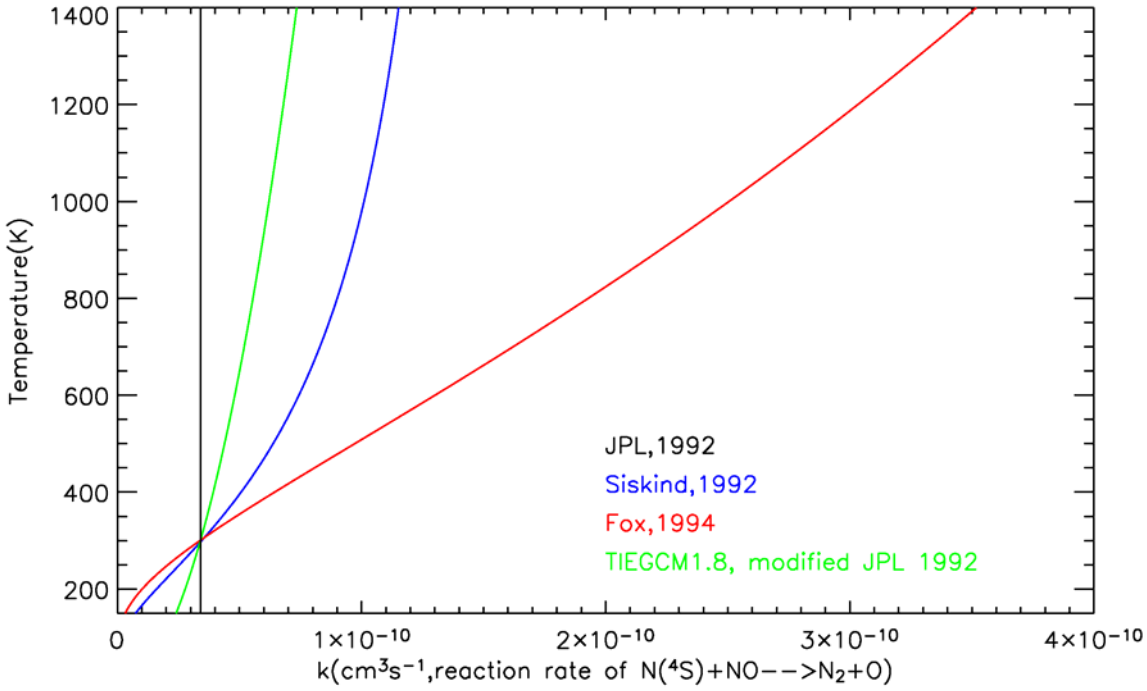

Figure 2.26: Some suggested rates for the NO loss reaction: $N(^4S) + NO \rightarrow N_2$.

Figure 2.27 shows the simulated difference between using the modified JPL rate and the rate of Fox [1994]. Utilization of the modified JPL rate causes a large change for the solar maximum condition: the temperature decreases by 12% and the density decreases by 40% in the upper thermosphere. Under solar minimum conditions, the percentage difference in temperature and density in the upper thermosphere are around 4% and 25%, respectively. The rate for the reaction is greatly overestimated under solar maximum conditions since the typical thermosphere temperature under solar maximum conditions is around 1200 K, the region where the Fox [1994] formula gives a large rate. This likely explains why the discrepancy between the TIEGCM1.7 and the MSIS00 shown in figure 2.21 is greater for solar maximum conditions than that for solar minimum conditions.

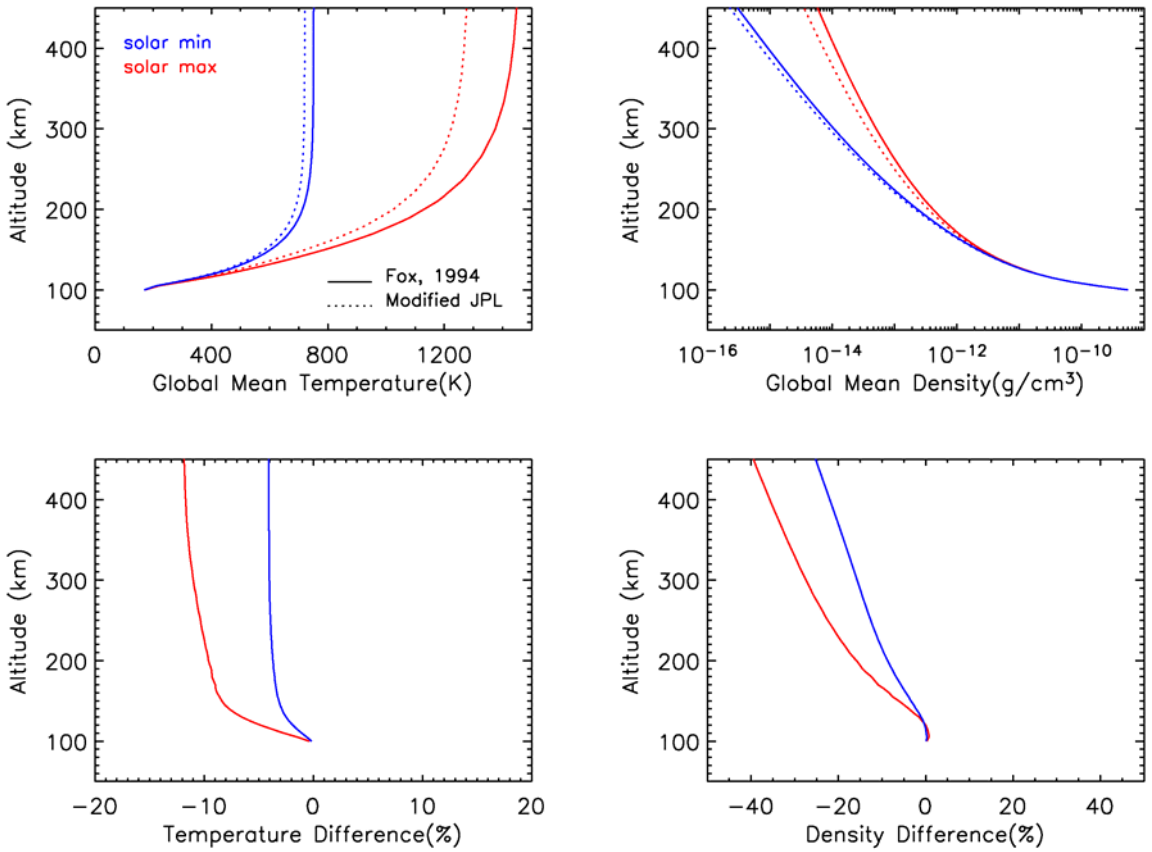

Figure 2.27: Difference in global mean temperature and density when the TIEGCM uses two different reaction rates for $N(^4S) + NO \rightarrow N_2$, under solar minimum and solar maximum conditions. Upper panels: variation in temperature and density profile; Lower panels: the percentage difference.

Table 2.7 lists the modifications made in this thesis study for model tuning from the TIEGCM version 1.7 to version 1.8. Other major updates include the new solar energy deposition scheme, improvements to the dynamo calculation, and some bug fixes.

Table 2.7: Parameters that are modified from the TIEGCM version 1.7 to the version 1.8.

	TIEGCM1.7	TIEGCM1.8
$K_E(s^{-1})$	5×10^{-6}	2.5×10^{-6}
$k_{NO\leftrightarrow O}(cm^2s^{-1})$	6.5×10^{-11}	4.2×10^{-11}
$k_{CO_2\leftrightarrow O}(cm^2s^{-1})$	$T<300K$: $k=4.0\times10^{-12}$ $T\geq300K$: $k=4.0\times10^{-12}\left(\frac{T}{300}\right)$	$T<260K$: $k=1.56\times10^{-12}$ $260K\leq T\leq300K$: $k=(2.6-0.004\times T)\times10^{-12}$ $T>300K$: $k=1.4\times10^{-12}$
$k_{(N(^4S)+NO\rightarrow N_2)}(cm^3s^{-1})$	$2.5\times10^{-10}\sqrt{\frac{T}{300}}e^{-\frac{600}{T}}$	$3.4\times10^{-11}\sqrt{\frac{T}{300}}$

The comparison of global mean thermospheric temperature and density profiles between the TIEGCM version 1.8 (TIEGCM1.8) and the MSIS00 is shown in figure 2.28. The TIEGCM1.8 is in reasonable agreement with MSIS00 in the global mean sense. This thesis study uses the TIEGCM1.8. The TIEGCM referred in this thesis hereafter means the TIEGCM1.8.

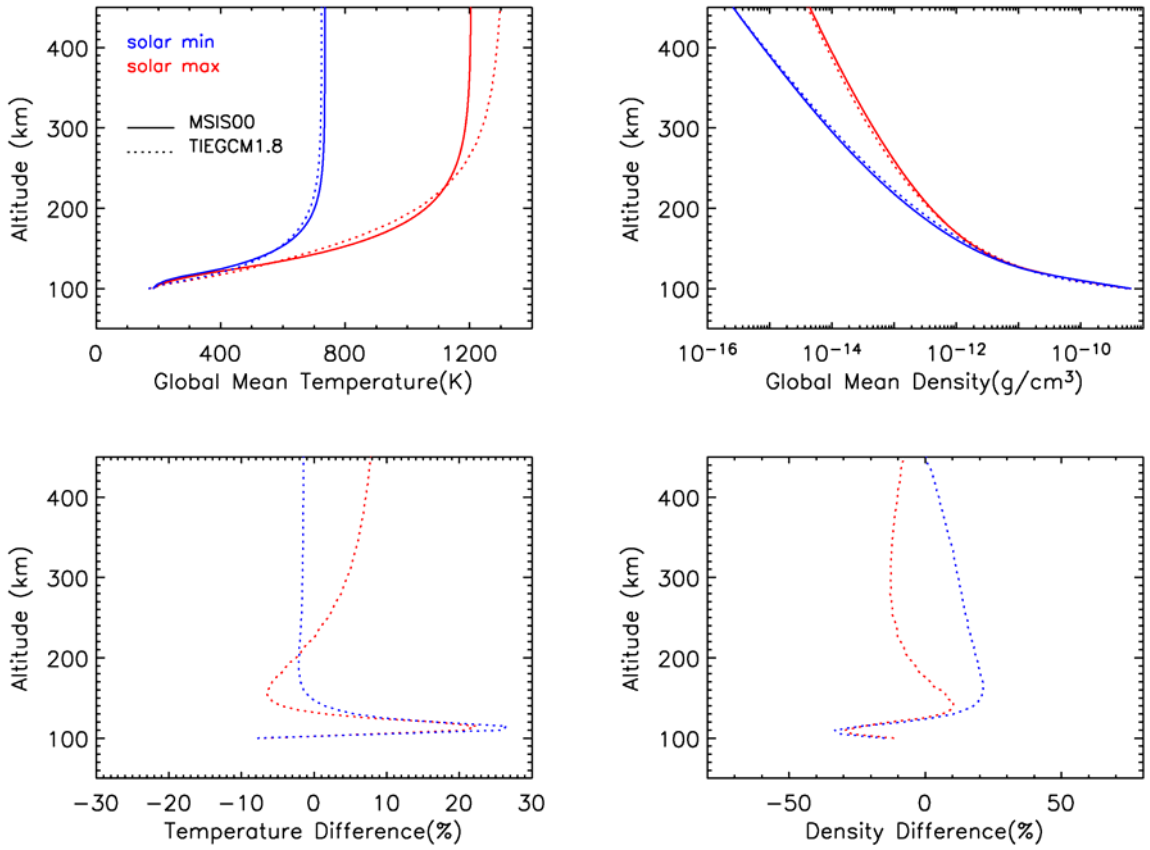

Figure 2.28: A comparison of the global mean temperature and density between the MSIS00 and the TIEGCM1.8 under solar minimum and solar maximum conditions. Upper panels: the global mean temperature and density profiles; Lower panels: the percentage difference.

2.4 The MSIS Empirical Model

The Mass Spectrometer and Incoherent Scatter (MSIS) model evolved from an empirical model of the thermosphere to an empirical model of the atmosphere from the ground to the exobase. The first version the MSIS [Hedin, et al., 1977a, 1977b] gave empirical prediction of thermospheric temperature, density, and composition from 120 km to the exobase. The MSIS-83 [Hedin, 1983] extended the lower boundary to 85 km; the MSIS-86 [Hedin, 1987] had the same altitude coverage as the MSIS-83. The MSIS-90 [Hedin, 1991] extended the lower boundary to the ground, and the latest version the

NRLMSISE-00 [Picone, et al., 2002] covers the same altitude range as the MSIS-90. The MSIS-86 model is the thermospheric portion (above 120 km) of the COSPAR International Reference Atmosphere (CIRA 1986). The output of these MSIS-class models is temperature, number density of O, O_2, N_2, H, He, N, Ar, and total mass density. Section 2.4.1 describes the thermospheric portion of the MSIS-class models; Section 2.4.2 briefly introduces the rest of the lower atmosphere formulation; and Section 2.4.3 discusses the evolution of the MSIS-class model with focus on data addition and new features of each advanced version.

2.4.1 Model Formulation in the Thermosphere

The earlier versions of the MSIS-class model (up to the MSIS-86) only cover the thermosphere. The extension to the ground by the MSIS-90 did not change the formulation of the thermosphere but introduced modifications in the transition region between the thermosphere and the mesosphere. Therefore, the thermospheric formulation described in this section is for these earlier versions, and the next section will discuss the modifications in the transition region.

The thermospheric temperature profile consists of two analytical formulae: 1) the diffusive equilibrium Bates [Bates, 1959] temperature profile as a function of geopotential height for the upper thermosphere and 2) an inverse polynomial temperature profile as a function of geopotential height in the lower thermosphere, merged at an altitude determined by fitting data, around 117 km. The temperature at 120 km is the boundary condition for the temperature profiles. The variables of the temperature profiles, to be determined through fitting of data, are the temperature and temperature gradient at 120 km, the exospheric temperature, the temperature and shape parameter at the mesopause, and the mesopause height. All the variables are expressed as follows:

$$X = \overline{X}(1 + G(L)) \qquad \text{(Eq. 2.16)}$$

where X is one of the variables, $\overline{X}$ is the average value of the variable, *G(L)* is a combination of spherical harmonics, Fourier harmonics, and polynomial functions that represent a variable and its variation determined by the solar forcing, geomagnetic forcing, and dynamic processes such as tides. The *G(L)* function includes terms such as: a time-independent term, the $F_{10.7}$ effect term, a geomagnetic activity term, an annual term, a semiannual term, a diurnal term, a semidiurnal term, a terdiurnal term, a longitude variation term, a UT variation term. Composition data, mainly observed by the mass spectrometers, and temperature data obtained by the ground-based incoherent scatter radars are then fitted to find the coefficients for the various terms in the *G(L)* function for each variable.

In the upper thermosphere, the number density profile of each species is the diffusive equilibrium density profile obtained by integrating the hydrostatic equation using the Bates temperature profile [Walker, 1965], based on a density specified at the boundary 120 km. The diffusive equilibrium density profile is modified away from diffusive equilibrium due to the effects of chemical and dynamic processes as the altitude decreases and transits towards a fully mixing density profile at the turbopause. The mixing density profile is calculated by integration of the hydrostatic equation using the inverse polynomial temperature profile and the mean molecular weight for the lower atmosphere. The turbopause height is 105 km for N_2, O_2, Ar, and O, 100 km for He, and 95 km for H. The number density for a species at 120 km is expresses as follows:

$$n_i = \overline{n_i} \exp\left[G_i(L)\right] \qquad \text{(Eq. 2.17)}$$

where $\overline{n_i}$ is the average density of a particular species at 120 km. Again, $G_i(L)$ is a combination of spherical harmonics, Fourier harmonics, and polynomial functions for the species that includes terms as those for temperature. The set of coefficients for each species is determined through fitting of the mass spectrometer and incoherent scatter radar data.

2.4.2 Model Formulation in the Middle and Lower Atmosphere

The MSIS-90 extends the MSIS-86 downward to include the middle and lower atmosphere to the ground. The lower atmosphere portion of the CIRA 1986 [Barnett and Corney, 1985], i.e. the zonal-average tabulations of the temperature, densities, and pressures, was the principal guidance for the extension. Instead of using the polynomial temperature profile of the lower thermosphere/upper mesosphere mentioned in Section 2.4.1, the model uses a cubic spline formulation for the temperature profile between certain specified altitude points in an altitude range of 122.8–0 km [Hedin, 1991]. The temperature at the specified altitudes is harmonically expanded similar to Eq. 2.16 except for some slight modifications to emphasize terms that are more important to the lower atmosphere. The temperature and temperature gradient from the diffusive equilibrium Bates temperature profile and the cubic spline temperature are matched at 122.8 km. Densities below 122.8 km are calculated by first integrating up from 120 km to 122.8 km using the diffusive equilibrium Walker density profile [Walker, 1965] and then integrating down using the cubic spline profile of the temperature, based on hydrostatic equilibrium and perfect gas law, and using the mean molecular weight of the lower atmosphere.

2.4.3 Evolution of the MSIS Model

The first version of the MSIS-class model, the MSIS, was developed by Hedin et al. [1977]. The dataset the model was built upon included temperature inferred from incoherent scatter radar at four ground stations (Arecibo, Jicamarca, Millstone Hill, and St. Santin); N_2 density from mass spectrometers aboard five satellites (AE-B, Ogo 6, San Marco 3, Aeros A, and AE-C); O, He, and Ar density from neutral gas mass spectrometers on four satellites (Ogo6, San Marcos, Areos A, and AE-C); and O_2 and H from ion mass spectrometers on AE-C. The overall dataset covered the period from 1965 to 1975, and had an approximate altitude range of 140–600 km, solar activity conditions with the mean $F_{10.7}$ of 75–80, and quiet to moderate geomagnetic activities. The lower

boundary of the model was 120 km. The model did not include longitude variation but provided zonal-mean temperature, zonal-mean densities of O, O_2, N_2, H, He, Ar.

The MSIS-83 [Hedin, 1983] advanced the MSIS with more comprehensive data that cover a wider range of solar activities and geomagnetic activities. The MSIS-83 dataset comprises data from seven satellites (added AE-D, AE-E, and ESRO 4), five incoherent scatter stations (added Malvern), and a comprehensive summary of rocket probe data. The O_2 data come from direct measurements by the neutral gas mass spectrometers and EUV absorption rather than derived from ion measurements using chemistry consideration. The composition, temperature, and density data by rocket measurements provide some data in the mesosphere and lower thermosphere region where data coverage was poor. The main new features were extension of the lower boundary to 85 km, additional coefficients for the time independent terms, additional coefficients for the geomagnetic terms, and longitude variation.

The MSIS-86 [Hedin, 1987] augments its dataset over the MSIS-83 with new incoherent scatter temperature data from St. Santin, new composition and temperature from the Dynamic Explorer (DE) satellite, and atomic nitrogen data from the AE-C, -D, -E and DE satellites. In particular, the MSIS-86 uses temperature and composition data from the DE satellite to improve data coverage in the polar region, and the MSIS-86 improves over the MSIS-83 in representing the polar region morphology. New terms and new coefficients were added to reflect hemispherical and seasonal differences in the polar region and local time variations in the geomagnetic activity effect. In addition, a new species, N, was added to the composition list covered by the MSIS-83.

The MSIS-90 [Hedin, 1991] revised the MSIS-86 by extending the lower boundary to the ground and thus provides a single analytic empirical model to describe the temperature and density from the ground to the exobase. The harmonic expansion formulation was slightly modified to emphasize terms that are important to the middle and lower atmosphere. The extension is based on data including the zonal-average tabulations of temperature, density, and pressure, from the Middle Atmosphere Program (MAP) Handbook 16 by Barnett and Corney [1985], which is proposed as the lower atmosphere portion of the international reference atmosphere the CIRA 1986, along with

rocket and incoherent scatter data in the upper mesosphere and lower thermosphere region.

The NRLMSISE-00 [Picone, et al., 2002] is the latest version of the MSIS-class model. It incorporates recent data sets and new categories of data: 1) satellite drag data (1961–1973); 2) recent accelerometer data; 3) recent incoherent scatter data (1981–1997) and; 4) O_2 density data from the Solar Maximum Mission. In addition, it adds "anomalous oxygen" to allow for O^+ and hot atomic oxygen contributions to the total mass density that becomes appreciable above 500 km. The MSIS00 referred to and used in this thesis study is this 2002 version of the MSIS-class model.

Chapter 3

Data

Data used in this thesis study include thermospheric neutral density data derived from satellite drag measurements and solar spectral irradiance data measured by the Thermosphere-Ionosphere-Mesosphere Energetics and Dynamics (TIMED) Solar EUV Experiment (SEE). Section 3.1 introduces the thermospheric neutral density data provided by Bruce Bowman of the Air Force Space Command and Section 3.2 presents the TIMED/SEE solar spectral irradiance data provided by the Laboratory for Atmospheric and Space Physics of the University of Colorado.

3.1 Satellite Drag Data

The neutral density data used in this study are the daily averaged density at satellite perigee locations derived from five low-earth orbiting satellites, for the years 2002, 2003, and 2004. The NORAD satellite catalog numbers, the names, and the launch dates of the satellites are listed in table 3.1. The five satellites are spherical satellites with similar moderately eccentric orbits. The average perigee altitudes of the satellites are between 380 km and 430 km, and the average apogee altitudes are between 1300 km and 1650 km. The orbit characteristics, including the altitudes of the perigees and the apogees, the latitudes of the perigees, and the solar local time of the perigees, are shown in figure 3.1. The perigee altitude is an accurate height above the reference ellipsoid of the perigee point obtained from least squares fitting of perigee heights from each revolution over each given day (-12h to +12h UT). The daily perigee height is then further corrected based on another least squares fitting of daily perigee height residuals over a six-month period. The apogee is an approximate height above the reference ellipsoid. It is used only for judging the amount of drag around perigee. If the orbit is eccentric, then the majority of the drag occurs very close to the perigee point. If the orbit is near circular then the drag

effects are instead based on an average over the entire orbit. The satellites undergo approximately three latitude cycles (figure 3.1, (c)) and five local time cycles (figure 3.1, (d)) in a year.

Table 3.1: The satellites of which the drag data are used for the study.

NORAD Catalog Number	Name	Launch Date
07337	COSMOS 660	1974-06-18
08744	COSMOS 807	1976-03-12
12138	COSMOS 1238	1981-01-16
12388	COSMOS 1263	1981-04-09
14483	COSMOS 1508	1983-11-11

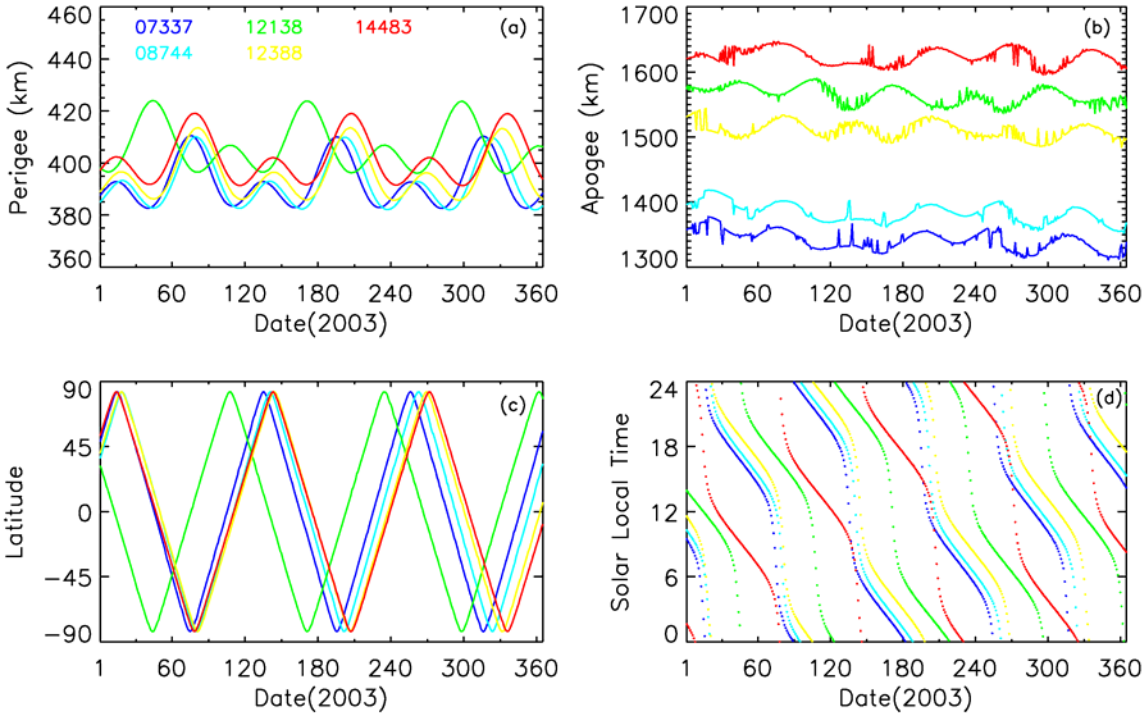

Figure 3.1: Orbital characteristics of the satellites. (a) perigee altitude; (b) apogee altitude; (c) latitude; (d) solar local time.

The total mechanical energy of a satellite is the sum of its kinetic energy and potential energy. The satellite gradually loses its altitude due to atmospheric drag force as follows:

$$F = -\frac{1}{2}\rho A C_D v^2 \qquad \text{(Eq. 3.1)}$$

where ρ is the mass density of the atmosphere, A is the cross-sectional area of the satellite, C_D is the drag coefficient, and v is the satellite velocity relative to the atmosphere. When the satellite loses its potential energy, part of it is used to overcome the drag force and part of it is used to speed up the satellite to sustain its orbit at a lower altitude. Energy loss of each orbit revolution can be determined using a six-element Keplerian orbit state vector, i.e., orbital inclination, right ascension of ascending node, argument of perigee, eccentricity, mean motion, and mean anomaly based on radar and optical observation of satellites orbits. Then atmospheric mass density can be derived from the orbital energy dissipation rate and the satellite ballistic coefficient as follows:

$$B = \frac{A}{m} C_D \qquad \text{(Eq. 3.2)}$$

where A is the cross-sectional area of the satellite, C_D is the drag coefficient, and m is the mass of the satellite.

The thermospheric neutral density at satellite perigees was calculated using a method developed by Bowman et al. [2004b]. The method uses a special perturbation orbit determination, a daily orbital energy dissipation rate, and a "true" ballistic coefficient to accurately determine density with errors within 2–4%. The calculation of the density was performed by Bruce Bowman using a five-step procedure briefly described here.

Step 1: Determination of the standard six Keplerian elements and ballistic coefficient. A differential orbit correction program using special perturbation orbit integration is used to fit radar and optical observations of satellite orbits to obtain the Keplerian elements and ballistic coefficients. The special perturbation integration includes third-body gravitational effects of the sun and moon, the solar radiation pressure, and the acceleration effects due to atmospheric drag. A modified Jacchia 1970 model incorporated into the Air Force's High Accuracy Satellite Drag Model (HASDM) is used to provide atmospheric density required by the integration. Instead of using a constant drag coefficient, a variable drag coefficient based on number densities of the atmospheric

constituents is employed in the integration. This effect is important for solar minimum conditions since the dominant species can change from O to He as low as 500 km and thus change the drag coefficient by nearly 30%. In addition, the selection of the observation span is crucial for accurate orbit fitting and accurate *B* values. A minimum three-day observation span is used to ensure an adequate amount of observations for each fit.

Step 2: Calculation of daily energy dissipation rate (EDR) using orbital fitting parameters and the fitted *B*. Orbital parameters obtained from step 1 are used as input to the modified Jacchia 70 model to calculate atmospheric density. The modified Jacchia 70 density values and the fitted *B* values from step 1 are then used to compute the orbital energy dissipation rate (EDR) over each observation span (typically three to eight days). Overlapping EDRs are computed by moving observation spans by one day at a time to a next orbit fit with the same observation span. A daily EDR is then obtained by averaging overlapped EDRs for each day.

Step 3: Calculation of daily temperature correction between the temperature computed by the modified Jacchia 70 model and the observed temperature derived from the daily EDR obtained in step 2. A "true" ballistic coefficient is calculated for each satellite by averaging the fitted *B* for each satellite over the entire observation period (up to 30 years). This "true" ballistic coefficient has proved to be consistent within 2–3% by comparing "true" ballistic coefficients for many of the same type of satellites. A modeled daily EDR is then calculated using the modified Jacchia 70 density and the "true" ballistic coefficient. The daily temperature difference between the modeled temperature and the observed temperature is then obtained based on the observed daily EDR from step 2 and the model calculated EDR.

Step 4: Calculation of daily density. The daily temperature correction from step 3, the local solar time and latitude of the perigee, the perigee height, the solar flux based on $F_{10.7}$ and $\overline{F}_{10.7}$, and the three-hour geomagnetic A_p index are used by the Jacchia density model to compute the density. Density is calculated every three hours from -12 hours to +12 hours of 00:00UT for each day using the three-hour A_p index (the rest of the input

including daily temperature correction from step 3 remain same). The daily averaged density is then obtained by averaging the eight density values centered at 00:00UT.

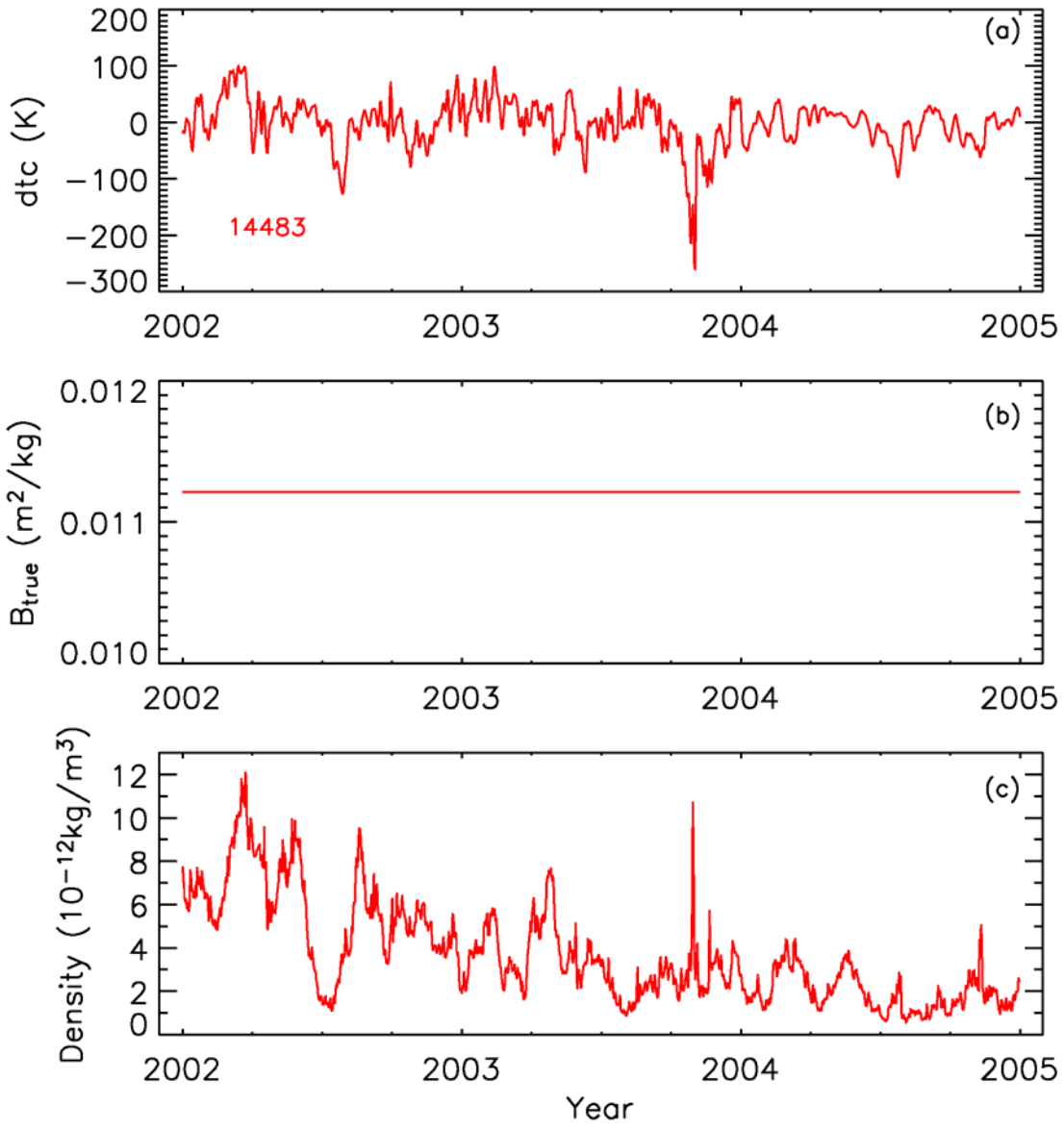

Figure 3.2: The daily temperature correction (dtc), "true" ballistic coefficient, and daily perigee density for satellite 14483, for the years 2002, 2003, and 2004.

Figure 3.2 shows the daily temperature correction, the "true" ballistic coefficient, and the daily-average perigee density for satellite 14483. The largest temperature correction occurs during the 2003 "Halloween" geomagnetic storm indicating the less

adequate empirical representation of atmospheric state during this strong geomagnetic activity. The “true” ballistic coefficient is a constant since the satellite perigees are within an altitude range where major species remain same. Density enhancement by strong geomagnetic activities is evident during the 2003 “Halloween” storm period. The 27-day solar-rotational variation is the dominant feature in panel (c) of figure 3.2. In addition, solar-cycle variation is also evident since the density systematically decreases from the beginning of 2002 towards the end of 2004 (figure 3.2, (c)).

The daily drag-derived density values have been shown to be accurate to within 2–4% by comparisons of the daily drag values using numerous calibration satellites in a wide variety of orbits [Bowman et al., 2004b]. In this thesis study, modeled densities from the TIEGCM and the MSIS00 were sampled at satellite perigee locations to be compared with the satellite drag derived density.

3.2 Solar Spectral Irradiance Measured by the TIMED/SEE

The Thermosphere Ionosphere Mesosphere Energetics and Dynamics (TIMED) Solar EUV Experiment (SEE) measures solar spectral irradiance from 0.1–194 nm [Woods et al., 2005]. The TIMED satellite was launched on 7 December 2001 and normal operation was started on 22 January 2002. The satellite orbits the earth 15–16 times a day and each orbit takes approximately 96 minutes. The SEE instruments measure solar spectral irradiance for three minutes per orbit. The TIMED/SEE consists of two types of instruments: 1) the EUV Grating Spectrograph (EGS) component covers wavelengths from 26–194 nm with a spectral resolution of 0.4 nm and 2) the X-ray Photometer System (XPS) component covers wavelengths from 0.1–34 nm that includes band passes of nine photometers, with spectral resolution of 5–10 nm. The TIMED/SEE provides two types of data: 1) SEE level-3 data is daily averaged solar spectral irradiance with flares removed and 2) SEE level-3A data is ~ 3-minute, observation-averaged solar spectral irradiance with flares included. However, since the TIMED/SEE only observes about three minutes for each orbit, only a few flares are observed. Both types of data are solar spectral irradiance in the range of 0–194 nm on 1-nm intervals. The EGS

observation is used to construct the spectrum from 27–194 nm and the XPS observation provides 0–27 nm part of the spectrum. Beginning in March 2003, the SORCE XPS measurements replace the TIMED/SEE XPS measurements to construct a data product in the range of 0–27 nm due to some instrument failures of the TIMED/SEE XPS. The TIMED/SEE measurements have been calibrated by periodic rocket flights. The data used in this study are the TIMED/SEE version 8, level 3 data. Figure 3.3 is an example of a TIMED/SEE spectrum.

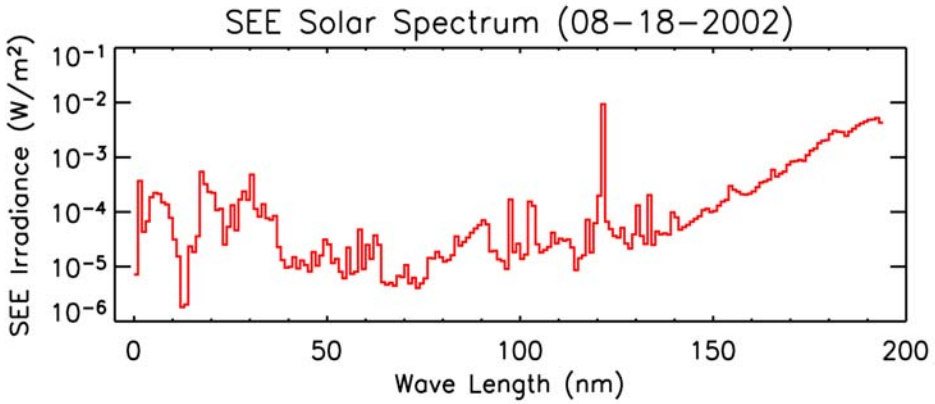

Figure 3.3: A TIMED/SEE level 3 solar irradiance spectrum on 1-nm interval.

Comparison between the TIMED/SEE measurements and solar indices was conducted to examine how the measured solar irradiance correlates with solar indices. Solar indices have been used in solar EUV, UV, and total solar irradiance models to provide solar input for upper atmospheric empirical models, upper atmospheric general circulation models, and satellite drag models, etc. The most widely used index is the $F_{10.7}$ index due to its availability since 1947. The $F_{10.7}$ index is the radio emission from the Sun at a wavelength of 10.7 cm. The global daily value of $F_{10.7}$ is measured at local noon at the Dominion Radio Astrophysical Observatory in Penticton, Canada. The $F_{10.7}$ index is considered to be a good index for coronal emission. The Mg II core-to-wing ratio has also been studied and widely used in the upper atmospheric modeling. The Mg II index is a ratio of the Mg II chromospheric emission at 280 nm to the photospheric radiation in the line wings. The Mg II index has been available since 1978 and is a good measure of solar chromospheric emission.

The TIMED/SEE integrated XUV (0–27nm) irradiance, mostly from coronal emission, was compared with the $F_{10.7}$ index while the TIMED/SEE integrated EUV (27–105 nm), mostly chromosphere fluxes, was compared with the Mg II index (figure 3.4). Both the measured XUV and EUV correlate very well with the indices, indicating that both the indices adequately represent the solar variability in the designated solar irradiance ranges. However, there are also time periods when the solar variability morphology shows discrepancy between the measured irradiance and the indices.

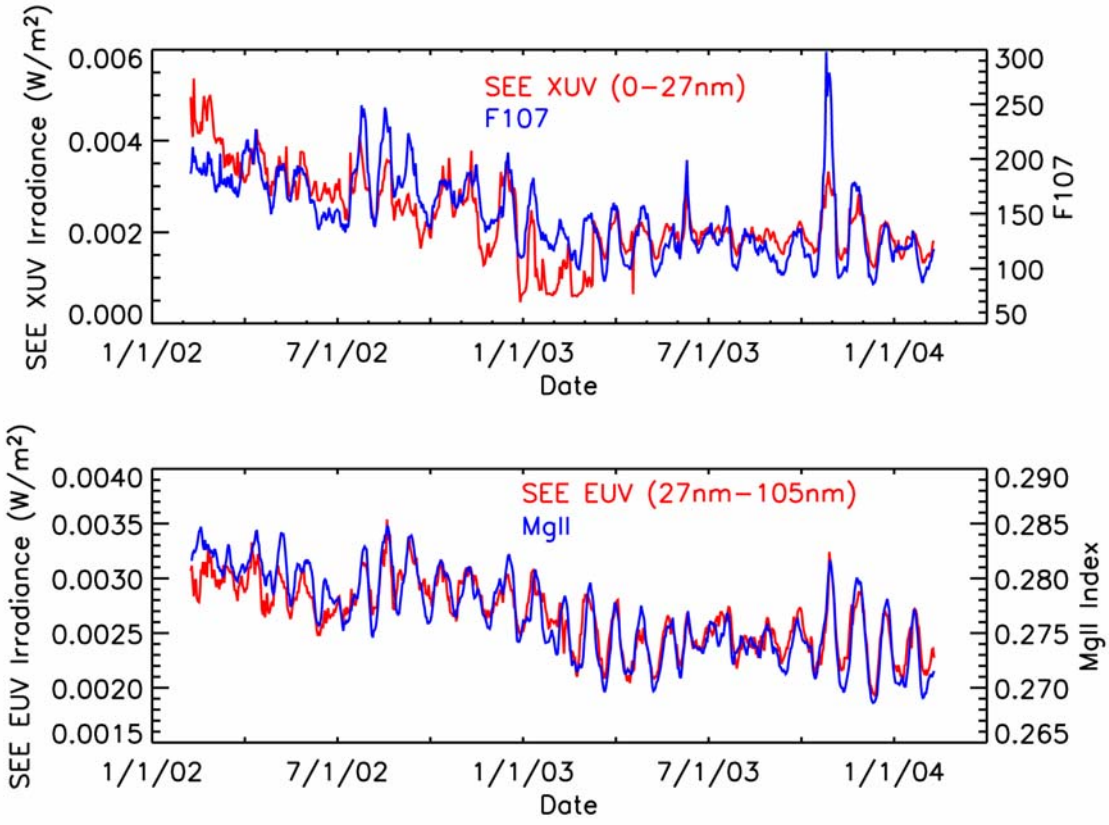

Figure 3.4: Comparison of the TIMED/SEE measurements to solar indices. Upper panel: the TIMED/SEE XUV versus the $F_{10.7}$ index; Lower pane: the TIMED/SEE EUV versus the Mg II index.

Another way to examine the TIMED/SEE measurements is to compare the TIMED/SEE measurements to solar proxy models. The default solar input for the TIEGCM is a solar proxy model of which the 5–105 nm range is based on the EUVAC solar proxy model [Richards, et al., 1994] and the 105–175 nm range is based on the

Woods and Rottman model [Woods and Rottman, 2002] (see Chapter 2, Section 2.2.2). The TIMED/SEE data that were binned on 1-nm resolution were processed into the low-resolution binning scheme by the solar irradiance interface introduced in Section 2.2.1 of chapter 2. The solar minimum reference solar spectrum and the solar variability factor based on the EUVAC model and the Woods and Rottman model on the low resolution binning scheme are listed in table 2.3. The solar spectrum at a given solar activity is then given by Eq. 2.11.

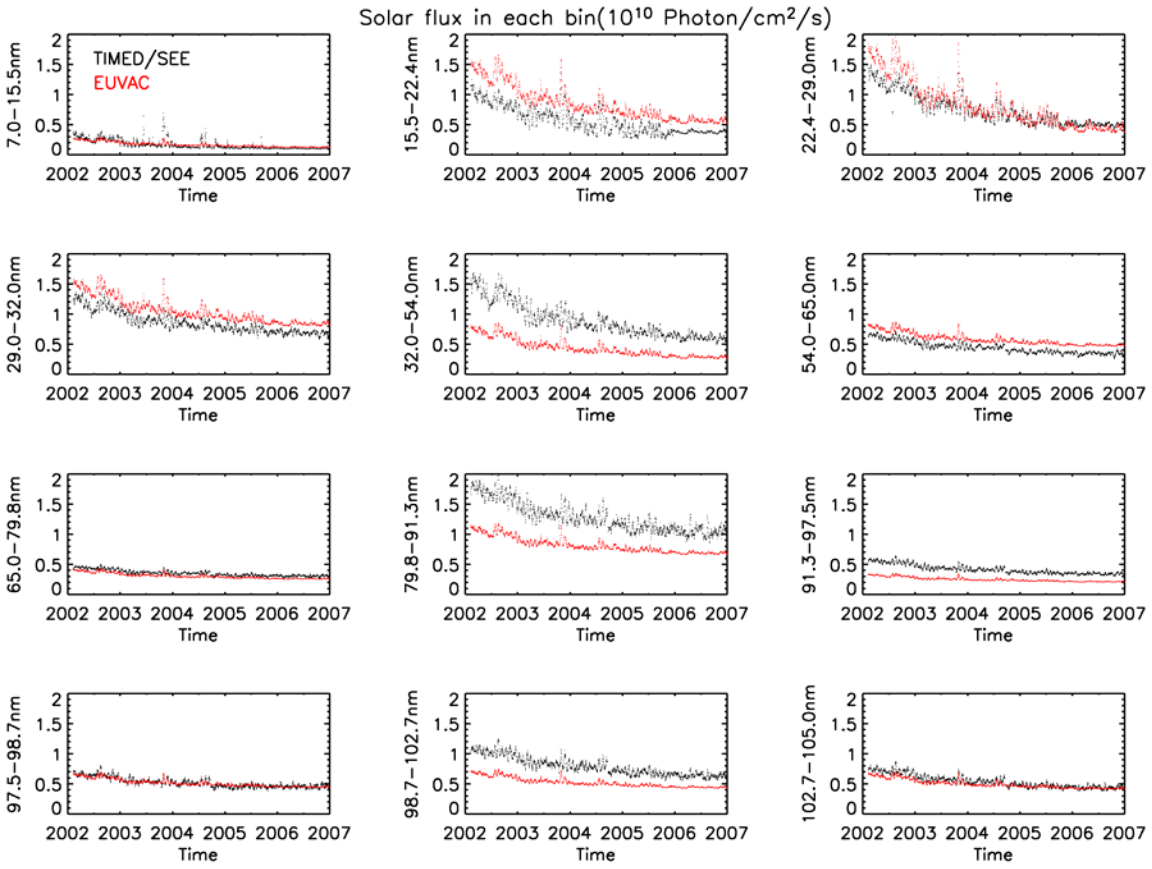

Figure 3.5: Solar flux in each bin from 7–105 nm on the low-resolution binning scheme based on the TIMED/SEE measurements and the EUVAC solar proxy model, from 2002-2006. Black: the TIMED/SEE; Red: the EUVAC model.

Figure 3.5 shows the solar flux in each bin from 7–105 nm on the low-resolution binning scheme, from the beginning of the TIMED/SEE mission to the end of 2006, based on the TIMED/SEE measurements and the EUVAC solar proxy model. The

TIMED/SEE and the EUVAC agree reasonably well for majority of the bins. The largest discrepancy occurs in the bin 32.0–54 nm and 79.8–91.3 nm. Figure 3.6 shows the solar flux in each bin from 105–175 nm on the low-resolution binning scheme, from the beginning of the TIMED/SEE mission to the end of 2006, based on the TIMED/SEE measurements and the Woods and Rottman solar proxy model. The TIMED/SEE and the Wood and Rottman model also agree reasonably well for majority of the bins. The largest discrepancy occurs in the bin 110–115 nm. There are some interesting features shown in figure 3.5 and figure 3.6: 1) solar-cycle variation as evident in reduction of solar flux from 2002 toward 2007; 2) stronger solar-rotational variation during strong solar activity periods than during quieter periods and; 3) overall larger solar-rotational variation by the TIMED/SEE measurements. Some sensor degradation of the TIMED/SEE instruments is evident in the data towards 2005 and 2006. For example, in the FUV bins greater than 135 nm. The TIMED/SEE measurements are calibrated by periodic rocket flights. The last rocket calibration included in the TIMED/SEE version 8 data was in 2004. The TIMED/SEE version 9 data includes the most recent rocket calibration of 2006. This study used the TIMED/SEE version 8 data since the version 9 data was just released in April of 2007.

There is overall agreement as well as some discrepancies between the TIMED/SEE measurements and the solar indices and the solar proxy models. Chapter 4 will examine the effect of the measured solar irradiance on density calculation when used as solar input for the TIEGCM.

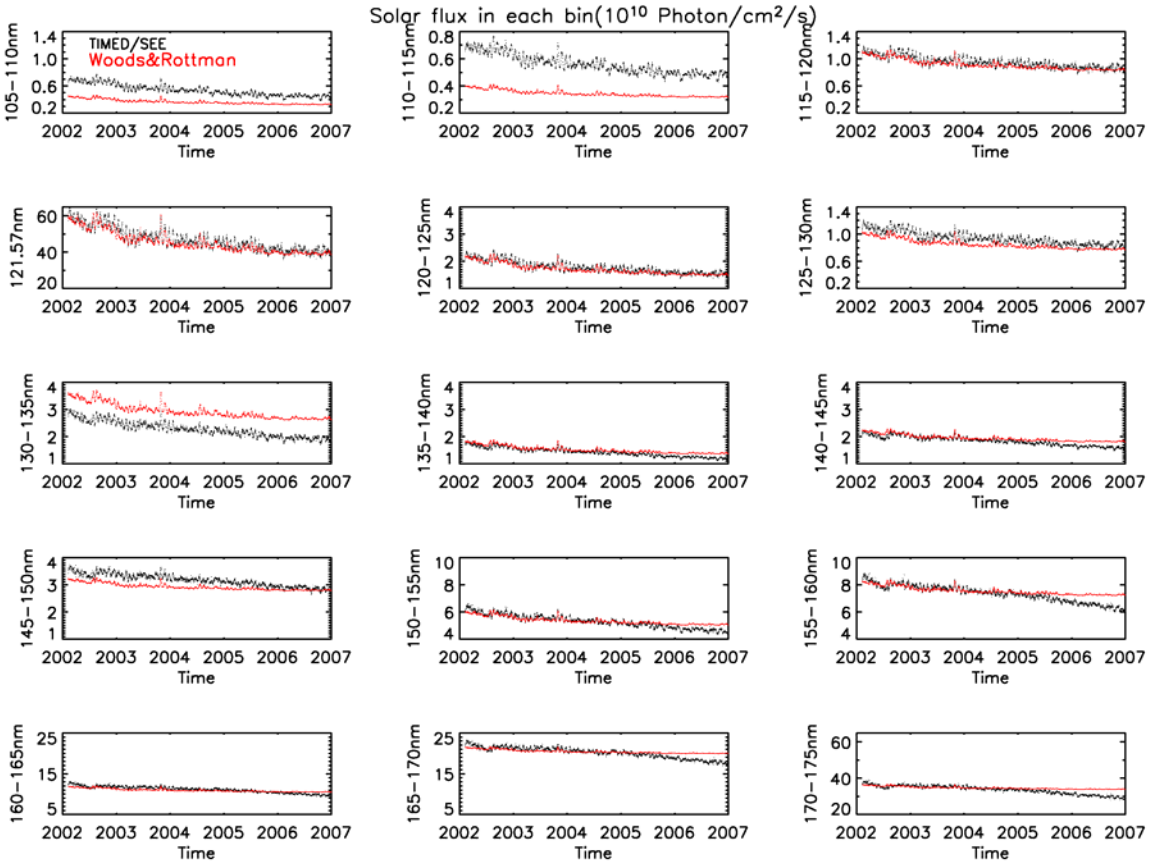

Figure 3.6: Solar flux in each bin from 105–175 nm on the low-resolution binning scheme based the TIMED/SEE measurements and the Woods and Rottman solar proxy model, from 2002–2007. Black: the TIMED/SEE; Red: the Woods and Rottman model.

Chapter 4

ANALYSIS OF MODEL SIMULATIONS

The TIEGCM model was run for the period from 2001 to 2006. The solar proxy model described in Chapter 2 and TIMED/SEE solar spectral measurements were used as solar forcing. The TIEGCM simulations were compared to the satellite drag-derived density dataset described in Chapter 3 and the MSIS00 model to investigate thermospheric neutral density and its temporal and geographical variations. The global mean version of the TIMEGCM was run for the period from 1970 to 2000 and solar cycle 24 to examine long-term trend of thermospheric neutral density. Section 4.1 gives an inclusive general description of thermospheric density variations using the TIEGCM simulations. Section 4.2 examines the annual/semiannual density variation and proposes eddy diffusion as a mechanism for the annual/semiannual variation. Section 4.3 describes the effect of using the TIMED/SEE measurements as solar input for the TIEGCM model and compares the TIEGCM simulation and the MSIS00 density to the satellite drag-derived density. Section 4.4 investigates long-term trend of thermospheric neutral density.

4.1 Thermospheric Density Variations

Thermospheric neutral density varies with changes in solar radiation, geomagnetic activity, dynamics, and mixing by lower atmospheric processes. It varies from the shortest time scale in minutes driven by solar flares to global change driven by greenhouse gas cooling, and undergoes variations driven by geomagnetic storms in the order of hours, diurnal variation, 27-day solar-rotational variation, semiannual/annual variation, and solar-cycle variation in between. It also varies with geographic locations.

In this section, all these variations except the global change will be briefly reviewed, using the TIEGCM simulation. The global change will be investigated in Section 4.4.

The TIEGCM model was run for the years 2001–2006. The solar proxy model (see Section 2.2.2) was used as solar input for 2001001 to 2002038 and the TIMED/SEE was used for 2002039 to present. Thermospheric neutral density from 2001 to 2006 is shown in panel (a) of figure 4.1. The black line is the satellite drag-derived density for satellite #12388 at its perigee locations. As shown in Chapter 3, the perigee altitude for this satellite fluctuates between 385 km and 415 km, the perigee latitude changes from 83^{o}S to 83^{o}N and the perigee local time changes from 0 to 24 (figure 3.1). The red line is the TIEGCM simulation. The TIEGCM simulation was sampled at the satellite perigee locations from 2001 to 2004 and the daily average density at 400 km at (2.5^{o}N and 0^{o}E) is given for 2005 and 2006. Panel (b) shows the TIMED/SEE integrated (5 nm to 105 nm) solar EUV flux from 2002039 to 2006365. The solar activity index $F_{10.7}$ and geomagnetic activity index A_p from 2001 to 2006 are given in panel (c).

The density in figure 4.1 is a composite of density variations with time-scales from hours to decades and variations with geophysical locations due to variation in satellite perigee latitudes and altitudes. The density overall follows the morphology of the $F_{10.7}$ index, which indicates that solar irradiance is the main forcing of thermospheric neutral density. As $F_{10.7}$ changes from over 200 in 2001 during solar maximum to around 80 in 2006 near solar minimum, density decreases about one order of magnitude from 2001 to 2006. Solar-rotational variation of density can be identified, with an average period of 27 days. Accompanying the overall variation with solar irradiance are impulsive variations with geomagnetic forcing. This is evident by observing the spikes in density and the spikes of geomagnetic A_p index. An annual density variation is also obvious with a minimum around July and a maximum in January. In addition, in some of the years, for example 2002 and 2006, a semiannual variation is also evident, with density showing maximum near equinoxes and minimum near solstices. Other variations not evident but included in Panel (a) of figure 4.1 are the diurnal variation as perigee local time changes from 0 to 24, latitudinal variation as perigee latitude varies between the southern hemisphere and the northern hemisphere, variation with height as perigee

altitude varies between 385 km and 415 km, and a global change due to increase of greenhouse gases (see section 4.4). Variation caused by solar flares is not included in figure 4.1 since satellite drag-derived density is daily-averaged density at perigee locations and the TIEGCM simulation is driven by daily-averaged TIMED/SEE measurements, which exclude flares. The rest of this section provides some detailed discussions of density variations mentioned here.

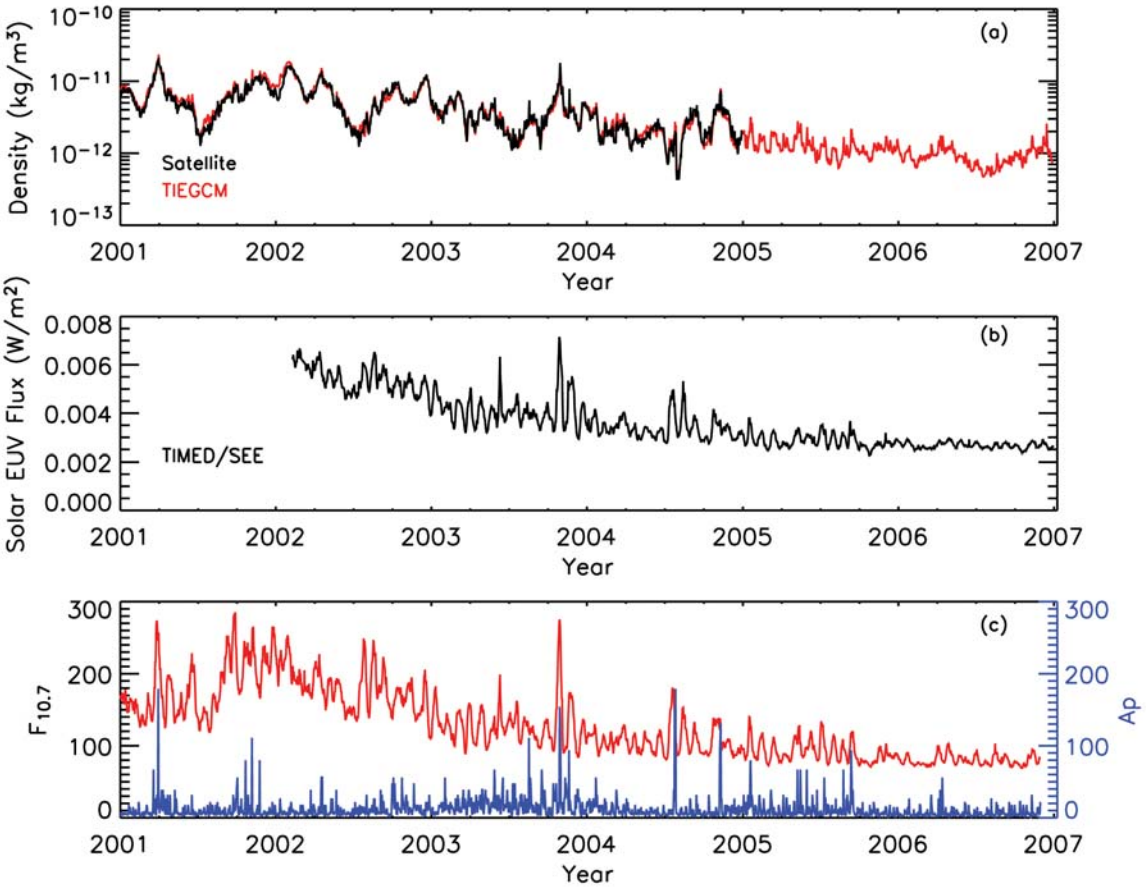

Figure 4.1: Thermospheric neutral density around 400 km from 2001 to 2006. Panel (a): Black: Satellite drag derived density; Red: TIEGCM simulation. The density is daily-averaged density at satellite perigee locations from 2001 to 2004, and daily averaged-density at a fixed location (2.5^{o}N, 0^{o}E, 400 km) from 2005 to 2006. Panel (b): the TIMED/SEE integrated (5–105 nm) solar EUV flux from 2002039 to 2006365. Panel (c): the corresponding solar activity index $F_{10.7}$ and geomagnetic activity index A_p.

4.1.1 Variation with Solar Flares

Solar flares are sudden, rapid, and intense releases of magnetic energy built up in twisted magnetic fields of the Sun's atmosphere, usually in regions with sunspots. Flares produce a burst of radiation across the Sun's electromagnetic spectrum and release energetic particles into the solar wind. The most distinguished phenomenon is the brightness in X-ray radiation. Solar flares are classified by the X-ray brightness from 0.1–0.8 nm (table 4.1). There are 4 classes of solar flares from class B with no noticeable effect on the Earth to class X that triggers planet-wide radio blackouts and radiation storms. During a class X solar flare, X-ray and XUV increase dramatically with the X-rays from 0.1–0.8 nm observed by the GOES satellite increasing more than 3 orders of magnitude and EUV flux increasing around 20%. The increased XUV and EUV heat the thermosphere and enhance the density. The left panel of figure 4.2 gives an example of solar flare simulation by the TIEGCM. The lower portion of the left panel shows solar flux from 0.1–0.8 nm measured by the GOES10 satellite on 28 October 2003. The onset of the solar flare was 11:13 am universal time, and it is officially an X17 solar flare. The X-ray solar flare spectrum was obtained based on the TIMED/SEE XPS measurement by Rodgers et al. [2006]. The solar flare spectrum was then added to the background TIMED/SEE daily average measurements to produce the total spectrum for the TIEGCM. The upper portion of the left panel of figure 4.2 shows the density for 28 October 2003 at 400 km at 2.5^{o}N at solar local time, 12:00 noon. The sudden increase of solar irradiance, especially in the XUV and EUV region, drives a sudden increase in density with a peak around 1 hour later than the peak of X-ray intensity. The dayside density at low latitude increases around 20% during this X17 solar flare, which agrees with accelerometer measurements of density by the CHAMP satellite [Sutton et al., 2005].

Table 4.1: Classification of X-ray solar flares.

Class	Peak Intensity (W/m^2, 0.1–0.8 nm)
B	$I < 10^{-6}$
C	$10^{-6} \leq I < 10^{-5}$
M	$10^{-5} \leq I < 10^{-4}$
X	$I \geq 10^{-4}$

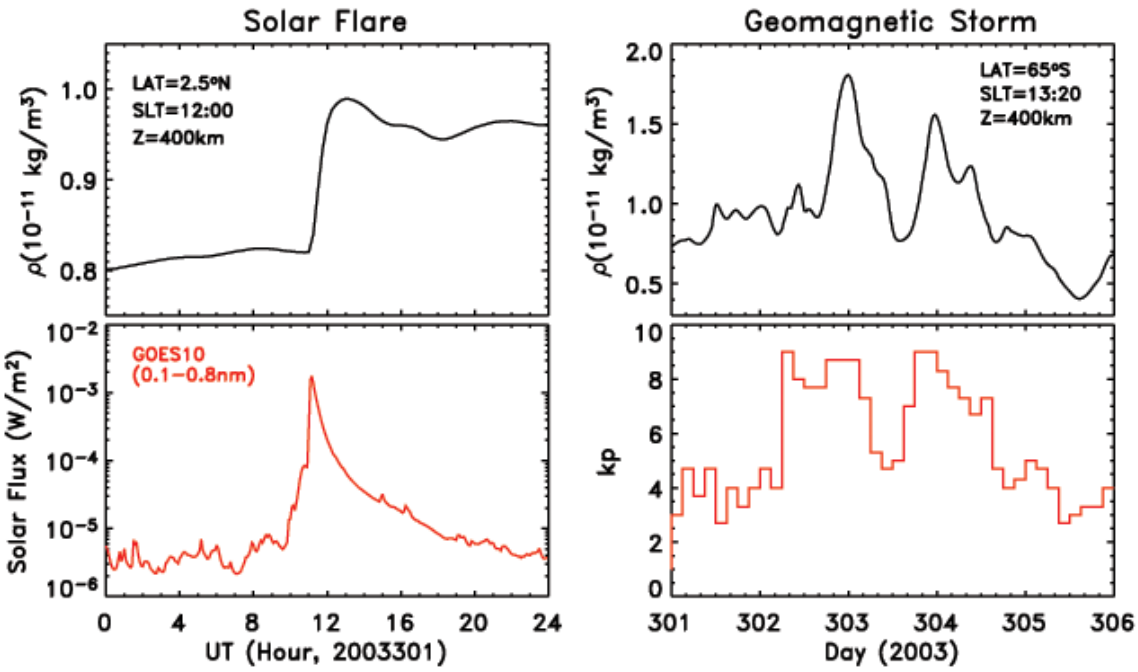

Figure 4.2: TIEGCM simulation of density variation with solar flares and geomagnetic storms. The left panel: TIEGCM simulation of a solar flare on 28 October 2003; the right panel: TIEGCM simulation of the 2003 "Halloween Storm" period from 28 October 2003 to 1 November 2003.

4.1.2 Variation with Geomagnetic Storms

During the 2003 "Halloween Storm" period, the geomagnetic index K_p maintained high values up to nine for almost three days. The K_p index is a code that indicates fluctuations observed by ground-based magnetometers relative to a quiet day during a three-hour interval. It ranges from zero to nine and is given in three-hour intervals. A K_p index of five or higher indicates storm-level geomagnetic activities. The A_p index mentioned earlier is an indication of daily-average level of geomagnetic activity. The relationship between A_p and K_p is given in table 4.2.

Table 4.2: Relationship between K_p and A_p indices.

K_P	0	1	2	3	4	5	6	7	8	9
A_p	0	3	7	15	27	48	80	140	240	400

Geomagnetic storms occur as a result of a sudden increase of dynamic pressure in the solar wind caused by coronal mass ejections (CME) or to a less degree, by solar flares. The solar wind energy is transferred from the magnetosphere to the ionosphere and the thermosphere through plasma convection and energetic particle precipitation; both are high latitude phenomena. The increased plasma convection causes a substantial increase in Joule heating, and energetic particle precipitation heats the thermosphere and the ionosphere in the auroral region through ionization, dissociation, and excitation of neutral constituents by energetic particles, mainly at E-layer altitudes. Joule heating usually dominates particle heating during large geomagnetic storms [Wilson, et al., 2006]. The thermosphere responds to the heating with increased temperature, intensified large-scale circulation, redistribution of composition, and increased density. The localized heating can also excite gravity waves at high latitude [Bruinsma, et al., 2006]. The thermosphere disturbance at high latitude is then propagated towards lower latitudes by large-scale circulation and waves, causing perturbation at lower latitudes with several hours delay [Bruinsma, et al., 2006]. As a result, geomagnetic storm-driven increases of density can be a global phenomenon.

The lower portion of the right panel in figure 4.2 shows the K_p index from 28 October 2003 to 1 November 2003. The upper diagram of the right panel is the TIEGCM simulated density for the same period at 400 km at latitude 65°S, with a solar local time of 13:20. The high-latitude dayside density responds to geomagnetic storms with little delay. The increase of density for this storm period is on the order of 200%, in good agreement with CHAMP accelerometer measurements for the same storm period [Liu and Lühr, 2005; Sutton et al., 2005].

4.1.3 Diurnal Variation

Since solar irradiance is the main forcing for the thermosphere, thermospheric density exhibits large diurnal variation. Panel (a) of figure 4.3 shows the TIEGCM simulation of diurnal variation of density at the spring equinox. The sample point is (2.5°N, 0°E) at 400 km. The density reaches minimum around 5:00 am and maximum around 4:00 pm with density increase around 100% from minimum to maximum.

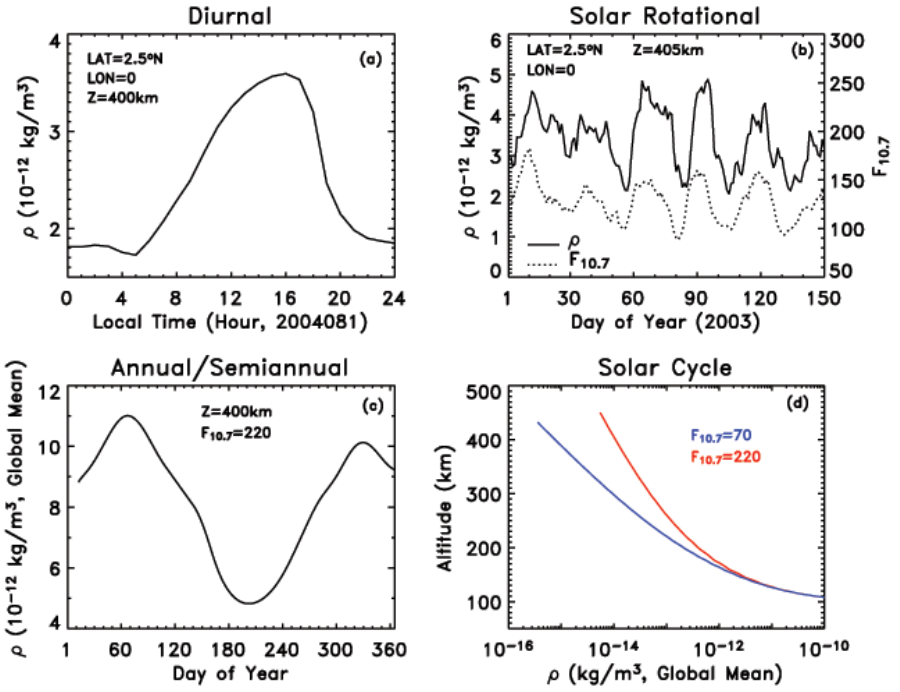

Figure 4.3: TIEGCM simulation of diurnal, solar-rotational, annual/semiannual, and solar- cycle variations of thermospheric neutral density.

4.1.4 Solar-Rotational Variation

Solar-rotational variation of thermospheric density is caused by the appearance and disappearance of the Sun's active regions as the Sun rotates in an average 27-day period. The active regions can be seen through the Sun's hydrogen image that features bright regions identified as solar plages. Plages are localized regions with intense magnetic activities that are usually associated with sunspots. Plages are distributed non-uniformly and appear primarily within 30^{o} latitude on each side of the equator of the Sun. These features usually appear and disappear over a period of several months. As the Sun rotates with an approximate 27-day period, the non-uniform active regions emerge and vanish to the Earth's atmosphere. This produces a rotational variability in solar irradiance with a magnitude proportional to the contrast and fractional areas between active regions and quiet regions. Since the Sun is very active under solar maximum conditions, solar-rotational variation of solar irradiance is larger under solar maximum conditions compared to solar minimum conditions. Panel (b) of figure 4.3 shows more than 5 solar rotations of 2003 as indicated by the $F_{10.7}$ index. The TIEGCM simulated density is daily-averaged density sampled at (2.5^{o}N, 0^{o}E) at 400 km. As $F_{10.7}$ changes about 60 units during a solar rotation, density changes about 80% from minimum to maximum.

4.1.5 Annual/Semiannual Variation

The Earth's orbit has an eccentricity of 0.017. The Earth reaches its perihelion in early January each year, and passes through its aphelion point at the beginning of July. Due to the orbital eccentricity, the insolation is 7% larger in January than in July. Sensitivity study using the global mean TIMEGCM shows that the 7% variation in solar irradiance can cause a 2%–5% temperature variability and ~20% density difference at 400 km. However, the global mean model does not include large-scale circulation. The temperature difference, when coupled with dynamics, can introduce a global annual density variation in the order of 60%, as will be seen in Section 4.1.7.

Global semiannual density variation was first discovered by Paetzold and Zschörner [1961]. They analyzed satellite drag data and found that there is a global semiannual density variation that maximizes in April and October, shortly after equinoxes, and minimizes around July and January. Fuller-Rowell [1998] proposed a mechanism to explain the global semiannual density variation. It was proposed that stronger inter-hemispheric, large-scale circulation near solstices caused by uneven solar heating acts like a "thermospheric spoon" to mix lighter species and heavier species causing less diffusive separation. Scale height decreases due to increases of mean molecular mass. As a result, density at a fixed pressure level (excluding thermal expansion/contraction) will decrease. Near equinoxes, the inter-hemisphere circulation is much weaker because solar heating is evenly distributed on the two hemispheres. Neutral species are more diffusively separated, and density at fixed pressure level is larger due to larger scale height when mean molecular mass is smaller.

The analysis of satellite drag data suggests that the amplitudes of the annual component and semiannual components are comparable [Paetzold and Zschörner, 1961; Volland and Mayr, 1973]. Panel (c) of figure 4.3 shows global mean density at 400 km for a high solar activity year with $F_{10.7}$ of 220. This is the combined annual and semiannual density variation. The magnitude of variation from minimum to maximum is around 120%. Therefore, the magnitude of annual variation and semiannual variation is around 60%.

The TIEGCM simulations in this thesis study (Section 4.2) indicated that effects of the sun-earth distance and the "thermospheric spoon" can not fully account for the annual/semiannual amplitude observed by satellite drag. An additional mechanism will be discussed in detail in Section 4.2: turbulent mixing (eddy diffusion) caused by gravity waves breaking near the mesopause. Gravity wave breaking causes eddy diffusion which influences the upper thermospheric composition. Observations [Kirchhoff and Clemesha, 1983; Fukao, et al., 1994; Lübken, 1997; Khattatov, et al., 1997; Rao, et al., 2001; Sasi and Vijayan, 2001] and gravity wave breaking theory [Garcia and Solomon, 1985] suggested that eddy diffusion in the mesopause region shows an annual/semiannual variation, and thus an annual/semiannual forcing to the thermosphere.

4.1.6 Solar-Cycle Variation

Solar-cycle variation is driven by the intrinsic variability of magnetic activity in the Sun. During a solar cycle, the plage fractional area over the solar disk varies from 0 to around 0.2. The variability of solar irradiance, mainly the EUV, drives a solar-cycle variability of thermospheric neutral density of more than one order of magnitude. Panel (d) of figure 4.3 shows the TIEGCM simulation of global mean density profiles for solar minimum and solar maximum conditions. The density at 400 km under solar maximum conditions is about 14 times of the density under solar minimum conditions.

4.1.7 Latitudinal Variation

The density variations addressed so far are density variations with time. Another aspect of density variation worth mentioning is its latitudinal variation. The total mass density is determined by the densities of major species. At a fixed altitude, the number densities of atmospheric constituents are thermally and dynamically governed. Panel (a) of figure 4.4 shows zonal-averaged neutral density at 350 km under solar minimum conditions from the TIEGCM simulation. At the June solstice, neutral density minimizes at the south pole and gradually increases towards the north pole. At the December solstice, it minimizes at the north pole and increases towards the south pole. At equinoxes, the density exhibits little variation with latitudes. The latitudinal variation of neutral density from the winter pole to the summer pole is approximately 40%. Since neutral density is determined by composition, and composition is determined by temperature and large-scale circulations, it is helpful to investigate the latitudinal variation of temperature and composition redistribution by large-scale circulations. Panel (b) of figure 4.4 is the corresponding zonal-mean temperature. The summer pole temperature is approximately 27% higher than the temperature at the winter pole. During equinoxes, temperature is more evenly distributed along latitudes except at high latitudes where heating by geomagnetic activities contributes a higher temperature in the regions. Panel (c) and panel (d) of figure 4.4 give O and N_2 number density, respectively. The O

number density shows little latitudinal variation while N_2 number density shows a latitude-dependency similar to that of the temperature but with a larger amplitude reaching one order of magnitude. At 350 km, O makes the primary contribution to the total mass density and N_2 makes the secondary contribution. The total mass density shows a latitudinal variation with amplitude between those of O and N_2.

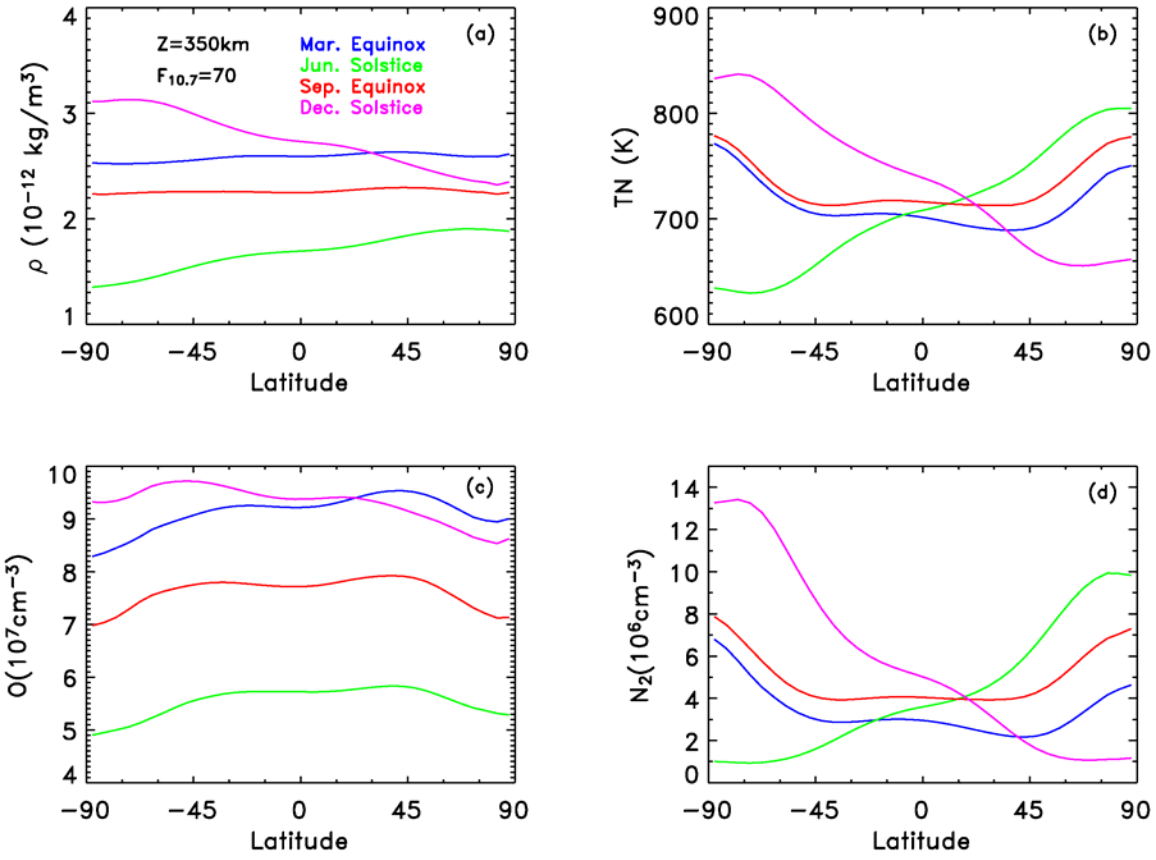

Figure 4.4: Latitudinal distributions of zonal-mean density, temperature, and composition at 350 km at equinoxes and solstices. The results are from the TIEGCM simulation under solar minimum conditions.

The difference in the latitudinal distributions of O and N_2 is determined by the differences in O and N_2 responses to thermal and dynamic forcing due to the difference in molecular weight of O and N_2. The seasonal-latitudinal variation in solar irradiance causes a pressure gradient from the summer hemisphere to the winter hemisphere. The pressure gradient drives a large-scale inter-hemisphere circulation from the summer to

the winter hemisphere. The large-scale circulation transports lighter species to the winter hemisphere and accumulates heavier species in the summer hemisphere. The effect of the large-scale circulation can be seen on a fixed pressure surface where the effect of thermal expansion does not show since it is built in when the pressure surface is thermally lifted to a higher altitude. The O number density in panel (a) of figure 4.5 shows an enhancement in the winter hemisphere and depletion in the summer hemisphere, while the N_2 number density (panel (b) of figure 4.5) shows an enhancement in the summer hemisphere and depletion in the winter hemisphere. At a fixed altitude, for a lighter species O, the number density change due to the large-scale circulation compensates for the number density change due to thermal expansion/contraction, which results in weak latitude-dependency in O distribution (panel (c) of figure 4.4). For a heavier species N_2, the dynamic forcing augments the thermal forcing and N_2 shows large latitudinal variation (panel (d) of figure 4.4). At equinoxes, both O and N_2 have weak latitude dependencies except at high latitude where there is depletion in O number density and enhancement in N_2 number density. The difference in high latitude distribution of O and N_2 is caused by geomagnetic forcing. The geomagnetic activities in the high-latitude regions heat the atmosphere, cause divergence in the area, transport lighter species away from the region, and accumulate heavier species in the region.

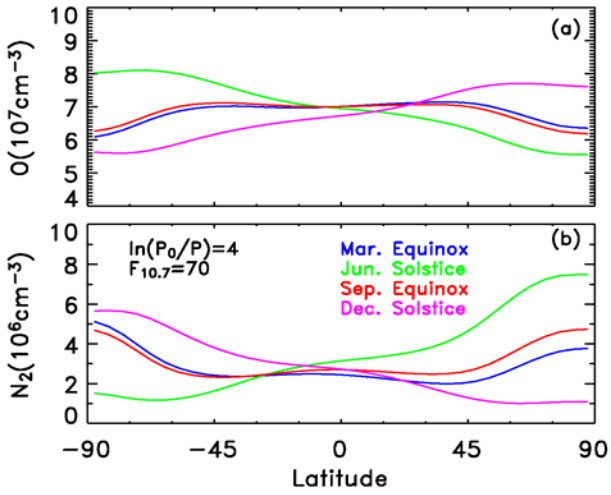

Figure 4.5: Latitudinal distributions of zonal-mean O and N_2 number density at $\ln(P_0 / P) = 4$ at equinoxes and solstices. The results are from the TIEGCM simulation under solar minimum conditions.

There is a distinct difference in density annual variation (variation between the two solstices) in the Arctic circle and the Antarctic circle; the density annual variation in the Antarctic circle is much larger than that in the Arctic circle (figure 4.4). The explanation can be found by investigating the change of sun-earth distance in a year. At June solstice, when the Arctic circle north of 66.5^{o}N is having 24 hours of daylight, the Earth is near the aphelion point where it is farthest from the Sun. At the December solstice, when the Arctic circle is having 24 hours nighttime, the Earth is near the perihelion point where it is closest to the Sun. This means that for the Arctic circle, the variation in insolation caused by sun-earth distance is opposite to the annual variation and thus partially cancels the annual temperature difference. Consequently, the annual temperature variation in the Arctic circle is smaller (~150 K) than that in the Antarctic circle (~200 K) (the middle panel of figure 4.4). The smaller annual variation in density in the Arctic circle reflects the reduction in temperature annual variation in the region. The latitudinal asymmetry in the amplitude of annual temperature variation, together with the latitudinal redistribution of composition by the larger-scale inter-hemisphere circulation and lower atmosphere processes, causes a global mean annual density variation seen in the top panel of figure 4.4, with a magnitude about 60%.

4.2 Eddy Diffusion and Annual/Semiannual Variation

Paetzold and Zschörner [1961] found an annual thermospheric density variation with a narrow minimum from May to August and a broad maximum during the rest of the year with a secondary minimum around January, through analyzing satellite drag data. The magnitude of the annual minimum to maximum variation is more than 100%. Using harmonic analysis, they further proposed that the annual variation is a semiannual variation superimposed on an annual variation, and the ratio of the amplitude of the annual and semiannual variation is 3:2. Since the amplitude is too large to be explained by the insolation variation due to the sun-earth distance, they suggested that the annual and semiannual variation is likely caused by interaction of the terrestrial upper atmosphere and interplanetary matter.

In his 1965 thermospheric empirical density model (J65), Jacchia [1965] represented semiannual density variation with semiannual temperature variation. However, difficult arose when the J65 predicted semiannual density variation showed large discrepancy with drag data from satellites that have altitudes beyond the altitude range of 250 km to 600 km [Cook, 1967; Cook, 1969], the altitude range of the data upon which the J65 was based. Jacchia [1971b] then reappraised the J65 model's approach to semiannual density variation and suggested that the semiannual density variation can be represented as a pure density variation with amplitude as a function of height. The semiannual density variation referred in Jacchia model shows maximum in April and October, primary minimum in July, and secondary minimum in January. From hereafter, this pattern of density variation will be referred to as annual/semiannual density variation since it consists of an annual component and a semiannual component. The MSIS-class model represents annual/semiannual density variation with combined contribution from an annual/semiannual temperature variation and an annual/semiannual composition variation. The annual/semiannual composition is imposed at 120 km and propagates to the entire thermosphere through diffusion.

Empirical models can reproduce the annual/semiannual density variation, but mechanisms for the variation are not addressed. Walterscheid [1982] suggested that there is a globally averaged temperature variation between solstice and equinox due to geomagnetic activities being stronger at equinoxes than at solstices. However, the semiannual variation in geomagnetic activities is too small [Detman, 1996] to account for the large semiannual amplitude in density variation. The detection of composition anomalies, such as winter bulges of lighter species in the thermosphere [Hedin et al., 1974, 1977; Jacchia, 1974; Potter, 1977] and the depletion of O and He at high latitude during magnetic storms [Taeusch et al., 1971; Jacchia et al., 1976, 1977; Prölss, 1977], prompted attribution of latitudinal and seasonal variations in composition to large-scale circulation induced by uneven heating of solar irradiance and geomagnetic storms [Johnson and Gottlieb, 1970; Mayr and Volland, 1971, 1972; Mayr et al., 1978]. Fuller-Rowell [1998] further proposed that large-scale circulation is an important mechanism for global semiannual density variation. In addition, efforts were made to explain the

semiannual density variation in terms of lower atmospheric processes. Changes in turbopause height were used to interpret density variation in the thermosphere [Shimazaki, 1971; Chandra and Sinha, 1974; Schuchardt and Blum, 1977]. Nevertheless, the mechanism remains speculative due to lack of understanding of eddy diffusion at mesopause and the effect of eddy diffusion on the thermosphere. In this section, eddy diffusion will be examined as a mechanism for thermospheric annual/semiannual density variation using the TIEGCM.

4.2.1 Characteristics of Annual/Semiannual Variation

The relatively long history of satellite drag observation provides a wealth of data for thermospheric density study. Bowman [2004a] analyzed drag data of 13 satellites with perigee heights between 200 km and 1100 km, to characterize the annual/semiannual density variation from 1970–2002. The satellites have either moderate eccentric orbits or near spherical orbits, and they have a variety of inclinations from low to high. Following the Jacchia 70 [Jacchia, 1970] model convention, which describes annual/semiannual density variation as follows:

$$\Delta \log_{10} \rho = F(Z)G(t) \qquad \text{(Eq. 4.1)}$$

where *F(Z)* is altitude-dependent amplitude from density minimum to density maximum and *G(t)* is the phase of the variation, Bowman [2004a] obtained *F(Z)* and *G(t)* function through satellite drag data analysis. Figure 4.6 shows the *G(t)* function sorted into solar minimum and solar maximum conditions. The *G(t)* is calculated as follows: first, the difference between the satellite drag-derived daily density and the density from the High Accuracy Satellite Drag Model (HASDM) [Storz, 2002] modified Jacchia model, without annual/semiannual variation imposed, is calculated; second, the difference is normalized by the amplitude of the year, i.e., *F(Z)*. Figure 4.6 indicates that both the phase and amplitude of the annual/semiannual density variation change from year to year, and it seems that phase variation is more complicated under high solar activity conditions. As for the amplitude, Bowman found that the amplitude increases with altitude between 200

km to around 800 km and then declines with altitude. The amplitude variability with solar activity is not significant for low-earth orbit satellites, i.e., around 400 km, but the amplitude increases with solar activity at greater altitudes, and the amplitude can range between around 30% to as much as 250%, depending on altitude and solar activity.

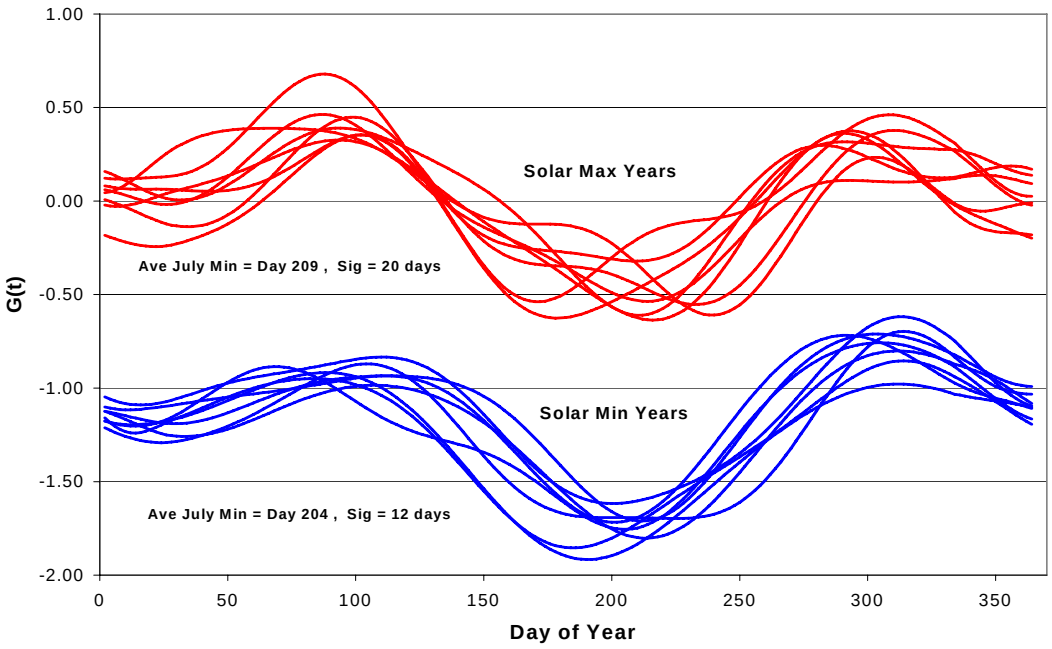

Figure 4.6: The yearly G(t) for different years for solar minimum and solar maximum conditions, adapted from Bowman [2004a].

Figure 4.7 shows the empirical annual/semiannual variation in the thermosphere under moderate solar activity ($F_{10.7} = \overline{F}_{10.7} = 150$) and quiet geomagnetic conditions (A_p=4) using the MSIS00 model [Picone et al., 2002]. As mentioned earlier, the annual/semiannual variation in density is represented partially by an annual/semiannual variation in temperature and partially by an annual/semiannual variation in composition imposed at 120 km. Both O and N_2 number density, and consequently, the O/N_2 ratio, have annual/semiannual variations that are in phase with each other at 120 km. Such annual/semiannual variation is maintained above 120 km through diffusive equilibrium. Temperature is calculated to produce observed N_2 density. At altitude 400 km, both composition and temperature, and thus, density, have annual/semiannual variations that

are in phase with each other. The total amplitude is about 60%, smaller than the amplitudes obtained by drag data analysis [Bowman, 2004a].

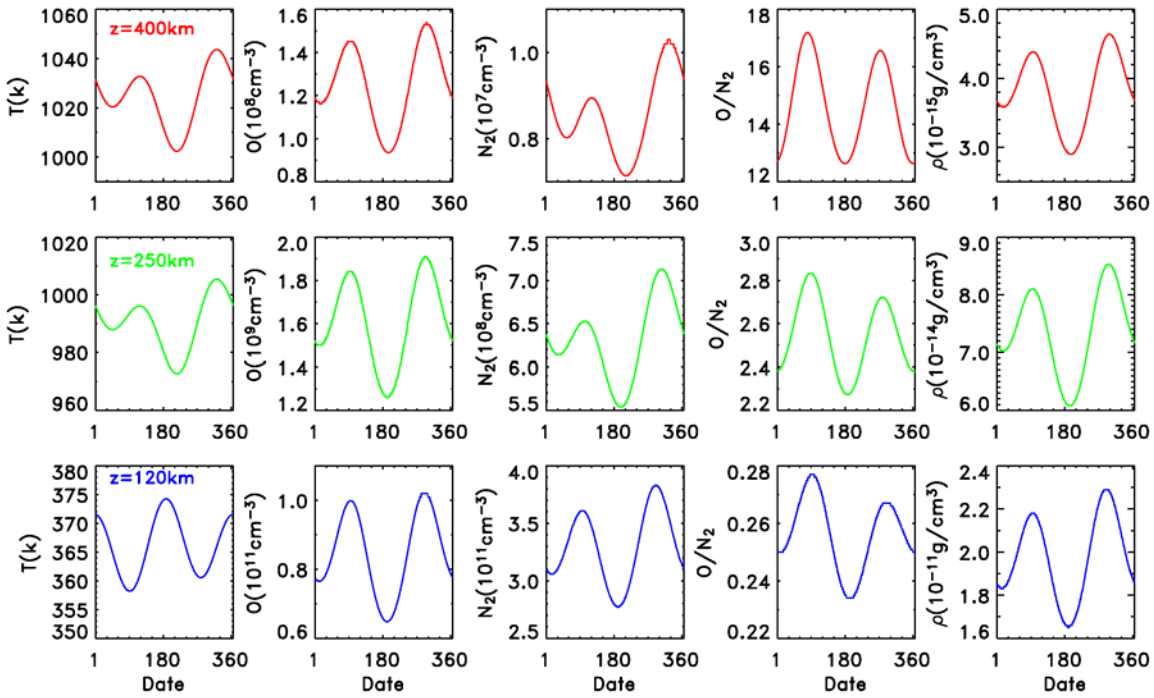

Figure 4.7: Thermospheric annual/semiannual variation from the MSIS00.

4.2.2 Annual/Semiannual Variation with Constant Eddy Diffusion

Fuller-Rowell [1998] found that the thermospheric neutral density exhibits semiannual variation even with a constant lower boundary at the mesopause. It is not straightforward to explain the observed global semiannual density variation in the thermosphere. Geomagnetic activity shows a semiannual variation but is too small to explain the semiannual amplitude. The thermosphere is largely in diffusive equilibrium, without a semiannual forcing at lower boundary, the thermospheric density will not have a semiannual variation through a diffusion process. However, solar irradiance and geomagnetic storms generate large-scale circulation in the thermosphere, together with

variations in the sun-earth distance, evidently yielding global annual/semiannual variations in temperature, composition, and density.

Vertical motions associated with the large-scale circulation drives the thermosphere away from diffusive equilibrium and the atmosphere is more mixed as a result. There are two types of vertical motions, one is caused by thermal expansion and contraction and the other due to horizontal divergence and convergence. Thermal expansion and contraction result in the rise and fall of a fixed pressure surface. In the process of expansion and contraction, different species move at the same speed, and therefore, thermal expansion and contraction does not change density at a fixed pressure surface. Horizontal divergence and convergence can be introduced by a momentum source or heat source and will be accompanied by vertical motion. Such vertical motion moves air parcels relative to a fixed pressure surface and drives the atmosphere away from diffusive equilibrium. In the case of a heat source, local enhanced heating produces divergence and upwelling, air mass flows towards and converges at colder areas accompanied by downwelling. Energy is transported from the heated area to the colder area through adiabatic cooling in the upwelling and adiabatic heating in the downwelling. There is a return flow at lower altitude from the colder area to the heated area. Since density decreases with altitude, by continuity of mass, the return flow is much slower than the flow at the greater altitude. Horizontally, due to the large difference in the speed of the two flows, lighter species that have larger scale height than the mean scale height will be effectively transported from the heated area to the colder area. The opposite is true for heavier species; the heavier species will accumulate in the heated area. Vertically, a heavier species, having smaller scale height than the mean scale height, is more abundant in the lower altitudes. An upward motion will increase its mixing ratio at higher altitude but decrease the mixing ratio of lighter species. The net effect of the horizontal and vertical redistribution of atmospheric constituents is that the atmosphere is less diffusively separated. The thermospheric density will be changed, whether on a fixed pressure surface or at a fixed altitude. On a fixed pressure surface, the density is changed by large-scale circulation involving horizontal divergence and convergence; while at a fixed altitude, the density is influenced by both types of vertical motions. The effects can

be seen through a general circulation model simulation with the TIEGCM. The large-scale circulation is stronger during solstices than equinoxes, which makes the thermosphere more mixed during solstices and more diffusively separated during equinoxes. It drives a semiannual pattern in thermospheric density with density smaller during solstices and larger during equinoxes.

The departure from diffusive equilibrium by large-scale circulation is simulated self-consistently by the TIEGCM. To emphasize annual and semiannual density variation, a one-year TIEGCM simulation was conducted with constant solar forcing to remove solar-rotational variation and constant geomagnetic forcing was used to remove geomagnetic impulsive variations. The constant solar and geomagnetic forcing used are high solar activity and quiet geomagnetic conditions. Eddy diffusion is a constant at the lower boundary of the TIEGCM and it decreases exponentially as pressure interfaces go upward. Therefore, the simulation should highlight annual/semiannual variation in the thermosphere maintained by inter-hemispheric large-scale circulation and variation in the sun-earth distance. The results of the simulation are shown in figure 4.8**.** The left side of the figure is global-averaged density, temperature, and composition at the fixed pressure interface $\ln(P_0/P)=2$ which is approximately around 400 km. The right side of the figure is for the same parameters at a fixed altitude of 400 km.

As mentioned earlier, changes of composition at a fixed pressure level are due to vertical motion by horizontal convergence and divergence. During solstices, the summer hemisphere receives more solar heating than the winter hemisphere. The solar and geomagnetic heating on the summer hemisphere set up large pressure gradients and drive a strong interhemisphere circulation from the summer hemisphere to the winter hemisphere. During equinoxes, the solar heating is evenly distributed on the two hemispheres. The polarward circulation cells driven by solar heating and the equatorward circulation cells driven by geomagnetic forcing compensate for each other. Consequently, the overall circulation is much weaker than the solstice circulation. On a fixed pressure surface, there is depletion of O during solstices compared to equinoxes (figure 4.8, a_1). In contrast, the heavier species N_2 increases during solstice compared to equinoxes (figure

4.8, a_2). A semiannual variation in composition is generated by the interhemisphere large circulation, as shown in O, N_2 density and the O/N_2 ratio (figure 4.8, a_3).

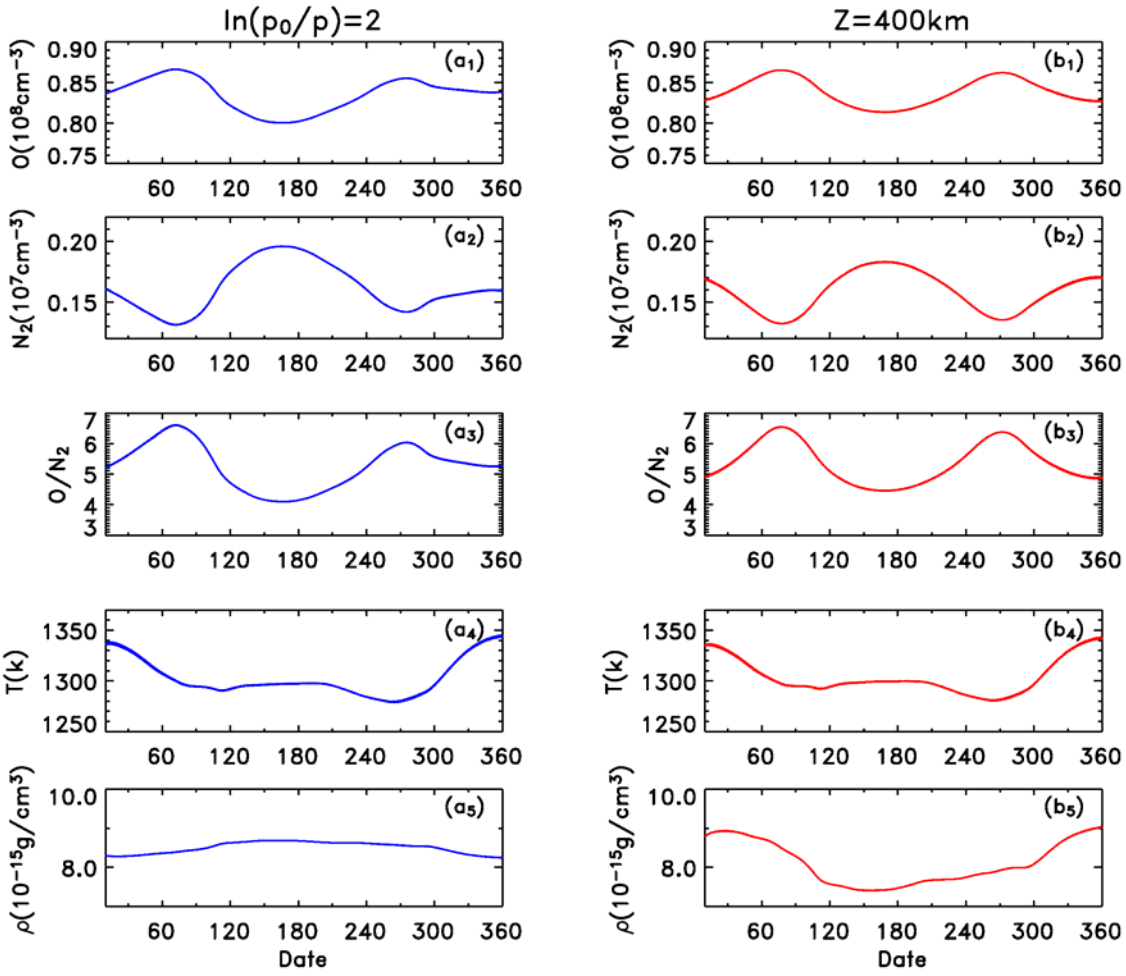

Figure 4.8: "Thermospheric Spoon": the effect of large-scale circulation on the thermospheric temperature, composition, and density.

The sun-earth distance difference between aphelion point (begin of July) and the perihelion point (beginning of January) introduces an insolation change of 7%. A sensitivity test by the global mean upper atmospheric model indicates that the 7% change in insolation generates a 2–5% variability in temperature. An annual temperature variation can be seen in panel a_4 of figure 4.8. A secondary maximum in temperature around the June solstice (figure 4.8, a_4) suggests that there is a semiannual component produced by the interhemispheric large circulation. The global-averaged temperature

increase around solstices is likely due to changes in radiative cooling since adiabatic heating (cooling) and energy transport between the hemispheres only redistribute energy. The large-scale circulation decreases the ratio of O/N_2 at higher altitudes but increases the O/O_2 ratio in the lower thermosphere where the peak density of NO resides. Near the altitude of peak density of NO (110 km), the main production of NO is as follows:

$$N(^2D) + O_2 \rightarrow NO + O \qquad \text{(Eq. 4.2)}$$

And the loss of NO is mainly by the following:

$$NO + N(^4S) \rightarrow N_2 + O \qquad \text{(Eq. 4.3)}$$

The following reaction transfers $N(^2D)$ to $N(^4S)$ and thus regulates NO density.

$$N(^2D) + O \rightarrow N(^4S) + O \qquad \text{(Eq. 4.4)}$$

The concentration of $N(^2D)$ is affected by the reaction of Eq. 4.4. An increase in O/O_2 ratio decreases NO concentration and therefore causes less radiative cooling.

The composition change at the fixed pressure surface introduces a small change in total mass density at the fixed pressure (figure 4.8, a_5). Density variation at the fixed pressure surface will not be addressed further since the annual/semiannual density variation, discovered through analysis of satellite drag data, concerns density variation at fixed altitude.

The right side of figure 4.8 shows global-averaged composition, temperature, and density at 400 km. Compared to the fixed pressure surface, composition and density at fixed altitude is affected by both types of vertical motions, i.e., thermal expansion/contraction and vertical motion by horizontal convergence/divergence. Thermal expansion around January increases both the O and N_2 number density. The thermal expansion effect, added onto the semiannual patterns established by large-scale circulation, serves to lessen the semiannual pattern in O concentration (figure 4.8, b_1) and enhance the semiannual pattern in N_2 concentration (figure 4.8, b_2) and the O/N_2 ratio (figure 4.8, b_3). Since the thermosphere is nearly isothermal at the altitude range addressed, the temperature pattern at the fixed pressure surface and the fixed altitude is

same (figure 4.8, b_4). The temperature variation compensates for the semiannual variation in O/N_2 and yields the variation in density as seen in figure 4.8, b_5. The concerted effects of the sun-earth distance and the large-scale circulation simulated by the TIEGCM is largely an annual variation in density but lacks a semiannual variation (figure 4.8, b_5).

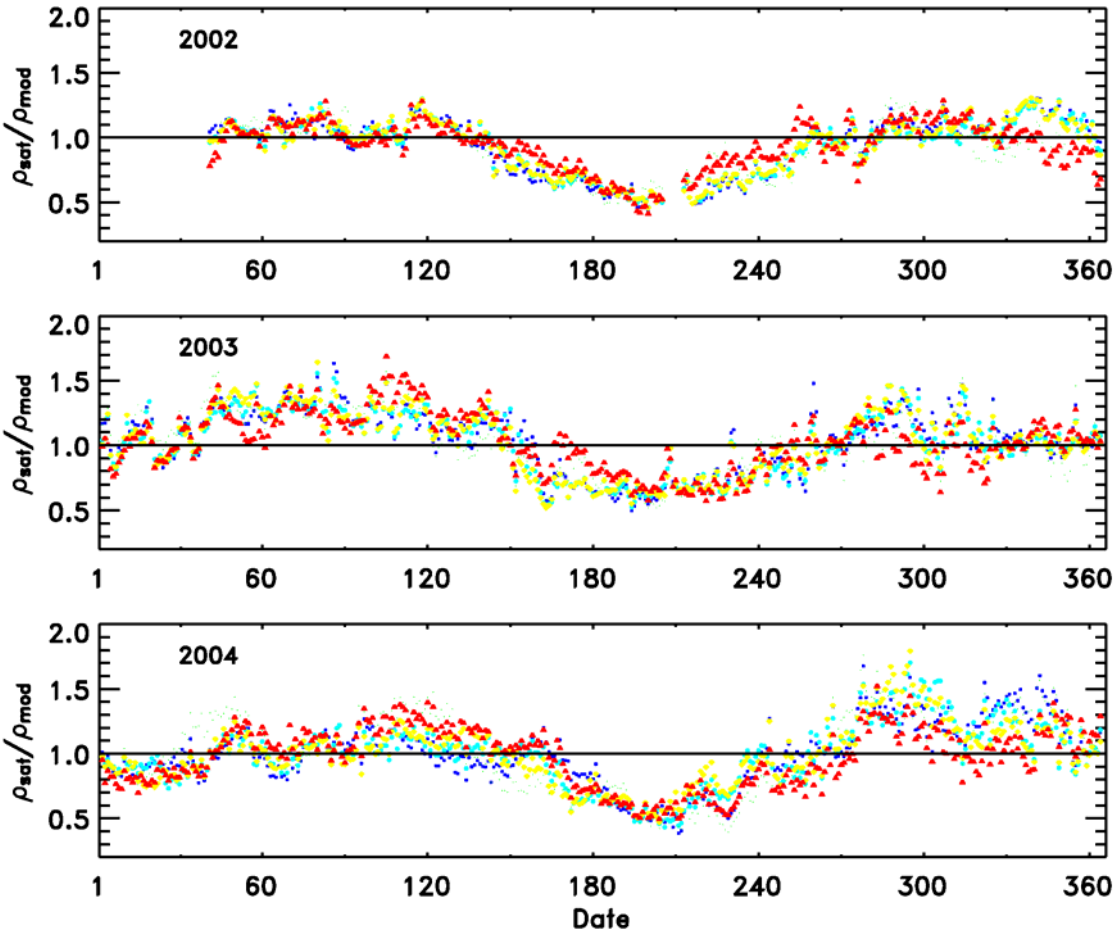

Figure 4.9: Ratios of satellite drag-derived density to the TIEGCM simulated density at satellite perigee locations, for 2002, 2003, and 2004. Each color represents one satellite.

The lack of semiannual variation in mass density can be seen in the comparison of the TIEGCM simulation with satellite drag derived density. The satellite data are from the five satellites introduced in Chapter 3. The TIEGCM simulation was sampled at perigee locations of each satellite and a daily-averaged density was calculated in the same manner as the daily-averaged drag-derived density, i.e., centered at UT 0. The TIEGCM was run for 2002, 2003, and 2004. Ratios of the satellite drag derived density to the

TIEGCM density were calculated for the five satellites and are given in figure 4.9. The ratios reveal a consistent annual/semiannual pattern, i.e., the TIEGCM simulation lacks a semiannual variation in density, as well as some annual amplitude.

Panels (a)-(d) of figure 4.10 are a comparison of global-averaged temperature and composition at 400 km from the TIEGCM and the MSIS00 models for the year 2003. The most persistent difference between the two models is during the northern hemisphere summer; both temperature and O and N_2 concentration of the TIEGCM are higher than the MSIS00. Panel (e) of figure 4.10 compares the modeled density to satellite drag-derived density. Both the MSIS00 and the TIEGCM underestimate density in February and March. During the northern hemisphere summer, the MSIS00 density is in good agreement with measurements but the TIEGCM density overestimates density. In addition, the MSIS00 density is higher than the measurement in October and November. Both the MSIS00 and the TIEGCM do not quite reproduce annual/semiannual density variation seen in the satellite drag data.

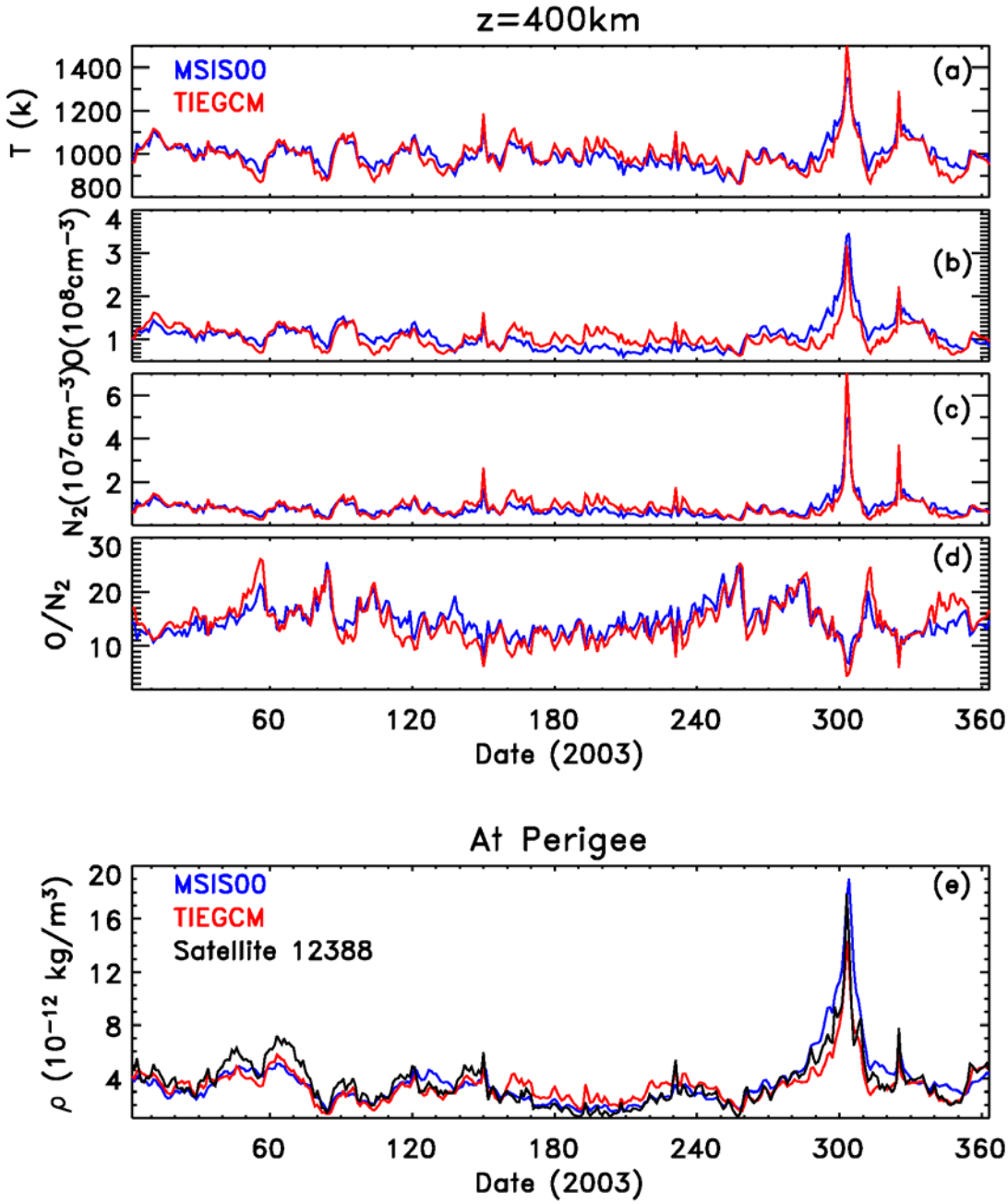

Figure 4.10: (a)-(d): comparison of global mean thermospheric temperature and composition at 400 km for 2003 by the TIEGCM and the MSIS00; (e): comparison of satellite drag-derived density to the TIEGCM and the MSIS00 density at satellite perigee locations for 2003.

4.2.3 Annual/Semiannual Forcing from the Lower Atmosphere

In exploring possible reasons for the deficit in annual/semiannual density variation in the TIEGCM simulation, attention was paid to forcing from the lower atmosphere. The TIEGCM has a lower boundary at the pressure interface $\ln(P_0/P) = -7$, which is about 97 km. This is the region where waves and tides strongly affect atmospheric dynamics and energetics. The TIEGCM includes fluctuation of tides using the GSWM [Hagan and Forbes, 2002, 2003] calculation and climatological annual tides [Fleming, et al., 1990], and it implicitly includes effect of gravity wave breaking using a constant eddy diffusion. However, by using constant eddy diffusion, it does not consider effect of seasonal variation in gravity wave breaking.

Gravity waves breaking in the MLT region have been studied intensively [Hodges, 1969; Hines, 1970; Lindzen, 1971; Garcia and Solomon, 1985; Akmaev, 2001a, 2001b], and it is suggested that gravity wave breaking exhibits strong seasonal variation. Gravity waves are excited in the troposphere by mechanisms such as convection, topography, and fronts. A gravity wave can propagate upward without being filtered by the mean flows, with its amplitude growing exponentially as atmospheric density reduces. It eventually becomes unstable and breaks in the MLT region. The circulation induced by gravity wave momentum deposition causes cold summer mesopause; the summer mesopause at high latitude is about 50 K colder than the winter mesopause at high latitude even though the latter does not receive direct solar irradiance. The mechanism is as follows. In the lower and middle mesosphere, the mean flow is westward in the summer hemisphere and eastward in the winter. As a result, the westward propagating gravity waves in the summer hemisphere and the eastward propagating gravity waves in the winter hemisphere are filtered by the mean flow in the lower and middle mesosphere around 50 km - 80 km. The eastward propagating gravity waves in the summer hemisphere pass through filtering, break in the upper mesosphere, deposit eastward momentum in the region, and cause mean flow to reverse to the east. The opposite is true for the winter hemisphere. Subsequently, the Coriolis force produces a meridional wind from the summer hemisphere to the winter hemisphere. The

meridional flow drives vertical motions in the upper mesosphere and thermosphere. In the mesosphere below the layer of the meridional flow, there will be upwelling in the summer high latitudes and downwelling in the winter high latitudes, and the adiabatic cooling in the summer and adiabatic heating in the winter causes the summer mesopause to be about 50 K colder than the winter mesopause. In the mean time, gravity wave breaking produces small-scale turbulence and gravity wave energy is dissipated into heat through eddy diffusion. Formulas of eddy diffusion coefficients have been derived [Hodges, 1969; Hines, 1970; Kirchhoff and Clemesha, 1983]. Both the gravity wave-induced circulation and eddy diffusion will change dynamics and energetics in the MLT region, and potentially influence density in the upper thermosphere through diffusion and energy budget. At the TIEGCM lower boundary, the gravity wave momentum deposition is not considered and the eddy diffusion coefficient is set to be constant. In the next two sections, the effects of gravity wave-induced circulation and eddy diffusion will be investigated using the TIEGCM.

4.2.3.1 Gravity Wave Induced Circulation

In order to investigate the effect of gravity wave induced circulation on the thermosphere properties, the zonal acceleration calculated by the TIMEGCM gravity wave parameterization was added to the zonal momentum equation at the lower boundary of the TIEGCM. The upper panel of figure 4.11 is output of zonal-averaged zonal wind acceleration in the upper mesopause region for 2003, calculated by the TIMEGCM. It shows that the zonal acceleration by gravity wave drag is eastward in the summer hemisphere and westward in the winter hemisphere. The opposite direction of the wind acceleration in the two hemispheres in solstice seasons contributes towards an inter-hemisphere flow from the summer hemisphere to the winter hemisphere. In equinox seasons, the wind acceleration from gravity waves is much smaller and there is no distinct difference in directions in the two hemispheres. The semiannual zonal wind acceleration pattern is in good agreement with a simulation by Akmaev [2001a], who found that the simulated gravity wave-induced circulation in the MLT region compares

favorably with empirical models and observations. A semiannual variation in vertical motion can be expected when the semiannual wind acceleration pattern is enforced in the lower boundary of the TIEGCM, with the possibility to affect the thermosphere semiannually. The wind acceleration data was fitted using Fourier harmonic fitting including one cycle per year to 4 cycles per year for each latitude. The Fourier fitting is given in the lower panel of figure 4.11. The fitted zonal wind acceleration was then put into the lower boundary of the TIEGCM as a momentum source from gravity waves breaking.

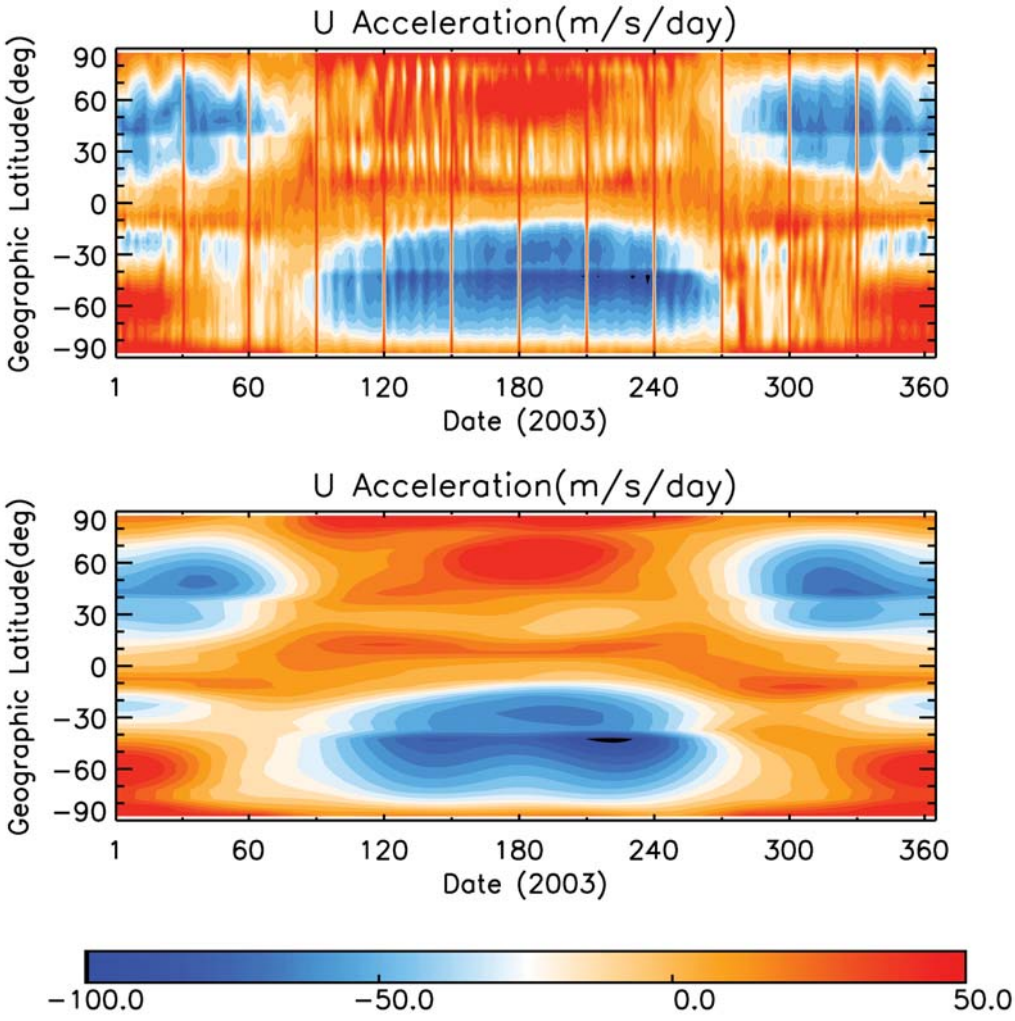

Figure 4.11: Zonal wind acceleration produced by gravity wave breaking in the upper mesosphere region. Top: simulation by the TIMEGCM model; Bottom: Fourier fitting of the simulation.

The TIEGCM simulated percentage difference in global-averaged thermospheric temperature, composition, and density caused by the gravity wave momentum source is shown in figure 4.12. At 120 km, the thermosphere is more mixed by the induced vertical motion during solstice seasons, which decreases the O number density (figure 4.12, a1) and increases the N_2 number density (figure 4.12, b1) during solstice seasons. The semiannual pattern in O number density is preserved with increasing altitude (figure 4.12, a2,a3) but the semiannual pattern in N_2 density gradually vanishes at higher altitude (figure 4.12, b2,b3), suggesting that the lighter species O is more influenced by vertical motion than N_2 and thus less in diffusive equilibrium than N_2. N_2 is more thermally controlled (figure 4.12, d3) and is closest to being in diffusive equilibrium among the atmospheric constituents. This is the reason the diffusive equilibrium empirical models of the MSIS and the Jacchia model derive temperature based on N_2 number density. The O/N_2 ratio has a semiannual variation consistent with the semiannual pattern in O. The semiannual morphology in neutral density is controlled by N_2 density at 120 km and O at 400 km since N_2 is the dominant species at 120 km while O is the dominant gas at 400 km. Although the vertical motion induced by gravity wave drag generates a semiannual density fluctuation in the altitude range of interest, the magnitude is too small to account for the shortage of annual/semiannual amplitude in the TIEGCM simulated total mass density.

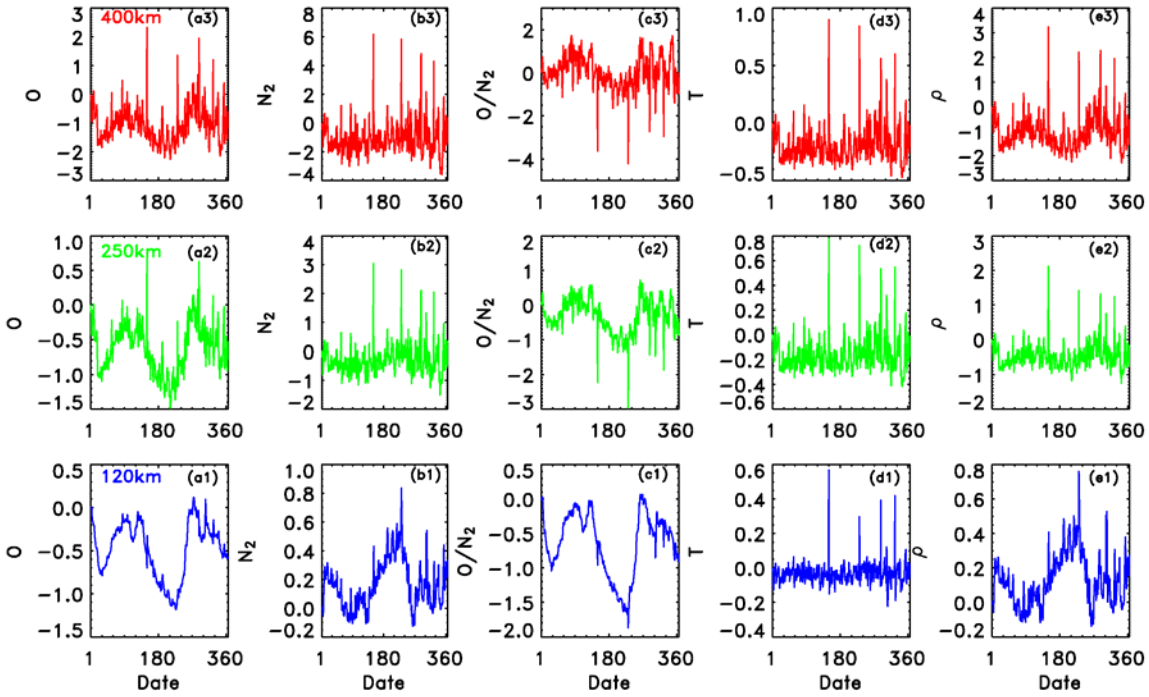

Figure 4.12: TIEGCM simulated percentage difference in thermospheric temperature, composition, and density generated by gravity wave momentum deposition in the mesopause region.

4.2.3.2 Eddy Diffusion

Both ground-based and satellite observations reveal that eddy diffusion in the mesopause region exhibits strong seasonal variation [Kirchhoff and Clemesha, 1983; Fukao, et al., 1994; Lübken, 1997; Khattatov, et al., 1997; Rao, et al., 2001; Sasi and Vijayan, 2001]. Eddy diffusion is larger during solstices than equinoxes with stronger turbulence in summer than in winter. The difference can be as large as one order of magnitude. Modeling efforts on seasonal variation in eddy diffusion [Blum and Schuchardt, 1978; Garcia and Solomon, 1985; Akmaev, 2001b] show good agreement with observations. Gravity wave breaking contributes a large amount to the turbulence in the mesopause region.

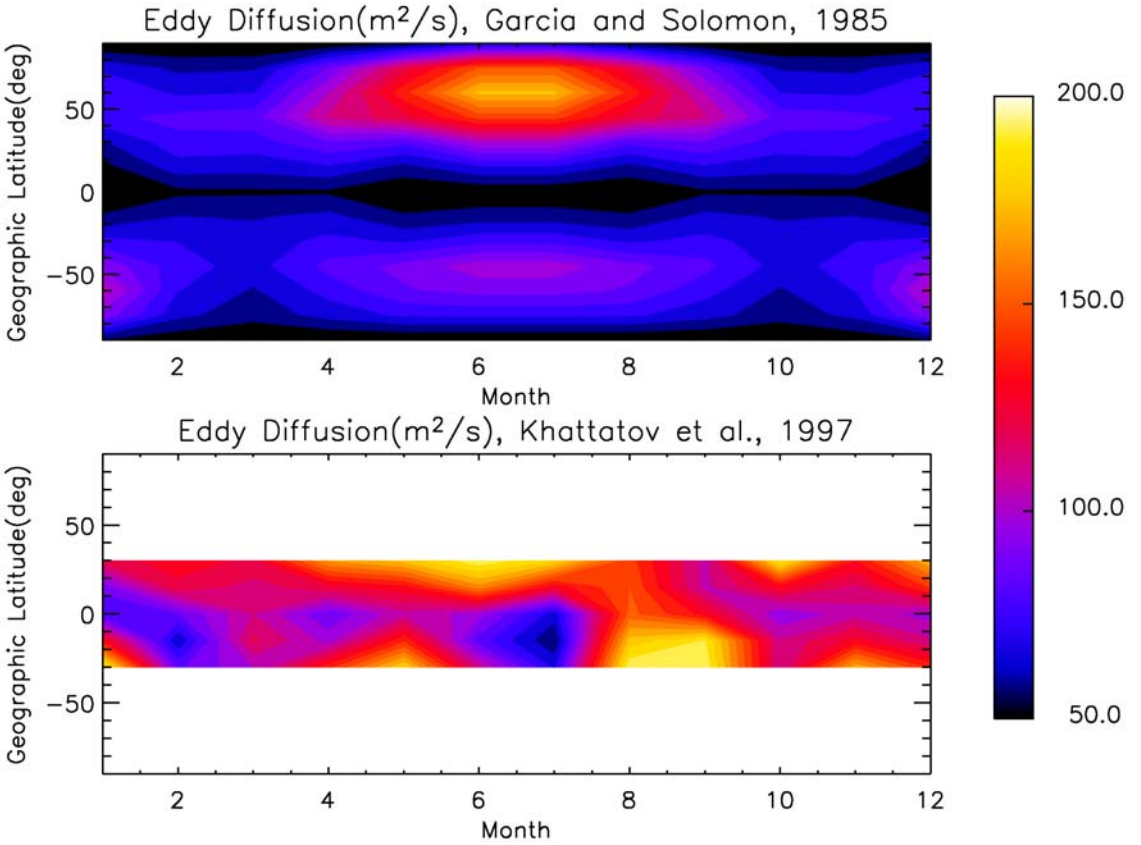

Figure 4.13: Eddy diffusion coefficient averaged in the altitude range from 84 km to 96 km. Top: simulated by Garcia and Solomon [1985]; Bottom: derived from HRDI wind data aboard the UARS satellite by Khattatov et al. [1997].

The upper panel of figure 4.13 is the eddy diffusion coefficient calculated by Garcia and Solomon [1985]. They incorporated a gravity wave parameterization scheme developed by Lindzen [1981] into a two-dimensional MLT dynamics and chemical model [Garcia and Solomon, 1985], to study the effect of breaking gravity waves on the dynamics and chemical composition in the MLT region. The eddy diffusion coefficient shown in the upper panel of figure 4.13 is a vertically-averaged value in the upper mesosphere area from 84 km to 96 km since gravity wave-induced turbulence tends to be confined into a narrower altitude range in the summer while it spreads to a greater altitude range in the winter. It would give a better representation of eddy mixing effect on composition in the MLT region to use turbulence in an altitude range immediately below the lower boundary of the TIEGCM (a pressure interface) than to use turbulence at one

fixed altitude. Except at low latitudes, the eddy diffusion coefficient exhibits a consistent seasonal variation with larger turbulence during solstices than during equinoxes, with larger value in the summer than in the winter, and with larger value during the June solstice than during the December solstice. Garcia and Solomon [1985] attributed the seasonal variation in eddy diffusivity to the seasonal variation of radiative forcing. Zonal winds in the mesosphere altitudes are driven by radiative forcing and mechanical forcing of wave momentum deposition. The difference between zonal wind and breaking wave phase speed is larger during solstices due to stronger radiative forcing. The weaker radiative drive during equinoxes causes zonal wind towards the phase speed of the breaking gravity waves. Eddy diffusivity generated by gravity wave breaking is very sensitive to the difference between the mean zonal flow and the phase speed of breaking gravity waves. As a result, the eddy diffusion coefficient is larger during solstices than during equinoxes. Khattatove et al., [1997] derived the eddy diffusion coefficient using wind data measured by High Resolution Doppler imager (HRDI) aboard the upper atmosphere research satellite (UARS) and compared their results with the result of Garcia and Solomon [1985]. They suggested that the results calculated by the two different methods are complimentary. The Lindzen gravity wave parameterization in Garcia and Solomon [1985] calculation is constrained to obtain wind reversal around 85–100 km and a cold summer mesopause, features that occur mainly at mid to high latitudes. The Khattatov et al. [1997] derivation of the eddy diffusion coefficient is calculated to be consistent with HRDI/UARS observations of the diurnal tides, which is a feature at low latitudes between 30^{o}S and 30^{o}N. The Khattatov et al. [1997] result is given in the lower panel of figure 4.13 for latitudes between 30^{o}S and 30^{o}N. The seasonal variation can also be seen at low latitudes. There is peculiarity in June and July, especially in the southern hemisphere. Khattatov et al. [1997] attributed it to the fact that there were only a few days of HRDI observations for the two months. The eddy diffusion coefficient derived by Khattatov et al. [1997] is generally higher than the Garcia and Solomon [1985] calculation. It seems that the seasonal variation in eddy diffusion coefficient is a global phenomenon.

Bowman [2004a] obtained the *F(Z)* and *G(t)* functions of Eq. 4.1 by fitting satellite drag-derived density. The amplitude *F(Z)* function is presented as a function of $F_{10.7}$ and altitude while the phase function *G(t)* is a Fourier harmonic from one cycle per year to 4 cycles per year regulated by $F_{10.7}$ as well. In Chapter 2, a sensitivity test was conducted to measure thermosphere response to changes in eddy diffusivity. It indicated that a doubling of eddy diffusivity caused a reduction in globally-averaged density by 20% at 400 km. The annual/semiannual density variation characterized by Bowman [2004a], the sensitivity of thermospheric neutral density to eddy diffusion, and the comparison of the TIEGCM simulation to the satellite drag derived density shown in figure 4.9 were used to calculate eddy diffusion variation. Eddy diffusion is represented as a Fourier harmonic function from one cycle per year to four cycles per year as follows.

$$K_E(\omega) = A_1 + A_2 \sin(\omega) + A_3 \cos(\omega) + A_4 \sin(2\omega) + A_5 \cos(2\omega) + A_6 \sin(3\omega) + A_7 \cos(3\omega) + A_8 \sin(4\omega) + A_9 \cos(4\omega) \quad \text{(Eq. 4.5)}$$

where $\omega = 2\pi\theta, \theta = (day - 1)/365$, and A_1-A_9 are coefficients determined by data fitting. The unit of eddy diffusion coefficients used in the TIEGCM is s^{-1}. Table 4.3 gives the *A* coefficients for eddy diffusion coefficients used in the TIEGCM for the year 2002, 2003, and 2004. Eddy diffusion coefficients in units of m^2/s for 2002–2004 are shown in figure 4.14. It exhibits an annual/semiannual variation comparable to those of Garcia and Solomon [1985] and Khattatov et al. [1997].

Table 4.3: Fourier coefficients for eddy diffusion annual/semiannual variation for the years 2002, 2003, and 2004.

	A_1	A_2	A_3	A_4	A_5	A_6	A_7	A_8	A_9
2002	4.18e-6	-1.10e-6	-3.83e-6	1.60e-6	2.18e-6	-3.18e-7	-4.12e-7	8.77e-8	5.40e-8
2003	3.23e-6	-1.20e-6	-2.85e-6	1.22e-6	2.22e-6	-7.78e-7	-5.05e-7	2.20e-7	4.34e-7
2004	3.66e-6	-3.71e-7	-2.73e-6	2.14e-6	2.58e-6	-9.83e-7	-7.97e-7	1.04e-6	3.58e-7

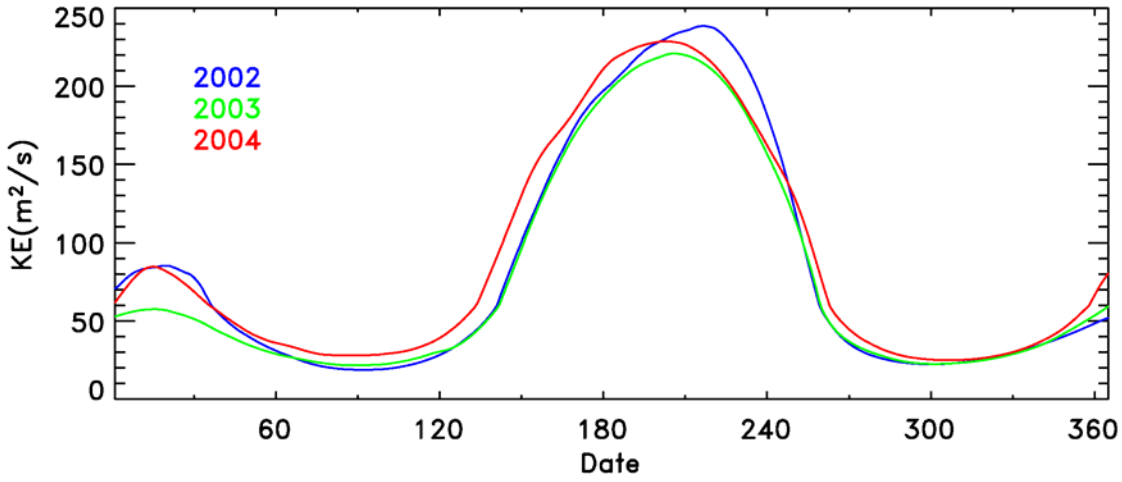

Figure 4.14: Eddy diffusion coefficients in the mesopause region used at the lower boundary of the TIEGCM.

Since the Khattatov et al. [1997] calculation and the Garcia and Solomon [1985] calculation differ in magnitude in eddy diffusion coefficient, and since the purpose of this study is to investigate eddy diffusion as a possible mechanism for annual/semiannual density variation in the thermosphere, the eddy diffusion coefficient shown in figure 4.14 was applied to the TIEGCM lower boundary ($K_E(0)$). The eddy diffusivity then decreased exponentially with increases of the TIEGCM pressure interfaces as follows:

$$K_E(z) = K_E(0) \times e^{(-7-z)} \qquad \text{(Eq. 4.6)}$$

where z represents the TIEGCM pressure interfaces (z=ln(P_0/P). Figure 4.15 is the simulated percentage difference in the globally-averaged thermospheric temperature, composition, and density at altitudes 120 km, 250 km, and 400 km. Eddy diffusion is expected to transport O downward and O_2 and N_2 upward. At 120 km, the large eddy diffusivity in the northern hemisphere summer causes nearly a 40% decrease in O number density (figure 4.15, a1). Since the molecular weight of N_2 is very close to the mean molecular weight at this altitude, eddy diffusion has a much smaller effect on N_2 (figure 4.15, b1). The reduction in O number density at the lower thermosphere propagates upward through molecular diffusion (figure 4.15, a2, a3). The amplitude of N_2 increases with altitude (figure 4.15, b2, b3) due to the fact that N_2 is more thermally controlled and there is increased amplitude in temperature variation at greater altitudes

(figure 4.15, d2, d3). The percentage difference in the ratio of O/N_2 shows an annual/semiannual variation that is consistent with variations in O and N_2 (figure 4.15, c1, c2, c3).

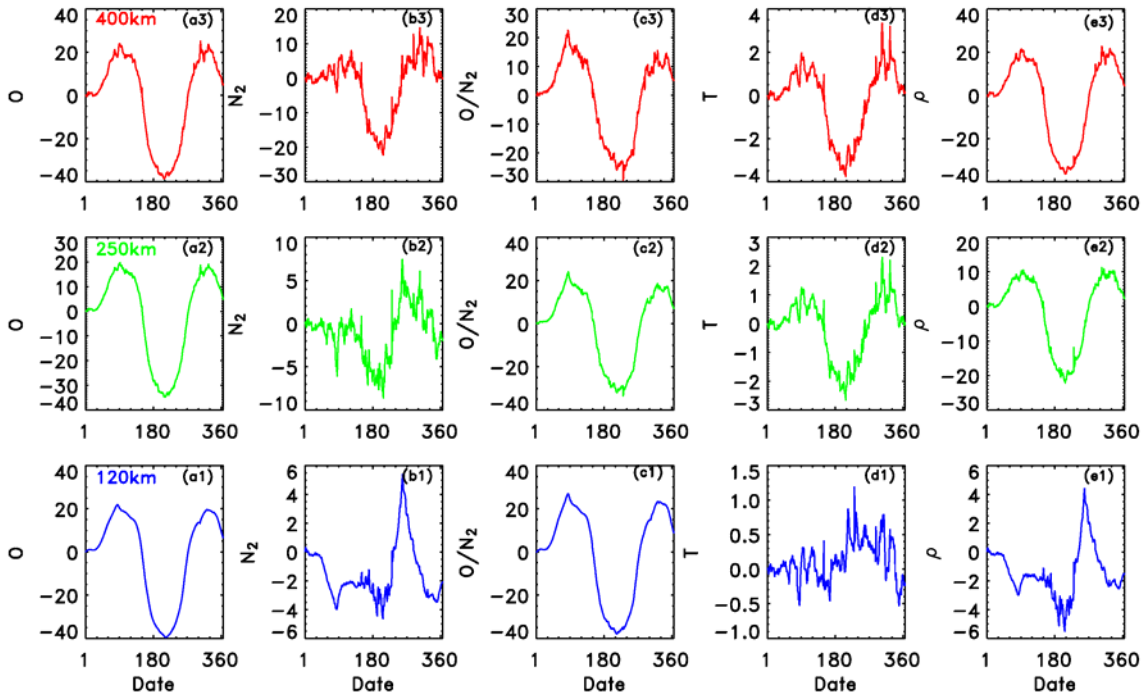

Figure 4.15: TIEGCM simulated percentage difference in thermospheric temperature, composition, and density introduced by an annual/semiannual variation in eddy diffusion at 97 km, for the year 2003.

The percentage difference in temperature is small at 120 km but increases with altitudes (figure 4.15, d1, d2, d3). A close look at energy budget reveals that the decrease in temperature during the northern summer is caused by reduction in solar heating. Solar irradiance ionizes, dissociates, and excites neutral atmosphere and transfers its energy to the kinetic energy of electrons and ions and to the chemical potential energy of ions and neutrals. The neutral atmosphere is then heated through exothermic ion-neutral and neutral-neutral chemical reactions and collisions of neutral composition with electrons and ions. The latter becomes the dominant heating source above 250 km. In the upper thermosphere where O is the dominant species, production of ions is mainly through ionization of O as follows:

$$O + h\nu \rightarrow O^+ + e \qquad \text{(Eq. 4.7)}$$

Loss of ions is through atom-ion interchange as follows:

$$\begin{aligned} O^+ + N_2 &\rightarrow NO^+ + N \\ O^+ + O_2 &\rightarrow O_2{}^+ + O \end{aligned} \qquad \text{(Eq. 4.8)}$$

And subsequent dissociative recombination is as follows:

$$\begin{aligned} O_2{}^+ + e &\rightarrow O + O \\ N_2{}^+ + e &\rightarrow N + N \end{aligned} \qquad \text{(Eq. 4.9)}$$

Since O and N_2 are dominant constituents in the upper thermosphere, the electron/ion density is proportional to O/N_2. A reduction in the O number density (figure 4.15, a2, a3) reduces the amount of photoionization. A reduction in O/N_2 (figure 4.15, c2, c3) reduces electron and ion density. Consequently, solar heating of neutral atmosphere is reduced due to increased eddy diffusivity. Other factors can also decrease temperatures. The increase of NO due to the decreased O/O_2 ratio (Eq. 4.2–Eq. 4.4) causes increased NO infrared cooling. Increased eddy diffusion increases cooling by downward eddy transport of heat. But their contributions are secondary compared to the reduction in solar heating. The main loss of heating, the downward molecular heat conduction, actually reduces. The smaller O and N_2 number density and the lower temperature causes a smaller thermal conductivity coefficient and thus less thermal conduction, which contributes to increase of temperature. The combined effects from solar heating, NO cooling, eddy conduction, and thermal conduction caused by larger eddy diffusivity yield a decrease in temperature.

The combined effect of reduction in O density and thermal contraction causes the amplitude in percentage difference of neutral density increase with altitude (figure 4.15, e1, e2, e3). At 400 km, the density decreases nearly 40% during the northern hemisphere summer and increases about 20% during equinox seasons. The seasonal variation in eddy diffusivity (figure 4.14) imposed at the lower boundary of the TIEGCM produces an annual/semiannual variation in neutral density at the perigee altitudes of the low-earth orbit satellites, with magnitude large enough to compensate for the deficiency of annual/semiannual variation in the TIEGCM simulation seen in figure 4.9.

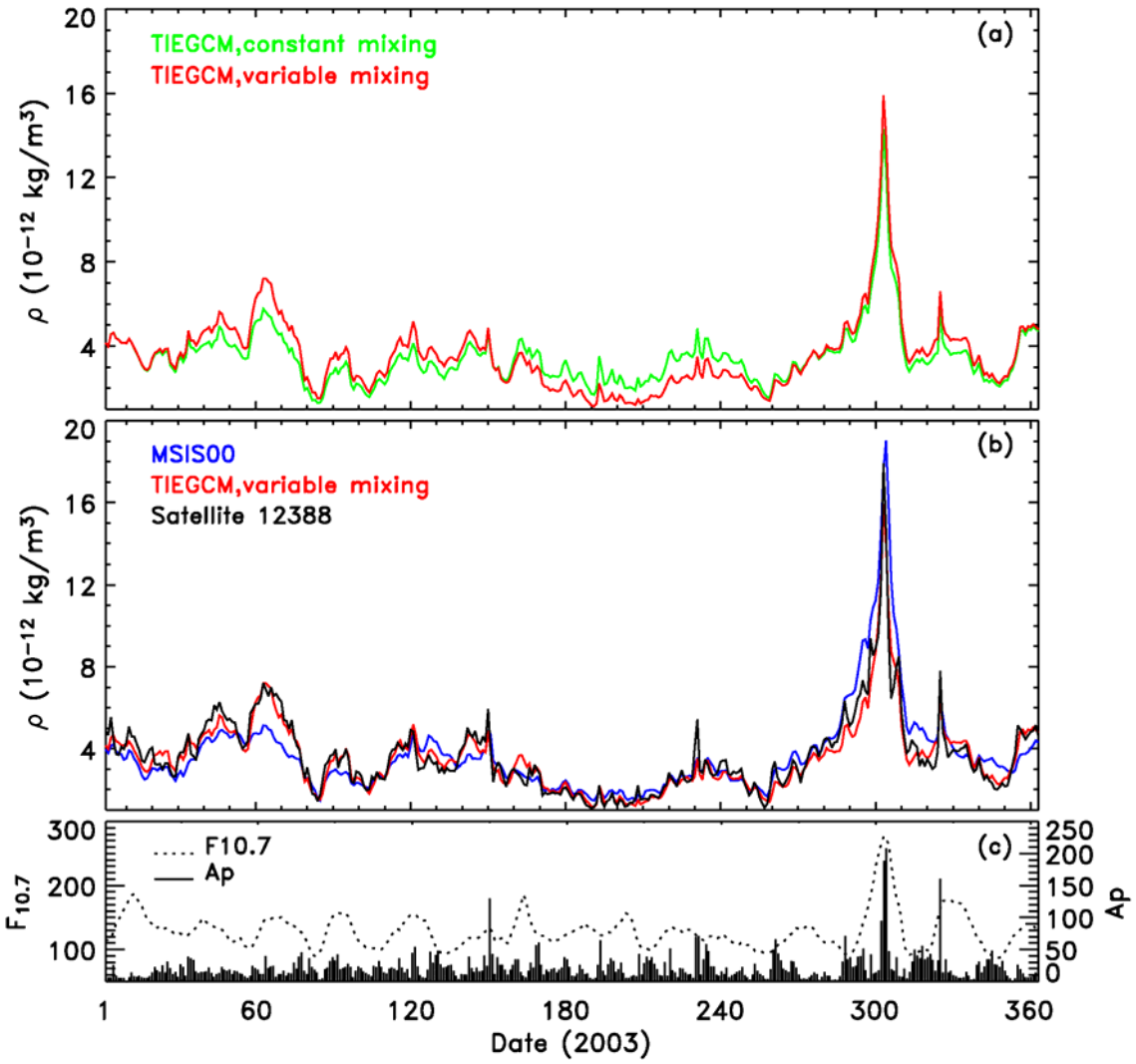

Figure 4.16: Annual/semiannual density effect generated by annual/semiannual variation in eddy diffusivity. (a): comparison of the TIEGCM simulated density with constant eddy mixing and with semiannually varying eddy diffusivity at satellite perigee locations for 2003; (b) comparison of satellite drag derived density to the TIEGCM simulation with variable eddy mixing, and to the MSIS00 density, for 2003; (c) $F_{10.7}$ index and A_p index for 2003.

Panel (a) of figure 4.16 compares the TIEGCM simulation with constant eddy diffusion versus variable eddy diffusion for the year 2003. The density shown is sampled at the perigee location of satellite #12388. An annual/semiannual effect caused by the seasonal variation in turbulence is clearly seen. Panel (b) of figure 4.16 compares the satellite drag measured density, the MSIS00 density, and the TIEGCM density with

variable eddy diffusion. Again, the model density is sampled at the perigee location to be compared with the satellite measurements. While some deficiency in annual/semiannual variation is shown in the MSIS00 density, the TIEGCM simulation agrees well with the measurement. It is also interesting to note how the models represent the effects of solar irradiance and geomagnetic activity. Panel (c) of figure 4.16 gives $F_{10.7}$ index for solar irradiance and the geomagnetic A_p index. Both modeled density and measurements show that thermospheric neutral density follows the general morphology of the $F_{10.7}$ index and thus demonstrates that solar energy is the main forcing that drives thermospheric neutral density. Embedded in this dominant variation is impulsive variation of density that clearly points to the impact of geomagnetic forcing, and both the MSIS00 and the TIEGCM characterize the "Halloween storm" reasonably well.

Figure 4.17 compares the TIEGCM simulation with constant turbulence and variable turbulence for all satellites. The TIEGCM density was sampled at perigee locations for each satellite, the ratio of the measured density to the TIEGCM density was calculated, and the average ratio was then calculated for each year. The results demonstrate consistent improvement in annual/semiannual density variation with consideration of an annual/ semiannual variation in eddy diffusivity.

Thermospheric temperature and composition are strongly controlled by large-scale dynamics [Dickinson and Rishbeth, 1973; Johnson, 1973, 1974; Mayr et al., 1978]. The large-scale circulations transport energy and mass between the summer hemisphere and the winter hemisphere and result in high latitude dependency in temperature and O/N_2 seen in figure 4.4 (Section 4.1.7). Latitudes with high temperature usually associate with lower O/N_2. However, much of the effect on neutral density is canceled in the global mean sense: areas of upwelling compensate for areas of downwelling, neutral density shows weak latitude dependency, and the semiannual density variation is largely a global phenomenon [Paetzold and Zschörner, 1961; Cook, 1970; Mayr and Volland, 1972; Bowman, 2004a]. Nevertheless, the large-scale inter-hemispheric circulation induces a semiannual variation in density [Fuller-Rowell, 1998] due to increased global mixing during solstice seasons, and shown in figure 4.8.

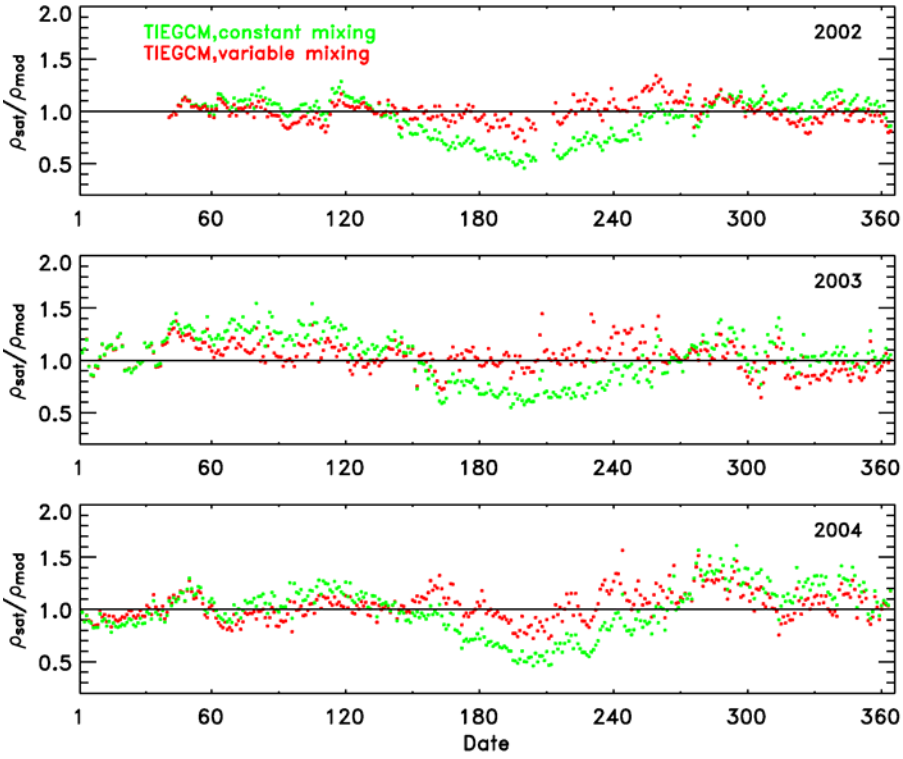

Figure 4.17: Ratios of satellite drag-derived density to the TIEGCM simulated density at satellite perigee locations, for 2002, 2003, and 2004. Green: average ratios of all satellites with the TIEGCM using constant eddy mixing; Red: average ratios of all satellites with the TIEGCM using variable eddy mixing.

However, in the global mean thermosphere the effect of the large-scale circulations is not significant since the large-scale circulations mainly redistribute energy and mass between the two hemispheres. The composition is largely affected by the eddy diffusion property near the turbopause, especially at longer time scales since eddy diffusion has a time scale of 10–15 days near the turbopause. Eddy diffusion can effectively influence the thermosphere globally. The effect of eddy diffusion on composition compounds the effect of eddy diffusion on temperature in influencing the total mass density: increased eddy diffusivity decreases O density, subsequently reduces temperature, and then thermally reduces total mass density.

Furthermore, it seems that the seasonal variation of eddy diffusivity at turbopause is largely a global feature. Fukao et al. [1994] derived a seasonal variation of approximately one order of magnitude with maximum in the summer and minimum in

the equinoctial seasons by radar measurements at 35°N. Kirchhoff and Clemesha [1983] obtained a minimum eddy diffusion coefficient of 45 m^2/s during fall and a maximum of 123 m^2/s during summer based on radar measurements at 23°S. Sasi and Vijayan [2001] analyzed Doppler radar data over a station at 13.5°N and found that eddy diffusion varies from ~ 25–300 m^2/s during September and June, and such seasonal variation is not significantly different at different latitudes. Lübken [1997] investigated turbulent properties in the MLT region using sounding rocket data over 68°N and 69°N and found that the maximum eddy diffusion coefficient in the upper mesosphere is 183 m^2/s in the summer and 100 m^2/s in the winter. Garcia and Solomon [1985] found an eddy diffusion coefficient of ~300 m^2/s in the summer, ~100 m^2/s for the winter, and ~ 50 m^2/s during equinoxes at 61°N in the height range of 80 km to 100 km, and Khattatov et al. [1997] also found that the magnitudes of the eddy diffusion coefficients at middle latitude ranges from 50 up to 300 m^2/s in the region 80–100 km.

While the magnitude of the seasonal variation in eddy diffusivity is not definitely known, the seasonal variation is evident. Variation in eddy diffusion effectively changes thermospheric neutral density due to the sensitivity of thermospheric neutral density to eddy diffusion shown in Chapter 2. This has been demonstrated by consistent good agreement with satellite measurements in the annual/semiannual density variation when the global uniform seasonal variation from about 30 m^2/s to 230 m^2/s was imposed at the lower boundary of the TIEGCM. An annual/semiannual variation in eddy diffusion generated appreciable annual/semiannual density variation in the upper thermosphere, suggesting that an annual/semiannual variation in eddy diffusion is a mechanism for the annual/semiannual density variation in the thermosphere.

4.3 TIEGCM Simulation with Measured Solar Irradiance

In Chapter 3, the TIMED/SEE measurements were compared to the EUVAC solar proxy model for the EUV and to the Woods and Rottman model for the FUV. The comparison showed that the TIMED/SEE measurements are in general agreement with the solar proxy models but there also exist discrepancies in some of the wavelength bins.

There are larger discrepancies at high solar activity for the EUV and at low solar activity for the FUV. In addition, the TIMED/SEE measurements tend to have stronger solar-rotational variation than the solar proxy models. This section investigates the effect of using the TIMED/SEE measurements as solar input for the TIEGCM. In addition, the TIEGCM simulation using the TIMED/SEE measurements, variable eddy diffusion, and the MSIS00 density will be compared to the satellite drag-derived density.

4.3.1 Effect of Using Solar Measurements on Solar-Rotational Variation

The integrated solar irradiance from 2–175 nm obtained by the TIMED/SEE measurements and the proxy model for the TIEGCM (Chapter 2), and the corresponding TIEGCM simulated density at perigee locations of satellite #12388 are shown in figure 4.18 for 2003. The solar-rotational variation is a clear and dominant feature in the integrated solar irradiance. The TIMED/SEE and the proxy model are in phase in the rotational variation but the TIMED/SEE generally has larger solar-rotational amplitude. The density comparison in the lower panel of figure 4.18 indicates that the measured solar spectral irradiance and the proxy model are in good agreement for simulating solar-rotational variation of the neutral density. The larger solar-rotational amplitude of the TIMED/SEE solar irradiance also yields slightly larger solar-rotational amplitude in the thermospheric neutral density.

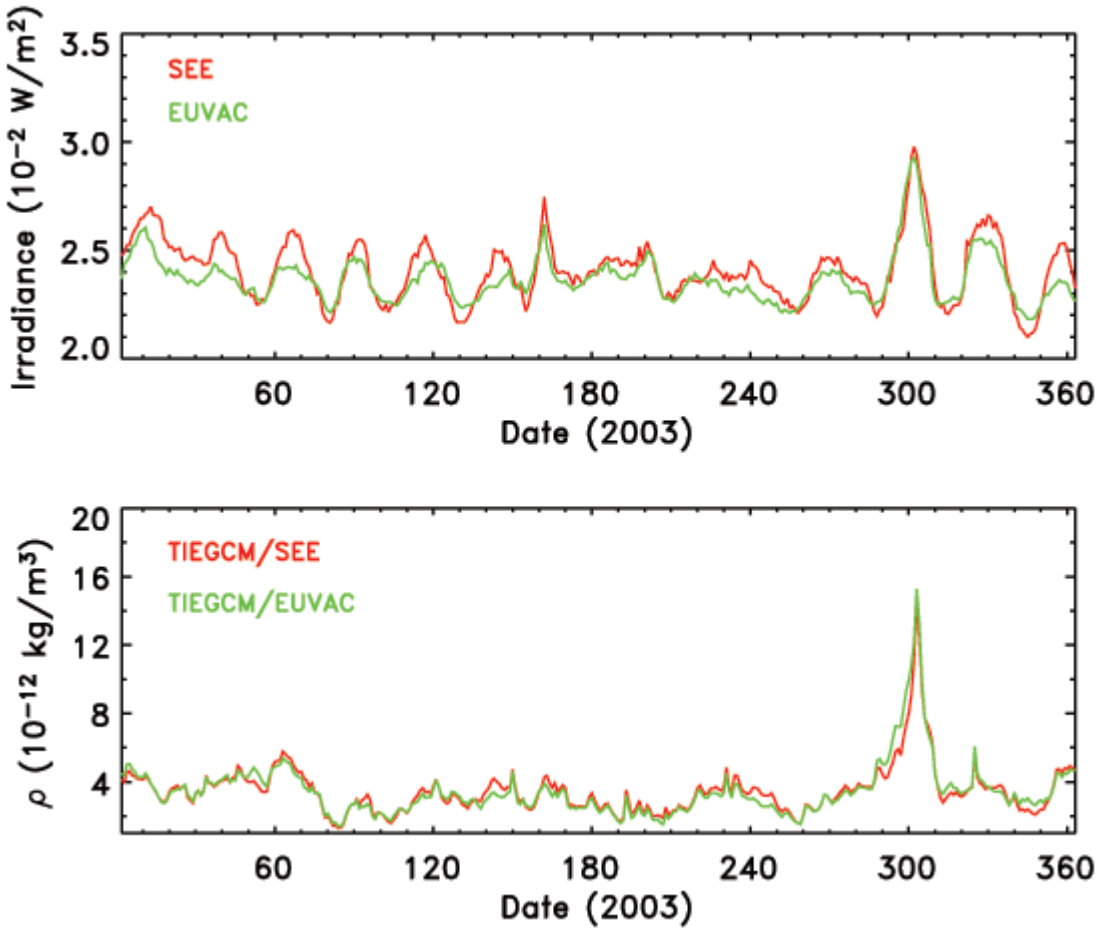

Figure 4.18: (a) Integrated solar irradiance from 2 nm to 175 nm for 2003. Red: the TIMED/SEE measurements. Green: the proxy model. (b) TIEGCM simulation of the thermospheric neutral density for 2003 sampled at satellite #12388 perigee locations. Red: the TIMED/SEE measurements used as solar input. Green: the solar proxy model used as solar input.

4.3.2 Effect of Using Solar Measurements on Solar-Cycle Variation

Marcos et al. [2005] analyzed daily averaged drag data from five satellites from 1970 to 2000 and found that density calculated by thermosphere empirical models, such as the J70 model [Jacchia, 1970, 1971a], showed solar-cycle dependencies. They found that the ratio of satellite drag-derived density to J70 density showed a non-linear

relationship with $F_{10.7}$ (figure 4.19), particularly with a bias at low solar activity. The J70 model systematically overestimated (as much as 25%) density at low solar activity.

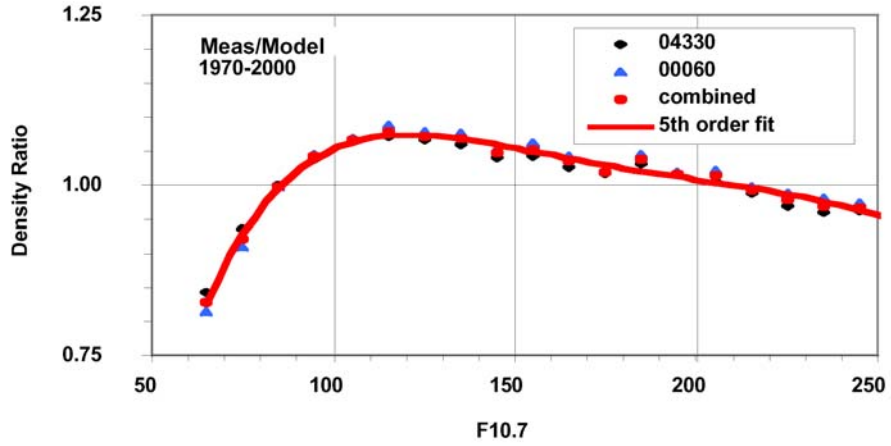

Figure 4.19: The ratio of satellite drag-derived density to the J70 density as a function of $F_{10.7}$. Adapted from Marcos et al. [2005].

The TIEGCM simulation using the TIMED/SEE measurements was investigated to see whether the TIEGCM simulation has the solar-cycle dependency. The ratios of the satellite drag-derived density to the TIEGCM density for all of the five satellites were calculated and binned into $F_{10.7}$ bins with intervals of 10 $F_{10.7}$ units. The ratio of the satellite drag-derived density to the MSIS00 density for the five satellites was also calculated. Figure 4.20 compares the ratios for the TIEGCM and the MSIS00. The MSIS00 density, similar to the J70 density shown in figure 4.19, shows a non-linear dependency with $F_{10.7}$, with overestimation of density at low solar activity. However, the TIEGCM simulated density did not exhibit low solar activity bias.

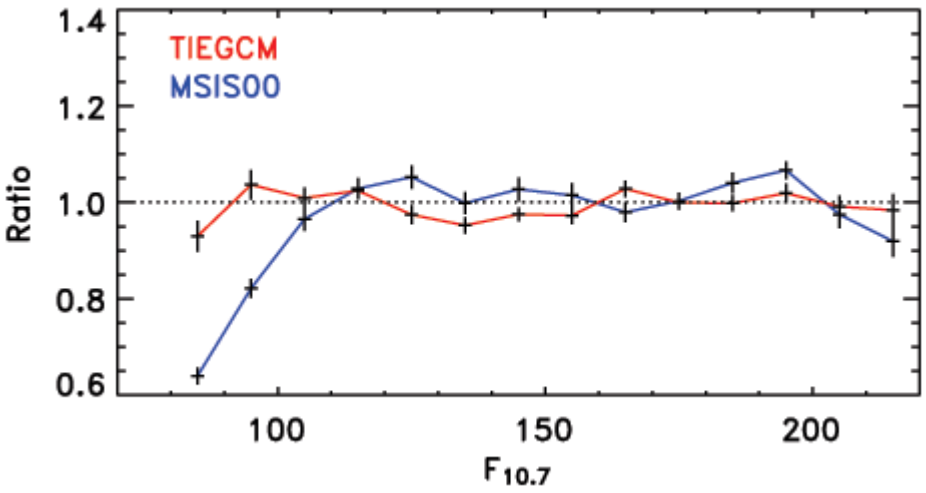

Figure 4.20: Ratio of the satellite drag-derived density to the TIEGCM density, from 2002039 to 2004220, as a function of $F_{10.7}$. The ratios are binned into intervals of 10 $F_{10.7}$ units. The mean of the ratios for each bin is plotted and the standard error is calculated for each bin and plotted as an error bar. Red: the TIEGCM using the TIMED/SEE data as input. Blue: ratio using the MSIS00.

The empirical models, both the J70 and the MSIS model, use $F_{10.7}$ to parameterize the effect of solar variability on neutral density. An updated version of J70, referred to as JB2006 [http://sol.spacenvironment.net/~JB2006/], improved representation of the solar variability effect with additional solar indices [Tobiska et al., 2006]. The JB2006 is able to improve the solar-cycle dependency in neutral density prediction (private communication with Bruce Bowman, Air Force Space Command). The fact that TIEGCM simulation using TIMED/SEE measurements did not have the solar-cycle dependency, together with the improvement of solar-cycle dependency with additional solar indices in JB2006, suggest that the solar-cycle dependency shown in the $F_{10.7}$-based J70 and MSIS00 density have been caused by inadequate representation of solar variability at low solar activity.

Long-term trend of thermospheric neutral density might also contribute to the low solar activity bias. Both model simulations and long-term satellite drag data analysis suggest that thermospheric neutral density has a long-term decreasing trend due to increases of greenhouse gases from anthropogenic activity [Roble and Dickinson,1989; Rishbeth and Roble, 1992; Akmaev and Fomichev, 1998, 2000; Keating et al. 2000;

Emmert et al. 2004a, b; Marcos et al. 2005, Qian et al., 2006]. The trend of climatological decrease depends on solar activity. It maximizes under low solar activity conditions with the rate of decreasing about three times that under solar maximum conditions. The long-term trend of thermospheric neutral density will be examined in Section 4.4. The satellite drag-derived density includes the component of long-term decrease of the density, however, empirical density models, such as J70, are largely formulated using earlier density data that do not reflect a long-term decrease. As a result, the ratio of satellite drag-derived density to density from empirical models is smaller than the ratio if it is calculated with the empirical models including the long-term decrease. Since long-term decrease maximizes under solar minimum conditions, the density ratio should also show a low solar activity minimum. However, the long-term trend should be a negligible contribution. The long-term decrease of density is very small, around a few percent per decade, while the low solar activity bias is ~25%.

4.3.3 Comparison of the TIEGCM and the MSIS to Drag Measurements

The previous two sections described the effect of using the TIMED/SEE measured solar irradiance as solar input for the TIEGCM model, on solar-rotational and solar-cycle variations of thermospheric neutral density. In this section, the TIEGCM simulation and the MSIS00 empirical model calculations will be compared to the satellite drag-derived density. Both the TIEGCM density and the MSIS00 density were sampled at perigee locations of satellites. The satellite perigee parameters for each satellite were shown in Chapter 3. The TIEGCM model run was conducted with the TIMED/SEE solar measurements as solar input and variable eddy diffusion at the lower boundary (Section 4.2).

Figure 4.21 compares drag-derived density, the MSIS00 density, and the TIEGCM density for two solar-rotational periods and a geomagnetic storm period for 2003. The satellite density shown in the figure is from satellite #12388. The figures on the left show solar-rotational variation of thermospheric neutral density from 2003050 to 2003110 and the corresponding $F_{10.7}$ index and A_p index. The TIEGCM simulated density had a solar-

rotational variation in very good agreement with the satellite drag-derived density for both of the solar-rotational periods. The MSIS00 showed a weaker solar-rotational variation. The figures on the right represent density response to geomagnetic forcing from 2003290 to 2003350. Both the TIEGCM and the MSIS00 density exhibited impulsive variation responding to geomagnetic storm activities.

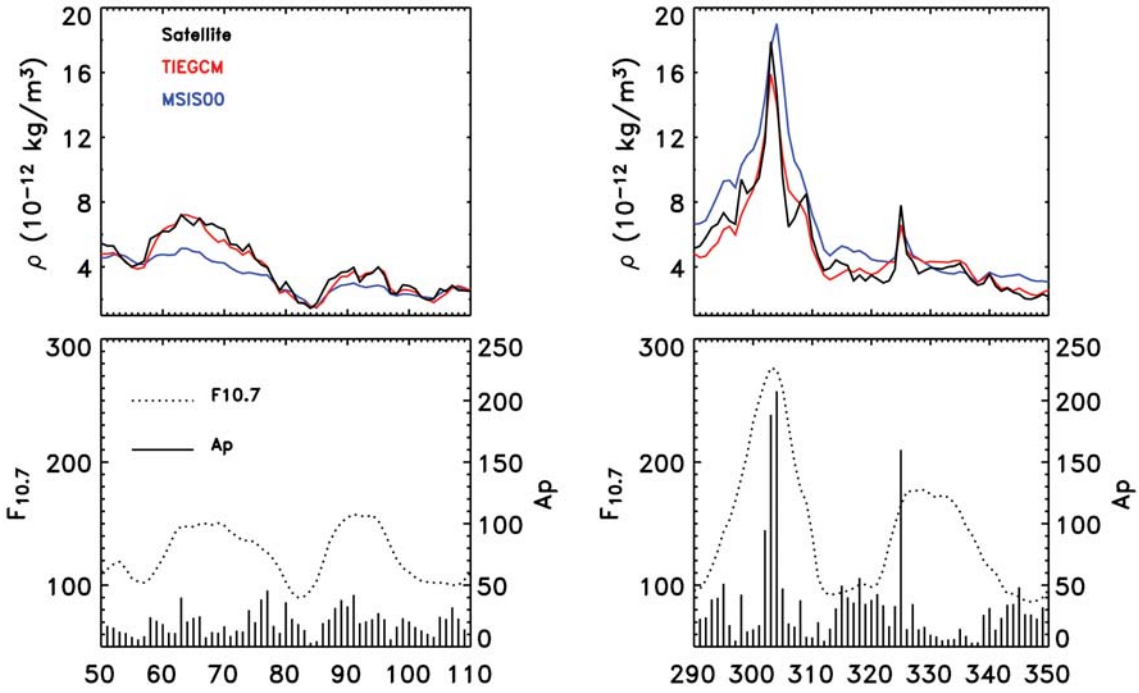

Figure 4.21: Comparison of the TIEGCM and the MSIS00 to the satellite drag measurements for solar-rotational variation and geomagnetic storm responses. Left: two solar-rotational periods from 2003050 to 2003110; Right: a geomagnetic storm period from 2003290 to 2003350 that includes the 2003 November "Halloween" storm.

Figure 4.22 compares the modeled density to the satellite density for the entire year of 2003 for all five satellites. The TIEGCM density is in good agreement with satellite drag-derived density for all five satellites. This shows that the TIEGCM can simulate solar-rotational variation of thermospheric neutral density very well, with appreciable improvement upon the MSIS00, for example, during the period from day 40 to day 90. The comparison during October and November is noteworthy because there were a series of geomagnetic storms during this period. The storm effect is better simulated in the

TIEGCM than that in the MSIS00. This suggests that numerical models can improve upon empirical models in simulating geomagnetic storm effects. It is probably because the TIEGCM captures geomagnetic storm effects by physically solving the upper atmosphere while empirical models represent storm effect statistically based on observations. The ratios of the modeled density to the satellite density were calculated and given in Figure 4.23 for each satellite corresponding to figure 4.22.

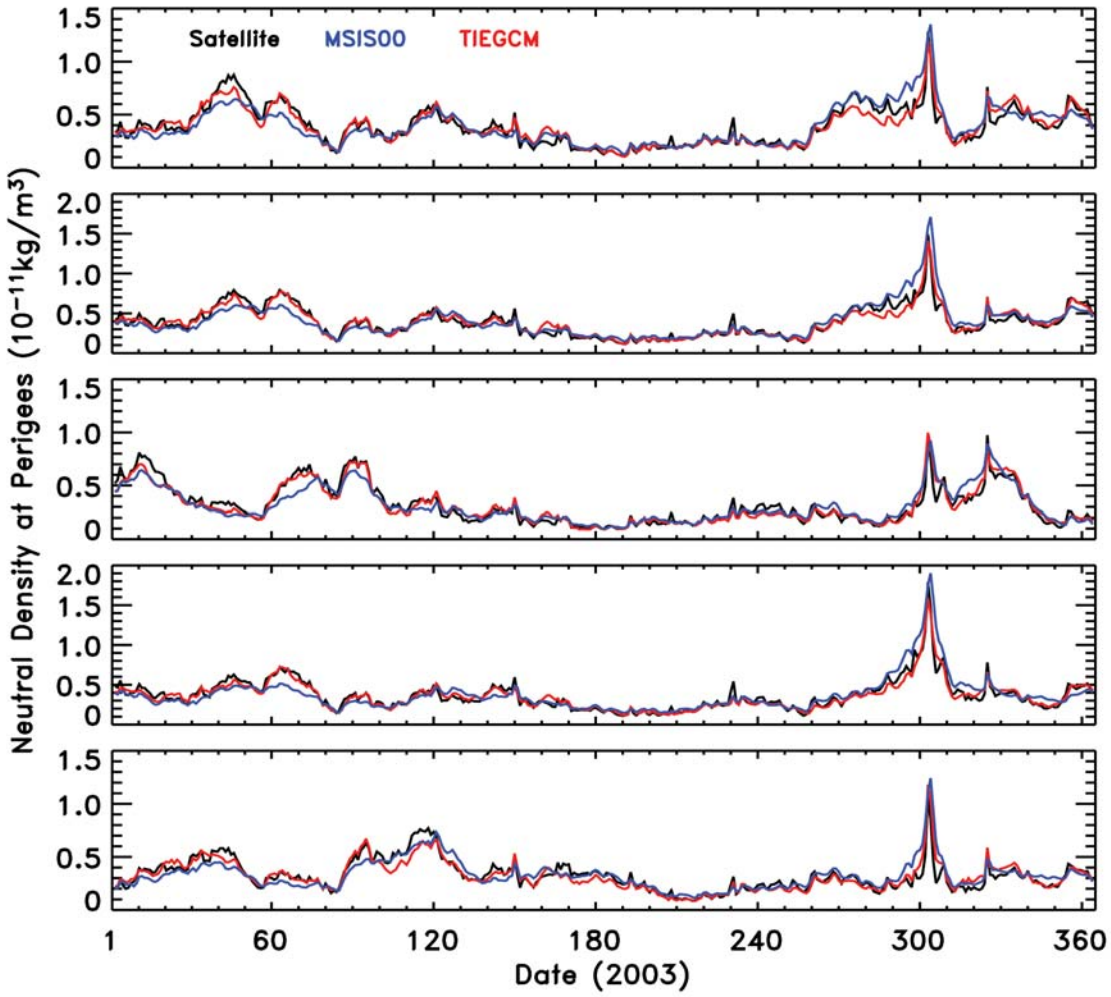

Figure 4.22: Daily averaged thermospheric neutral density of 2003 at perigee locations of the five satellites. Black: satellite drag-derived density; Red: density calculated by the TIEGCM using the TIMED/SEE data as solar input, with a semiannual eddy diffusivity variation imposed at the model lower boundary; Blue: density calculated by the MSIS00.

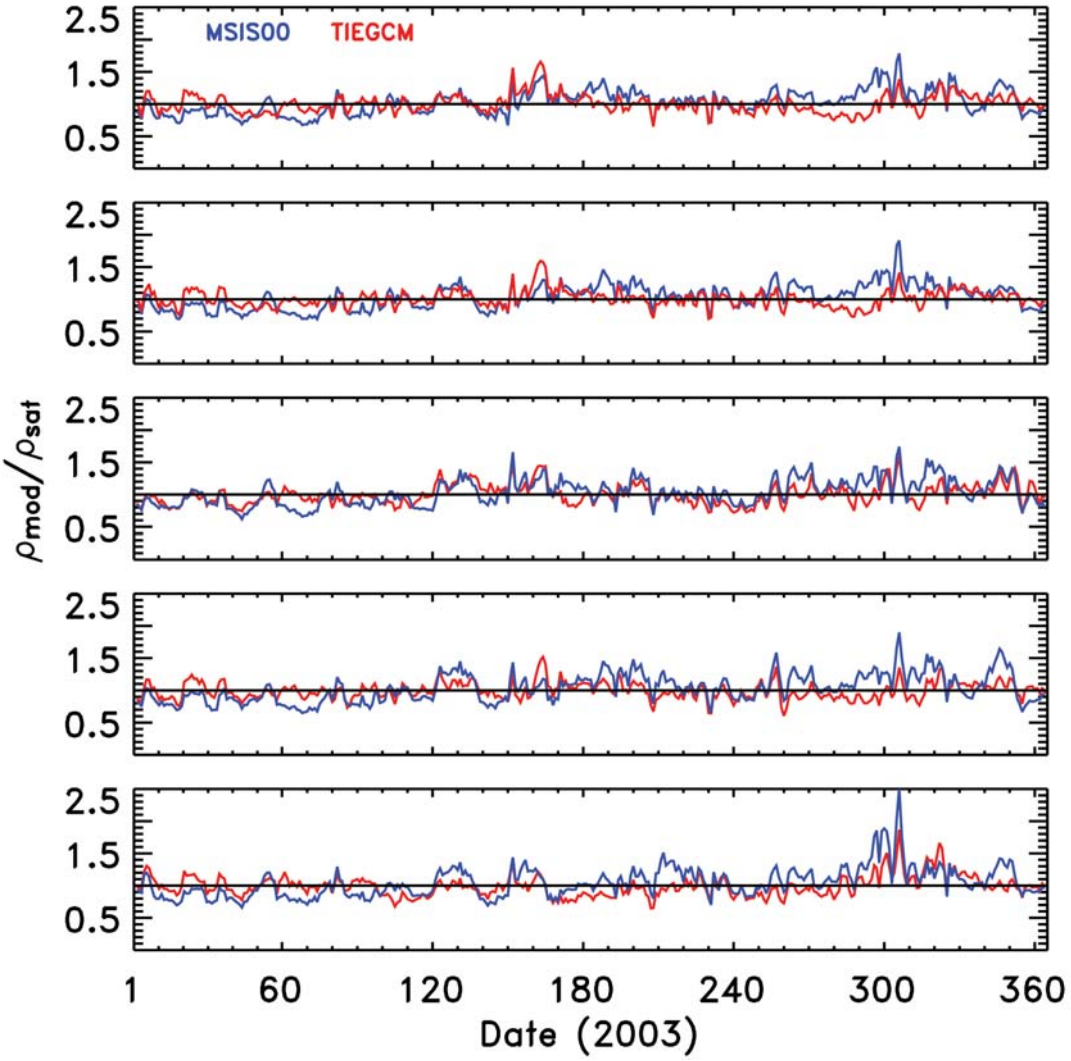

Figure 4.23: The ratios of the modeled density to the satellite drag-derived density for 2003 for all five satellites. Red: the ratios for the TIEGCM; Blue: the ratios for the MSIS00.

The average ratio of all five satellites was calculated and shown in figure 4.24 for the TIEGCM, in red, and for the MSIS00, in blue. The mean value of the ratios shown in figure 4.24 and the standard deviations are shown in table 4.4

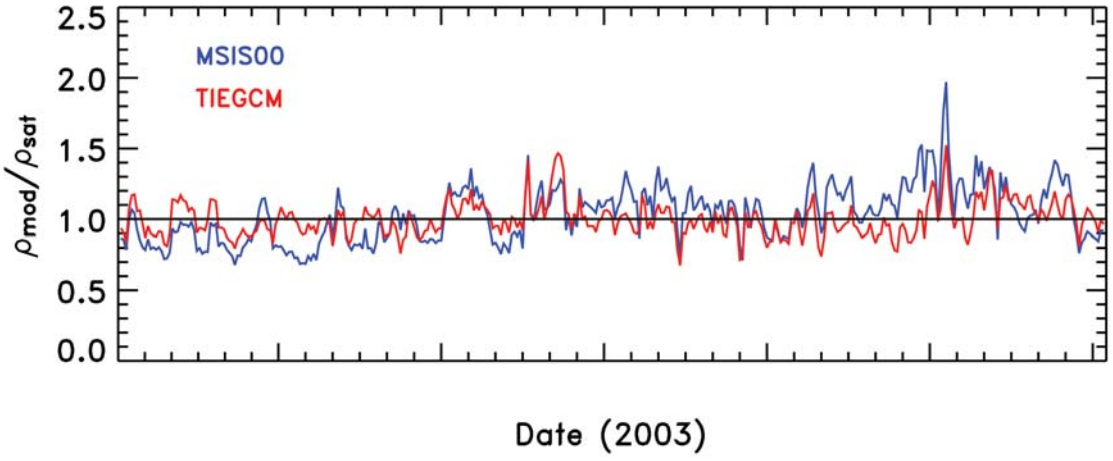

Figure 4.24: The average ratios of all five satellites for the TIEGCM and the MSIS00 for 2003. Red: the TIEGCM ratio; Blue: the MSIS00 ratio.

Table 4.4: The mean and standard deviations of the average ratios of the satellite drag-derived density to the model density for all five satellites for 2002-2004.

	MSIS00	TIEGCM
Mean	1.03	0.99
Standard Deviation	0.20	0.14

4.4 Long-Term Trend of Thermospheric Neutral Density

The global average temperature at the Earth's surface has increased by about 0.55^{o}C since 1970s to the present attributed to increase of greenhouse gas concentrations [IPCC, 2007]. However, the effect of increase of greenhouse gas concentrations in the upper atmosphere is opposite to its effect in the lower atmosphere; it causes global cooling. Greenhouse gases such as CO_2 both radiate and absorb infrared radiation. In the

troposphere where the atmosphere is dense, CO_2 absorbs infrared radiation and transfers the energy to kinetic energy by frequent collisions with neutral constituents before it gets the chance to radiate. Thus, it heats the atmosphere and serves as a greenhouse effect. In the stratosphere, radiative forcing of O_3 dominates that of CO_2. As the atmosphere becomes less and less dense with increasing altitudes, CO_2 radiates infrared radiation and thus cools the atmosphere in the mesosphere and the thermosphere. Roble and Dickinson [1989] initiated study of the impact of greenhouse gases on long-term changes in the thermosphere and ionosphere using a global mean upper-atmosphere model. They concluded that global changes will occur in the upper atmosphere as well as in the lower atmosphere, and they found that a doubling of CO_2 and CH_4 concentrations will cause a ~50 K decrease of thermospheric temperature and a ~40% decrease of atomic oxygen near 300 km under solar minimum conditions. Since then, theoretical models have been used to investigate global change in the upper atmosphere [Rishbeth and Roble, 1992; Akmaev and Fomichev, 1998, 2000; Akmaev, 2002; Akmaev et al., 2006; Gruzdev and Brasseur, 2005]. These model studies have generally supported Roble and Dickinson's original findings. The long-term trends in the closely-coupled ionosphere have been more controversial. There has been suggestion and evidence [Rishbeth, 1990; Bremer, 1998; Laštovička and Bremer, 2004; Laštovička et al., 2006a] indicating that changes in the ionosphere accompany the neutral atmosphere changes, including a slight decrease in the E-layer altitude and small increases in the maximum electron density of the E-layer and the F1-layer. Analysis of global ground-based ionosonde data has revealed complex trends of peak electron density and peak electron density altitude for the F2-layer [Bremer, 1998; Mikhailov and Marin, 2000; Mikhailov and Marin, 2001; Danilov, 2003; Laštovička, 2005; Laštovička et al., 2006b]. Recently, satellite orbital decay data have been analyzed to estimate the long-term trend of thermospheric neutral density. Keating et al. [2000] evaluated the long-term orbital decay of five satellites during solar minimum years and found a 4.9±1.3% per decade decline of density near 350 km over 20 years. Emmert et al. [2004a, b] derived long-term changes in upper thermosphere density using 27 near-earth orbiting objects for all levels of solar activity during the period 1966–2001. Their results indicated that the long-term decline ranged from 2–5% per decade in the

upper thermosphere from 200 km to 700 km, with the trend increasing with altitude and largely independent of geomagnetic activity, local time, latitude, and season. Marcos et al. [2005] analyzed several satellite measurements over the period 1970–2000 and detected an average long-term density decrease of 1.7% per decade near 400 km. Lean et al. [2006] calculated density between 200 km and 475 km using orbital data for the three Starshine satellites from 1999–2003, and found an average density ~4% lower than calculated by the NRLMSISE-00 model [Picone et al., 2002], which is based partially on data collected in the 1970s and 1980s. This indicates a mean density decrease of around 2% per decade. These experimental results are reasonably consistent, considering the wide range of altitudes and solar activity levels sampled. Although the Keating et al. [2000] results appear to be a considerably larger change than the Marcos et al. [2005] finding, the fact that Keating et al. [2000] used data from solar minimum years may explain some of the discrepancy, as discussed below.

Previous model studies have been limited to sensitivity studies of density change using a fixed greenhouse gas concentration. In this study, CO_2 concentration measurements at Mauna Loa Observatory and solar EUV variation over the last three decades were used in the global mean version of the TIMEGCM to quantify the long-term trend of upper thermospheric neutral density. To quantify the impact of solar activity on the density trend, the trend over the past 30 years assuming solar minimum and solar maximum conditions was also calculated. The three trends were then compared to density trends derived from satellite drag measurements. In light of a recent prediction of the strength of solar cycle 24 [Dikpati et al., 2006], a long-term climatological forecast of thermospheric density was developed for solar cycle 24.

The CO_2 concentration data used in this study are measurements from Mauna Loa Observatory [Keeling and Whorf, 2005]. Figure 4.25 shows CO_2 concentration from 1965–2005. CO_2 concentration has increased consistently from around 320 ppmv in 1965 to around 380 ppmv by the end of 2005. At this location, CO_2 concentration also has a seasonal variation with a fluctuation around 6 ppmv. This mixing ratio is applied to the model as a lower boundary condition at 30 km altitude.

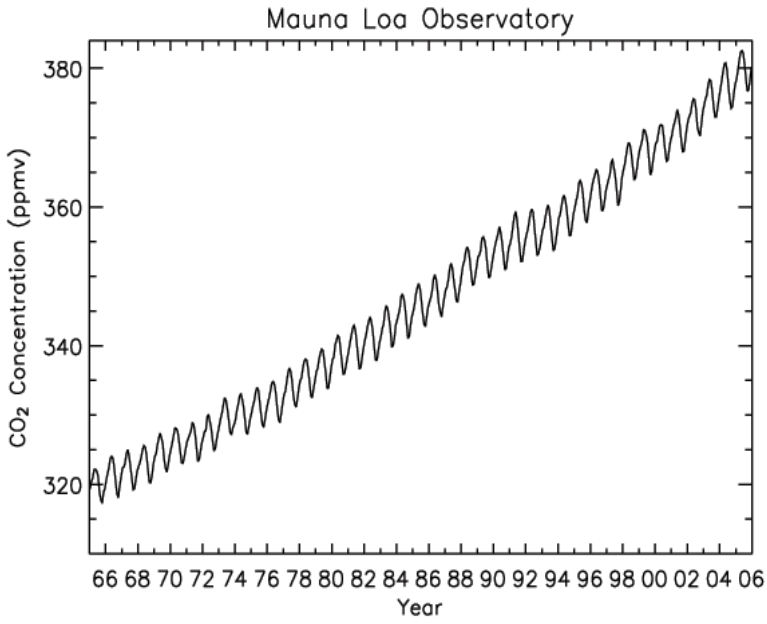

Figure 4.25: CO_2 concentration from 1965–2003 measured at Mauna Loa Observatory.

4.4.1 Global Change over the Recent Three Decades

The time period of long-term trends derived from published satellite drag measurements ranges from 1970–2000. Figure 4.26 shows the global mean thermospheric temperature, density, and density trends at 400 km for a model run covering this period. The $F_{10.7}$ and its 81-day average for this period are also shown.

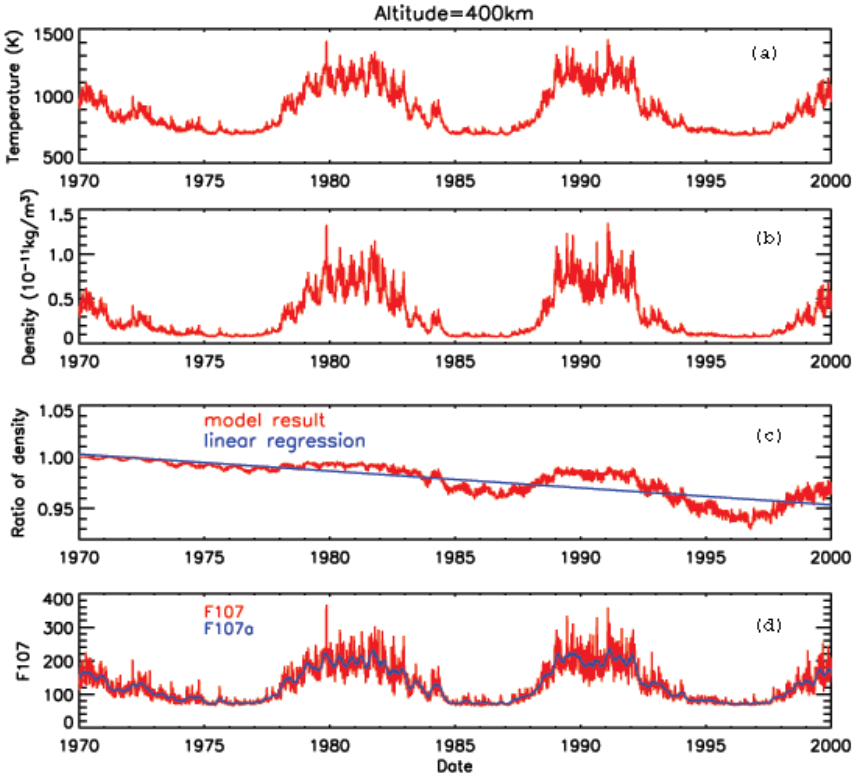

Figure 4.26: (a) Global mean temperature at 400 km. (b) Global mean neutral density at 400 km. (c) Red: ratio of thermospheric neutral density from two model runs. First run: density calculated with varying CO_2 and solar EUV variation from 1970–2000; Second run: density calculated with CO_2 fixed at 1970 levels and with solar EUV variation from 1970–2000. The ratio of the two model runs is calculated to remove the influence of solar activity on density variation. Blue: linear regression to the ratio curve. The linear regression shows the average density decrease for the recent three decades is 1.7% per decade. (d) Red: $F_{10.7}$ index; Blue: 81-day average $F_{10.7}$ index.

To remove the solar activity influence on density variation, a second model run was conducted with constant CO_2 concentration applied at the lower boundary, fixed at 1970 levels. The ratio of density from the first run to the second run was then calculated and is shown in figure 4.26, (c). A linear regression gives an average decline of 1.7% per decade. Marcos et al. [2005] found that the average decline of density near 400 km during 1970–2000 was 1.7% per decade, in very good agreement with our calculation,

and roughly consistent with the Starshine results [Lean et al., 2006]. Emmert et al. [2004a, b] derived a slightly larger average decline of density near 400 km from 1966–2001 of ~3% per decade.

Emmert et al. [2004a, b] found that the density trend increases with altitude. Figure 4.27 shows altitude profiles of temperature and density trends for the three decades from 1970–2000. Both temperature and density trends increase with height. The temperature reduction from 1970–2000 is around 1.3 K at 150 km and increases to about 5.3 K at 400 km. The average density trend for the three decades is in the range of 1.2% per decade to 1.7 % per decade from 150 km to 400 km. This is comparable to the results of Emmert et al. [2004a, b], which show changes of from 2% to 5% per decade in the upper thermosphere from 200 km to 700 km.

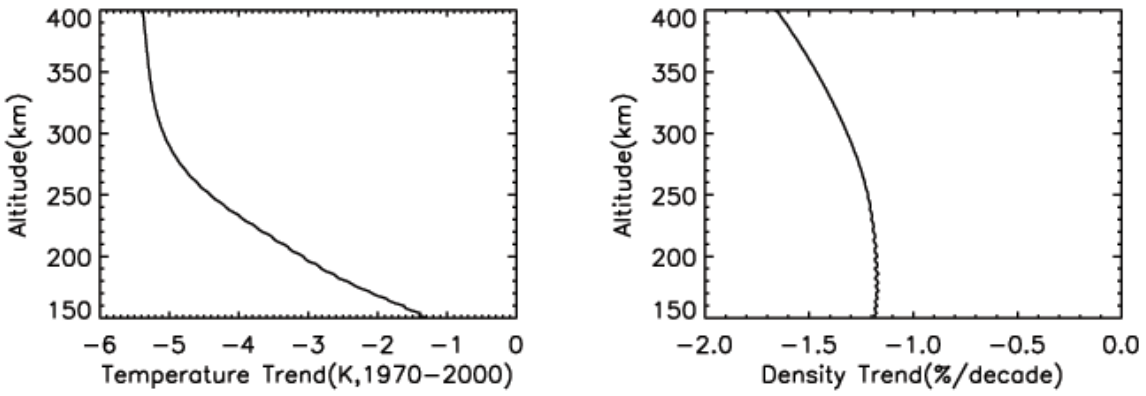

Figure 4.27: The height profiles of temperature and density trends in the thermosphere for the period from 1970–2000 simulated by the global mean model.

4.4.2 Global Change under Solar Minimum and Maximum Conditions

Model studies [Roble and Solomon, 2005] and satellite measurements [Emmert et al., 2004a, b; Marcos et al., 2005] suggest that the density trend in the upper thermosphere depends on solar activity and is smaller for solar maximum conditions and

larger for solar minimum conditions. One important mechanism of this dependency is that CO_2 cooling is dominant during solar minimum, while NO cooling becomes more important during maximum due to its increased density. Since the long-term decline of density in the upper thermosphere is mainly caused by increases in CO_2, the change should be larger during solar minimum conditions.

To quantify this, the model was run with the historical CO_2 measured concentrations at the lower boundary but under "perpetual" solar minimum and solar maximum conditions. The $F_{10.7}$ proxy index was set to 70 for the solar minimum run and to 210 for the solar maximum simulation. These calculations show that (figure 4.28) under solar minimum conditions the average density decrease was 2.2% per decade at 350 km and 2.9% per decade at 450 km from 1970–2000. Under solar maximum conditions, the average density decreases were only 0.7% per decade at 350 km and 0.8% per decade at 450 km. The density trend increases with height for both solar minimum and solar maximum conditions, and that increase is more apparent during solar minimum due to the lower scale heights. These results compare favorably with the density estimates derived from satellite drag measurements, since the larger changes found by Keating et al. [2000] used solar minimum data.

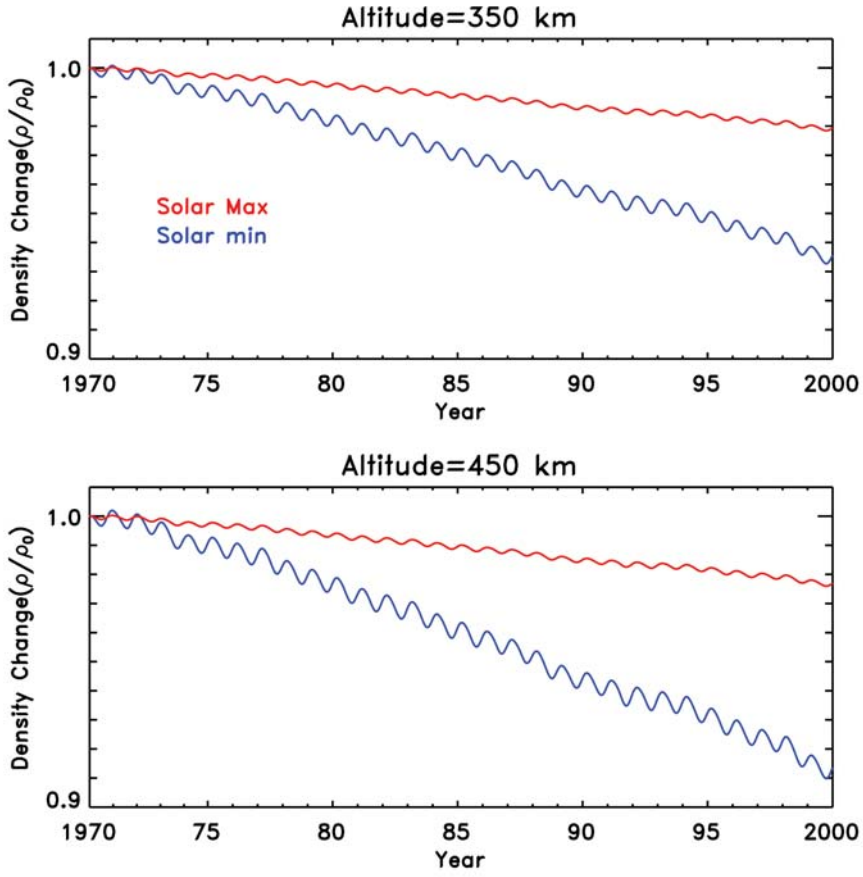

Figure 4.28: Density trends simulated by the global mean model for the period from 1970–2000 assuming solar minimum and solar maximum conditions, using CO_2 concentration measured at Mauna Loa Observatory. (a): density trends at 350 km. Blue: solar minimum conditions; Red: solar maximum conditions; (b): density trends at 450 km. Blue: solar minimum conditions; Red: solar maximum conditions.

4.4.3 A Thermospheric Density Forecast for Solar Cycle 24

Dikpati et al. [2006] have recently predicted the strength of the next solar cycle using a flux-transport solar dynamo model. Their conclusion is that cycle 24 will have a 30–50% larger amplitude than cycle 23. Other recent predictions for solar cycle 24 have

been made, using a variety of techniques. Svalgaard et al. [2005] and Schatten [2005] have predicted that cycle 24 will be weaker than cycle 23, while Hathaway and Wilson [2004] predict a stronger cycle but with an earlier start, and Sello [2003] concludes that the amplitude will be similar to cycle 23. It will be interesting to track this over the next several years as solar activity increases, to observe whether the physical modeling approach of Dikpati et al. [2006] will make a significant improvement in this field. In anticipation that it will, an approximation of their forecast was applied to thermospheric density modeling using.

Since the global mean model uses the $F_{10.7}$ index as a proxy for solar EUV radiation, it is necessary to transform the Dikpati et al. [2006] prediction into a realistically varying solar proxy index. The prediction provides an estimate of the intensity of cycle 24, but not the shape or rotational variation within the cycle. In addition, the strength of cycle 24 is predicted in terms of magnetic flux in the solar shear layer, which directly corresponds to sunspot area. Past measurements of sunspots and $F_{10.7}$ suggest that a 30–50% increase of sunspot area corresponds to approximately a 10% increase of $F_{10.7}$ [Hathaway and Wilson, 2004]. Based on figure 2 of Dikpati et al. [2006], historical measurements of $F_{10.7}$ during solar cycle 22 was employed as a reasonable approximation of the predicted cycle 24 for the purpose of these calculations. The time sequence used as input to the global mean model uses measured $F_{10.7}$ through the end of 2005, and then extends through the present and future by repeating values from the end of cycle 21 and throughout cycle 22, with the nadir of solar minimum in mid-2007. An estimation of CO_2 concentration for the next 12 years is also required. For this simulation, future CO_2 levels were estimated using linear extrapolation of the present trend.

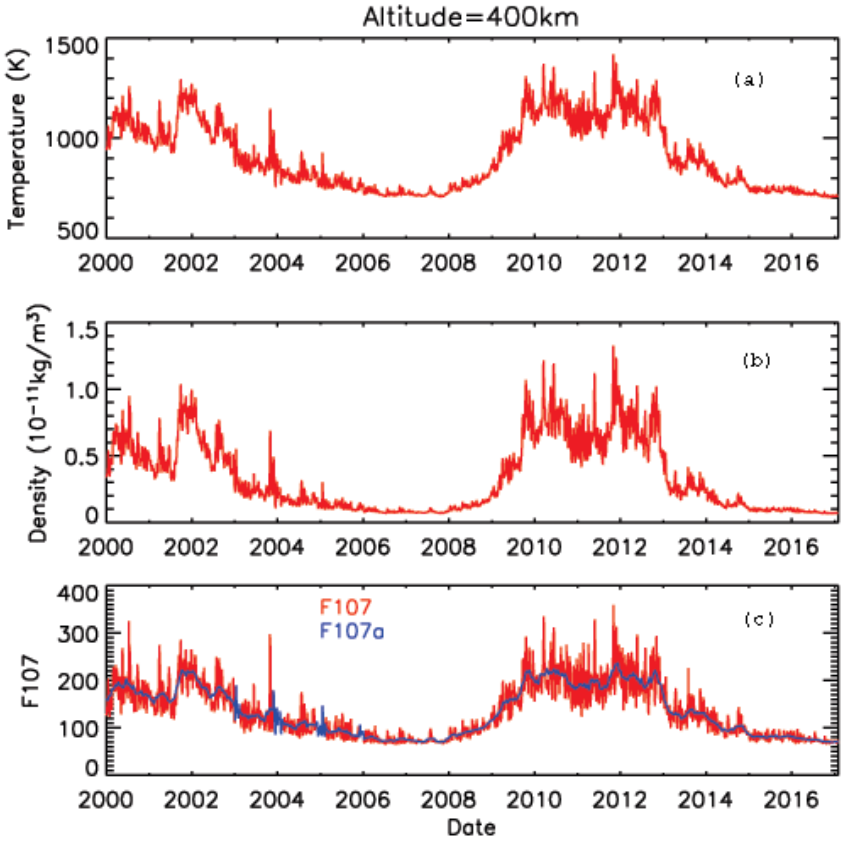

Figure 4.29: Thermosphere temperature and neutral density from 2000 to the end of solar cycle 24. (a) Predicted thermosphere temperature; (b) Predicted thermosphere neutral density; (c) Measured $F_{10.7}$ from 2000–2005 and estimated $F_{10.7}$ from 2006 to the end of solar cycle 24, based on the prediction of Dikpati et al. [2006].

The calculated thermospheric temperature and neutral density and the prediction of $F_{10.7}$ for solar cycle 24, are shown in figure 4.29. Because the predicted solar activity is based on an estimate of cycle amplitude with historical data superimposed, the structure of the prediction should be considered as merely speculative; to represent what a typical large-amplitude even-numbered solar cycle might look like. To extract the long-term change caused by increasing CO_2 concentrations, an additional model run was performed with the lower boundary CO_2 concentration fixed at 2006 levels but with the same predicted solar input. The ratio of densities from the two model runs was then calculated to remove the change caused by the change of solar activity. Figure 4.30 shows the trend

of density change from the beginning of 2006 to the end of cycle 24. A linear regression indicates that the thermospheric density will decrease at 400 km from the present to the end of cycle 24 at a rate of 2.7% per decade, a higher rate than the average decrease of 1.7% per decade for the past three decades.

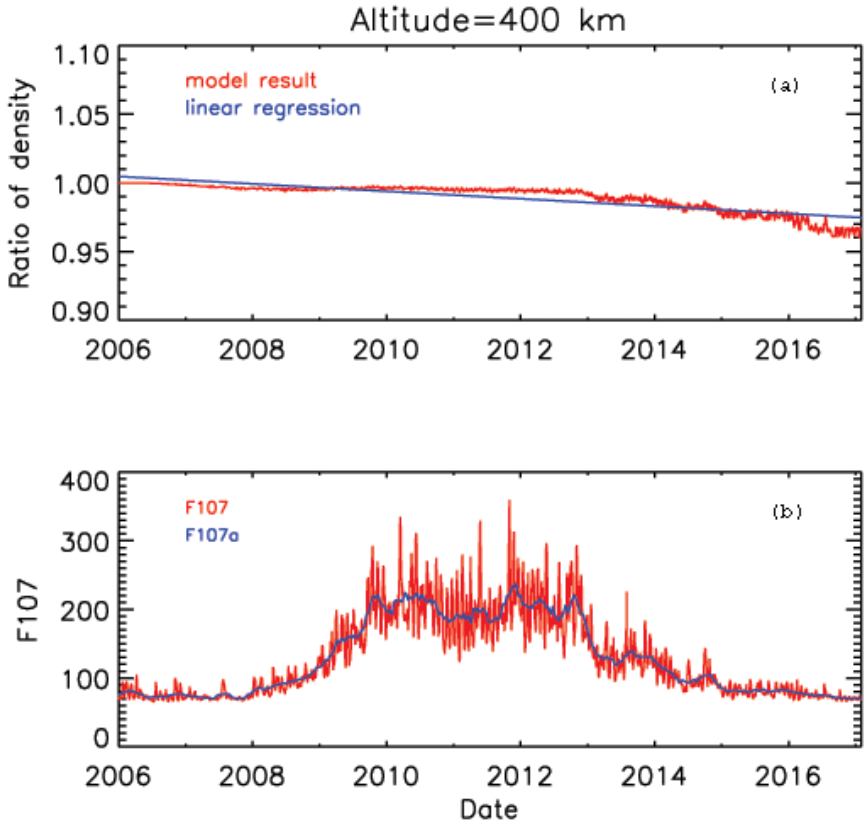

Figure 4.30: (a) Red: ratio of thermospheric neutral density from two model runs. First run: density calculated with varying CO_2 and varying $F_{10.7}$; second run: density calculated with CO_2 fixed at 2006 levels varying $F_{10.7}$. The ratio of the two model runs was calculated to remove the influence of solar activity on density variation. Blue: linear regression to the ratio curve. The linear regression suggests that the density decrease from 2006 to the end of solar cycle 24 will be 2.7% per decade. (b) Estimation of $F_{10.7}$ based on the prediction of Dikpati et al. [2006]. Red: $F_{10.7}$ index; blue: 81-day average $F_{10.7}$ index.

4.4.4 Drivers of Global Change in the Thermosphere

Roble and Dickinson [1989] and Rishbeth and Roble [1992] studied climate changes in the upper atmosphere caused by increased CO_2 and CH_4 concentrations. Akmaev and Fomichev [1998, 2000] investigated the effect of long-term changes in CO_2 concentrations on the mesosphere and lower thermosphere. Gruzdev and Brasseur [2005] calculated long-term changes in the mesosphere influenced by observed changes in the past 50 years in concentrations of greenhouse gases CO_2, CH_4, H_2O, N_2O, and CFCs. Recently, Akmaev et al. [2006] investigated the effect of stratospheric O_3 depletion and water vapor increasing on long-term changes in the mesosphere and lower thermosphere. It is considered that CO_2 drives the main greenhouse cooling in the upper atmosphere, but other radiatively active gases, such as O_3 and H_2O, also influence the climate in the upper atmosphere, with larger effect in the mesosphere and decreasing towards the thermosphere.

Table 4.5: Minor species concentrations based on Brühl & Crutzen, 1988.

Species	Year 2000	Year 2100
CH_4	$O.6\times10^{-6}$	1.34×10^{-6}
CO_2	360×10^{-6}	$720.\times10^{-6}$
H_2	0.5×10^{-6}	1.0×10^{-6}
CO	1.1×10^{-8}	2.2×10^{-8}
H_2O	4.4×10^{-6}	8.8×10^{-6}
NO	2.7×10^{-9}	16.0×10^{-9}
NO_2	4.2×10^{-9}	8.4×10^{-9}
O_3	8.3×10^{-6}	4.15×10^{-6}
CL_X	S-G*	S-G* $\times1.5$

S-G* stands for values based on Solomon and Garcia [1984]

In order to quantify the contribution of the main cooling gas CO_2, sensitivity tests were conducted using the global mean TIMEGCM. The control run was driven by concentrations of greenhouse gases and other minor species in the year 2000 at the model lower boundary of 30 km. In the first sensitivity test run, the CO_2 concentration was doubled. In the second test run, the concentrations of the following list of greenhouse gases and other minor species, CH_4, CO_2, H_2, CO, H_2O, NO, NO_2, O_3, CL_X, were set to be the projected levels for the year 2100 [Brühl & Crutzen, 1988]. Table 4.5 lists the concentrations of minor species for the year 2000 and year 2100 based on scenarios from [Brühl & Crutzen, 1988]. The altitude profiles of density differences between the sensitivity test run and the control run are shown in Figure 4.31. The increase of CO_2 concentration alone causes nearly 90% of density reduction in the upper thermosphere.

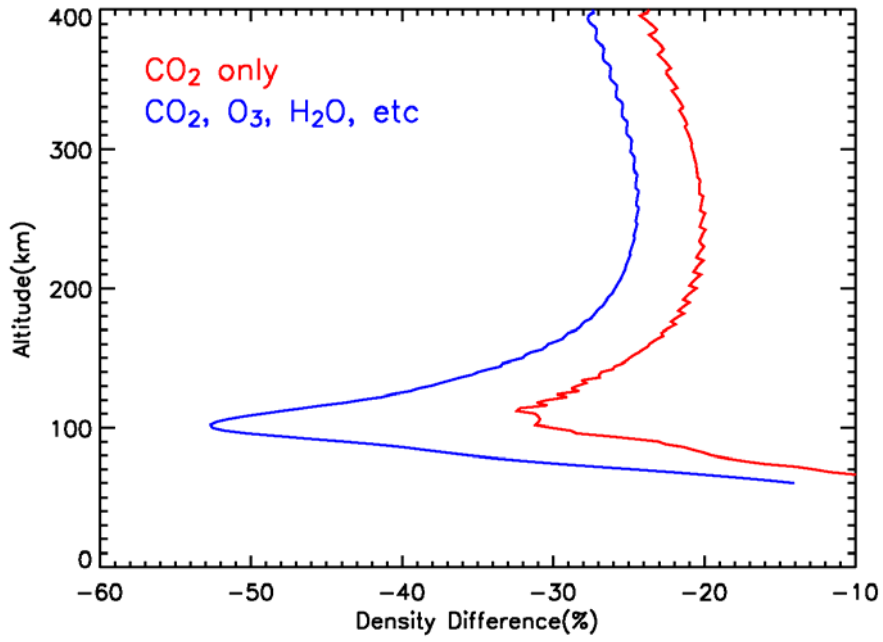

Figure 4.31: Simulated density difference in the upper atmosphere between the year 2000 and 2100. Solid: including variations in all minor gases; Dotted: including variation in CO_2 only.

In order to understand the effect of CO_2 on the upper atmosphere, it is easier to first look at its effect at fixed pressure levels. This is because the effect of thermal contraction/expansion is built-in on a pressure surface and thus does not need to be considered. The temperature and density difference on pressure surfaces produced by doubling of CO_2 is shown in figure 4.32. Cooling takes place at all pressure surfaces, from the upper stratosphere to the thermosphere. It reaches maximum at the lower thermosphere pressure surface $\ln(P_0/P)$ =-5. The cooling lessens from pressure surface -5 to 0 and remains nearly constant above (panel (a)). Conforming to the perfect gas law, density increases as temperature decreases at all pressure surfaces with maximum at pressure surface 5 (panel (b)).

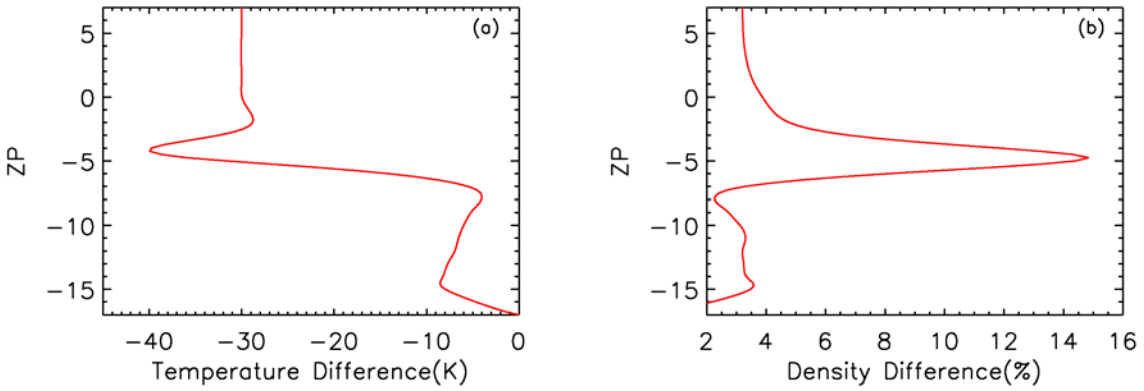

Figure 4.32: Temperature and density difference at fixed pressure surfaces caused by doubling of CO_2.

Figure 4.33 gives the corresponding cooling terms. Panel (a) includes total infrared cooling in the middle and upper atmosphere and other dominant cooling which breaks down to downward molecular heat conduction in the upper thermosphere and downward eddy conduction in the lower thermosphere. Panel (b) presents CO_2 infrared cooling at 15 μm, NO infrared cooling at 5.3 μm, and $O(^3P)$ fine structure infrared cooling at 63 μm. Both NO and $O(^3P)$ peak in the region where downward heat conduction is the dominant cooling mechanism while CO_2 peaks slightly above pressure surface $\ln(P_0/P)$=-5, where downward heat conduction is minor and CO_2 cooling is the

dominant cooling mechanism. CO_2 infrared cooling dominates total infrared cooling from this level downward. An increase in CO_2 concentration thus increases cooling from pressure surface -17 to -5, reaches maximum cooling at pressure surface -5 where the dominant cooling is taken over by the downward heat conduction, and secondarily, by NO and O(3P) cooling.

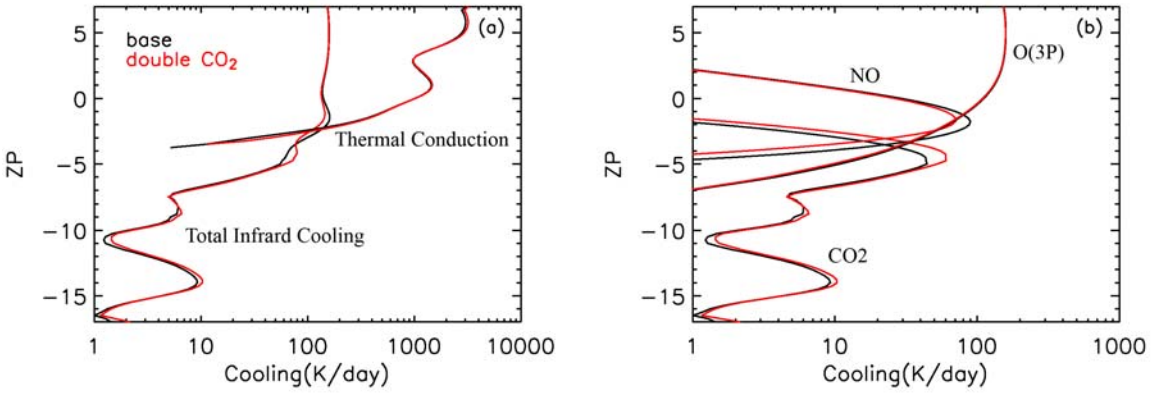

Figure 4.33: Comparison of cooling between the base case and the case with doubled CO_2. (a): Dominant cooling mechanisms, i.e., downward thermal conduction and infrared cooling. (b) Dominant infrared cooling, i.e., 15 μm CO_2 cooling, 5.3 μm NO cooling, and 63μm O(^{3}P) fine structure cooling.

Figure 4.34 shows the corresponding temperature and density change at fixed altitudes. It shows a very different picture from the changes at fixed pressure surfaces shown in figure 4.32. Instead of cooling at all pressure surfaces, there is a warming layer between 100 km and 170 km. Instead of increasing density at all pressure surfaces, density decreases at all altitudes. The difference is caused by thermal contraction. At a fixed altitude, air is replaced by thinner and warmer air from above when the atmosphere in the thermosphere thermally contracts. The effect maximizes where temperature gradient is the greatest, which is between 100 km and 170 km (figure 4.35), where the effect by thermal contraction is larger than the effect of infrared cooling, and thus causes warming in this particular region.

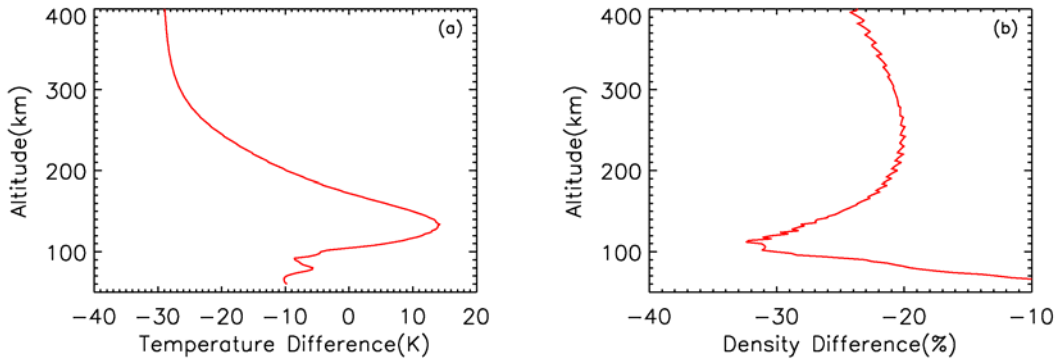

Figure 4.34: Temperature and density difference at fixed altitudes caused by doubling of CO_2.

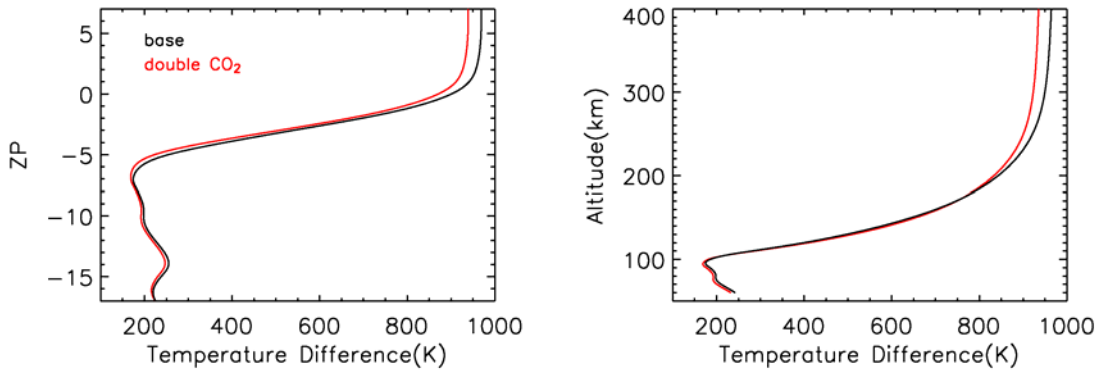

Figure 4.35: Comparison of temperature profiles of the base case and the case with doubled CO_2. (a): on pressure surface. (b): on altitudes.

Chapter 5

CONCLUSIONS

The NCAR Thermosphere-Ionosphere-Electrodynamics General Circulation Model and a global-mean version of the Thermosphere-Ionosphere-Mesosphere-electrodynamics General Circulation Model (TIMEGCM) were used to quantify thermospheric neutral density and its variations, with focus on annual/semiannual variation, effect of using measured solar irradiance on model calculation of solar-cycle variation, and long-term trend of thermospheric neutral density. Satellite drag-derived neutral density and the MSIS00 empirical model were compared with the TIEGCM simulations.

5.1 Mechanisms of Annual/Semiannual Variation

The TIEGCM simulations indicated that eddy diffusion and its annual/semiannual variation is a mechanism for annual/semiannual density variation in the thermosphere. Eddy diffusion, together with annual insolation variation and large-scale circulation, generated global annual/semiannual density variation observed by satellite drag.

The global annual/semiannual density variation was detected and well defined through satellite drag data analysis. It is included in thermospheric empirical models; however, mechanisms have not been well defined. The global mean TIMEGCM sensitivity test indicated that a 7% annual insolation change caused ~ 20% of annual density variation. Fuller-Rowell [1998] proposed “thermospheric spoon” as a mechanism for the semiannual variation in neutral density. The “thermospheric spoon” suggested that large-scale inter-hemispheric circulation causes a semiannual variation in neutral density with maximums during equinox seasons and minimums during solstice seasons, due to stronger large-scale circulation during solstices. In this study, comparison of the

TIEGCM simulation and satellite drag data showed that contributions by the annual insolation change and large-scale circulation cannot fully account for the annual/semiannual amplitude seen in satellite drag data (figure 4.9).

Middle and lower atmospheric processes were investigated for an annual/ semiannual forcing. It has been found by both observations and gravity-wave breaking studies that eddy diffusion at mesopause exhibits strong annual/semiannual variations, with stronger eddy diffusion during the solstice seasons than during the equinox seasons, with maximum eddy diffusion in summer. TIEGCM sensitivity tests showed that eddy diffusion can effectively influence thermospheric neutral density. The neutral density at 400 km increased 15% responding to a 100% reduction in eddy diffusion at the mesopause. It decreased 10% responding to an increase of mesopause eddy diffusion of 50% and decreases 20% further when the eddy diffusion was increased by 100%.

An empirical global annual/semiannual variation in eddy diffusion was obtained based on comparison of satellite drag derived density to the corresponding TIEGCM simulation. It is comparable to eddy diffusion and its variability based on both observations and gravity wave-breaking studies. The global annual/semiannual variation of eddy diffusion was then imposed at the lower boundary of the TIEGCM demonstrating consistent improvement in annual/semiannual density simulation.

The close link between global annual/semiannual variation of thermospheric neutral density and annual/semiannual variation of eddy diffusion can be explained by how eddy diffusion can effectively influence global thermospheric neutral density. The effect of eddy diffusion on temperature augments the effect of eddy diffusion on composition in influencing total mass density. Increased eddy diffusion decreases O density, subsequently reduces temperature, and then thermally reduces neutral density. Compared to eddy diffusion, the effect of large-scale circulation in the global mean thermosphere is not significant since large-scale circulation mainly redistributes energy and mass between the two hemispheres. The effect of dynamic forcing on the dominant species O is compensated for by thermal forcing.

5.2 Solar-Cycle Dependency of Empirical Neutral Density

Satellite drag data analysis has shown that $F_{10.7}$-based thermospheric empirical models overestimate thermospheric neutral density at low solar activity, thus exhibit a solar-cycle dependency in density prediction. However, the JB2000, an updated J70 model that uses additional solar indices other than $F_{10.7}$, showed improvement of the solar-cycle dependency. TIEGCM simulations, using TIMED/SEE solar spectral irradiance measurements, did not show the solar-cycle dependency. This result, together with improvement of the solar-cycle dependency by the JB2000, suggests that the solar-cycle dependency has been caused by inadequate representation of solar variability at low solar activity in the $F_{10.7}$-based empirical models. Although long-term decrease of thermospheric neutral density can also contribute to the low solar activity bias, the effect should be negligible, since the long-term decrease of density is small (a few percent per decade), while the low solar activity overestimation is ~25%.

Variation of density on solar-rotational time scales calculated by the TIEGCM was also improved compared to the empirical model MSIS00.

5.3 Long-Term Trend of Neutral Density

Previous model studies of global change in the upper atmosphere have been limited to sensitivity studies using a fixed greenhouse gas concentration. In this study, CO_2 measurements at Mauna Loa Observatory and solar EUV variation over the last three decades were used in the global mean TIMEGCM to quantify the global change of the thermosphere. The simulations showed that thermospheric neutral density at 400 km had an average long-term decrease of 1.7% per decade from 1970–2000. The trend exhibited an altitude-dependency with 1.2% per decade at 150 km increasing to 1.7 % per decade at 400 km. In addition, the trend depended on solar activity. Under solar minimum conditions, the average decreases were 2.2% per decade at 350 km and 2.9% per decade at 450 km from 1970–2000. Under solar maximum conditions, the average density decreases were 0.7% per decade at 350 km and 0.8% per decade at 450 km.

A forecast of density decrease for solar cycle 24 based on the solar intensity prediction of Dikpati et al. [2006] suggested that thermospheric density will decrease at 400 km from present to the end of solar cycle 24 at a rate of 2.7% per decade, which is larger than the average decrease of 1.7% per decade for the past three decades.

Reduction in thermospheric density causes less atmospheric drag on earth-orbiting space objects. The implication of this long-term decrease of thermospheric neutral density is that it will increase lifetime of satellites but it will also increase the amount of space junk.

It has been found that long-term cooling of the thermosphere is caused by long-term changes in minor species concentrations, such as increases of CO_2 and H_2O, and depletion of O_3. Model sensitivity studies based on the projected changes of minor species concentrations in Brühl and Crutzen [1988] showed that from year 2000 to year 2100, increases of CO_2 concentration alone caused nearly 90% of density reduction at 400 km, which suggested that increased concentration of the greenhouse gas CO_2 is the main forcing of global change in the thermosphere.

5.4 A Summary of Other Neutral Density Variations

TIEGCM simulation of the 28 October 2003 X17-solar flare showed a 20% daytime increase of neutral density at 400 km in the equatorial region. The sudden increase of solar irradiance in the XUV and EUV caused a sudden increase in density with about one hour delay.

The 2003 “Halloween” geomagnetic storms caused density enhancement in the upper thermosphere in the order of 200% with little delay. During the period, the geomagnetic index K_p remained at high values up to nine for almost three days from 28 October 2003 to 1 November 2003. The geomagnetic forcing became the dominant energy source and governed density variation at high latitudes. In addition, intense geomagnetic heating can excite waves. The in-situ waves, together with large-scale circulation, can propagate density disturbance to low latitudes, with several hours delay.

Consequently, density disturbances during strong geomagnetic storms can be a global phenomenon.

Thermospheric neutral density exhibited strong diurnal variation, with an amplitude in the order of 100% in the upper thermosphere. At spring equinox, neutral density reached minimum around 5:00 am and maximum around 4:00 pm in the equatorial region.

During a moderately strong solar rotation with $F_{10.7}$ variation of 60 units, neutral density changed approximately 80% in the upper thermosphere. The 27-day solar-rotational variation of thermospheric neutral density is caused by appearance and disappearance of the Sun's active regions during the Sun's 27-day rotation. Since the Sun is very active under solar maximum conditions, the 27-day solar-rotational variation of the density is stronger at solar maximum than at solar minimum.

The global-average thermospheric neutral density from the TIEGCM simulation showed maximums in equinox seasons and minimums around July. A secondary minimum was seen around January, with combined annual/semiannual amplitude in the order of 120%, consistent with satellite drag measurements. Other studies, through satellite drag data analysis suggested that annual amplitude and semiannual amplitude in density variation were comparable. Sensitivity study using the global-mean version of the TIMEGCM found that a 7% variation in insolation caused by the variation in the sun-earth distance contributed approximately 20% to density variation. An annual/semiannual variation of eddy diffusion, together with annual insolation variation and large-scale circulation, caused the annual/semiannual density variation observed by satellite drag.

The TIEGCM simulation showed that in the upper thermosphere near 400 km, thermospheric neutral density at solar maximum was 14 times the density at solar minimum. Solar-cycle variation of neutral density is driven by intrinsic variability of magnetic activities in the Sun. During a solar cycle, the fractional area of active regions over the solar disk varies from 0 to around 0.2, which causes a solar-cycle variability of solar irradiance. The solar-cycle variability of solar irradiance drives a solar-cycle variation in thermospheric neutral density.

The TIEGCM simulated neutral density showed a winter hemisphere to summer hemisphere variation of 40%. This variation is determined by a weak latitudinal variation in atomic oxygen and a large latitudinal variation in molecular nitrogen. The temperature at the summer pole was approximately 27% higher than that at the winter pole. Dynamic transport of O compensates for thermal forcing and causes a weak latitude-dependency in O while dynamic forcing compounds thermal forcing for N_2, and N_2 showed a large latitudinal variation of one order of magnitude. In addition, there was a latitude-dependency in annual density variation with larger annual variation in the southern hemisphere. This is a manifestication of a larger summer to winter temperature difference in the southern hemisphere caused by the sun-earth distance. The average neutral density at the December solstice was approximately 60% larger than that at the June solstice. Furthermore, neutral density did not show a high latitude anomaly as shown in both the O and N_2 number densities. Dynamic depletion of the O number density due to upwelling of geomagnetic heating is compensated for by the enhancement of thermal expansion, and the O number density was slightly depleted at high latitudes. The dynamic accumulation of N_2 due to upwelling of geomagnetic heating is compounded by the enhancement of thermal expansion, and N_2 showed a high latitude bulge of 200%.

5.5 Further Study

5.5.1 Thermosphere/Ionosphere Annual Anomaly

Ionospheric structure is closely related to thermospheric properties. Understanding the thermosphere can facilitate understanding of the ionosphere and vise versa. In the ionosphere, the daytime F2 peak electron density, NmF2, is usually near steady state which means production of ionization is balanced by chemical loss. As a result, NmF2 depends on the O/N_2 ratio. The dependency is evident in seasonal variation of NmF2 and the geomagnetic storm response of NmF2. The seasonal variation of NmF2 is directly linked to the seasonal variation of O/N_2 governed by seasonal circulations. The

geomagnetic response of NmF2 is the ionospheric manifestation of the geomagnetic response of the O/N_2 ratio. However, other ionospheric anomaly, such as the annual/semiannual anomaly in NmF2 and total electron content (TEC), remains uncertain in terms of the mechanisms for the anomaly and how much it is related to the thermospheric annual/semiannual variation. Mendillo et al. [2005] calculated a global ionospheric asymmetry index in TEC obtained from GPS satellite signals, to characterize a globally-distributed annual asymmetry in TEC, with the TEC larger in December than in June. They combined the TEC from equivalent points in the northern and southern hemispheres and defined the asymmetric index as: AI= (Dec-June)/(Dec+June). They found that the asymmetric index is larger than asymmetry of solar irradiance caused by the sun-earth distance, and concluded that the ionospheric annual asymmetry is likely, at least partially, attributed to asymmetry in the neutral O/N_2 ratio in the thermosphere with mechanisms to be determined. Rishbeth [2006] suggested that dynamical effect through lower atmospheric coupling is the most promising direction in finding the mechanisms.

Recent data analysis of electron density measurements by the Constellation Observing System for Meteorology Ionosphere & Climate (COSMIC) satellites [Private communication with Zhen Zeng, postdoctoral Fellow at NCAR and COSMIC] showed maximum NmF2 during equinoxes, minimum during June solstice, and a secondary minimum during December solstice. She also found the annual asymmetry characterized by Mendillo et al. [2005] in the COSMIC TEC in the COSMIC data.

The questions are whether the annual/semiannual anomaly in the ionosphere is determined by the annual/semiannual variation in thermospheric composition and what causes the anomaly. The annual/semiannual variation in the thermospheric neutral density and its mechanisms is investigated in this study in global mean sense. In order to explore that answers to the questions, the global distribution of annual/semiannual variation in the TIEGCM simulated composition (O/N_2) needs to be investigated to find if and how much the global distribution of annual/semiannual variation in O/N_2 can explain the global distribution of annual/semiannual variation in ionospheric properties. Eddy diffusion coefficient derived from gravity-wave breaking (figure 4.13) showed a pronounced annual asymmetry with larger eddy diffusion in June than in December, and

hemispheric asymmetry with larger eddy diffusion in northern hemisphere summer than southern hemisphere summer. It is in the right direction of a smaller O/N_2 in June than in December, and thus, smaller NmF2 and TEC in June than in December. Does the annual/hemisphere asymmetry in eddy diffusion cause annual/hemisphere asymmetry in O/N_2, and thus a mechanism for annual anomaly in TEC?

Further study will focus on three areas: (1) research on observational results on eddy diffusion coefficient in the turbopause region to improve eddy diffusion parameterization for the TIEGCM lower boundary; (2) investigate the TIEGCM simulated global distribution of O/N2 and its annual/semiannual variation, and compare it to the global distribution of annual/semiannual anomaly in TEC and NmF2; (3) explore the link between the lower atmospheric processes and the thermosphere/ionosphere anomaly.

5.5.2 Global Change in the Ionosphere

Roble and Dickinson [1989] examined global change in the mesosphere and thermosphere due to long-term changes in greenhouse gas concentrations, and suggested that long-term cooling in the thermosphere will cause a long-term decrease of the E- and F-layer peak densities. Rishbeth [1990] used the basic theory of the ionosphere [e.g. Rishbeth, 1988] to study the effects of the long-term cooling in the thermosphere proposed by Roble and Dickinson [1989]; it was concluded that the long-term cooling in the thermosphere would lower the E- and F2-layer peak heights but changes in the E- and F2-layer electron density would be small. Rishbeth and Roble [1992] investigated long-term changes in the ionosphere using the TIGCM with doubling of CO_2 and CH_4 concentrations and found that the height of the F2-layer peak dropped on average by about 15 km but the F2-layer electron density was hardly changed. Prompted by these theoretical and modeling studies, ground-based ionosonde data have been used to detect long-term changes in the ionosphere [e.g. Bremer, 1998; Clilverd et al, 2003; Danilov, 2003]. It has been found that the E-layer including the peak E-layer height had a long-term decrease and the E- and F1-layer electron density had a long-term increase in the

past three to four decades [Bremer, 1998; Laštovička and Bremer, 2004; Laštovička et al., 2006a]. However, long-term changes of F2 parameters have been controversial [Bremer, 1998; Mikhailov and Marin, 2000, 2001; Clilverd et al., 2003; Danilov, 2003; Laštovička, 2005; Laštovička et al., 2006a; Laštovička et al., 2006b], in terms of the methods of data analysis, the results obtained, and the interpretations of the results. Both negative and positive trends of F2 parameters have been detected; long-term changes of geomagnetic activities and long-term changes of greenhouse gas concentrations have been used to interpret the results.

In order to explain the controversies and facilitate the data detection, the global mean TIMEGCM will be used to investigate global change in the ionosphere. Long-term changes of the E- and F-layer parameters will be quantified; the basic physics of the ionospheric layers will be used to understand long-term changes of each ionospheric layer.

Bibliography

Akmaev, R. A., and V. I. Fomichev (1998), Cooling of the mesosphere and lower thermosphere due to doubling of CO_2, *Ann. Geophys.*, *16*, 1501-1512.

Akmaev, R. A., and V. I. Fomichev (2000), A model estimate of cooling in the mesosphere and lower thermosphere due to the CO_2 increase over the last 3-4 decades, *Geophys. Res. Lett.*, *27*, 2113-2116.

Akmaev, R. A. (2001a), Simulation of large-scale dynamics in the mesosphere and lower thermosphere with the Doppler-spread parameterization of gravity waves 1. Implementation and zonal mean climatologies, *J. Geophys. Res, 106*, 1193-1204.

Akmaev, R. A. (2001b), Simulation of large-scale dynamics in the mesosphere and lower thermosphere with the Doppler-spread parameterization of gravity waves 2. Eddy mixing and the diurnal tide, *J. Geophys. Res, 106*, 1205-1213.

Akmaev, R. V. (2002), Modeling the cooling due to CO_2 increases in the mesosphere and lower thermosphere, *Physics and Chemistry of the Earth 27*, pp. 521–528.

Akmaev, R. A., V. I. Fomichev, and X. Zhu (2006), Impact of middle-atmospheric composition changes on greenhouse cooling in the upper atmosphere, *Journal of Atmospheric and Terrestrial Physics 68*, pp. 1879-1889.

Bailey, S. M., C. A. Barth, and S. C. Solomon (2002), A model of nitric oxide in the thermosphere, *J. Geophys. Res., 107 (A8)*, 1206, doi:10.1029/2001JA000258.

Barnett, J., and M. Corney (1985), Middle atmosphere reference model derived from satellite data, *Handb. MAP, 16*, edited by K. Labitzke, J.J. Barnett, and B.Edwards, pp. 47-85, Sci. Comm. For Sol. Terr. Phys. Secr., Univ. of Ill., Urbana.

Barth, C. A., K. D. Mankoff, S. M. Bailey, and S. C. Solomon (2003), Global observations of nitric oxide in the thermosphere, *J. Geophys. Res., 108(A1)*, 1027, doi:10.1029/2002JA009458.

Bates, D. R. (1959), Some problems concerning the terrestrial atmosphere above the 100 km level, *Proc. R. Soc. London, Ser. A, 253*, 451-462.

Berger, C., and F. Barlier (1981), Response of the equatorial thermosphere to magnetic activity analyzed with accelerometer total density data, asymmetrical structure, *J. Atmos. Terr. Phys., 43*, 121-133.

Blum, P. W., K. G. H. Schuchardt (1978), Semi-theoretical global models of the eddy diffusion coefficient based on satellite data, *J. Atmos. Terr. Phys., 40*, 1137-1142.

Bowman B. R. (2004a), The semiannual Thermosphere Density Variation From 1970 to 2002 Between 200-1100km, AAS 2004-174, AAS/AIAA Spaceflight Mechanics Meeting, Maui, Hi, February.

Bowman, B. R., F. A. Marcos, M. Kendra (2004b), A Method for Computing Accurate Daily Atmospheric Density Values from Satellite Drag Data, AAS 2004-173, AAS/AIAA Spaceflight Mechanics Meeting, Maui, Hi, February.

Bowman B. R., W. K., Tobiska, F. A., Marcos (2006), A new empirical thermosphere Density model JB2006 using new solar indices, AIAA 2006-6166.

Bowman B. R., W. K., Tobiska (2006), Improvements in modeling thermospheric densities using new EUV and FUV solar indices, AAS 2006-237, AAS/AIAA Spaceflight Mechanics Meeting, Tampa, Florida, January.

Bremer, J. (1998), Trends in the ionospheric E and F regions over Europe, *Ann. Geophysicae*, **16**, 986-996.

Bruinsma, S., J. M. Forbes, R. S. Nerem, and X. Zhang (2006), Thermosphere density response to the 20–21 November 2003 solar and geomagnetic storm from CHAMP and GRACE accelerometer data, *J. Geophys. Res.*, *111*, A06303, doi:10.1029/2005JA011284.

Brühl, C., and P. J. Crutzen (1988), Scenarios of possible changes in atmospheric temperatures and ozone concentrations due to man's activities, estimated with a one-dimensional coupled photochemical climate model, *Climate Dynamics, 2*, 173-203.

Carignan, G. R., and W. H. Pinkus (1968), Ogo-F04 experiment description, *Tech. Note 08041-3-T*, Univ. of Mich., Ann Arbor, Mich..

Chandra, S., and A. K. Sinha (1974), The role of eddy turbulence in the development of self-consistent models of the lower and upper thermosphere, *J. Geophys. Res., 79*, 1916.

Clilverd, M. A., T. Ulich, and M. J. Jarvis (2003), Residual solar cycle influence on trends in ionospheric F2-layer peak height, *J. Geophys. Res.*, 108(A12), 1450, doi:10.1029/2003JA009838.

Cook, G. E. (1967), The large semiannual variation in exospheric density: A possible explanation, *Planet. Space Sci., 15*, 627-632.

Cook, G. E. (1969), The semiannual variation in the upper atmosphere: A review, *Ann. Geophys., 25*, 451-469.

Cook, G. E. (1970), The semiannual variation in the upper atmosphere during 1967 and 1968, *Planet. Space Sci., 18*, 565-582.

Danilov, A. D. (2003), Long-term trends in foF2 independent of geomagnetic activity, *Annales Geophysicae 21*, pp. 1167–1176.

DeJager, C. (1964), Solar X-radiation, in Astronomical Observations From Space Vehicles, edited by J.-L. Steinberg, p. 45, Taffin-Lefort, Liège, Belgium.

DeMore, W. B., S. P. Sander, D. M. Golden, R. F. Hampson, M. J. Kurylo, C. J. Howard, A. R. Ravishankara, C. E. Kolb, and M. J. Molina (1992), Chemical kinetics and photochemical data for use in stratospheric modeling, evaluation number 10, *JPL Publ., 92-20*, 240 pp..

Detman, T. R. (1996), Cross varidation comparisons of autonomous Ap predictions, in *Proceedings of Workshop on the Evaluation of Space Weather Forecasts*, edited by K. Doggett, P. 149, NOAA, ERL, Boulder, Colorado.

Dickinson, R. E., and H. Rishbeth (1973), Planetary scale motions at F-layer heights, *Space Res., 13*, 413.

Dickinson, R. E., E. C. Ridley, and R. G. Roble (1981), A three-dimensional general circulation model of the thermosphere, *J. Geophys. Res., 86*, 1499-1512.

Dickinson, R. E., E. C. Ridley, and R. G. Roble (1984), Thermospheric general circulation with coupled dynamics and composition, *J. Atmos. Sci., 41*, 205-219.

Dikpati, M., G. De Toma, and P. A. Gilman (2006), Predicting the strength of solar cycle 24 using a flux-transport dynamo-based tool, *Geophys. Res. Lett.*, *33*, L05102, doi:10.1029/2005GL025221.

Emmert, J. T., J. M. Picone, J. L. Lean, and S. H. Knowles (2004a), Global change in the thermosphere: Compelling evidence of a secular decrease in density, *J. Geophys. Res.*, *109*, A02301, doi:10.1029/2003JA010176.

Emmert, J. T., J. M. Picone, J. L. Lean, and S. H. Knowles (2004b), Correction to "Global change in the thermosphere: Compelling evidence of a secular decrease in density," *J. Geophys. Res., 109*, A04307, doi:10.1029/2004JA010462.

Fennelly, J. A., and D. G. Torr (1992), Photoionization and photoabsorption cross sections of O, N_2, O_2, and N for aeronomic calculations, At. Data Nucl. Data Tables, 51, 321.

Fesen, C. G., R. E. Dickinson, and R. G. Roble (1986), Simulation of thermospheric tides at equinox with the National Center for Atmospheric Research thermospheric general circulation model, *J. Geophys. Res., 91*, 4471-4489.

Fleming, E. L., S. Chandra, J. J. Barnett, and M. Corney (1990), Zonal mean temperature, pressure, zonal wind and geopotential height as functions of latitude, *Advances in Space Research, Volume 10*, Issue 12, Pages 11-59.

Forbes, J. M., R. G. Roble, and C. G. Fesen (1993), Acceleration, heating and compositional mixing of the thermosphere due to upward propagating tides, *J. Geophys. Res., 98*, 311-321.

Forbes, J. M., R. Gonzalez, F. A. Marcos, D. Revelle, and H. Parish (1996), Magnetic storm response of lower thermosphere density, *J. Geophys. Res., 101*, 2313-2319.

Forbes, J. M., G. Lu, S. Bruinsma, S. Nerem, and X. Zhang (2005), Thermosphere density variations due to the 15–24 April 2002 solar events from CHAMP/STAR accelerometer measurements, *J. Geophys. Res.*, *110*, A12S27, doi:10.1029/2004JA010856.

Foster, J. C., J. M. Holt, R. G. Musgrove, and D. S. Evans (1986), Ionospheric convection associated with discrete levels of particle precipitation, *Geophys. Res. Lett., 13*, 656-659.

Fox, J. L. (1994), Rate coefficient for the reaction N + NO, *J. Geophys. Res., 99*, 6273-6276.

Fritts, D. C. (1984)**,** Gravity wave saturation in the middle atmosphere: A review of theory and observations, *Rev. Geophys.*, *22*, 275–308.

Fritts, D. C. and W. T. Lu (1993), Spectral estimates of gravity wave energy and momentum fluxes, II: Parameterization of wave forcing and variability, *J. Atmos. Sci., 50*(22), 3695-3713.

Fritts, D. C., and M. J. Alexander (2003), Gravity wave dynamics and effects in the middle atmosphere, *Rev. Geophys.*, *41*(1), 1003, doi:10.1029/2001RG000106.

Fukao, S., M.D. Yamanaka, N. Ao, W. K. Hocking, T. Sato, M. Yamamoto, T. Nakamura, T. Tsuda, and S. Kato (1994), Seasonal variability of vertical eddy diffusivity in the middle atmosphere 1. Three-year observations by the middle and upper atmosphere radar, *J. Geophys. Res. 99*, 18973-18987.

Fuller-Rowell, T. J., D. Rees (1980), A three-dimensional, time-dependent, global model of the thermosphere, *J. Atmos. Sci. 37*, 2545.

Fuller-Rowell, T. J., D. Rees (1983), Derivation of a conservative equation for mean molecular weight for a two constituent gas within a three-dimensional, time-dependent model of the thermosphere. *Planet. Space Sci., 31*, 1209.

Fuller-Rowell, T. J., D. Rees, S. Quegan, R. J. Moffett, M. V. Codrescu, and G. H. Millward (1996), A Coupled Thermosphere-Ionosphere Model (CTIM), *Solar Terrestrial Energy Program (STEP) Handbook*, edited by R. W. Schunk, pp. 217-238.

Fuller-Rowell, T. J. (1998), The "thermospheric spoon": A mechanism for the semiannual density variation, *J. Geophys. Res.*, *103*, pages 3951-3956.

Garcia, R. R., S. Solomon (1985), The effect of breaking gravity waves on the dynamics and chemical composition of the mesosphere and lower thermosphere, *J. Geophys. Res., 90*, 3850-3868.

Gruzdev A. N., G. P. Brasseur (2005), Long-term changes in the mesosphere calculated by a two-dimensional model, J. Geophys. Res., 110, D03304, doi:10.1029/2003JD004410.

Hagan, M. E. and J. M. Forbes (2002), Migrating and nonmigrating diurnal tides in the middle and upper atmosphere excited by tropospheric latent heat release, *J. Geophys. Res., 107*(D24), 4754, doi: 10.1029/2001JD001236.

Hagan, M. E. and J. M. Forbes (2003), Migrating and nonmigrating semidiurnal tides in the upper atmosphere excited by tropospheric latent heat release, *J. Geophys. Res., 108*(A2), 1062, doi:10.1029/2002JA009466.

Harris, M. J., N. F. Arnold, A. D. Aylward (2002), A study into the effect of the diurnal tide on the structure of the background mesosphere and thermosphere using the new

coupled middle atmosphere and thermosphere (cmat) general circulation model, *Ann. Geophy.*, *20*, 225.

Hathaway, D. H., R. M. Wilson (2004), What the sunspot record tells us about space climate, *Solar Physics, 224*, 5-19.

Heelis, R. A., J. K. Lowell, and R. W. Spiro (1982), A model of the high-latitude ionospheric convection pattern, *J. Geophys. Res.*, 87, 6339-6345.

Hedin, A. E., H. G. Mayr, C. A. Reber, N. W. Spencer, and G. R. Carignan (1974), Empirical model of global thermospheric temperature and composition based on data from the Ogo-6 quadrupole mass spectrometer, *J. Geophys. Res., 79*, 215-225.

Hedin, A. E., and D. Alcaydé (1974), Comparison of atomic oxygen measurements by incoherent scatter and satellite-borne mass spectrometer techniques, *J. Geophys. Res., 79*, 1579.

Hedin, A. E., J. E. Salah, J. V. Evans, C. A. Reber, G. P. Newton, N. W. Spencer, D. C. Kayser, D. Alcayde, L. Cogger, and J. P. Mcclure (1977a), A global thermospheric model based on mass spectrometer and incoherent scatter data, MSIS 1, N2 density and temperature, J. *Geophys. Res.*, 82, 2139-2147.

Hedin, A. E., C. A. Reber, G. P. Newton, N. W. Spenser, H. C. Brinton, H. G. Mayr, and W. E. Potter (1977b), A global thermospheric model based on mass spectrometer and incoherent scatter data, MSIS 2, composition, *J. Geophys. Res.*, 82, 2148-2156.

Hedin, A. E. (1983), A revised thermospheric model based on mass spectrometer and incoherent scatter data: MSIS-83, *J. Geophys. Res.,* 88, 10170-10188.

Hedin, A. E. (1987), MSIS-86 thermosphere model, *J. Geophys. Res.,* 92, 4649-4662.

Hedin, A. E. (1991), Extension of the MSIS thermosphere model into the middle and lower atmosphere, *J. Geophys. Res.,* 96, 1159-1172.

Henke, B. L., E. M. Gullikson, and J. C. Davis (1993), X-ray interactions: Photoabsorption, scattering, transmission, and reflection at E = 50–30,000 eV, Z = 1–92, At. Data Nucl. Data Tables, 54, 181.

Heroux, L., and J. E. Higgins (1977), Summary of full disk solar fluxes between 250 and 1940 Å, *J. Geophys. Res., 82*, 3307.

Heroux, L., and H. E. Hinteregger (1978), Aeronomical reference spectrum for solar UV below 2000 Å, *J. Geopgys. Res., 83*, 5305.

Hines, C. O. (1960), Internal atmospheric gravity waves at ionospheric heights, *Can. J. Phys.*, *38*, 1441–1481.

Hines, C. O. (1970), Eddy diffusion coefficients due to instabilities in internal gravity waves, *J. Geophys. Res., 75*, 3937-3939.

Hinteregger, H. E. (1981a), Representations of solar EUV fluxes for aeronomical applications, *Adv. Space Res., 1*, 39-52.

Hinteregger, H. E., K. Fukui, and G. R. Gilson (1981b), Observational, reference and model data on solar EUV, from measurements on AE-E, *Geophys. Res. Lett.*, *8*, 1147.

Hodges, R. R. (1969), Eddy diffusion coefficients due to instabilities in internal gravity waves, *J. Geophys. Res., 74*, 4087-4090.

Horan, D. M., and R. W. Kreplin (1981), Simultaneous measurements of EUV and soft

X-ray solar flare emission, Solar Phys., 74, 265.

Hwang E. S., K. J. Castle, and J. A. Dodd (2003), Vibrational relaxation of NO (v = 1) by oxygen atoms between 295 and 825 K, J. Geophys. Res., 108 (A3), 1109, doi:10.1029/2002JA009688.

IPCC (2007): *Climate Change 2007: The Physical Science Basis. Contribution of Working Group 1 to the Fourth Assessment Report of the Intergovernmental Panel on Climate Change* [Solomon, S., D. Qin, M. Manning, Z. Chen, M. Marquis, K.B. Averyt, M. Tignor and H.L. Miller (eds.)]. Cambridge University Press, Cambridge, United Kingdom and New York, NY, USA.

Jacchia, L. G., and J. Slowey (1963), Accurate drag determinations for eight artificial satellites; atmospheric densities and temperatures, Smithsonian Contr. Astrophys., vol. 8, pp. 1-99.

Jacchia, L. G. (1965), Static diffusion models of the upper atmosphere with empirical temperature profiles. Smithsonian Contr. Astrophys., vol. 8, pp.215-257.

Jacchia, L. G. (1970), New static models of the thermosphere and exosphere with empirical temperature profiles. *Smithsonian Astrophys. Obs*. *Special Report No.* 313, 87pp.

Jacchia, L. G. (1971a), Revised Static Models of the Thermosphere and Exosphere with Empirical Temperature Profiles, *Smithsonian Astrophys. Obs. Special Report No. 332*, 113pp.

Jacchia, L. G. (1971b), Semiannual variation in the heteorosphere: A reappraisal, *J. Geophys. Res.*, 76, 4602-4607.

Jacchia, L. G. (1974), Variations in thermospheric composition: A model based on mass spectrometer and satellite drag data, *J. Geophys. Res, 79*, 1923.

Jacchia, L. G., J. W. Slowey, and U. von Zahn (1976), Latitudinal changes of composition in the disturbed thermosphere from Esro 4 measurements, *J. Geophys. Res,81*, 36.

Jacchia, L. G. (1977), Thermospheric Temperature, Density, and Composition: New Models, *Smithsonian Astrophys. Obs. Special Report No. 375*.

Johnson, F. S., and B. Gottlieb (1970), Eddy mixing and circulation at ionospheric levels, *planet. Space Sci., 18*, 1707.

Johnson, F. S. (1973), Horizontal variations in thermospheric composition, *Rev. Geophys. Space Phys., 11*, 741.

Johnson, F. S. (1974), Energy input to the lower thermosphere, *J. Atmos. Terr. Phys., 36, 1707*.

Keating, G. M., and E. J. Prior (1968), The winter He bulge, *Space Res., 8*, 982.

Keating, G. M., R. H. Tolson, and M. S. Bradford (2000), Evidence of long-term global decline in the Earth's thermospheric densities apparently related to anthropogenic effects, *Geophys. Res. Lett.*, *27*, 1523-1526.

Keeling, C. D. and T. P. Whorf (2005), Atmospheric CO_2 records from sites in the SIO air sampling network, in *Trends: A Compendium of Data on Global Change*, Carbon Dioxide Information Analysis Center, Oak Ridge National Laboratory, U.S. Department of Energy, Oak Ridge, Tenn.

Khattatov, B. V., M. A. Geller, and V. A. Yubin (1997), Diurnal migrating tides as seen

by the high-resolution Doppler imager/UARS 2. Monthly mean global zonal and vertical velocities, pressure, temperature, and inferred dissipation, *J. Geophys. Res., 102*.

Khvorostovskaya, L. E., I. Y. Potekhin, G. M. Shved, V. P. Ogibalov, T. V. Uzyukova (2002), Measurement of the rate constant for quenching CO2(01(1)0) by atomic oxygen at low temperatures: Reassessment of the rate of cooling by the CO2 15-mu m emission in the lower thermosphere, *IZVESTIYA ATMOSPHERIC AND OCEANIC PHYSICS 38 (5)*: 613-624.

Kirchhoff, V. W. J. H., and B. R. Clemesha (1983), Eddy diffusion coefficients in the lower thermosphere, *J. Geophys. Res., 88*, 5765-5768.

Kreplin, R. W., K. P. Dere, D. M. Horan, and J. F. Meekins (1977), The solar spectrum below 10 Å, in The Solar Output and its Variation, edited by O. R. White, p. 287, Colo. Assoc. Univ. Press, Boulder, Colo.

Laštovička, J., and J. Bremer (2004), An overview of long-term trends in the lower ionosphere below 120 km, *Surveys in Geophysics 25*, pp. 69–99.

Laštovička, J. (2005), On the role of solar and geomagnetic activity in long-term trends in the atmosphere-ionosphere system, *Journal of Atmospheric and Solar-Terrestrial Physics 67*, pp. 83–92.

Laštovička, J., R. A. Akmaev, G. Beig, J. Bremer, and J. T. Emmert (2006a), Global change in the upper atmosphere, *Science*, *314*, pp. 1253 – 1254.

Laštovička, J., A.V. Milkhailov, T. Ulich, J. Bremer, A. G. Elias, N. Ortiz de Adler, V. Jara, R. Abarca del Rio, A. J. Foppiano, E. Ovalle, A. D. Danilov (2006b), Long-term trends in foF2: A comparison of various methods, *Journal of Atmospheric and Solar-*

Terrestrial Physics 68, pp. 1854-1870.

Lean, J. L., J. M. Picone, J. T. Emmert, and G. Moore (2006), Thermospheric densities derived from spacecraft orbits: Application to the Starshine satellites, *J. Geophys. Res.*, *111*, A04301, doi:10.1029/2005JA011399.

Lindzen, R. S. (1971), Tides and gravity waves in the upper atmosphere, in *Mesoapheric Models and Related Experiments*, edited by G. Fiocco, 198pp., D. Reidel, Hingham, Mass.

Lindzen, R. S. (1981), Turbulence and stress owing to gravity wave and tidal breakdown, *J. Geophys. Res., 86*, 9707-9714.

Liu, H., and H. Lühr (2005), Strong disturbance of the upper thermospheric density due to magnetic storms: CHAMP observations, *J. Geophys. Res.*, *110*, A09S29, doi:10.1029/2004JA010908.

Liu, H., H. Lühr, V. Henize, and W. Köhler (2005), Global distribution of the thermospheric total mass density derived from CHAMP, *J. Geophys. Res.*, *110*, A04301, doi:10.1029/2004JA010741.

Lübken F. J. (1997), Seasonal variation of turbulent energy dissipation rates at high latitudes as determined by in situ measurements of neutral density fluctuations, *J. Geophys. Res., 102*, 13441-13456.

Lyon, J. G., J. A. Fedder, and C. M. Mobarry (2004), The Lyon-Fedder-Mobarry (LFM) Global MHD Magnetospheric Simulation Code, J. Atm. And Solar-Terrestrial Phys., 66, Issue 15-16, 1333-1350.

Manson J. E. (1977), The solar spectrum between 10 and 300 Å, The Solar Output and its

Variation, Edited by White.

Marcos, F. A., H. B. Garrett, K. S. W. Champion and J. M. Forbes (1977), Density variations in lower thermosphere from analysis of AE-C accelerometer measurements. *Planet. Space Sci. 25* 5, pp. 499–507.

Marcos, F. A., J. O. Wise, M. J. Kendra, N. J. Grossbard, and B. R. Bowman (2005), Detection of a long-term decrease in thermospheric neutral density, *Geophys. Res. Lett., 32*, L04103, doi:10.1029/2004GL021269.

Marsh, D. R., S. C. Solomon, and A. E. Reynolds (2004), Empirical model of nitric oxide in the lower thermosphere, J. Geophys. Res., 109, A07301, doi:10.1029/2003JA010199.

Mayr, H. G., and H. Volland (1971), Semiannual variation in the neutral composition, *Ann. Geophys., 27*, 513.

Mayr, H. G., and H. Volland (1972), Theoretical model for the latitude dependence of the annual and semiannual variations, *J. Geophys. Res., 77*, 6774.

Mayr, H. G., I. Harris, and N. W. Spenser (1978), Some properties of upper atmospheric dynamics, *Rev. Geophys. Space Phys., 16*, 539-565.

Mendillo, M, C.L. Huang, X. Pi, H. Rishbeth, and R. Meier (2005), The global ionospheric asymmetry in total electron content, *J. Atmos. Terr. Phys.,67*, 1377-1387.

Mikhailov, A. V., and D. Marin (2000), Geomagnetic control of the foF2 long-term trends, *Annales Geophysicae 18*, pp. 653–665.

Mikhailov, A. V., and D. Marin (2001), An interpretation of the foF2 and hmF2 long-term trends in the framework of the geomagnetic control concept, *Annales Geophysicae 19*, pp. 733–748.

Millward, G. H., R. J. Moffett, S. Quegan, and T. J. Fuller-Rowell (1996), A Coupled Thermosphere-Ionosphere-Plasmasphere Model (CTIP), *Solar Terrestrial Energy Program (STEP) Handbook*, edited by R. W. Schunk, pp. 239-279.

Nagy, A. F., and P. M. Banks (1970), Photoelectron fluxes in the ionosphere, *J. Geophys. Res., 75*, 6260.

Norton, R. B., and R. G. Roble (1974), Molecular oxygen between 95 and 210 km determined from Solrad 10 Occultation measurements, *J. Geophys. Res., 79*, 3876.

Paetzold, H. K., and H. Zschörner (1961), An annual and a semiannual variation of the upper air density, *Pure Appl. Geophys, 48*, 85.

Picone, J. M., A. E. Hedin, D. P. Drob, and A. C. Aikin (2002), NRLMSISE-00 empirical model of the atmosphere: Statistical comparisons and scientific issues, *J. Geophys. Res.*, *107(A12)*, 1468, doi:10.1029/2002JA009430.

Picone, J. M., J. T. Emmert, and J. L. Lean (2005), Thermospheric densities derived from spacecraft orbits: Accurate processing of two-line element sets, *J. Geophys. Res., 110*, A03301, doi:10.1029/2004JA010585.

Potter, W. E., D. C. Kayser, H. C. Brinton, L. H. Brace, and M. Oppenheimer (1977), Comparison of measured and calculated thermospheric molecular oxygen densities, *J. Geophys. Res., 82,* 5243.

Prölss, G. W., and U. von Zahn (1977), on the global morphology of negative ionospheric storms, *Space Res., 17*, 433.

Qian, L., R. G. Roble, S. C. Solomon, and T. J. Kane (2006), Calculated and observed climate change in the thermosphere, and a prediction for solar cycle 24, *Geophys. Res. Lett.*, 33, L23705, doi:10.1029/2006GL027185.

Qian, L., S. C. Solomon, R. G. Roble, B. R. Bowman, and F. A. Marcos (2007), Thermospheric neutral density response to solar forcing, *Adv. Space Res*., submitted.

Rao, D. N., M. V. Ratnam, T. N. Rao, and S. V. B. Rao (2001), Seasonal variation of vertical eddy diffusivity in the troposphere, lower stratosphere and mesosphere over a tropical station, *Ann. Geophys., 19*, 975-984.

Rees, D., T. J. Fuller-Rowell (1988), Understanding the transport of atomic oxygen in the thermosphere using a numerical global thermospheric model, *Planet. Space Sci., 36*, 935.

Rees, D., T. J. Fuller-Rowell (1990), Numerical simulations of the seasonal/latitudinal variations of atomic oxygen and nitric oxide in the lower thermosphere and mesosphere, *Adv. Space Res., 12*, 59.

Reigber, C., R. Bock, C. Förste, L. Grunwaldt, N. Jakowski, H. Lühr, P. Schwintzer, and C. Tilgner (1996), CHAMP Phase B executive summary, *Sci. Tech. Rep.* STR96/13, GeoForschungszentrum Potsdam, Potsdam, Germany.

Reiff, P. H., and J. G. Luhman (1986), Solar wind controls of the polar cap voltage, Proceedings of solar Wind Magnetosphere Coupling, editors Y. Kamide and J.A. Slaven, D. Riedel, Publishing Co., Boston, P. 453.

Richards, P. G., and D. G. Torr (1984), An investigation of the consistency of the ionospheric measurements of the photoelectron flux and solar EUV flux, *J. Geophys. Res., 89,* 5625.

Richards, P. G., and D. G. Torr (1988), Ratio of photoelectron to EUV ionization rates for aeronomic studies, *J. Geophys. Res., 93*, 4060.

Richards, P. G., J. A. Fennelly, and D. G. Torr (1994), EUVAC: A solar EUV flux model for aeronomic calculations, *J. Geophys. Res., 99*, 8981 – 8992.

Richmond, A. D., M. Blanc, B. A. Emery, et al. (1980), An empirical model of quiet-day ionospheric electric fields at middle and low latitudes, *J. Geophys. Res., 85*, 4658-4664.

Richmond, A. D. (1992), Assimilative mapping of ionospheric electrodynamics, *Adv. Space Res., Vol 12*, No 6, pp (6)59-(6)68.

Richmond, A. D., E. C. Ridley, and R. G. Roble (1992), A thermosphere/ionosphere general circulation model with coupled electrodynamics, *Geophys. Res. Lett.*, *19*, 601.

Richmond, A. D. (1995), Ionospheric electrodynamics using magnetic apex coordinates, *J. Geomagn. Geoelectr., Vol 47*, 191-212.

Rishbeth, H. (1988), Basic Physics of the ionosphere: a tutorial review, *Proc. Inst. Elect. Rad. Engrs. 58*, S207-223.

Rishbeth, H. (1990), A greenhouse effect in the ionosphere? *Planet. Space Sci.* **38**, 945-948.

Rishbeth, H., and R. G. Roble (1992), Cooling of the upper atmosphere by enhanced greenhouse gases: Modeling of thermospheric and ionospheric effects, *Planet. Space Sci., 40*, 1011-1026.

Rishbeth, H. (2006), F-region links with the lower atmosphere? *J. Atmos. Terr. Phys.,68*, 469-478.

Roble, R. G., E. C. Ridley, and R. E. Dickinson (1982), Global circulation and temperature structure of the thermosphere with high latitude convection, *J. Geophys. Res., 87*, 1599-1614.

Roble, R. G., and E. C. Ridley (1987), An auroral model for the NCAR thermosphere general circulation model (TGCM), *Annales. Geophysicae, 5A*, (6), 369-382.

Roble, R. G., and E. C. Ridley, and R. E. Dickinson (1987), On the global mean structure of the thermosphere, *J. Geophys. Res., 92*, 8745-8758.

Roble, R. G., E. C. Ridley, A. D. Richmond, R. E. Dickinson (1988), A coupled thermosphere/ionosphere general circulation model, *Geophys. Res. Lett.*, *15*, 1325.

Roble, R. G., and R. E. Dickinson (1989), How will changes in carbon dioxide and methane modify the mean structure of the mesosphere and thermosphere? *Geophys. Res. Lett.*, *16*, 1144-1441.

Roble, R. G. (1993), Energetics of the mesosphere and lower thermosphere, *Chapman Conference on the Mesosphere and Thermosphere*, Asilomar.

Roble, R. G. and E. C. Ridley (1994), Thermosphere-ionosphere-mesosphere-electrodynamics general circulation model (TIME-GCM): Equinox solar min simulations, 30-500 km, *Geophys. Res. Lett., 21*, 417.

Roble, R. G. (1995), Energetics of the mesosphere and thermosphere, in *The Upper Mesosphere and Lower Thermosphere: A Review of Experiment and Theory, Geophys. Mono., 87*, 1-21.

Rodgers E. M., S. M. Bailey, H. P. Warren, T. N. Woods, F. G. Eparvier (2006), Soft X-ray irradiances during solar flares observed by TIMED-SEE, *J. Geophys. Res., 111*, A10S13, doi:10.1029/2005JA011505.

Russell, C. T., and R. L. McPherron (1973), Semiannual variation of geomagnetic activity, *J. Geophys. Res., 78*, 92.

Sasi, M. N., L. Vijayan (2001), Turbulence characteristics in the tropical mesosphere as obtained by MST radar at Gadanki (13.5^{o}N, 79.2^{o}E), *Ann. Geophys., 19*, 1019-1025.

Schatten, K. H. (2005), Fair space weather for solar cycle 24, *Geophys. Res. Lett.*, *32*, L21106, doi:10.1029/2005GL024363.

Schuchardt, K. G. H., and P. W. Blum (1977), Correlation between the homopause height and density variations in the upper atmospheres, *Space Res., 13*, 335.

Sello, S. (2003), Solar cycle activity: A preliminary prediction for cycle #24 *Astron. and Astrophys.*, *410*, 691.

Shimazaki, T. (1971), Effective eddy diffusion coefficient and atmospheric composition in the lower thermosphere, *J. Atmos. Terr. Phys., 33*, 1383.

Smith E. V. P., D. M. Gottlieb (1974), Solar flux and its variation, *Space Science Reviews* 16, 771-802.

Solomon, S, and R. R. Garcia (1984), On the distributions of long-lived tracers and

chlorine species in the middle atmosphere, *J. Geophys. Res., 89*, 1633-1644.

Solomon, S. C., P. B. Hays, and V. J. Abreu (1988), The auroral 6300 Å emission: Observations and modeling, *J. Geophys. Res., 93*, 9867-9882.

Solomon, S. C., and V. J. Abreu (1989), The 630 nm dayglow, *J. Geophys. Res., 94*, 6817-6824.

Solomon, S. C. (1991), Optical aeronomy, *U.S. Natl. Rep. Int. Union Geod. Geophys. 1987-1990, Rev. Geophys., 29,* 1089.

Solomon, S. C., C. A. Barth, and S. M. Bailey (1999), Auroral production of nitric oxide measured by the SNOE Satellite, Geophys. Res. Lett., 26, 1259.

Solomon, S. C., S. M. Bailey, and T. N. Woods (2001), Effect of solar soft X-rays on the lower ionosphere, *Geophys. Res. Lett.*, 28(11), 2149–2152.

Solomon, S. C., L. Qian, G. R. Gladstone, S. M. Bailey, and E. M. Rogers (2005), Thermospheric Response to Solar EUV during Quiet and Flare Conditions, Eos Trans. AGU, 86(52), Fall Meet. Suppl., Abstract SA43A-1108.

Solomon, S. C., and L. Qian (2005), Solar extreme-ultraviolet irradiance for general circulation models, *J. Geophys. Res.*, 110, A10306, doi:10.1029/2005JA011160.

Storz, M. F., B. R. Bowman, and J. I. Branson (2002), High Accuracy Satellite Drag Model (HASDM), paper AIAA 2002-4886, paper presented at Astrodynamics Specialist Conference, Am. Inst. of Aeronaut. and Astronaut., Monterey, Calif., Aug.

Strickland, D. J., and G. E. Thomas (1976), Global atomic oxygen density derived from Ogo-6 1304 A airglow measurements, *Planet. Space Sci., 24*, 313.

Sutton, E. K., J. M. Forbes, and R. S. Nerem (2005), Global thermospheric neutral density and wind response to the severe 2003 geomagnetic storms from CHAMP accelerometer data, *J. Geophys. Res.*, *110*, A09S40, doi:10.1029/2004JA010985.

Svalgaard, L., W. E. Cliver, and Y. Kamide (2005), Sunspot cycle 24: smallest cycle in 100 years? *Geophys. Res. Lett.*, *32*, L01104, doi:10.1029/2004GL021664.

Taeusch, D. R., G. R. Carignan, and C. A. Reber (1971), Neutral composition variation above 400 km during a magnetic storm, *J. Geophys. Res., 76,* 8318.

Tapley, B. D., S. Bettadpur, M. Watkins, and C. Reigber (2004), The gravity recovery and climate experiment: Mission overview and early results, *Geophys. Res. Lett., 31*, L09607, doi:10.1029/2004GL019920.

Tobiska, W. K., and C. A. Barth (1990), A solar EUV flux model, *J. Geophys. Res., 95*, 8243.

Tobiska, W. K. (1991), Revised solar extreme ultraviolet flux model, *J. Atmos. Terr. Phys., 53*, 1005.

Tobiska, W. K., and E. G. Eparvier (1998), EUV97: Improvements to EUV irradiance modeling in the soft X-rays and FUV, *Solar Phys., 177*, 147.

Tobiska, W. K., T. N. Woods, F. Eparvier, R. Viereck, L. Floyd, D. Bouwer, G. Rottman, O. R. White, and R. F. Donnelly (2000), The SOLAR2000 empirical solar irradiance model and forecast tool, *J. Atm. Solar Terr. Phys., Volume 62, Issue 14*, 1233-1250.

Tobiska, W. K., S. D. Bouwer, B. R. Bowman (2006), The development of new solar indices for use in thermospheric density modeling, AIAA 2006-6165.

Torr, M. R., D. G. Torr, R. A. Ong, and H. E. Hinteregger (1979), Ionization frequencies for major thermospheric constituents as a function of solar cycle 21, *Geophys. Res. Lett., 6*, 771.

Volland, H. and H. G. Mayr (1973), Note on the semiannual effect in the thermosphere, *J. Geophys. Res., 78*, 3991.

Wagner, W. J. (1988), Observations of 1-8Å solar X-ray variability during solar cycle 21, *Adv. Space Res*. Vol 8, No 7, pp. (7)67-(7)76.

Walker, J. C. G. (1965), Analytic representation of upper atmosphere densities based on Jacchia's static diffusion models, *J. Atmos. Sci., 22*, 462.

Walterscheid, R. L. (1982), The semiannual oscillation in the thermosphere as a conduction mode, *J. Geophys. Res., 87*, 10527.

Wang, W., T. Killeen, A. Burns, R. G. Roble (1999), A high-resolution, three-dimensional, time-dependent nested grid model of the coupled thermosphere-ionosphere, *J. Atmos. Terr. Phys. 61*, 385.

Weimer, D. R. (2001), An improved model of ionospheric electric potentials including substorm perturbations and application to the Geospace Environment Modeling November 24, 1996, event, *J. Geophys. Res., 106,* 407-416.

Wilson G. R., D. R. Weimer, J. O. Wise, F. A. Marcos (2006), Response of the thermosphere to Joule heating and particle precipitation, J. Geophys. Res., 111, A10314, doi:10.1029/2005JA011274.

Woods, T. N., G. J. Rottman, S. M. Bailey, S. C. Solomon (1998), and J. Worden, Solar extreme ultraviolet irradiance measurements during solar cycle 22, *Solar Physics, 177*, 133-146.

Woods, T. N., and G. J. Rottman (2002), Solar ultraviolet variability over time periods of aeronomic interest, in Comparative Aeronomy in the Solar System, Geophys. Monogr. Ser., vol. 130, edited by M. Mendillo, A. F. Nagy, and J. H. Waite, AGU, Washington, D. C.

Woods, T. N., F. G. Eparvier, S. M. Bailey, P. C. Chamberlin, J. Lean, G. J. Rottman, S. C. Solomon, W. K. Tobiska, and D. L. Woodraska (2005), Solar EUV Experiment (SEE): Mission overview and first results, J. Geophys. Res., 110, A01312, doi:10.1029/2004JA010765.

VITA

Liying Qian

Educations:

1984 – 1988	BS in Atmospheric Sciences Nanjing University, China
1988 – 1991	MS in Atmospheric Sciences Institute of Atmospheric Physics, Chinese Academy of Science, China
1994 – 1998	ME in Computer Sciences and Engineering The Pennsylvania State University, USA
1994 – 2007	PhD in Meteorology The Pennsylvania State University, USA

Appointments:

1991 – 1994	Research Associate Institute of Atmospheric Physics, Chinese Academy of Science, China
1999 – 2001	Software Engineer for Meteorological Applications, IPS MeteoStar, USA
2002 – present	Associate Scientist High Altitude Observatory, National Center for Atmospheric Research

Research Interests:

I am interested in upper atmospheric physics, chemistry, dynamics, and electrodynamics. In particular, I am interested in studying thermospheric neutral density and its variations in time scale ranging from hours, daily, solar rotational, solar cycle, to climatological, using upper atmospheric general circulation models and observational data.

Relevant Publications:

Qian, L., R. G. Roble, S. C. Solomon, and T. J. Kane (2006), Calculated and observed climate change in the thermosphere, and a prediction for solar cycle 24, *Geophys. Res. Lett.*, 33, L23705, doi:10.1029/2006GL027185.

Solomon, S. C., and L. Qian (2005), Solar extreme-ultraviolet irradiance for general circulation models, *J. Geophys. Res.*, *110*, A10306, doi:10.1029/2005JA011160.

Qian, L., G. S. Young, W. M. Frank (1998), A Convective Wake Parameterization Scheme for Use in General Circulation Models, *Monthly Weather Review***,** Vol. 126, No. 2, pp. 456–469**.**

Qian, L., S. C. Solomon, R. G. Roble, B. R. Bowman, and F. A. Marcos (2007), Thermospheric neutral density response to solar forcing, *Adv. Space Res*., submitted.